Growth of Epitaxial Graphene: Theory and Experiment

H. Tetlow[†], J. Posthuma de Boer[‡], I. J. Ford[♯], D. D. Vvedensky[‡], J. Coraux[♮] and L. Kantorovich[†1]

[†] *Physics Department, King's College London, Strand, London WC2R 2LS, United Kingdom*
[‡] *The Blackett Laboratory, Imperial College London, London SW7 2AZ, United Kingdom*
[♮] *Université Grenoble Alpes, Institut NEEL, F-38042, Grenoble, France, and CNRS, Institut NEEL, F-38042, Grenoble, France*
[♯] *Department of Physics and Astronomy and London Centre for Nanotechnology, University College London, Gower Street, London WC1E 6BT, United Kingdom.*

Abstract

A detailed review of the literature for the last 5-10 years on epitaxial growth of graphene is presented. Both experimental and theoretical aspects related to growth on transition metals and on silicon carbide are thoroughly reviewed. Thermodynamic and kinetic aspects of growth on all these materials, where possible, are discussed. To make this text useful for a wider audience, a range of important experimental techniques that have been used over the last decade to grow (e.g. CVD, TPG and segregation) and characterize (STM, LEEM, etc.) graphene are reviewed, and a critical survey of the most important theoretical techniques is given. Finally, we critically discuss various unsolved problems related to growth and its mechanism which we believe require proper attention in future research.

Contents

1 Introduction **3**

2 Fundamentals of nucleation and growth **5**
2.1 Main processes . . . 5
2.2 The nucleation process . . . 6
2.3 Thermodynamics and kinetics of growth . . . 8

3 Experimental techniques **9**
3.1 Scanning tunneling microscopy (STM) . . . 11
3.2 Atomic force microscopy (AFM) . . . 12
3.3 Transmission electron microscopy (TEM) . . . 13
3.4 Low-energy and photoemission microscopy (LEEM and PEEM) . . . 14
3.5 Surface-sensitive electron diffraction (LEED and RHEED) . . . 15
3.6 Scanning electron microscopy (SEM) . . . 16
3.7 Raman spectroscopy and microscopy . . . 17
3.8 Surface-sensitive X-ray diffraction (SXRD) . . . 18
3.9 X-ray and ultraviolet photoelectron spectroscopy (XPS/UPS) . . . 18
3.10 Near-edge X-ray absorption fine structure (NEXAFS) . . . 19
3.11 X-ray standing waves (XSW) . . . 20

4 Simulation methods **20**
4.1 Atomistic modeling methods . . . 20
4.1.1 Density Functional Theory . . . 21
4.1.2 Dispersion interaction within DFT methods . . . 23
4.1.3 Tight Binding and Empirical Potentials based methods . . . 24

[1] The corresponding author

4.1.4 Formation energies . . . 25
4.1.5 Nudged Elastic Band Method . . . 26
4.2 Simulations of dynamics of growth processes . . . 26
4.2.1 Molecular dynamics simulations . . . 26
4.2.2 Kinetic Monte Carlo simulations . . . 27
4.2.3 Grand Canonical Monte Carlo simulations . . . 29
4.3 Continuum equations . . . 29
4.3.1 Burton-Cabrera-Frank Theory and Phase-field Method . . . 29
4.3.2 Rate Equations . . . 30

5 Growth Methods **31**
5.1 Chemical Vapor Deposition (CVD) . . . 31
5.1.1 Nucleation . . . 32
5.1.2 Island morphology and growth . . . 33
5.1.3 CVD with carbide as a transient state . . . 37
5.2 Temperature Programmed Growth (TPG) . . . 38
5.2.1 Method . . . 38
5.2.2 Observations . . . 39
5.2.3 Ripening . . . 40
5.2.4 Cluster Formation . . . 41
5.2.5 Using TPG to Optimize Further Growth . . . 42
5.3 Carbon Feedstock . . . 43
5.4 Segregation . . . 45
5.4.1 Ru(0001) . . . 45
5.4.2 Nickel . . . 46
5.5 SiC Sublimation . . . 48
5.5.1 Graphene on SiC . . . 48
5.5.2 The Growth Process . . . 49
5.5.3 Multilayer Growth . . . 52

6 Structure of Graphene on Substrates **52**
6.1 Metallic Substrates . . . 52
6.1.1 Ru(0001) . . . 54
6.1.2 Rh(111) . . . 56
6.1.3 Re(0001) . . . 57
6.1.4 Ir(111) . . . 58
6.1.5 Au(111) . . . 59
6.1.6 Pt(111) . . . 59
6.1.7 Ni(111) and Co(0001) . . . 60
6.1.8 Cu(111) and Cu(100) . . . 60
6.2 SiC . . . 60

7 Simulation of graphene growth on metals **64**
7.1 Rate Equation Analysis of Growth . . . 65
7.2 Atomistic approaches from first principles . . . 67
7.2.1 Dehydrogenation . . . 67
7.2.2 Carbon monomers and dimers on metal surfaces . . . 69
7.2.3 Early stages of growth: small C clusters . . . 72
7.2.4 Atomistic Attachment Processes . . . 79
7.3 Role of defects . . . 83
7.3.1 Defects in free standing graphene . . . 84
7.3.2 Defects in graphene on transition metal surfaces . . . 85
7.4 Attempts to simulate the growth . . . 89

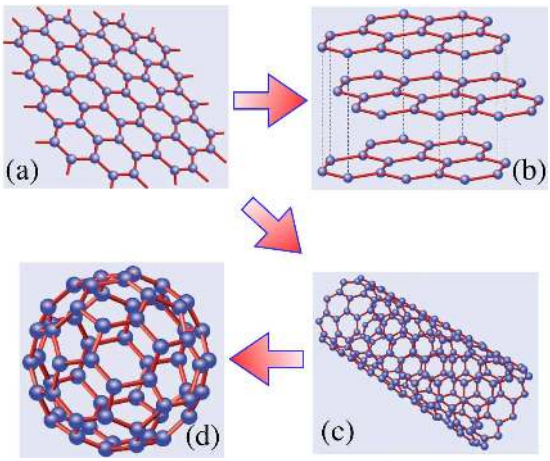

Figure 1: Various form of carbon: (a) graphene; (b) graphite; (c) nanotube; (d) buckyball. [Adapted with permission from [2].]

8 Simulations of graphene growth from silicon carbide **95**
8.1 Explorations into growth of graphene on SiC 95
8.2 Simulations of growth dynamics 98
8.3 Finger-like growth: phenomenological models 102

9 Discussion **103**

1. Introduction

Graphene, one of the allotropic forms of elemental carbon, is a planar monolayer of carbon atoms arranged on two-dimensional hexagonal lattice with a carbon-carbon bond length of 0.142 nm [1]. Graphene is also the conceptual building block for some of these allotropes, including graphite, which is layered graphene, as well as nanotubes, which are graphene sheets that are seamlessly rolled up into cylinders with nanometre-scale diameters, and buckminsterfullerene ("buckyballs"), which are graphitic molecular cages (Fig. 1).

While the existence of graphene has been known for some time, the name "graphene" was formally adopted by IUPAC only in 1997 as a replacement for the term "graphitic layers" in their *Compendium of Chemical Technology*. The explosive growth in graphene research began in 2004-2005 with the publication of a series of papers by several groups, pioneered by those at Manchester in the United Kingdom [3, 4, 5] and the Georgia Institute of Technology [6] and Columbia [7] in the United States. There are several reasons for this worldwide interest in graphene, above all the remarkable electronic, mechanical, optical, and transport properties [8] that have generated many avenues for applications [9, 10, 11, 12, 13, 14]. For example, graphene is optically transparent (between 70%–97% transparency, depending on thickness), and has outstandingly high electronic and thermal transport and thermal conductivity. The pace of progress has been so frantic that, in May 2011, the British Broadcasting Corporation (BBC) dubbed graphene the "miracle material" [15]. Additionally, there was already a community of scientists working on carbon materials, most notably nanotubes and fullerenes, that was quick to recognize the potential of graphene. Finally, small samples of graphene could be produced by mechanical exfoliation (the "scotch tape" method) [3]. Though simple and cost-effective and ideally suited for laboratory work, this method is unsuitable for the amount of material that would be required for mass production. The search for alternative methods for producing large amounts of graphene has been attempted in many research groups worldwide over the last decade or so and will be discussed below. Government agencies have been quick to seize the potential of graphene by funding several large-scale programs: the European Union is funding a 10-year 1.35 billion euros flagship program on graphene, South Korea is spending $350 million on commercialization initiatives, and the United Kingdom is investing £50 million in a commercialization hub.

The remarkable electronic properties of graphene are due ultimately to its crystal structure of a honeycomb lattice of carbon atoms, which can be regarded as two interpenetrating triangular lattices. The s^2p^2 configuration of atomic carbon hybridizes in graphene into a configuration in which the $2s$, $2p_x$, and $2p_y$

orbitals of each carbon are sp^2-hybridized to form in-plane σ bonds with its three nearest neighbors. The remaining p_z orbital is oriented along the z-direction, perpendicular to the graphene plane, and forms π-bonds which merge with neighboring $2p_z$ orbitals to form delocalized states across the graphene plane. The ease of movement of electrons in these π states is responsible for the extraordinary electrical conductivity of graphene. The graphene unit cell has two π orbitals forming two bands that may be thought of as bonding (the lower energy valence band) and anti-bonding (the higher energy conduction band) in nature. These are referred to as π and π^* bands, respectively. The gap between the π and π^* bands closes at the K-points of the Brillouin zone, resulting in an energy-momentum dispersion which is approximately *linear* around the K points. This behavior is one of the many fascinating properties of graphene and is largely responsible for much of the excitement about this material. Interestingly, this basic picture of the electronic bands of graphene was known as far back as 1947, when Wallace [16] used a two-band tight-binding model incorporating the bonding and anti-bonding π-bands to obtain these results for a single graphite layer.

But there are other noteworthy properties of graphene. The σ bonds between the relatively light carbon atoms are quite strong, creating a bonding situation similar to that in diamond: the speed of sound in graphene is very high, and so is its thermal conductivity, being mainly governed by phonons. The conductivity is in fact comparable to that of diamond and an order of magnitude larger than in conventional semiconductors, which can be harnessed for applications. In particular, graphene could be useful for applications in electronic devices, since a high thermal conductivity facilitates the diffusion of heat to the contacts and allows for more compact circuits. Another consequence of the in-plane bonding is that graphene has a very high spring constant $K \sim 50$ eV Å^{-2} [17], elastic modulus $Y \sim 1$ TPa [18], and tensile strength of 130 GPa [18], making graphene the strongest material ever measured. Various combinations of these properties can be used in applications either to replace existing materials, or to create new device concepts. However, a major obstacle in the transfer of proof-of-concept from the laboratory to the commercial sector is the production of high-quality graphene in sufficient quantities.

The initial studies which provided the first glimpses of the intriguing properties of graphene were made on relatively small samples produced by a mechanical exfoliation method developed by Geim and Novoselov [3]. A highly oriented pyrolytic graphite (HOPG) precursor was subjected to oxygen plasma etching to create 5 μm-deep mesas which were then pressed into a layer of photoresist. The photoresist was baked and the HOPG cleaved from the resist. Scotch tape was used to repeatedly peel flakes of graphite from the mesas. These thin flakes were then released in acetone and captured on the surface of Si/SiO_2. Mechanical exfoliation can produce graphene samples with areas up to 1 mm^2 with good electrical properties. The ease and cost-effectiveness of mechanical exfoliation is a key factor in the rapid expansion of fundamental studies of graphene. However, this is time-consuming and suited only to small-scale production. The realization of the potential of graphene, for example, as a post-silicon electronic material, will require the development of techniques for the production of high-quality large-area sheets of graphene.

An attractive alternative to mechanical exfoliation is the epitaxial growth of graphene on a hexagonal substrate. Considerable progress has been achieved in this direction, using both silicon carbide and close-packed metals as the substrate. The thermal decomposition of SiC consists of heating the sample in ultra-high vacuum (UHV) to temperatures between 1273 K and 1773 K, which causes Si to sublimate, leaving a carbon-rich surface. This technique is capable of generating wafer-scale graphene layers and is potentially of interest to the micro-electronics industry. In contrast to the thermal decomposition of SiC, where carbon is already present in the substrate, in chemical vapor deposition (CVD), carbon is supplied in gas form and a metal is used as both catalyst and substrate to grow the graphene layer. CVD more closely resembles the epitaxial methods that have been developed since the 1960s to produce films of semiconductors, metals, and other materials, and some considerable work has been done to date to understand the epitaxial growth of graphene. Still, there have been few systematic studies of the atomistic formation kinetics of epitaxial graphene by any method on any substrate, so no coherent picture of the growth mechanisms is available. It is the purpose of this review to assemble the information available from theory and experiment on the epitaxial kinetics of graphene in the light of the vast work that has been done on other materials and to highlight where additional work is required to provide a more complete understanding of graphene growth kinetics.

The review covers both experimental and theoretical aspects of the growth of graphene. The idea behind this was that we wanted to present first the existing experimental picture, limiting ourselves mainly to the results relevant for understanding of growth and kinetics; then we review existing literature with the idea to rationalize, as much as possible, the substantial volume of various experimental results. Therefore, in

Section 3 we briefly review the main experimental techniques that have been employed to study and grow graphene and then we consider in some considerable detail those which became popular over the last decade. These include CVD, temperature programmed growth (TPG) and segregation based methods, as well as growth of graphene by sublimation from SiC. We believe that these sections should be useful mostly for non-experimentalists wishing to understand better how theory can be compared with experiment. Then in Section 6 we discuss mostly structural properties of graphene on a number of metal surfaces; in particular, we consider such surfaces as Ru(0001), Rh(111), Ir(111), Pt(111), Ni(111), Cu(111) and Cu(100). In Section 4 we briefly review some of the existing simulation techniques which have proven extremely useful in understanding graphene growth. These include density functional theory (DFT), tight binding (TB) and empirical (classical) potential methods, which have been found useful in obtaining relaxed structures, formation energies and thermodynamic properties. These are the subject of Section 4.1. In Section 4.2 the main techniques that are useful in studying the dynamics of growth are briefly reviewed, such as molecular dynamics (MD), kinetic Monte Carlo (KMC) and continuum methods. We believe this introductory section should be useful for experimentalists wishing to appreciate the capabilities of theory, and how theory may assist their experiments in providing the necessary background for understanding growth and hence devising and optimizing the growth methods they use. This is followed by our review of various theoretical results relevant to graphene growth. We first discuss available results relevant for CVD and TPG growth. In Section 7.1 rate equation based methods are considered. Then in Section 7.2 we discuss various atomistic approaches, mostly based on first principles DFT simulations, that have been used to date for studying various stages of graphene growth. These include dehydrogenation of hydrocarbon molecules, early stages of the nucleation and growth of carbon clusters, attachment of carbon species to existing graphene islands and the role of defects in free-standing as well as metal-supported graphene. Then in Section 7.4 we review several dynamic approaches that have been explored so far to simulate the process of growth itself. A special Section 8 is devoted to simulations of growth of graphene by the sublimation of SiC where we present a variety of results from structure studies up to phenomenological growth models. Finally, a general discussion and conclusions are contained in Section 9 where we summarize the main current achievements of both theory and experiment in understanding of graphene growth, and discuss unsolved problems and possible directions of further studies.

There have been many reviews written on all aspects of graphene [8, 19, 20, 11, 21, 22, 23, 24, 25, 26, 12, 27, 28, 29, 30, 31, 32, 33, 34, 35], but this is the first review devoted exclusively to growth.

2. Fundamentals of nucleation and growth

2.1. Main processes

Figure 2 illustrates typical processes that occur during epitaxy. Depending on the material and the growth method, some of these processes may need to be amended. We begin with deposition. This an experimentally controllable process both in terms of the deposition rate and the species being deposited. In the simplest case, the deposited species is the atomic (or molecular) constituent of the growing material; we assumed in the Figure that these are polyatomic precursors E since this is what is frequently used in growing graphene. In the latter case, the reaction kinetics become important, as certain surface sites may dominate catalytic activity, and the reaction products (shown as hydrogen molecules H_2) must desorb from the surface. Even the atoms of the growing material may desorb from the surface at high temperatures (not shown). After deposition and, possibly, decomposition kinetics, the atomic species M diffuse on the surface. Even such an ostensibly simple process might have complex steps, such as exchange processes, or even involve the formation of dimers D or larger carbon clusters C that migrate along the surface. The concentration of diffusing species increases as deposition proceeds and eventually attains a level where islands G can nucleate. There are several processes by which this might occur. In *homogeneous nucleation*, islands are formed by the collision of two or more migrating species which then bind to form an island. Depending on the temperature, this island may be stable, or may break up. Eventually, the concentration of the migrating species is sufficient to induce island formation, however many individual units are required. In *heterogeneous nucleation*, the rate of nucleation is increased by the presence of a surface defect such as a vacancy, a screw dislocation, or a pre-existing step edge. Island size distributions can be used to study nucleation mechanisms and, in favorable circumstances, to identify the nucleation mechanism.

Once the islands are formed, they can grow by the capture of migrating units. This attachment process may have additional barriers. Similarly, the reverse of this process, detachment, is the process by which atoms are separated from an island. The shapes of islands can be strongly influenced by edge diffusion, that

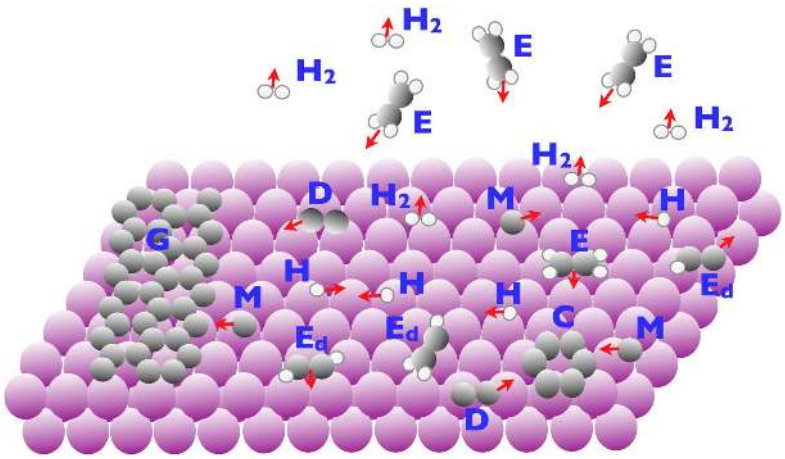

Figure 2: Schematic representation of fundamental processes during epitaxy: hydrocarbon molecules E are deposited on the surface, undergo decomposition via a series of dehydrogenation reactions giving rise to various C_xH_y species shown as E_d, and H atoms. The new species are all able to diffuse across the surface. Smaller carbon species M and D form and diffuse on the surface, aggregating into larger clusters C. H atoms of the original molecule migrate on the surface, and form H_2 molecules that evaporate from the surface. Finally, some of the species like M and D, or even their bigger clusters C, may attach to the island G at its edge. Other processes (not shown) are also possible based on e.g. diffusion of atoms along the edge of an island, nucleation of second- and higher layers on the islands, downward movement of atoms adsorbed on top of islands to lower layers, and the break up, or dissolution, of islands.

is, the motion of atoms around the edge of an island. At low temperatures, some systems exhibit fractal islands which, despite having a large surface energy, cannot reduce it by any type of rearrangement because surface migration is too slow. At higher temperatures, edge diffusion becomes effective at reducing the edge lengths of islands, which are now more compact. As the islands grow, they become large enough such that deposition on the islands becomes appreciable. Two processes then become important. The first is downward hops when species (e.g. atoms) diffuse down from the upper layers of the islands. If there is no barrier at step edges, then the atoms can hop down from an island to the terrace below with no additional impediment. If there is an additional barrier, the atoms have a longer residence time on the island, which builds up their concentration and makes second-layer nucleation more likely.

2.2. The nucleation process

Beginnings are often complicated and messy, and difficult to understand after the event, irrespective of whether they relate to historical, social or scientific processes. The formation, or nucleation, of new materials or phases of matter lies firmly within this category. What makes nucleation hard to pin down is the relative inaccessibility of the process to experimental investigation. Nucleation events involve the coming together of precursor species on a molecular scale, and in a quasi-random fashion, with a successful event often lasting a very short time from start to finish. It is akin to a chemical reaction scheme with many intermediate steps, some of which are very rare. Added to this is the relative difficulty of placing the process within a fully developed theoretical framework, together with the sensitivity of calculations to the details of the assumed intermolecular interactions. Yet theoretical progress can be made in tandem with experiment and the nucleation of phase transformations in materials science is now becoming better understood as a result of the new richness of experimental methods on the nanoscale.

Our objective is to review current understanding of the nucleation and growth of islands of graphene on various substrates, driven by a range of thermal and chemical processing schemes, but it is necessary to start with a general survey of the basic ideas that are used in discussions of phase transformations [36, 37]. Our allusion to a sequence of chemical reactions is a perfectly valid kinetic description, but on top of this a thermodynamic framework has been built that provides a simplifying viewpoint. We shall start, as is often the case, with an appeal to the second law of thermodynamics, an imperative placed on the universe to increase its entropy, or equivalently, a requirement that systems in weak contact with their surroundings should evolve to reduce a free energy or grand potential of some kind [38]. Of course, according to a strict interpretation in equilibrium thermodynamics, free energies properly characterize equilibrium states, and not

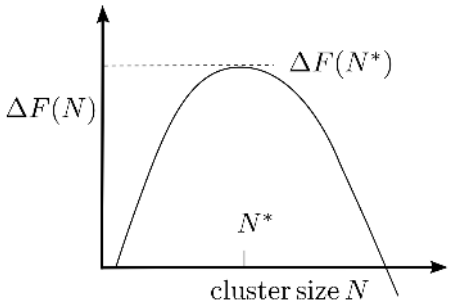

Figure 3: Nucleation is often described using a free energy $\Delta F(N)$ defined for clusters of size N. The peak in free energy at the critical size N^* is related to the nucleation rate.

states that are evolving towards equilibrium, but we take the point of view that these concepts can transfer across to nonequilibrium processes as long as the states of the system in question exist for long enough to achieve an internal thermalization and equilibration.

Thus the phase of a material with the lowest chemical potential under the prevailing conditions is naturally selected, and this approach underpins the construction of phase diagrams. But such considerations are seriously flawed, since they will not account for supercooling of a liquid below its freezing point or metastability of any kind. The reason that materials can disregard the mandate of a phase diagram is that the conversion from liquid into solid, or indeed carbon adatoms into graphene sheets, must go through an intermediary structure that is thermodynamically less stable than the initial phase, even though the final phase is ultimately more stable. The process of transformation has to proceed through a bottleneck: viewed thermodynamically, a system will apparently need to increase its free energy in order ultimately to decrease it. Conspiracies against the second law such as this are not illegal, of course, since the law is only to be obeyed on the average. But in order to quantify the process of nucleation, we need to understand the statistical physics of molecular attachment and detachment from relatively short-lived molecular clusters.

The classic diagram of nucleation theory is the so-called free energy barrier sketched in Figure 3. This represents a difference in thermodynamic potential ΔF of a cluster of N atoms or molecules (referred to generically as monomers) calculated with respect to that of a single monomer, and specific to the prevailing conditions of temperature and monomer chemical potential in the environment. It is commonly referred to as a cluster free energy but more properly it is a difference in grand potential [39]. The size of the cluster is defined in some fashion that usually involves a minimum separation between monomers, or a requirement that the cluster energy should lie below some monomer emission threshold [40]. ΔF is employed to estimate the probability of generating a cluster of a given size from the complex dynamics operating between the cluster and its environment. The probability is estimated to be $P(N) = P(1)\exp(-\Delta F(N)/k_BT)$ where $P(1)$ is the probability of generating a cluster consisting of a single monomer and T is the temperature of the environment. This formulation is consistent with Einstein's theory of fluctuations.

The free energy difference may be written

$$\Delta F(N) = F_{\rm ex}(N) - N\Delta\mu \ , \tag{1}$$

where $\Delta\mu$ is the difference in chemical potential between the metastable and stable thermodynamic phase (for example the chemical potential of C atoms on the substrate minus that in the graphene flake) under the prevailing environmental conditions. The negative sign of the second term therefore reflects the tendency for the new, or stable phase to grow in accordance with the second law. However, the first term, known as the excess free energy, is a positive contribution that impedes the transformation to the new phase. It represents the thermodynamic cost of forming a fragment of the new phase, rather than the new phase in bulk. It is often characterized as an interfacial free energy cost, though it can arise from more profound features of the fragment, related to structural or density differences with respect to the bulk. In the very simplest approach, known as the classical theory of nucleation, the excess free energy for the fragment, or nucleus, is taken to be proportional to the surface area, for growth of a three dimensional structure, with a proportionality constant given by the surface tension γ of the bulk planar interface. The free energy barrier may then be written

$$\Delta F(N) = \gamma A(N) - N\Delta\mu = \theta N^\alpha - N\Delta\mu,$$

where $A(N)$ is the surface area of the cluster, and the proportionality to cluster size N raised to the power $\alpha = 2/3$ follows on the grounds of geometry; θ is a constant related to bulk density of the new phase. For a fragment that is two-dimensional, like a sheet or flake, the excess free energy might be taken to depend on cluster size raised to the power $\alpha = 1/2$. In either case, the free energy barrier in Figure 3 will possess a peak at the so-called critical cluster size N^*. We interpret this to mean that a nucleus with this size is thermodynamically unstable with respect to both the addition or loss of monomers. The probability of a nucleation event might then be represented as the probability of forming the critical cluster (per unit time and system volume) multiplied by the probability of its subsequent growth, which is presumed to be of order one half. The rate of nucleation is therefore proportional to $\exp(-\Delta F(N^*)/kT)$ and the height of the free energy barrier $\Delta F(N^*)$ is then clearly a measure of the likelihood that a nucleation event will take place quickly or slowly.

The classical theory can be criticized for its use of a bulk, planar interfacial tension to represent the excess free energy, but more realistic models can be developed using specific intermonomer interactions. There are other difficulties with the theoretical framework, but they can be removed by developing a set of kinetic or master equations to represent the attachment and detachment of monomers from the nucleus, and indeed to bring into consideration processes involving dimers, trimers etc. Thus the intuitive picture offered by Figure 3 remains central to nucleation theory. The critical free energy barrier is a principal ingredient of many approaches, supplemented by a variety of kinetic models to account for growth by attachment of clusters as well as monomers. Such models would then describe coalescence between clusters, known as Smoluchowski ripening [41].

Should it be doubted that the free energy can really be employed to describe small and short-lived nuclei, then nonequilibrium corrections to the thermodynamics and hence the kinetics can be introduced, allowing them, for example, to relax towards a quasiequilibrium state in a finite time. Additional features of the theory can be included to allow attachment of more than one monomer species [42], and to explore more complicated definitions of cluster size .

The framework relies on specifying an environmental monomer chemical potential, and this is not always a constant. Furthermore, the phenomenon of Ostwald ripening follows from a coupling between clusters through their common environment. There is a tendency for clusters larger than the critical size to grow, leading to the depletion of monomers in the environment, which then has the effect of making clusters smaller than the critical size become more unstable. The overall effect is the increase in size of large clusters at the expense of small clusters, and this is accompanied by an increase in the critical size, destabilizing small clusters further. Of course this is not a nucleation mechanism but rather a process of redistribution of material and the coarsening of a size distribution of clusters. It tends to be a delicate process since the relative differences in stability between clusters of different sizes tends to be small and the process is slow rather than fast.

2.3. Thermodynamics and kinetics of growth

The growth of a system such as graphene using material from a specific source is reasonably well understood from a thermodynamic perspective. It is necessary that there should be species (single carbon atoms or clusters of atoms), available on or beneath the surface of the substrate, that have a higher chemical potential than that of the same species when incorporated into the growing graphene sheet. Such precursors might be generated from other species. For example adsorbed carbon dimers might form from carbon monomers, if it is thermodynamically favorable to do so, before they are then incorporated into the graphene phase. This is an example of Ostwald's rule of stages, whereby a thermodynamically favored transformation might take place through intermediaries that are less metastable than the original feedstock.

The important point, therefore, is to give careful consideration to the nature of the attaching species and to calculate the free energy change associated with such a process. According to phenomenological nonequilibrium thermodynamics, the rate of growth is proportional to this change. For example, if the attaching species were adsorbed carbon monomers then the appropriate free energy change would be $\Delta\mu = \mu_C^{\rm ad} - \mu_C^{\rm gr}$, where the chemical potentials on the right hand side refer to carbon atoms in the metastable and stable situations of surface adsorption and within graphene, respectively. There is, of course, a situation where the chemical potentials are equal, where no growth occurs and the flake is in equilibrium with the adsorbed monomers. Since we can often write $\mu_C^{\rm ad} \propto \ln c$ where c is the density (or concentration) of adsorbed monomers, we obtain $\Delta\mu \propto \ln(c/c^{eq})$ where c^{eq} is the concentration of adsorbed monomers when

in equilibrium with graphene. If we define an adsorbed monomer supersaturation by $S = c/c^{eq}$ then this becomes $\Delta\mu \propto \ln S \approx S-1$ for small supersaturations. This formulation when written as $\Delta\mu \propto c - c^{eq}$ allows growth to be interpreted kinetically as a balance between the attachment and detachment of monomers at rates proportional to their (meta)stable concentrations. Furthermore, for edges of graphene flakes that have a significant radius of curvature, the detachment rate will be modified by a Kelvin factor that represents the thermodynamic destabilization of carbon in that phase, owing to the undercoordination of edge sites with respect to a planar interface.

But if the primary attaching species were carbon dimers, then the relevant free energy change associated with growth would be $\Delta\mu_{2C} = \mu_{2C}^{\mathrm{ad}} - \mu_{2C}^{\mathrm{gr}}$. Following the above argument, this would reduce to $\Delta\mu_{2C} \propto c_2 - c_2^{eq}$, for small deviations from equilibrium, in terms of concentrations of dimers. We might wish to relate this to the density of adsorbed carbon monomers, requiring a relationship between the chemical potentials of the dimer and the monomer, or equivalently between the (meta)stable dimer and monomer populations. We would expect $\mu_{2C}^{\mathrm{ad}} \approx 2\mu_C^{\mathrm{ad}} - \epsilon$ where ϵ is the adsorbed dimer binding energy with respect to the monomer, or equivalently we might appeal to a law of mass action that states that $c_2 \propto c^2$, etc. The attachment rate would then become proportional to c^2. In this way, nonlinear growth kinetics emerges from fundamentally linear attachment processes, as is well-known in chemical kinetics.

In practice, graphene growth laws appear to be nonlinear, a feature that allows us insight into the nature of the primary attaching species. But it is not simply the thermodynamics that determines the growth process; the kinetics also plays a role. In addition to the condition that attachment should be associated with a reduction in species chemical potential, the species in question needs to be mobile enough to make its way to the edge of the growing flake, and this is usually size and structure dependent. An understanding of the kinetics of growth can often provide the proportionality factors that accompany the thermodynamic driving forces considered above, and conversely, experimental data can provide clues as to the nature of the attaching species. A combination of the two is necessary in order to reveal the nature of graphene growth.

3. Experimental techniques

Experiments addressing the growth of epitaxial graphene are in essence closely related to the study of graphene structure, a field covering eight orders of magnitudes of length-scales in the case of graphene growth, from sub-Ångström to millimeters. The picture of the snake biting its tail here largely applies, as often in materials science: one usually tracks the formation of graphene with structural observations, for instance of the hexagonal shape of growing islands, or of a typical reciprocal-space lattice revealed by diffraction; but one usually needs graphene growth to be optimized prior to such high resolution structural characterizations. The two-dimensional nature of graphene, with all of its atoms being surface atoms, naturally suits it for surface science studies, either scanning probe microscopies, or other microscopy or diffraction techniques in geometries and/or with energies yielding shallow penetration of electrons/photons into the supporting substrate used for graphene growth. There are however two examples of non-surface science techniques also being used: transmission electron microscopy (TEM) and Raman spectroscopy. The latter technique is well suited for studying such low amounts of matter as that contained in a single (or less than that) layer of graphene thanks to a resonance scattering process. Various techniques which have been applied thus far to the study of graphene growth and structure are summarized in Table 1.

Basically two types of approaches are employed for studying graphene growth: *in operando* analysis over time-scales down to (typically) a second while graphene is growing, and post-growth studies, which rely on the study of a collection of samples for which growth has been interrupted at various stages. The former requires ultra-high vacuum (UHV) conditions in all experiments performed thus far, while the later can involve ex situ studies, i.e. outside the growth environment, but UHV is necessary for the highest resolution characterizations. *In operando* studies offer a wealth of advantages, especially the absence of reproducibility issues and fast optimization of growth, but remain rather rare, presumably because they are only possible in a few instruments worldwide and because they are not suitable in certain growth conditions. For this reason, they are limited practically to the growth of graphene on metals, single crystals and SiC under UHV, but graphene growth in atmospheric conditions and/or very high temperatures (above 1500°C) retains many of its secrets.

None of the techniques which we will now briefly describe is able alone to provide a full picture of the structure or growth in a given system. Usually a combination of experimental techniques, sometimes

Table 1: Experimental techniques which have been used for studying the growth and structure of graphene, including their acronyms, physical mechanism, and operating conditions.

Acronym	Full name	Type	Spatial resolution	Pressure range (mbar)	Temperature range (K)	*in operando*
AFM	Atomic force microscopy	Scanning probe	$\lesssim$ Å in UHV, $\sim$ nm otherwise	10^{-10}–1	4–300	No
LEED, SPALEED, μLEED	Low-energy electron diffraction spot-profile-analysis-LEED, micro-LEED	Electron scattering	~ 100 μm	10^{-10}	300–1500	Yes
LEEM	Low-energy electron microscopy	Full-field microscopy based on electron scattering	$\sim$ nm	10^{-10}–10^{-7}	300–1500	Yes
PEEM	Photoemission electron microscopy	Full-field microscopy based on photoelectrons	10 nm	10^{-10}–10^{-7}	300–1500	Yes
Raman spectroscopy	–	Ensemble average or microscopy in a confocal microscope	~ 100 nm (diffraction limit)	1	4-700 (isolated from substrate)	No
RHEED	Reflection high-energy electron diffraction	Ensemble average based on electron scattering	~ 100 μm	$10^{-10} - 10^{-7}$	300-1500	Yes
SEM	Scanning electron microscopy	Scanning microscopy based on electron scattering	$\sim$ nm	10^{-6}	300	No
STM	Scanning tunneling microscopy	Scanning probe	$\lesssim$ Å	10^{-10}	$<$1–1100	Yes (with special instruments)
SXRD	Surface X-ray diffraction	Ensemble average based on photon scattering	~ 100 μm	10^{-10}	300–1100	No
TEM, HRTEM	Transmission electron microscopy, high-resolution TEM	Full-field microscopy	$\lesssim$ Å	$< 10^{-7}$	300–900	Yes (with special instruments)
STEM	Scanning transmission electron microscopy	Scanning electron beam	$\lesssim$ Å	$< 10^{-7}$	300	No
XSW	X-ray standing waves	Ensemble average based on photon scattering	~ 100 μm	10^{-10}	300	No
XPS/UPS	X-ray/UV photoelectron spectroscopy	Ensemble average based on electron excitation	~ 100 μm	10^{-10}–10^{-7}	4–1100	Yes

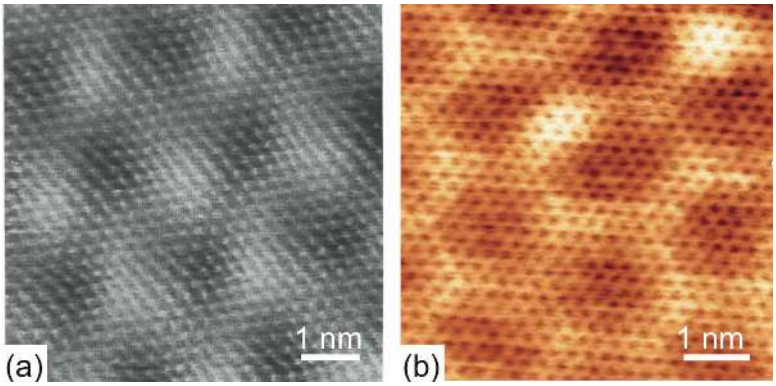

Figure 4: UHV atomic resolution STM topographs of graphene on (a) Pt(111) and (b) SiC(0001). The centers of carbon rings appear dark, while atoms appear bright. Only three out of six atoms of each ring are seen in (a) due to the effect of the tip, while in (b) one infers the positions of atoms to lie at the edges of the small bright hexagons. In addition to the atomic contrast, a larger scale contrast also appears: a moiré pattern between graphene and Pt(111) in (a) and a $\left(6\sqrt{3}\times 6\sqrt{3}\right) R30°$ pattern of the carbon buffer layer between SiC(0001) and graphene in (b). [Reprinted (a) from [48] with permission from Elsevier and (b) with permission from [49]. Copyright (2007) by the American Physical Society].

confronted by structural calculations, is required instead. Some quantities remain difficult to determine, a typical example being the distance between graphene and a metal, and its nanoscale variations.

3.1. Scanning tunneling microscopy (STM)

The scanning tunneling microscope was invented in 1982 [43]. It is a powerful tool for studying the structural and electronic properties of *conducting* surfaces, which can be employed in a variety of environments, from UHV to air and liquids [44]. It consists of a sharp tip scanning the surface of a sample, in a regime of such tip-sample distances that electrons can tunnel to (from) the tip from (to) the sample surface. In practice this implies very short distances between the surface and the tip apex, of the order of 1-10 Å. Due to the exponential decay of the tunneling current as a function of the tip-sample distance, STM is intrinsically well-suited to atomic resolution imaging [45]. Since the conductance (first derivative of the current with respect to the voltage) is approximately proportional to the local density of states [45], the technique is also capable of local electronic spectroscopy in a mode in which the current is measured as a function of the bias applied between tip and sample.

STM can be performed in the constant current or constant height mode. In the first mode, an electronic feedback loop modifies the distance between tip and sample on the fly during the scan, thereby ensuring a constant current during the image acquisition. In this case the STM image consists of spatial variations of the sample-tip apparent distance. Note that what is measured is only the *change* of the tip-sample distance during the scan, not the actual *absolute* distance which remains unknown. Also, even the change of the distance measured during the scan may not necessarily correspond to the actual change of the surface height (e.g. when scanning over a molecule) as what is basically measured is the local density of states. In the second mode, the feedback loop is opened (or set with a response time smaller than the scan rate), leaving the average sample-tip distance constant, and then the STM image consists of spatial variations of the tunneling current. The latter mode allows faster scanning, not being limited by the mechanical response time of the tip and its holder. Very roughly speaking, this is the basis of high speed STM imaging, which goes beyond video rate [46]. Most STM studies are performed from room temperature down to low or very low temperatures. The low temperature, when operating at liquid helium or nitrogen temperatures, provides thermal stability which is beneficial to high resolution distortion-free imaging, and is also a requirement for high energy resolution spectroscopic analysis. The operation of STM at temperatures above room temperature is more problematic, firstly due to appreciable thermal drifts, and secondly due to the tolerance of the instrument parts to temperatures of a few 100 K above room temperature. The so-called environmental STM is possible at temperatures approaching 1300 K, however, when specially designed instruments are used [47].

UHV STM has been the instrument of choice in a number of early and recent advanced surface science studies. The first atomic resolution images of graphene were actually obtained with this technique [48] in

the 1990's for graphene on Pt(111), as shown in Fig. 4(a). The technique gave a strong push to studies of the structure and growth of epitaxial graphene. It allowed the resolution of superstructures in graphene on SiC, see Fig. 4(b), and metals [50, 51, 52, 53, 54, 55, 56], revealed the presence of defects in graphene on substrates [57, 58, 59, 60], made it possible to study growth at different stages [61], including at elevated growth temperatures [62] and with time resolution at growth temperatures [63]. Determination of the structure around defects, as well as of the height or corrugation of graphene, remain difficult due to the mixed topography/electronic sensitivity of STM.

3.2. Atomic force microscopy (AFM)

The force microscope was invented in 1986 [64] shortly after the STM. Since then it has become a standard tool for characterizing surfaces in atmospheric conditions, and is capable of atomic resolution when employed in UHV in well-chosen detection modes [65]. It relies on the scanning of a sample surface with a sharp tip sufficiently close to it so that short-range atomic forces between tip apex and surface vary substantially during the scan. The tip force is transduced into an electrical signal [66], for instance by means of the optical detection of the movement of the cantilever holding the tip. The detailed analysis of the total force sensed by the tip is rather complex: the tip-surface interaction includes many contributions which have different dependence on the tip-surface distance and can be repulsive or attractive: van der Waals, electrostatic, ionic, frictional, chemical, and capillary forces might be of importance. Some of these contributions are more prominent in UHV (e.g. those of a chemical nature), others more in atmospheric conditions (e.g. capillary forces linked to the presence of a water meniscus between the tip and sample surface). Atomic resolution, if achieved, is solely due to short-ranged chemical and/or electrostatic forces and an appropriate apex structure of the tip (which is almost impossible to control); the long range interactions, such as van der Waals forces between the surface and the macroscopic part of the tip, provide the background contribution which may be dominant. This is why achieving atomic resolution with AFM can be difficult. Still, it has been achieved in many cases over the last decade, for different surfaces in UHV and using the dynamic mode of operation (see below). It is probably fair to say that achieving atomic resolution with AFM is more difficult than with an STM. Under atmospheric conditions, the operation of AFM is, however, usually much more convenient than that of an STM, as it can operate at larger working distances and accordingly cope with the presence of adsorbates on the surface. Besides, unlike STM, the usage of AFM is not restricted to conductive samples, i.e. the AFM is in principle more versatile.

Depending on the tip-surface working distance AFM is characterized by different mechanical behaviors, which define different AFM operation modes [67]. In the static mode, no vibration is imposed to the tip, which is merely dragged across the surface during the scan. This mode relies on soft cantilevers, which can be deflected by the weak atomic forces, and on suitable eigenfrequencies lying away from the resonance frequency of the cantilever. These requirements make this apparently simple mode of operation difficult to implement in many situations; in addition, it results in both the tip and surface being damaged during the scan. Dynamic modes, in which the tip is oscillating perpendicular to the surface while scanned, are more widely employed. Making the tip oscillate with an amplitude that may change between sub-Å for stiff cantilevers to hundreds of Å for soft ones avoids the problem where the tip jumps into contact with the surface and hence maintains both the tip and the surface intact during the scan. Two major scanning modes are in use: (i) in the amplitude modulation regime the oscillation frequency is kept constant and out of resonance and the oscillation amplitude and the phase are measured, while (ii) in the frequency modulation regime the oscillation frequency is maintained at resonance during the scan and the oscillation amplitude is kept constant. The latter mode, which for UHV is the most suited for achieving true atomic resolution, can be run either by keeping the resonance frequency constant and measuring the corresponding vertical displacement of the sample (similar to the constant current mode of STM), or by keeping the sample height unchanged and hence measuring changes in the resonance frequency (detuning), which is similar to the constant height mode of STM. The latter mode is also called the non-contact mode (NC-AFM), when the average working tip-surface distance is around 2-4 Å which is within the region of attractive forces; in the tapping mode the working distance is smaller, and mostly repulsive forces are probed. Dynamically probing the surface in AFM provides information about the topography of the surface through the measurement of the shift between the excitation and the actual tip oscillation needed to ensure a constant tip amplitude vibration in frequency modulation, or the variation of the amplitude of excitation needed to ensure a constant tip frequency vibration in amplitude modulation. AFM also provides information about energy dissipation at

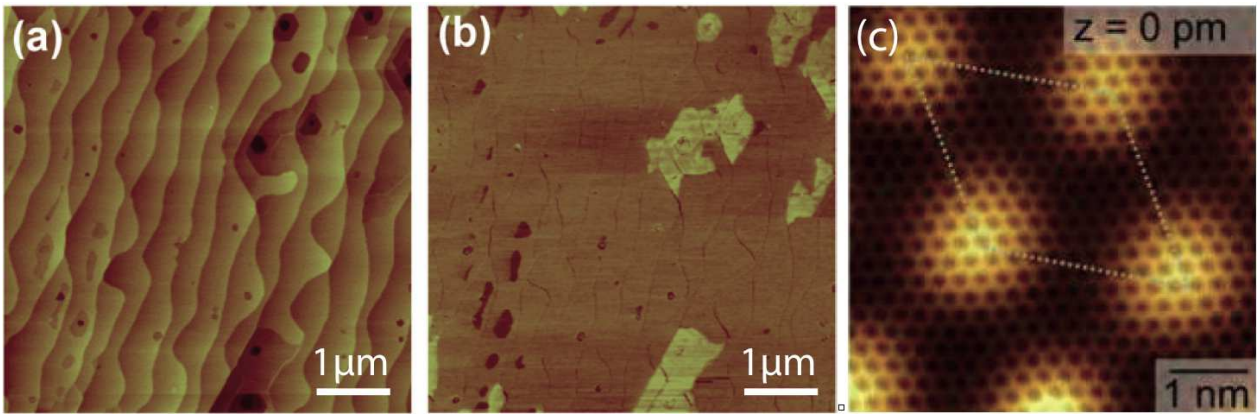

Figure 5: AFM (a) height and (b) phase images measured in tapping mode in air for graphene with various numbers of layers on SiC(0001): single, bi-, and trilayer graphene regions show up as dark, medium, and bright shades in (b). (c) Atomic resolution AFM map of the frequency shift, measured under UHV in dynamic non-contact frequency modulation mode with a tip made inert by termination with a CO molecule, of graphene on Ir(111). [Reproduced from [68] by permission of IOP Publishing. All rights reserved (a) and by permission of [69]. Copyright (2012) American Chemical Society (b).]

surfaces; this information is obtained either by monitoring the phase shift between excitation and tip vibration frequencies in the amplitude modulation mode, or by measuring the amplitude change during the scan in the frequency modulation.

AFM is widely used under atmospheric conditions for rapid and rough characterization of graphene on surfaces, usually at room temperature [70, 71, 72]. In this capacity it is mostly employed to check the uniformity of graphene. It was also realized that the phase signal, which is sensitive to the dissipation properties of materials under mechanical excitation of the tip, shows strong contrast from graphene-free regions to graphene-covered ones [73, 74], and even from a single layer graphene to few-layer graphene [68], see Fig. 5. Though the in-depth understanding of this effect is missing, it allows efficient determination of the number of layers and of the size of graphene flakes or multilayer patches.

Advanced AFM studies of graphene at high-resolution are rather scarce [75, 69, 76], especially in the case of epitaxial graphene. It was shown that for quantitative height determinations care should be taken considering the tip-graphene chemical interaction [69], Fig. 5(c), and concerning the working distance and frequency shift (i.e. the resonance frequency change when bringing the oscillating tip closer to the surface from infinity) in constant frequency shift imaging [76]. With such care, the height modulations in the moiré pattern between graphene and Ir(111) surface (see Section 6.1.4) could be estimated.

3.3. Transmission electron microscopy (TEM)

TEM development dates back to the 1930's [77]. The electrons generated by an electron source are injected into a column by means of electromagnetic lenses that shape a high energy electron beam (from several 10 keV to few 100 keV). The electrons then pass through a sample, and the sample plane is imaged through another set of electromagnetic lenses. The sample must be sufficiently small that it only absorbs a limited part of the electron beam. The high energy of the electrons allows high-resolution imaging of the sample; however, aberrations in the electron optics restricted the ultimate resolution achievable with TEM for a long time. Aberration-corrected instruments are now available and they allow resolutions close to 1 Å [78] and below. The electron optics column allows us to observe, instead of the image plane, the Fourier plane, i.e. to perform a diffraction experiment. The electron optics instrumentation in a conventional TEM is designed to make full-field images of the samples. Adding scanning coils and forming a small electron spot allows performance of STEM, i.e. imaging of the sample by scanning it. This technique enables energy dispersive X-ray spectroscopy, electron energy loss spectroscopy, or annular dark field imaging (the latter allowing atomic number contrast imaging) with ultra-high spatial resolution. The aberration corrected STEM offers spatial resolution below 1 Å [79]. Transmission electron microscopes capable of high resolution imaging of samples heated to high temperatures were demonstrated in the early 2000's [80]. Due to the cluttered environment around the sample in a TEM or STEM, there is however little space for performing *in operando* growth experiments.

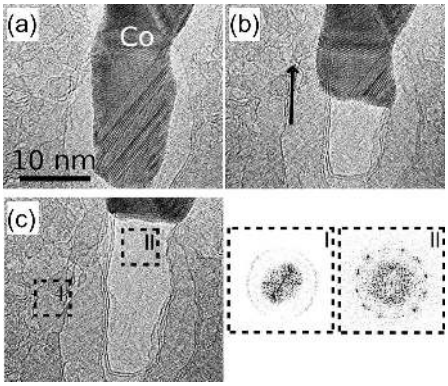

Figure 6: 10 nm thick lamella of Co on amorphous carbon, at 913 K, growing ((a) to (b)) and retracting ((b) to (c)) under an energetic (200 keV) electron beam, causing a transformation from amorphous carbon to graphene. The presence of graphene after the retraction of Co is confirmed in the Fourier transform of the images (II). [Reprinted with permission from [81]. Copyright (2011) American Chemical Society.]

The study of fragile samples, such as biological matter, and of materials composed of light (low atomic number) elements (e.g. graphene, boron nitride), required the development of high resolution TEM with the electron energy below 100 keV in order to prevent the knock-on of atoms by electrons. For carbon the knock-on occurs for electrons with about 80 keV energy [82]. Imaging graphene without inducing a substantial amount of defects thus is not possible using beams of above this energy. The purely two-dimensional nature of graphene is an additional difficulty in studies of its growth. Indeed, in a plane-view geometry (graphene observed from above), the presence of a substrate composed of strong electron scatterers (the metal atoms), and thicker than several nm, makes it impossible to detect the presence of graphene. In a cross-section geometry, detecting a single layer is a tedious task which requires simulation of TEM images, and observing the projection of a two-dimensional phenomenon (growth on a planar substrate) in one dimension (perpendicular to the cross-section) greatly complicates understanding. In practice very few studies of the growth of graphene with TEM exist. One noticeable exception is the plane-view *in operando* study of the transformation of amorphous carbon into graphene in the presence of a thin (few nanometres) metal catalyst [81] (Fig. 6). Noteworthy also are studies in the 1960s of the structure of graphene prepared by evaporation of carbon onto metal foils: after growth, graphene was transferred to TEM grids by chemically etching their metallic substrate, and was identified in TEM images with the help of electron diffraction [83], an approach which was used again years later [72].

3.4. Low-energy and photoemission microscopy (LEEM and PEEM)

The first images of surfaces obtained with PEEM and LEEM were published in 1966 [84] and 1985 [85, 86]. The two techniques rely, just like TEM, on an electron optics imaging column composed of electromagnetic lenses and operating using high energy (typically 20 keV) electrons. PEEM relies on the extraction of photoelectrons from the sample, which is usually achieved with an ultraviolet source (laser, lamp or X-rays). LEEM relies on secondary or reflected electrons, created by a low-energy electron beam. This beam is shaped from electrons created by an electron source, accelerated to high energy electron beam inside an electron column (like in TEM), and decelerated before reaching the sample surface. In both techniques the low energy (0-100 eV, typically) of the electrons used for imaging ensures extreme surface sensitivity to a few topmost layers of the sample.

Since no actual contact occurs between the electron optics elements and the sample surface, both techniques are well suited for temperature-dependent studies, and, as long as the pressure remains reasonably low (typically below 10^{-7}mbar), they can be run *in operando*, i.e. during the evaporation of species onto the sample surface or in the presence of gases reacting at the sample surface. Thanks to the strong interaction between low-energy electrons and matter and due to the fact that PEEM and LEEM are full-field microscopies, high measurement rates are possible, typically from 1 to 100 Hz, which allows true real time monitoring of the growth on surfaces, as anticipated early on [87]. These studies are routinely performed with lateral resolution of about 10 nm. Recent developments, using aberration-corrected electron optics inspired by TEM instrumentation, allow the attainment of lateral resolutions of a few nm [88].

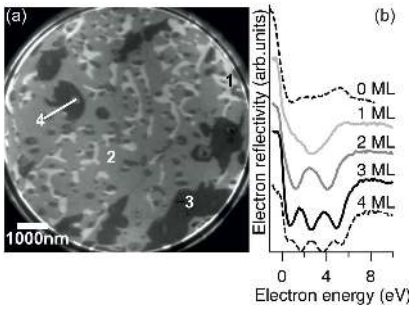

Figure 7: (a) LEEM image of graphene on SiC(0001) and (b) electron reflectivity at different locations in (a), allowing a count of the number of layers (the number of low energy oscillations plus one). [Reproduced from [90] by permission of IOP Publishing. All rights reserved.].

In PEEM, images reveal work function contrasts. In LEEM, the electron reflectivity is imaged, which is linked to the density of states and the sample structure perpendicular to the surface. As in a standard optical or transmission electron microscope, instead of observing the image plane, one can observe the Fourier plane. In LEEM, this allows the performance of LEED experiments (see next subsection), and micro-LEED experiments by using an aperture placed before the sample in order to select one region of the sample. In PEEM, provided that an energy analyzer is added after the imaging column, this allows performance of angle-resolved photoemission spectroscopy to obtain constant energy cuts of the electron band structure of the surface [89].

The first published LEEM studies of graphene [90] allowed determination of the extent of few-layer graphene regions and a count of the number of graphene layers in graphene/SiC samples by taking advantage of the electron reflectivity sensitivity to the out-of-plane structure, see Fig. 7. LEEM has been employed for an *in operando* analysis of the growth of graphene on Ru(0001) [91], which revealed for instance that graphene islands grow down the atomic step edge staircase of the substrate (see Section 5.4.1). In the same year it was established that electron reflectivity measurements, possible in a spatially-resolved manner in LEEM, allowed *in operando* measurements of the C adatom concentration on metal surfaces and a connection to be made to the elementary processes occurring during growth [54] (Sections 5.1.1 and 7.1). LEEM, coupled to micro-LEED measurements, was then employed to conveniently identify rotational variations in graphene on metals [92]. PEEM also has been employed to study the growth of graphene on metals [93], though it provides only limited structural information (no diffraction capability like in a LEEM).

3.5. Surface-sensitive electron diffraction (LEED and RHEED)

LEED and RHEED are two techniques whose use spread in the 1960s, as they were accompanying the development of UHV instrumentation and other techniques designed for studying the growth of highly crystalline surfaces. The first technique uses low-energy electrons (below 100 eV typically). Such electrons experience scattering events whereby they rapidly lose their energy, which makes the technique very sensitive to the few topmost layers of the sample. In the typical scattering geometry, LEED provides snapshots of in-plane cuts of the reciprocal space lattice of the topmost layer of the sample. RHEED uses high-energy electrons (typically a few 10 keV). Such electrons penetrate matter much deeper than the low energy electrons used in LEED. In RHEED however, this extended penetration is avoided by the scattering geometry, which corresponds to grazing incidence and exit. A RHEED image captures part of the scattering contribution which, due to the finite thickness of the sample (as seen by electrons), extends perpendicular to the surface. The aspect of the RHEED image is determined by the length-scale of the surface roughness as compared to the coherence length of the electron beam, which is typically of the order of 10 nm: electrons penetrate much deeper in samples with roughness length-scale well below this value, which yields spotty patterns, while in the opposite situation the sample is actually seen as two-dimensional which yields streaky patterns.

The analysis of electron diffraction diagrams can only be performed quantitatively in the rather complex framework of dynamical theory of diffraction explicitly taking into account multiple diffraction events [94, 95]. This is noticeably required for interpreting the variations of LEED intensity as a function of electron energy, from which one can derive valuable information about the structure of the sample. The location of the diffraction contributions in reciprocal space are, however, little affected by multiple diffraction effects, which

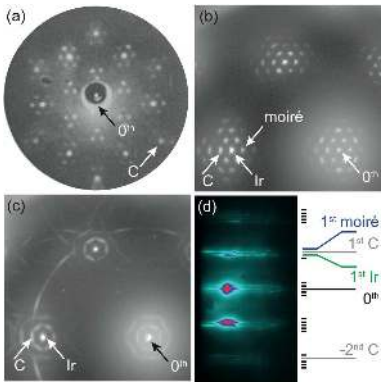

Figure 8: (a) LEED pattern of graphene on SiC(0001), and SPALEED pattern on Ir(111) covered by (b) an ill- and (c) a well-ordered graphene layer. The reflected beam (labeled 0^{th}) is marked by an arrow. The presence of diffusion rings around the reflected beam (c) signals a scatter in the in-plane orientation of graphene with respect to its substrate; on the contrary, well-defined spots track well-defined epitaxial relationships. (d) RHEED pattern of graphene on Ir(111) around the specularly reflected beam (labeled 0^{th}). All patterns were obtained under UHV conditions. Both LEED and RHEED reveal the presence of superstructures (e.g. moiré in (a) and (d)). [Reprinted from [98], with permission from Elsevier (a), from [99] by permission of IOP Publishing. All rights reserved (b,c) and with permission from [100]. Copyright (2011), AIP Publishing LCC. (d).]

allows straightforward determination of the lattice parameter in the plane of the surface. Best accuracy is usually achieved with the help of RHEED or of spot-profile analysis LEED [96]. Moreover, the strong interaction between electrons and matter allows fast acquisition rates, which is essential for the *in operando* monitoring of surface growth; RHEED, with its open geometry, is ideally suited for this purpose [97].

LEED structural studies are amongst the earliest characterizations of epitaxial graphene. They provided understanding of the first steps of graphene formation on SiC [98, 101] (Fig. 8(a)) and unveiled the moiré superstructure arising between graphene and a metallic substrate [102]. LEED was employed to understand the detailed structure of graphene on metals, not only in the plane of the surface (Fig. 8(b,c)) but also perpendicular to it, with the help of quantitative dynamical theory analysis [103, 104, 105]. More recently, when performed with micro-sized electron beams inside a LEEM, LEED revealed the presence of rotational variants in graphene on metals [106, 58]. RHEED has been used much less than LEED thus far for studying graphene, and mostly as a way to determine the graphene/substrate epitaxy [107, 108] (Fig. 8(d)). Clearly, the potential of this technique for studying graphene growth is far from being fully exploited.

3.6. Scanning electron microscopy (SEM)

The early development of the SEM instrumentation dates back, similarly to TEM, to the 1930s [109]. As in a TEM, electrons produced by an electron gun are shaped into a beam through a column composed of electromagnetic lenses, which is focussed onto the sample surface and scanned through it with the help of coils. The energy of the electron beam ranges from a few 100 eV to a few keV. Both secondary electrons (having experienced energy losses due to scattering events inside the sample) and back-scattered electrons (elastically scattered) can be analyzed independently using specific detectors. The secondary electrons, having low energy, can only escape the sample if they are produced sufficiently close to the impact point of the electron beam onto the surface, which allows high spatial resolution of the order of 1 nm. The back-scattered electrons are those reflected elastically from the sample. Since they have a rather high energy, they can scatter from rather deep within the sample (typically, hundreds of nm) from the surface. Back-scattering, being more efficient when the atomic number of the scatterer is high, provides chemical information about the sample. The back-scattered electrons may also be employed for performing diffraction experiments (electron back-scatter diffraction, EBSD) which is valuable for determining the bulk structure of the sample. Other detection modes are available in SEM, such as those based on exploiting X-rays, but we will not discuss them here. Environmental SEM was developed for a large variety of *in operando* studies of materials, especially at high temperature [110, 111] (note, however, that the time resolution is limited by the scanning time).

SEM is widely employed for *ex situ* characterizations of the growth of graphene [113, 114]. Because of its atomic thickness graphene is usually detected with secondary electrons (usually unspecified in publications) which probe only a small topmost fraction of the sample. It allows the study of defects such as wrinkles

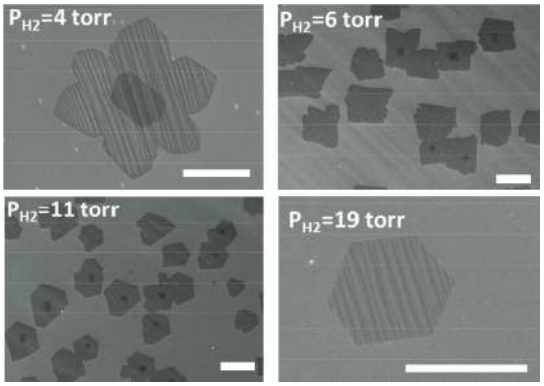

Figure 9: SEM images with secondary electrons of graphene prepared by CVD on Cu foils with various partial pressures of hydrogen. Copper appears bright. The graphene islands often contain a bilayer (or multilayer) region at their center. [Reprinted with permission from [112]. Copyright (2011) American Chemical Society.]

[115] and provided valuable insight into the growth of graphene on Cu foils, which was beneficial, e.g., to understand the dependence of the shape of graphene islands on growth conditions [112] (Fig. 9). Using back-scattered electrons, EBSD was also successful employed to relate the shape of graphene islands, as observed with secondary electrons, to the surface termination of the individual metal grains supporting the growth [116]. The full power of SEM has not yet been fully exploited, especially in the view of *in operando* studies, which are now possible at temperatures above 1300 K [117].

3.7. Raman spectroscopy and microscopy

Raman spectroscopy was used in materials science as early as the 1940's. The technique relies on the Raman effect, whereby an electromagnetic wave gains or loses part of its energy by exciting phonons in a material. The energy lost or gained measured in a Raman spectroscopy experiment characterizes, among other things, the bonds (e.g. interatomic, van der Waals) responsible for cohesion in the material of interest. A Raman spectrum thus provides a signature of a material, and contains information about processes that weaken or strengthen bonds (by charge transfers or strains, for example), and concerning interactions between phonons and other excitations (such as electronic waves, plasmons, etc). The typical energy losses (discussion of energy gains, yielding smaller Raman signals, is not discussed here) of photons in matter range between few 10 to few 1000 cm^{-1}, i.e. 1 to 100 meV.

In practice, the light source used for a Raman spectroscopy experiment is most often a visible light or infrared laser. After interaction with the sample, the beam is passed through a filter rejecting the strongest scattering contribution, which is elastic (Rayleigh, zero energy loss), and then injected into a spectrometer coupled to a high sensitivity detector. In an alternative setup Raman spectroscopy may be implemented in a confocal microscope, allowing for high spatial resolution (down to the diffraction limit) of samples.

Graphene has three main features in its Raman spectrum, the so-called D, G, and 2D (also called G') modes, appearing respectively at about 1350, 1580 and 2700 cm^{-1} [119], see Fig. 10(a). The first mode is only present in samples with defects. The G mode is a first order process, doubly degenerate, involving in-plane transverse optical and longitudinal optical excitations at the Brillouin zone center [120, 121]. The two others are second order modes, but doubly resonant (thus readily observable, like the G mode), involving one in-plane transverse optical phonon at the K point of the Brillouin zone and one defect for the D mode, and two in-plane transverse optical phonons at the K point for the 2D (G') mode [120, 121]. The relative intensity and width of the 2D mode [119], as well as the occurrence of a shear mode for small energy losses in polarized light experiments [122], provide valuable information about the number of layers in graphene stacks. Polarized light is useful in identifying the nature of the edges of graphene flakes [123]. The relative orientation of graphene layers in graphene stacks can be tracked by specific Raman signatures [124]. The high sensitivity of Raman scattering to the mass of the atomic nuclei makes the study of experiments performed with different carbon isotopes (Fig. 10(b-d)) a rich area for understanding growth, for instance the competition between surface and volume processes [118]. Raman modes are also strongly affected by various perturbations, including the strains of C-C bonds occurring under stress [125], which effectively modify the stiffness of the C-C bond

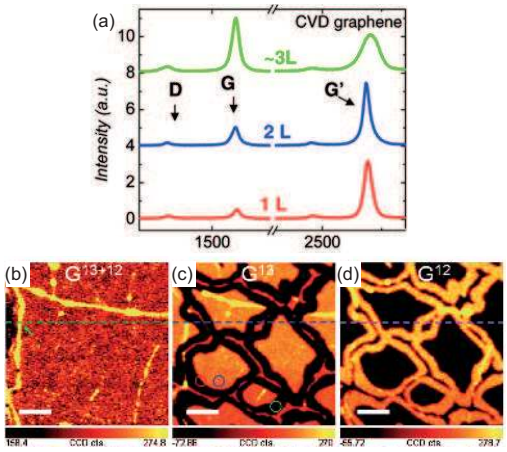

Figure 10: (a) Raman spectrum measured at various locations in a graphene film, prepared by CVD on Ni thin films and transferred to SiO_2/Si, for single, bi-, and trilayer regions, showing the presence of D, G, and G' (2D) peaks. (b-d) Raman maps of the G band intensity of a single layer of graphene prepared by CVD with $^{12}CH_4$ and $^{13}CH_4$ on Cu foils and transferred to SiO_2/Si. The growth has been performed in two steps, one with $^{12}CH_4$ and the other with $^{13}CH_4$. (b) is the sum of the intensities around the G bands of the two isotopes, (c) is the intensity around the G band of ^{12}C, and (d) the intensity around the G band of ^{13}C (the two bands are shifted by about 60 cm^{-1}). [Reprinted with permission from [72]. Copyright (2008) American Chemical Society (a) and [118]. Copyright (2009) American Chemical Society (b-d).].

and charge transfer [126] through the strong electron-phonon coupling in graphene. This sensitivity may be exploited, for instance, to characterize the nature of the interaction between graphene and its substrate.

3.8. Surface-sensitive X-ray diffraction (SXRD)

In the energy range corresponding to high resolution structural characterizations, typically 10 keV, X-rays interact only weakly with the electronic clouds of atoms. This results in large penetration depth of X-rays in matter. A grazing incidence geometry limits this penetration depth to a around 10 nm, which allows the study of interfaces close to the surface [127]. The study of surfaces with SXRD usually requires UHV and samples prepared *in situ* [128, 129] in order to avoid contaminations which would alter the surface. In an SXRD experiment, a well-focussed X-ray beam is directed onto the sample surface with an incidence angle of a few tenths of a degree. The requirement for a well-defined incidence angle makes low-divergence beams, such as those available from synchrotron sources, preferable. Due to the weak interaction between hard X-rays and matter, the high intensity available at such a source is another definitive advantage. An SXRD experiment consists of measuring the scattering from the sample perpendicular to its surface (by varying the exit angle) and along lines (crystal truncation rods) passing through the in-plane cut of the reciprocal space. The distance between these lines characterizes in-plane strains, the width of these lines is related to strain fields and the size of the structurally coherent domains, and the intensity modulation along the lines relates to the out-of-plane structure of the sample.

A study of graphene on a substrate with SXRD is in principle a difficult one: carbon is one of the lightest scatterers, and is only present in very low amounts. The first SXRD study was performed in a rather favorable situation of multilayer graphene on a substrate also composed of rather light scatterers, SiC. The study yielded the out-of-plane structure of multilayer graphene, revealing for instance rotational disorder [130], see Fig. 11. The first study on a single layer graphene on Ru(0001) revealed a surprisingly large superstructure and allowed determination of the graphene-metal distance [131]. SXRD was later employed for studying the growth of graphene on a metal, highlighting the role of preparation conditions in the formation of defects in graphene [132, 133], and the positive thermal expansion of graphene on a metal down to low temperature [133]. Many of the features observed in these studies are almost undetectable by other techniques. This high resolution however comes at the expense of demanding experiments and relatively heavy data analysis.

3.9. X-ray and ultraviolet photoelectron spectroscopy (XPS/UPS)

The development of X-ray photoelectron spectroscopy (XPS) and ultraviolet photoelectron spectroscopy (UPS), for the the investigation of the properties of materials, dates back to the 1950s [134] and 1960s [135],

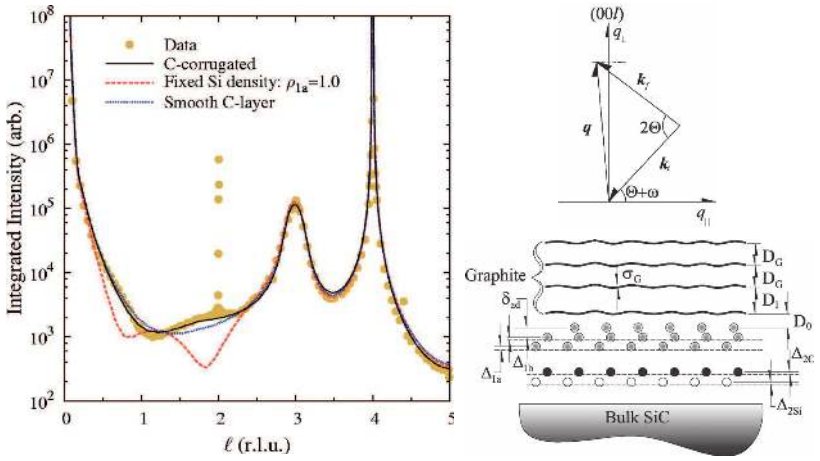

Figure 11: Specular reflectivity (X-ray scattered intensity along the reciprocal space coordinate l perpendicular to the surface) of nine-layer graphene on SiC(000$\bar{1}$), and fittings of the data (disk symbols) based on different structural models. The scattering geometry is shown in the top right cartoon; the various parameters employed for parametrizing the model employed for the fittings is shown at the bottom right. [Reprinted with permission from [130]. Copyright (2007) by the American Physical Society.]

respectively. These techniques are named after the photoelectron effect, whereby an energetic photon (X-ray, UV) excites a core-level electron above the Fermi level. If the photon energy is sufficient for the photoelectron to exceed the sample work-function, a free electron with sufficient kinetic energy is created which escapes from the sample. By measuring the energy threshold for photoemission, one may extract the work-function, and then subtracting it away from the photoelectron kinetic energy, measured with the help of an electron energy analyzer, an electron binding energy for each of the photo-excited core levels is obtained.

In the laboratory, metal anodes (e.g. Al) and discharge sources (e.g. He) are used as X-ray and UV sources. Relying on electrons, XPS and UPS are usually operated under high or ultra-high vacuum. Synchrotron radiation sources are valuable alternatives which offer high photon flux (thus allowing one to reduce considerably the counting times) and energy tunability (thus surface sensitive tunability). XPS and UPS are surface sensitive techniques, whose probing depth is set by the strong interaction between electrons and matter: depending on the sample atomic number, a photoelectron will only escape the sample, in the photon excitation energy range usually employed, from depths of between a few to a few tens of Ångströms. The precise value of the core level energy not only depends on the atomic element of interest, but also on the kind and nature of bonds these atoms form with their environment: chemical identification, hybridization state, and charge transfer/oxidation states are accordingly readily identified with XPS and UPS.

XPS and UPS are routinely used to characterize the degree of purity and presence of oxygen groups in graphene samples, which are obtained via chemical routes, by means of the analysis of the carbon core levels. XPS and UPS have also been employed since the 1990s to characterize graphene on metals [136], and more recently graphene on SiC [137]. In these studies the interaction between graphene and its support, as well as the number of graphene layers, could be analyzed by studying the carbon core levels. The study of metal core level changes upon graphene growth also made it possible to investigate the graphene-metal interaction [138, 139]. Noteworthy is also the use of XPS at synchrotron sources as a tool for *in situ* monitoring of the growth of graphene and its evolution upon, e.g. heating [140, 141].

3.10. Near-edge X-ray absorption fine structure (NEXAFS)

In X-ray absorption experiments in a transmission geometry, one measures elastically-scattered photons: above an absorption edge, corresponding to the excitation of photoelectrons from core levels, elastic scattering is strongly reduced (due to the increase of inelastic scattering corresponding to photoelectron excitation). One may also measure the electron yield, especially in a non-transmission geometry, which is linked to the absorption process. Synchrotron sources, owing to their energy tunability, high brilliance, and control over the photon polarization, have given a strong push to X-ray absorption spectroscopies, making it possible to extract polarization-dependent absorption *vs.* energy spectra with high signal to noise ratios, and accordingly,

to detect low amounts of absorbing atoms in matter and to derive valuable information about the local environment of the absorbing atoms. In the following we will address specifically the 10 eV-region above the absorption edge, the so-called near-edge X-ray absorption fine structure (NEXAFS) or X-ray absorption near edge structure (XANES) region. In this energy range, electronic transitions towards empty states close to the Fermi Level or low-energy continuum states are involved [142].

NEXAFS studies of graphene (on substrates) have focussed on the C 1s spectra. Addressing the spectra of the topmost substrate layer, for instance in order to explore the effects of the graphene-substrate interaction, is a challenging issue. Indeed, the absorption edges of Si and metals are generally above 1 keV, an energy at which a very grazing incidence is required to make the technique actually surface sensitive; even then, the surface sensitivity is no better than roughly 10 atomic layers from the substrate, which makes it difficult to extract information from the very surface of a sample. In the case of graphene on SiC, C is in both graphene and the substrate. In order to probe specifically C from graphene, a retarding potential of a few 100 V allows one to discriminate those low-energy electrons, detected in electron yield modes, which originate from layers deeper in the sample [143]. A typical C 1s NEXAFS spectrum exhibit several features, mainly three, associated each with electronic transition from the core level to the π^* and σ^* orbitals, like in graphite [144]. Adjusting the polarization vector of the X-ray beam with respect to the graphene surface makes it possible to probe selectively some of these specific transitions [145], and to detect the effects of the graphene-substrate interaction [146]. Other features make it possible to detect charge transfers and hybridization between graphene and the substrate [138].

3.11. X-ray standing waves (XSW)

X-ray standing waves is a technique which combines diffraction and a chemically sensitive process, such as X-ray fluorescence of photoemission [147]. It gives the positions of atoms in the standing wave field generated by a crystalline substrate, while providing information about the interaction between the atoms at the surface. The technique proved especially powerful in determining the structure of interfaces and atomic and molecular adsorbates in the sub-monolayer regime [148, 149]. A typical XSW experiment consists of measuring photoemission spectra from an adsorbate for various energies of the X-ray beam close to the Bragg condition. While the wavelength of the standing wave varies only slightly, the spatial phase shift of the standing wave varies strongly, and thus strong photoemission occurs when the adsorbate position coincides with the nodes of the standing wave. The tunability of the photon wavelength and the availability of intense beams at synchrotron sources allows high resolution and high sensitivity in XSW studies.

Only two studies of graphene have been performed with XSW [150, 151], though studying graphene does not impose more stringent conditions than those needed for studying molecules. This seems however to be an ideal method for the accurate determination of the graphene-metal distance, which is characteristic of the graphene-metal interaction.

4. Simulation methods

In this section we shall give a brief overview of theoretical techniques (see Fig. 12) and methods which we believe must be useful in graphene related modeling. In fact, each of these methods alone or together in various combinations have already proved extremely beneficial in existing theoretical simulations of graphene growth. The overview is intended not solely for consistency and convenience of our discussion; it is believed that a quick run over a modern toolkit in use for modeling surface processes should be useful to readers who are less familiar with them. Only a brief outline will be given as there are many good reviews (e.g. [152, 153, 154]) and books (e.g. [155, 156, 154, 157, 158]) on the subject.

4.1. Atomistic modeling methods

The observable properties of all solids are governed by quantum mechanics, as expressed by solutions of a Schrödinger equation for the motion of the electrons and the nuclei. However, because of the inherent difficulty of obtaining even grossly approximate solutions of the full many-body Schrödinger equation, one typically focuses on reduced descriptions that are believed to capture the essential features of the problem of interest.

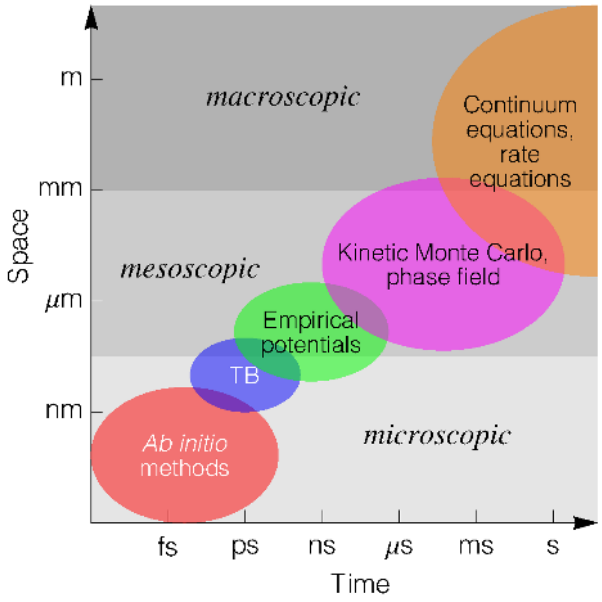

Figure 12: Comparison of various theoretical techniques with respect to the characteristic spatial extent and the time scale associated with them. Here TB stands for tight-binding and semi-empirical methods.

4.1.1. Density Functional Theory

Most of the computational techniques applied at the atomic scale to the graphene growth are based on Density Functional Theory (DFT) which is a reasonable compromise between efficiency and precision. In its standard formulation this method is only applicable to the ground state of a quantum system at zero temperature, and in most cases of crystal surfaces and carbon species on them, which is the main interest for us here, this is sufficient. Modern DFT methods allow us to calculate the total energy of a system of nuclei and electrons, as well as the forces acting on atoms, from first principles, i.e. without using any empirical information (such as experimentally measured interatomic distances, elastic moduli, optical and vibrational spectra, etc.). An ability to calculate the total energy in turn allows us to relax structures to their mechanical equilibrium geometries (corresponding to zero atomic forces), or to run molecular dynamics (MD) simulations to take account of temperature effects. Although no empirical parameters enter the calculation, it is essential to remember that the results (e.g. the total energy, atomic geometry and vibrational frequencies) are not "exact" since DFT methods employ density functionals which serve only as an approximation. We shall briefly discuss how precise DFT may be in regard to the problem of graphene on metals in sections 6.1.

The DFT is based on an exact statement [159] that the total energy of an arbitrary system of electrons in the ground state can be written as a functional of the electron density $\rho(\mathbf{r})$:

$$E\left[\rho\right] = F\left[\rho\right] + \int V_n(\mathbf{r})\rho(\mathbf{r})d\mathbf{r}\ , \tag{2}$$

where $V_n(\mathbf{r})$ is an external potential and $F[\rho]$ is a *universal functional* of the electron density which does not depend on the nature of the system, i.e. the number of electrons N_e, positions of atoms, their chemical identity, etc. The external potential in our case corresponds to the potential created by atomic nuclei and is the only term in the energy which explicitly depends on the atomic positions. However, since the electron density is obtained by varying the total energy with respect to it subject to the normalization condition

$$\int \rho(\mathbf{r})d\mathbf{r} = N_e\ ,$$

the electron density in the energy minimum (the "true" density) depends on the atomic positions as well. This fact is essential when calculating the forces on atoms.

The functional $F[\rho]$ is universal, and this is the indisputable strength of the DFT; however, its weakness is that this functional is not known. It is clear that it should contain the kinetic energy of the electrons

and their interactions between themselves, i.e. their Coulomb (Hartree) interaction, plus exchange and correlation, however, it is a very difficult (maybe impossible) task to find exactly all these contributions as density dependent functionals. Kohn and Sham [160] proposed a computational scheme which somehow remedies this problem by mapping the real system of interacting electrons to an artificial system of non-interacting electrons of the same density

$$\rho(\mathbf{r}) = 2 \sum_{i=1}^{N_e/2} |\psi_i(\mathbf{r})|^2 \ , \tag{3}$$

moving in an one-electron effective potential $V^{eff}(\mathbf{r}) = V_H(\mathbf{r}) + V_{xc}(\mathbf{r}) + V_n(\mathbf{r})$. This consist explicitly of the Hartree term, $V_H(\mathbf{r}) = \int \rho(\mathbf{r}') / |\mathbf{r} - \mathbf{r}'| \, d\mathbf{r}'$, exchange-correlation contributions $V_{xc}(\mathbf{r})$, , as well as the potential due to atomic cores. V_{xc} should non-trivially depend on the electron density. In Eq. (3) $\psi_i(\mathbf{r})$ is the one-electron wavefunction for an electron occupying the state i, and in the ground state it is assumed that the first $N_e/2$ states with the lowest one-electron energies, ϵ_i, are occupied (for simplicity we assume an even number of electrons, and that a pair of electrons with opposite spins occupy each one-electron energy level). The mapping to a non-interacting electron gas resolves the problem of the unknown kinetic energy term in the total energy since for the non-interacting electron gas the kinetic energy can be trivially written in terms of the one-electron orbitals ψ_i. However, this will not be the actual kinetic energy of the interacting gas; the introduced error is transferred into the exchange and correlation energy which now includes this discrepancy as well. The one-electron orbitals are obtained by varying the total energy with respect to them, subject to their orthonormality condition, yielding the Kohn-Sham equations [160]:

$$\left[-\frac{1}{2}\Delta + V_H(\mathbf{r}) + V_{xc}(\mathbf{r}) + V_n(\mathbf{r}) \right] \psi_i = \epsilon_i \psi_i \ , \tag{4}$$

where the Hartree, V_H, and exchange-correlation, V_{xc}, potentials are functionals of the density, and we adopted atomic units for simplicity. Since the density itself is composed of the orbitals, the equations (4) for all orbitals are highly non-linear with respect to them and their solution has to be sought self-consistently starting from some initial guess for the orbitals. Knowledge of the orbitals provides the electron density (3) and the total energy. This calculation can be conducted for various atomic positions (giving a different potential V_n due to the nuclei) which yields the dependence of the total energy of the electron-nuclei system on atomic positions in the electronic ground state. Therefore, as was mentioned above, this enables one to determine the whole potential energy surface (PES) of the system. In particular, one can find potential energy minima by relaxing the atomic geometry from different initial geometries [152], calculate the phonon spectrum at any geometry [154, 161] and investigate energy barriers along the minimum energy paths (MEP) connecting different minima. In addition, using atomic forces calculated entirely quantum-mechanically, one can run MD simulations by solving numerically Newton's equations of motion for atoms and hence attempt to investigate the temporal evolution of the system when in the electronic ground state. These tasks are greatly facilitated by the Hellmann-Feynman theorem [152] which allows atomic forces for the given geometry to be calculated from the orbitals directly; differentiating the orbitals with respect to atomic positions (which is not straightforward) is not required.

In practice, calculations are performed using periodic boundary conditions [152, 154] whereby the system of interest (e.g. a carbon cluster adsorbed on the Ir(111) surface) is periodically repeated along the surface; in turn the latter consists of a finite number of atomic layers, which together with the periodic array of molecules on them form a slab. Then the slabs are periodically repeated in the perpendicular direction to make the whole system 3D periodic. It is essential to have sufficient distance between the clusters on the slab (across the surface) to avoid artificial interaction between the images of the clusters; similarly, sufficient vacuum gap is to be selected between slabs to avoid interaction between them. Two other technical points also need to be mentioned. The first one is related to the fact that normally only valence electrons are explicitly represented in the calculation and this is accomplished by means of the method of pseudopotentials [152, 154]. Finally, the second point concerns the basis set used in expanding the orbitals ψ_i: these could be either plane waves $\sim e^{i\mathbf{K}\cdot\mathbf{r}}$ (with the reciprocal vector $\mathbf{K}$) or atomic orbitals centered on atoms. The former set is easy to control and bring to convergence, however, very many plane waves are normally needed for large systems and hence the calculations can be very expensive. The atomic basis set is localized and has a built-in quality of the constituent atoms; therefore, the behavior of the electrons around atoms can be

well reproduced with a rather limited number of orbitals, while adding a small number of additional diffused orbitals may be sufficient to reproduce the behavior of the electrons in the spaces between atoms. As a result, calculations in a localized basis set could be much cheaper than the plane wave calculations. In particular, in calculations of surface properties the vacuum gap can be taken as large as necessary with no detrimental effect on the performance; this is not true for the plane wave basis set since a bigger vacuum gap would result in a finer reciprocal lattice and, as a consequence, more plane waves need to be used to achieve the same precision. At the same time, calculations with the localized basis set are not so straightforward: it is much more difficult to converge the results of the calculations with respect to the basis set, and on top of that there is a specific error in calculating energy differences along a reaction path (e.g. an adsorption energy) as different parts of the system are calculated using basis sets which are not compatible. For instance, in the reaction $A + B \rightarrow AB$ different bases are used for calculating each reactant and the product (remember that only orbitals centered on atoms are used!), and hence the reaction energy $\Delta E = E_{AB} - E_A - E_B$ contains an error due to different levels of convergence of each energy component with respect to the basis set. This so-called basis set superposition error (BSSE) can be compensated to some extend by means of the counterpoise correction method [162].

Although DFT is a ground state theory, it can still be quite useful in trying to understand the mechanism of growth of graphene. To start with, one may study the stability of various carbon species such as monomers, dimers, trimers, etc. on the surfaces and their preferential adsorption sites via geometry optimization calculations. This information in turn provides understanding about which carbon species are in abundance on the surface under current experimental conditions and hence must play a dominant role in the growth. In this respect the problem of locating the global energy minimum on the PES is of special importance [163]. Normally the calculations start from a guessed initial geometry, and the forces on atoms are used to move the system across the PES to a lower energy geometry. This so-called geometry optimization procedure, however, may easily arrive at a local energy minimum; finding the lowest one (the global minimum on the PES) requires performing such simulations starting from many different initial geometries. Physical intuition may help here, however, and various techniques discussed in e.g. Refs. [163, 164, 165] may do a much better job. In particular, methods like *simulated annealing* are frequently used. In this method MD simulations are run at initially very high temperature allowing the system to explore the PES over a rather extensive portion of the phase space; then the temperature is gradually reduced to zero, trapping the system in the global minimum.

Although DFT based methods are in most cases highly reliable, they are computationally expensive, especially when large clusters of atoms need to be modeled on a surface. This is because periodic boundary conditions are normally employed, and a significant chunk of the surface needs to be included in the unit cell in order to ensure reasonable distances between cluster images such that there is no spurious interaction between them. Also, surfaces of crystals are modeled using slabs consisting of a number of surface layers, and in many cases many of those layers need to be explicitly included for the slab to be representative enough of the proper bulk termination [166, 167]. Finally, first-principles DFT simulations scale very unfavorably with the system size and become prohibitively expensive for systems containing more than a few hundred atoms, although attempts to develop more efficient methods which scale "linearly" with the system size are ongoing [165, 168, 169, 170, 171, 172]. The implementation of this strategy places many important phenomena within the capabilities of DFT.

4.1.2. Dispersion interaction within DFT methods

Over the years DFT has earned a lot of respect in the material science community due to its numerous successes in describing structure and a variety of ground state properties of a wide class of materials. The local density approximation (LDA) [173] and different flavours of the generalised gradient approximations (GGA), such as for instance the PBE density functional [174, 175], are the most popular exchange-correlation functionals being used today. The LDA density functional depends only on the electron density alone (the functional is local), while the GGA functionals also depend on the density gradient and are hence semi-local. This means that the dispersion interaction which is non-local in nature is not taken into account by LDA or GGA methods, and hence weakly bound layered compounds where the dispersion interaction must be mainly responsible for their stability, are to be described incorrectly by these methods. Indeed, if LDA overbinds the layers (which is due to the wrong reasons as the binding comes from the exchange while the missing dispersion interaction is the correlation effect by nature), GGA results in significant underbinding [176, 177].

Therefore, over the last decade a significant effort has been made to incorporate the dispersion interaction into the DFT methodology. A number of approaches is now available: (i) A semi-empirical DFT-D method due to Grimme [178, 179, 180] in which a pair-wise force-field expression proportional to C_6^{AB}/R^6 (where R is the distance between atoms A and B and C_6^{AB} a fitting parameter) is added to the DFT energy for all atomic pairs to account for the dispersion forces; the C_6^{AB} coefficients are fitted to high-quality data for a large number of molecules. (ii) van der Waals density functional (vdW-DF) methods [181, 182, 183, 184, 185, 184] in which the correlation energy is represented by a special functional which is non-local in electron density; as it vanishes for a uniform density, it is supplemented by the LDA correlation functional; various exchange functionals can then be added leading to a variety of different techniques (see e.g. [183, 186, 176]); (iii) Tkachenko-Scheffler many-body self-consistent screened theory (TS-SCT) [187, 188, 189] in which a Grimme-like energy contribution is added to the DFT energy with the C_6^{AB} coefficients derived from an adiabatic-connection fluctuation-dissipation theorem (ACFDT) [190].

In fact, the latter theorem allows us to formally obtain the exact exchange-correlation energy within the DFT framework. The calculation requires knowledge of the frequency-dependent density-response function for the interacting electrons, which in turn needs an object called the exchange-correlation kernel. Neglecting the latter altogether results in the so-called random-phase approximation (RPA) for the exchange-correlation functional [190, 191]. This is one of the most sophisticated many-body treatments of the electron correlations available today and is expected to be highly accurate for describing dispersion interactions. It is thought to be less accurate for treating short-range covalent interactions [177].

The quality of vdW-DF based approaches was recently [176, 177] compared with that of RPA for a wide class of layered materials. It was found that the results very much depend on which exchange functional is used. A general conclusion was reached that neither of the existing vdW-DF approaches is capable of reproducing correctly both geometry and binding energies (as compared to RPA) of all studied solids. At the same time, since the RPA calculations are about 200-300 times more expensive than GGA, it is currently still computationally prohibitively expensive to use them for complex systems requiring geometry optimisation; the number of atoms in the unit cell is also to be limited to a few. Therefore, RPA still cannot be used in realistic calculations of complex systems and one has to resort to simpler methods such as DFT-D, vdW-DF or TS-SCT. However, care is currently needed in applying these dispersion corrected DFT approaches as results may depend on the method used. Application of several techniques, such as e.g. vdW-DF and TS-SCT, to the same system (see e.g. [192]) may be required to make meaningful conclusions.

4.1.3. Tight Binding and Empirical Potentials based methods

The expense of the DFT approach is why atomistic simulations based on empirical potentials (EPs) have also been used, and we shall review some of the work which has been done using this type of theories. In these methods the total energy of the whole system is written using simplified analytical expressions (either pairwise or many-body) containing atomic positions explicitly. This allows a quick calculation of atomic forces, so that large systems can be considered and MD simulations evolved over long time scales. The energy expressions also contain fitting parameters, and these are determined by comparing the results of EP calculations with those done by DFT-based methods on the same systems, and/or from experimental data (e.g. bulk lattice and elastic constants, etc.). Because of the nature of EPs and the way in which their parametrization is derived (based on a limited set of trial systems and empirical information), one has to apply EP-based methods with care. Usually, these methods are able to produce reliable predictions of energies of various systems (e.g. comparison of cluster formation energies on a surface), but may fail to give correct energy barriers or predict new adsorption geometries or structures as these may deviate substantially from the trial set used to fit the parameters.

The choice of potential is determined by factors such as the bond type, the desired accuracy, transferability, and the available computational resources. Potentials can be categorized broadly as: (i) pair potentials and (ii) empirical many-body potentials. Two-body, or pair, potentials, such as the Lennard–Jones [193] and Morse [194] potentials, are used for large-scale simulations where computational efficiency is paramount, but where a generic description is sufficient, rather than detailed comparisons with a particular materials system. For systems where multi-body interactions are important [195], the Stillinger–Weber [196], Tersoff [197, 198], and Brenner [199] potentials are often used for covalent carbon-like materials, and embedded-atom [200, 201], effective medium [202], and Finnis–Sinclair potentials [203] are common choices for metals. Such potentials are empirical in that they are parametrized by fitting either to a set of experimental measurements or to

quantum mechanical calculations of representative atomic configurations.

There are also semi-empirical electronic structure methods available, such as the tight-binding (TB) technique, which have also been used for studying graphene growth related problems. These methods are intermediate between more rigorous DFT and EP methods [204, 205]. TB methods are based on a model Hamiltonian which is solved for each geometry giving the total energy and a set of one-electron wavefunctions. The Hamiltonian is parametrized to reproduce results of more refined (e.g. DFT) calculations and some experimental data, and hence may be more universal when compared with the EP approach. In spite of that, this is still a semi-empirical method, and hence the results should be carefully verified against more precise calculations from time to time.

4.1.4. Formation energies

As mentioned in Sections 2.2 and 2.3, calculations of the stability of various carbon species on metal surfaces play a central role in understanding which species are of special importance for graphene growth phenomena. Several definitions of the formation (or stabilization) energy, $E_f(N)$, of a C-cluster with N carbon atoms on a metal surface can be found in the literature. They are broadly based on the following formula:

$$E_f(N) = E_{tot} - (E_{metal} + N\mu_C) \, , \tag{5}$$

where E_{tot} is the total (e.g. DFT) energy of the cluster relaxed on the metal, E_{metal} is the energy of a bare metal surface, and μ_C is the energy of a single carbon atom, but sometimes referred to as its chemical potential (but this would only be appropriate terminology if the temperature were zero). The difference between various approaches adopted in the literature lies in the definition of μ_C. For instance, Gao *et al.* [206] define μ_C as being the formation energy per carbon atom of a free-standing graphene sheet. This is in contrast to Wesep *et al.* [207] who define μ_C to be the energy of an isolated carbon atom. In a different study by Riikonen *et al.* [208] both definitions were used and it was shown that there are differences, of course, in the values of the formation energies obtained using each definition. Although this matter might seem to be unimportant, it does affect our conclusions concerning the relative stabilities of clusters with different numbers N of atoms on the metal surface (as it is e.g. done in [209] as discussed in Section 7.2.3).

If μ_C is taken to be the energy of an individual carbon atom *on a terrace* then equation (5) can be used to compare binding energies of various carbon clusters on the terrace or at steps. In this case the expression would correspond to the formation energy of a cluster from individual adsorbed carbon atoms. In order to determine whether an existing diffusing cluster of N carbon atoms on a terrace might preferentially stick to a metal step, a slightly different definition is to be used:

$$E_f^s(N) = E_{tot} - E_{step} - E_f(N) \, , \tag{6}$$

where E_{tot} is the total energy of the cluster attached to the step, E_{step} is the energy of an bare metal step and $E_f(N)$ the formation energy (5) of the $N-$atom carbon cluster on the surface. A slightly more complex expression for the formation energy is required when assessing the stability of an $N-$atom carbon cluster at the edge of a graphene island (graphene ribbons are normally used in practical calculations relying on periodic boundary conditions implemented in widely used DFT codes) as detailed in Section 7.2.4.

Thermodynamic equilibrium between graphene islands and single carbon atoms and clusters requires the chemical potential μ_C of the C atoms to be the same in each phase. If the calculated chemical potential of C atoms in clusters is higher than that in islands, the clusters are thermodynamically unstable and should eventually attach to graphene; the same can be said for single carbon atoms roaming the surface. If however the chemical potential of C atoms in graphene flakes on the surface is higher that in clusters, graphene formation is not sustainable and large flakes will not grow; instead, there will be many C clusters on the surface. Using this kind of argument one might attempt to speculate on which cluster size is critical for the growth of graphene. This will be the size N for which the calculated energy per C atom of the cluster C_N on the surface, used as an estimate of its chemical potential, becomes lower (more negative) than the C atom energy (i.e. the chemical potential) in graphene *on the surface*. Note that the latter might be quite different from the C atom energy in the free standing graphene, especially in the cases of transition metals such as Ru(0001) and Rh(111) for which the interaction of the metal with graphene on top of it is the strongest. In the situation of a real experiment, however, this kind of analysis may only serve as a guide and hence should be used with care. It is more relevant for the nucleation stage (see Section 2.2) when the difference of chemical

potentials (supersaturation) drives the phase change. During growth the system is far from equilibrium, and the total energies of structures may be of less importance compared to the energy barriers which mostly determine the kinetics. In addition, there is a much richer variety of carbon containing species on the surface during growth, not just C atoms and clusters (see Section 7.2.1).

4.1.5. Nudged Elastic Band Method

Static calculations can provide a lot of information about the *dynamics of a* system as well, which is absolutely essential for understanding the growth phenomenon. For instance, ground state DFT calculations are well suited for studying carbon species mobility (i.e. diffusion barriers) by calculating the minimum energy paths (MEP) connecting two stable minima on the PES. This problem is related to that associated with finding a transition state (TS), or a saddle point, between two energy minima and hence a calculation of the energy barrier to cross from one minimum to the other. This task can be solved by so-called constrained minimization whereby the system is taken between initial and final states along a trajectory realized using a set of some selected atomic coordinate(s). For instance, a diffusion barrier can be calculated by taking a molecule between two adsorption sites by way of fixing the lateral (reaction) coordinates of a single atom of the molecule at each position along the diffusion path; all other coordinates of the system including the position of the atom in a plane orthogonal to the reaction coordinates are allowed to relax. Moving the atom between the initial and final states in small steps and relaxing the system in this manner can allow the system to be taken over the barrier.

The problem with this approach however is that in real situations it might be very difficult to guess what reaction coordinate one should choose that would allow passing exactly over the actual saddle point on the PES corresponding to the top point on the MEP. The wrong choice will result in the energy barrier being overestimated. The Nudged Elastic Band (NEB) method [210, 211, 212] eliminates this problem. In this method the MEP is found numerically by means of a finite number of "images" of the system which correspond to system geometries along the MEP. The image(s) in the middle of the sequence would correspond to the system geometry at or near the transition state on the MEP. Assuming there is only one TS along the MEP connecting the initial and the final states, the energy difference between the TS and the initial (final) state corresponds to the energy barrier for going from the initial (final) to the final (initial) state over the TS. The images are "connected" by springs to keep the images apart from each other and hence map the MEP uniformly. To avoid the band slipping off the actual MEP during the optimization process, only projections of forces on atoms due to springs which are parallel to the band are considered, while projections of DFT forces in the same direction are removed, i.e. only the perpendicular part of the DFT forces on atoms with respect to the band direction are kept. Using NEB one can also calculate attachment (and detachment) energies and associated barriers for carbon atoms and clusters to attach to (coalescence with) or detach from each other or step edges. This wealth of information can be compared with the corresponding results on terraces, and hence conclusions can be drawn concerning the role played by extended surface defects in the growth of graphene islands. Finally, detailed energetic information can be used in building up kinetic models of growth either at phenomenological (section 7.1) or atomic-scale (section 7.4) levels. We shall briefly explain the main ideas of kinetic simulations based on atomic-scale theories in the next section.

4.2. Simulations of dynamics of growth processes

4.2.1. Molecular dynamics simulations

During growth atoms move around to assume geometries and configurations which correspond to the lowest free energy under the given thermodynamic conditions (temperature T and pressure P). In this sense it seems natural in the atomistic simulations to allow the atoms to move according to the forces acting on them as this basically repeats what nature is doing. If $\mathbf{F}_i$ is the force acting on atom i, then atomic positions change according to Newton's equations of motion:

$$m_i \dot{\mathbf{v}}_i = \mathbf{F}_i \ , \quad \dot{\mathbf{r}}_i = \mathbf{v}_i \tag{7}$$

Here $\mathbf{r}_i(t)$ and $\mathbf{v}_i(t)$ are the position and velocity of atom i at time t. These equations are the essence of MD simulations. In practice the calculations are solved numerically using various discretization schemes [158]. Special algorithms have been also developed to simulate in these numerical experiments particular thermodynamic ensembles such as NVT (constant number of particles N, volume V and temperature T)

and NPT (constant N, T and pressure P) [158]. The latter ensemble is more relevant to the case of simulating the growth phenomenon as the pressure rather than the volume is kept constant in the experiments.

Although MD simulations at first glance seem to be the method of choice in studying growth processes, they are not strictly speaking designed for them. This is because growth is associated with many elementary (local) events requiring the surmounting of (sometimes large) energy barriers when the system jumps between different minima on the PES. Indeed, the basic limitation of the MD method that has prevented long simulation times is that the integration time step must be small enough to capture the dynamics of the vibration modes of the system, with frequencies of the order of $10^{13}\,\mathrm{s}^{-1}$. This requires time steps in the *femtosecond* range. But the residence time of, say, an adatom between hops can extend to *microseconds* because of the energy barriers that separate different energy minima on the PES, and the interactions responsible for aggregation phenomena occur over a time scale of *milliseconds* to *minutes*. If one attempts to run an MD simulation of a growth process in which numerous activation events are present, the system would spend most of the time sitting in the potential energy wells with extremely rare jumps between them; this is evident from the trajectories of mobile atoms, which are complex paths localized around their initial sites with only rare excursions to neighboring sites. In fact, if the energy barriers are much larger than k_BT (here k_B is Boltzmann's constant), no transitions will be observed at all during the course of a typical MD run, even if we run them over a very long time exceeding any available resources many times over. In spite of the fact that several methods have been developed for accelerating the MD treatment of such rare events, based on stimulating the transitions to occur faster than in an ordinary simulation [213], these methods are still very expensive and hence can only be applied in classical MD simulations. The other reason why MD simulations may be of more limited use in studying growth processes is that normally we are not really interested in the detailed knowledge on the atomic level of what the system is doing when spending most of its time sitting in the energy well; we are more concerned with the transitions themselves between the wells as the system attempts to reduce its free energy during growth of the new phase.

4.2.2. Kinetic Monte Carlo simulations

A necessary advance can be made by going beyond the atomistic detail and considering kinetic processes in a time (and space) coarse-grained manner. In Monte Carlo methods [214] the *deterministic* equations (7) of MD are replaced by equations based on *stochastic* transitions for the slow processes in the system. In their most general form, Monte Carlo methods are stochastic algorithms for exploring phase space, but their implementation for equilibrium and nonequilibrium calculations is somewhat different [215, 216]. Here, as we are interested in the simulation of growth driven by an external source of material, we will focus on the kinetic Monte Carlo method (KMC).

KMC simulations are capable of providing a realistic platform for studying system dynamics (kinetics) related to performing activation events, and this is modeled as a sequence of consecutive jumps between free energy minima, in real time [217, 218, 219, 220]. Suppose that the probability of finding a system in state σ at time t is $P(\sigma,t)$ and that the transition rate per unit time from σ to σ' is $W(\sigma,\sigma')$. The equation of motion for P is the master equation [221]:

$$\frac{\partial P}{\partial t} = \sum_{\sigma'} P(\sigma',t)W(\sigma',\sigma) - \sum_{\sigma'} P(\sigma,t)W(\sigma,\sigma')\,. \tag{8}$$

KMC methods are algorithms that solve the master equation by accepting or rejecting transitions with probabilities that yield the correct evolution of a nonequilibrium system. The effect of fast dynamical events is taken into account phenomenologically by stochastic transition rates for slower events. Hence in KMC simulations only jumps between states of the systems are considered, ignoring completely residence events, i.e. the time the system spends within a given state (potential well). Suppose at a given time t the system occupies a state i associated with a certain arrangement of atoms, clusters, molecules, etc. on the surface. We are interested in the evolution of the system in time as various surface species diffuse across the surface, desorb, decompose (e.g. hydrocarbon molecules lose their H atoms), and coalesce (e.g. C atoms attach to clusters, clusters attach to islands and so on). At each time step one has to specify then all the states j the system may propagate into from the given state i according to the various local processes mentioned above. For each of those processes one calculates the transition rate according to transition state theory (TST) [222]

$$r_{i\to j} = \nu_i \exp\left(-\frac{\Delta E_{i\to j}}{k_BT}\right)\,, \tag{9}$$

where ν_i is an attempt frequency which is of the order of the frequency of atomic vibrations (around $10^{12}-10^{13}$ s^{-1}) [223, 224] and $\Delta E_{i\to j}$ is the energy barrier required for making the transition $i \to j$ which can be calculated, for example, using NEB as was discussed earlier. The rate $r_{i\to j}$ corresponds to a single transition which takes the system from its current state i; the sum of the rates

$$R_i = \sum_{j\,(\neq i)} r_{i\to j}$$

corresponds to the total rate of leaving the current state, i.e. it is an *escape rate*. The probability $P_i(t) = \exp(-R_i \Delta t)$ to *remain* in the current state over time Δt is exponentially decaying with time since eventually the system would leave the current state and hence the probability to remain in it must decay to zero (because of transitions into other states). Consequently, the time of a successful transition can be determined at random from

$$\Delta t = -\,(1/R_i)\ln x_1\ ,$$

where x_1 is a random number between 0 and 1. To determine explicitly which state j is to be selected for the successful transition, we assume that the probability of each such event is given by the ratio $P_{i\to j} = r_{i\to j}/R_i$. In practice, the state j is calculated also at random by picking up the second random number $x_2 \in (0,1)$ and then picking the event j from the condition

$$\sum_{k=1}^{j-1} r_{i\to k} < x_2 < \sum_{k=1}^{j} r_{i\to k}\ .$$

Once the state j is chosen, all possible transitions from j to other states are analyzed again, the list of all of them is constructed and the total escape rate R_j calculated. Then two new random numbers are taken again to determine the time for the next transition Δt and which transition from the new list the system would jump into. This process is repeated many times until the required state of the system is reached, i.e. the new phase has been fully formed.

It is seen that during the evolution the system indeed jumps from one potential energy well to another. The states after each transition and the transition times are chosen at random, i.e. the system propagates in time via a particular trajectory which depends very much on the available elementary processes and their energy barriers. If at a given state i there are processes j with small and large barriers, the rates of these $r_{i\to j}$ will be strongly disparate and the transition with the smallest barrier (the largest rate) is most likely to be selected. As a result, it is probable that during the course of the evolution various events with the smallest barriers will play the dominant role; at the same time, it is worth remembering that least probable transitions can (and will) be selected as well from time to time. In fact, the system would progress quickly in time until all fast processes are realized (large rates, small time steps Δt); then further progress would require a less probable process to be chosen which is associated with a larger barrier, smaller rate and longer time Δt.

Although the details of the underlying mechanism for kinetic processes are lost, the explicit calculation of atomic trajectories is avoided, so KMC simulations can be performed over real times, running into seconds, hours, or days, as required. The KMC method offers considerable advantages over the MD method both in terms of the real time over which the simulation evolves, as well as in the number of atoms included in the simulation, because much of the computational overhead in MD used to evolve the system between rare events is avoided.

The main challenge for KMC simulations is to be able to identify all the essential states the system can jump into from a given state. Usually, to simplify the problem an intelligent selection of the moves performed on "the lattice" of system configurations is made, and the corresponding transition rates are obtained from the energy barriers calculated for the chosen "moves" before the KMC simulations. In some cases this approach may lead to oversimplified kinetics in which essential processes are missing. Therefore, care as well as detailed study of the possible elementary processes is required prior to devising the KMC simulation schemes. Thus KMC models can often benefit from a related classical or quantum MD simulation to identify the important physical process, and NEB simulations to estimate the prefactors and kinetic barriers. Quite often, experiments themselves can suggest a particular mechanism. The feasibility of performing detailed simulations over experimental time scales enables various parametrizations to be tested and models of kinetic phenomena to be validated.

4.2.3. Grand Canonical Monte Carlo simulations

Sometimes real dynamical simulations are replaced by an intuitive approach based on the Grand Canonical Monte Carlo (GCMC) method [158]. In this method the system of atoms is propagated by a sequence of "moves"; at each move the system is changed in a certain way, e.g. an atom is added from an atomic reservoir (the source), removed from the system into the reservoir (sink), or displaced on the surface, and then all atoms are relaxed to mechanical equilibrium. However, not all the moves are automatically accepted as the method has a stochastic element in it. The decision on whether to accept the move or reject it is made depending on the temperature and a comparison of the energy difference between the final and initial states with the chemical potential μ of the species of interest (e.g. of C atoms), which is the characteristic thermodynamic feature of the source-sink reservoir (assumed to be very large, i.e. macroscopic, e.g. carbon feedstock). This is done by employing a Metropolis-like algorithm: if the energy after adding/removing an atom is reduced, the probability of this event is taken as unity, however, if the energy is higher, then the step is accepted at random with a certain probability. In can be shown [158] that this method generates a sequence of system states that eventually converges to the correct grand canonical distribution of species (e.g. C atoms and C-clusters on the surface) in a sense that after some number of moves, depending on the nature of the system and the starting configuration, the system "equilibrates", i.e. new moves would sample the phase space according to the grand canonical distribution. However, care is needed here. Even though the moves may resemble real processes happening during growth, it is essential to realize that this kind of simulation cannot be considered as real kinetics, i.e. as a realistic propagation of the system in time, as the algorithm is not designed for this purpose. The method simply drives the simulated system to thermal equilibrium with the source-sink system (e.g. C gas above the surface), and the path along which this neighbourhood in the phase space is reached has nothing to do with the real time propagation of the system during growth. Moreover, as was already mentioned, during the growth process the system may be far from equilibrium, while the GCMC simulations is a genuinely equilibrium approach. And therefore there is a problem with this technique which is that it is not straightforward to connect the results of the simulations with experiment [225] as experimentally the chemical potential of carbon is not maintained at a fixed value.

4.3. Continuum equations

In models of nonequilibrium systems based on continuum equations, typically in the form of deterministic or stochastic partial differential equations, the underlying atomic structure of matter is neglected altogether and is replaced by a spatially continuous and differentiable mass density. Analogous replacements are made for other physical quantities such as energy and momentum. Differential equations are then formulated either from basic physical principles, such as the conservation of energy or momentum, or by invoking approximations within a particular regime, using e.g. a coarse-graining by smearing out fast degrees of freedom as compared to the characteristic time of interest (e.g. growth kinetics).

There are many benefits of a continuum representation of kinetic phenomena. Foremost among these is the ability to examine macroscopic regions in space over extended periods of time. This is facilitated by extensive libraries of numerical methods for integrating deterministic and stochastic differential equations. Complementing the numerical solution of partial differential equations is the vast analytic methodology for identifying asymptotic scaling regimes and performing stability analyses. Additionally, if a continuum equation can be systematically derived from atomistic principles, there is the possibility of discriminating between inherently atomistic effects and those that find a natural expression in a coarse-grained framework. Continuum equations also provide the opportunity for examining the effect of apparently minor modifications to the description of atomistic processes on the coarse-grained evolution of a system which, in turn, facilitates the systematic reduction of full models to their essential components. Because continuum theories based on methods such as the phase field for graphene are only beginning to emerge (see Section 7.4), these methods will be given a quick mention here, as they have the potential to uncover the growth kinetics of graphene at the mesoscopic scale. We hope that this would stimulate theorists in applying these techniques for studying this fascinating growth problem.

4.3.1. Burton-Cabrera-Frank Theory and Phase-field Method

The Burton–Cabrera–Frank (BCF) theory [226] describes growth on a stepped surface of a monatomic crystal in terms of the deposition and migration of single adatoms. The central quantity in this theory is, therefore, the adatom concentration $c(\mathbf{x}, t)$ at position $\mathbf{x}$ and time t. The processes which cause this quantity

to change are the surface migration of adatoms, which have diffusion constant D, the flux J of adatoms onto the surface from an incident flux, and desorption of the atoms from the surface at an average rate τ_s^{-1}. The equation determining $c(\mathbf{x}, t)$ on a terrace is a two-dimension diffusion equation with source and sink terms:

$$\frac{\partial c}{\partial t} = D\boldsymbol{\nabla}^2 c + J - \frac{c}{\tau_s}\,. \tag{10}$$

This equation is supplemented by boundary conditions which give the normal velocity of a step edge,

$$v_n = \left(D\boldsymbol{\nabla}c\big|_+ - D\boldsymbol{\nabla}c\big|_-\right)\cdot\boldsymbol{n}\,, \tag{11}$$

where the unit normal $\boldsymbol{n}$ points from the upper (denoted by "+") to the lower (by "-") terrace. The scale of the adatom concentration is determined by the competition between the deposition flux, which drives the surface away from equilibrium and *increases* the adatom density, and the relaxation of the surface towards equilibrium through adatom diffusion, which *decreases* the adatom density. Since the BCF theory neglects interactions between adatoms, the growth conditions must be chosen to ensure that the adatom concentration is maintained low enough to render their interactions unimportant. Thus, this theory is valid only for high temperatures and/or low fluxes, where growth is expected to occur by the advancement of steps.

The phase-field method provides a mathematical description to free-boundary problems for phase transformations, such as solidification and the assembly of structures on a surface, in which the interface has a finite, but small, thickness. The central quantity in this method is an auxiliary function, called the ***phase-field***, whose value identifies the phase at every point in space and time. The phase field model of the solid-liquid phase transition was first proposed by Langer [227], and has developed into a widely-used method of computing realistic growth structures in a variety of settings [228].

The phase field method has been applied to stress-induced instabilities [229], the motion of steps [230, 231, 232], island nucleation and growth [233, 234, 235], and self-organized nanostructures [236].

4.3.2. Rate Equations

With increasing temperature or decreasing deposition rate, growth by the nucleation, aggregation and coalescence of islands on the terraces of a substrate becomes increasingly likely and a description of growth by the advancement of steps is no longer appropriate. One way of providing a theoretical description of this regime within an analytic framework is with equations of motion for the densities of adatoms and islands. These are called rate equations [237].

We will consider the simplest rate equation description of growth, the most relevant to the issues being considered here, where adatoms are the only mobile surface species and the nucleation and growth of islands proceeds by the *irreversible* attachment of adatoms, i.e. once an adatom attaches to an island or another adatom, subsequent detachment of that adatom cannot occur. We will signify the density of surface atoms by $c \equiv c_1(t)$ and the density of n-atom islands by $c_n(t)$, where $n > 1$. Thus, the rate equation for c_1 is

$$\frac{dc}{dt} = J - 2D\sigma_1 c^2 - Dc\sum_{n=2}^{\infty}\sigma_n c_n \tag{12}$$

In common with most formulations of rate equations, the adatom and island densities are taken to be spatially homogeneous. In particular, there is no diffusion term, $D\nabla^2 c$, despite the fact that adatoms are mobile. This description is most suitable for flat surfaces, where there are no pre-existing steps to break the translational symmetry of the system and induce a spatial dependence in the adatom and island densities. But even in this case, spatial effects cannot be neglected altogether. This will be discussed below.

The first term on the right-hand side of (12) is the deposition of atoms onto the substrate (with rate J), which increases the adatom density, and so has a positive sign. The next term describes the nucleation of a two-atom island by the irreversible attachment of two migrating adatoms. This term decreases the number of adatoms (by two) and thus has a negative sign. The rate for this process is proportional to the *square* of the adatom density because two adatoms are required to form a two-atom island, and to D, the adatom diffusion constant, because these adatoms are mobile. The third term accounts for the depletion rate of adatoms due to their capture by islands with all possible numbers of atoms. This term is proportional to the product of the adatom and total island densities and must also have a negative sign. The quantities σ_i ($i \geq 1$), called "capture numbers", account for the diffusional flow of atoms into the islands [237, 238, 239, 240].

The rate equation for the density of n-atom islands $c_n(t)$ is

$$\frac{dc_n}{dt} = Dc\sigma_{n-1}c_{n-1} - Dc\sigma_n c_n \tag{13}$$

The first term on the right-hand side is the creation rate of n-atom islands due to the capture of adatoms by $(n-1)$-atom islands. Similarly, the second term is the depletion rate of n-atom islands caused by their capture of adatoms to become $(n+1)$-atom islands. There is an equation of this form for every island comprised of two or more atoms, so Eqs. (12) and (13) represent an infinite set of coupled ordinary differential equations. However, since the density of large (compared to the average size) islands decreases with their size, in practice the hierarchy in (13) is truncated to obtain solutions for $c(t)$ and the remaining $c_n(t)$ to any required accuracy. Notice that in writing (13) we have omitted any direct interactions between islands. This restricts us to a regime where there is no appreciable coalescence of these islands.

Rate equations produce correct scaling of island densities with D/J in the *aggregation regime* of island growth, i.e. where the island density has saturated and existing islands capture all deposited atoms. However, the scaling of c and c_n with coverage is not correctly accounted for. This can be traced to the approximation of constant capture numbers, which misses important aspects of island kinetics. The next level of approximation is to include the spatial extent of the islands in an average way by assuming that the local environment of each island is independent of its size and shape [238]. This produces the correct scaling of c_n with both D/J and coverage, but still not the correct distribution of island sizes. The calculation of the latter quantity requires proceeding one step further by including explicit spatial information in the capture numbers to account for the correlations between neighboring nucleation centers and the different local environments of individual islands [239, 241]. In practice, only total island densities are analyzed with rate equations; simulations or semi-analytic methods, such as the phase-field and level-set methods, are used for the quantitative analysis of measured island-size distribution functions.

5. Growth Methods

It is now known that graphene can be grown via several different methods. Of these some involve producing graphene epitaxially on transition metal surfaces [242]. In the major method of production called *chemical vapor deposition* (CVD) carbon or carbon based molecules are deposited onto a surface under conditions for which absorption into the bulk can be neglected. In CVD the species are deposited onto a surface that is originally at some high temperature. Though not discussed here, there has also been recent interest in depositing onto transition metal films supported on a separate substrate [243, 244, 245, 246, 100, 247]. As well as this method, *temperature programmed growth* (TPG) has also been used. In this approach temperature control is employed to stimulate graphene growth on a surface using as the carbon source hydrocarbons that are deposited on the surface initially at room temperature. Another kind of surface-confined growth on metals involves the formation of a surface carbide as a transient state. In another method, to be called the *segregation method* hereafter, carbon is deposited on a surface maintained at such a high temperature that a proportion of C atoms are absorbed into the bulk of the metal. Upon cooling, the absorbed carbon segregates from the bulk to the surface and becomes mobile forming graphene flakes, i.e. the segregated carbon in the bulk is used as a source. In addition to these methods where graphene is formed on metal surfaces, graphene can be grown on SiC. The most widespread approach consists in heating SiC to a high enough temperature for silicon to sublimate from the surface, leaving behind carbon atoms that may then form graphene. A less studied approach (especially from the point of view of the processes at play during growth) involves molecular beam epitaxy [248, 107] and CVD [249, 250] on SiC. In this section we review experimental observations of graphene growth using methods mentioned above. Since our main interest is understanding the growth of graphene, to which both experiment and theory have been contributing over the years, we start in this section discussing the main experimental techniques that have proven extremely useful in understanding the growth phenomenon.

5.1. Chemical Vapor Deposition (CVD)

We consider here the deposition of molecules containing carbon onto a transition metal surface. Typical carbon precursors are ethene or methane [92, 61] but it is also possible to grow graphene using a variety of different larger carbon based molecules [251]. Prior to the deposition of hydrocarbons the surface of the

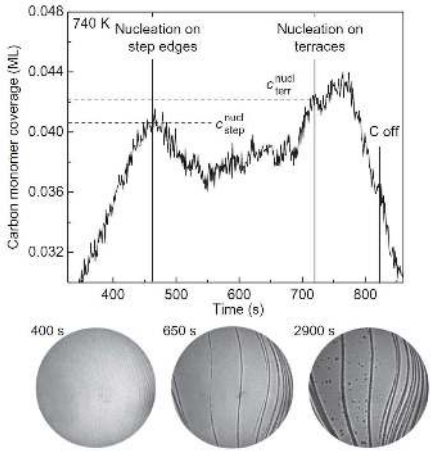

Figure 13: Time evolution of adatom coverage during and after C deposition (marked "C off") on Ru(0001) surface kept at 740 K (top panel), shown together with LEEM images (at the bottom) at various times during growth. The first decrease in adatom concentration corresponds to nucleation at step edges. This is clear from the LEEM image at 650 s which clearly shows Ru steps decorated with graphene. The second decrease in adatom concentration occurs at a higher coverage and corresponds to nucleation on terraces. [Reproduced from [54] by permission of IOP Publishing. All rights reserved.]

transition metal is cleaned. The sample is placed in a UHV chamber, with a base pressure of approximately 10^{-11} mbar and is subjected to cycles of room temperature sputtering with energetic (typically 1 keV) ions (e.g. Ar^+) and flash annealing between 1200 and 1500 K. Then the sample is kept at some specific temperature, usually greater than 700 K [61, 252]. Gaseous molecules are introduced onto the hot surface. The pressures and flow rates of vapors in the dosing tube are varied to produce different fluxes of molecules onto the transition metal surface.

There are a number of different substrates that have been used to grow graphene. These include crystalline substrates such as Cu(111) [253], Ni(111) [254, 255], Co(0001) [256, 257], Fe(110) [258], Au(111) [259], Pd(111) [62], Pt(111) [58], Re(10$\bar{1}$0) [260], Ru(0001) [106], Rh(111) [261], Ir(111) [61, 139, 54, 92], but also polycrystalline surfaces [262, 263, 252] and thin films evaporated onto a different bulk material [264, 265]. Here we only mention metals used for CVD; other substrates will be mentioned later on in Sections 5.2, 5.3 and 5.4. We now summarize some of the key observations concerning nucleation and growth of graphene for a number of transition metal surfaces. Unless stated, the experiments are carried out in UHV and it is ethene which is deposited onto a hot transition metal surface.

5.1.1. Nucleation

Nucleation of graphene on a surface can occur homogeneously on terraces or at defect sites on the surface (e.g. at steps). It is of particular interest to understand graphene nucleation for applications requiring extremely high quality material that is free of defects. This is because when graphene nucleates at many places on the surface the eventual coalescence of individual graphene islands can create grain boundaries or edge defects that can have detrimental effects on some of graphene's electronic properties. We thus consider some of the experimental observations on different surfaces.

On Ir(111) at an ethene partial pressure of 5×10^{-10} mbar, graphene islands nucleate almost exclusively at step edges for growth temperatures between 790-1320 K [61], although for temperatures greater than 1120 K there is an extremely small fraction of islands found to nucleate at terraces as well. This is similar to growth on Ru(0001) where nucleation also begins at step edges and specifically on lower terraces at low C atom concentrations, but also on terraces for high C atom concentration [54], see Fig. 13. This is in contrast to growth on Rh(111) and Pt(111) where nucleation has been observed to occur homogeneously on terraces [252, 251, 206] while on Cu(111) and polycrystalline copper surfaces, graphene has been observed to nucleate heterogeneously at steps, defects and impurities [262, 266, 267].

It was also observed in [267] that the number of nucleation events on copper is reduced with temperature as shown in Fig. 14. At not very high temperatures the dependence of the nucleation density is fitted well by an Arrhenius dependence with an effective activation energy of E_A =1 eV. This regime is attributed to an

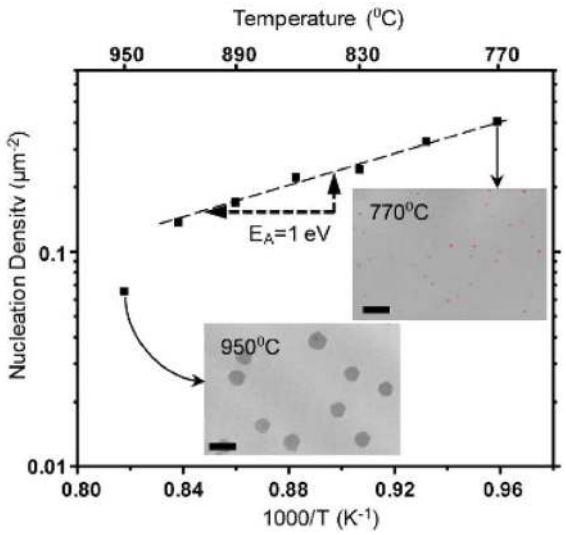

Figure 14: Measured nucleation density on copper fitted to an Arrhenius type of behavior across a temperature range from 1043 K (770°) to 1223 K (950°C). Insets: typical SEM images of the copper surface at the initial stages of graphene growth for 1043 K (770°) and 1223 K (950°C) (scale bar: 1 μm). [Reprinted with permission from [267]. Copyright (2013) American Chemical Society.]

attachment-limited nucleation. However, at higher temperature of 1223 K the nucleation density drops significantly. This data is corroborated by the SEM images shown in the insets for two temperatures. Although no specific explanation for this effect was suggested, it may be due to enhanced diffusion of active species during nucleation processes at higher temperatures. Indeed, the growth of fluctuations as the temperature is increased should lead to an increase of homogeneous nucleation events; however, this is not observed in experiment as small clusters formed in this way would quickly merge with other ones due to ripening processes leading to a smaller number of clusters at larger sizes.

5.1.2. Island morphology and growth

We expect the strength of the interaction between carbon species and the transition metal to be an important factor in influencing the shape of growing islands, and indeed, for different transition metals, which are thought to have different magnitudes of interaction with graphene, we see different island morphologies.

Ruthenium. A number of groups have demonstrated the step-down growth of graphene on Ru(0001), whereby islands are only able to grow from upper terraces to lower terraces over steps and not the other way round [92, 54, 91, 268, 269]. This particular scenario is seen to occur both when carbon is provided by carbon segregating from the bulk (Section 5.4) and also when carbon is deposited onto a hot transition metal surface. The processes occurring during the step down growth have been observed *in situ* using high temperature STM by dosing the surface held at 938 K with ethene at 2×10^{-8} mbar to induce nucleation, and then as soon as islands were observed the ethene pressure was reduced to 5×10^{-9} mbar [269]. In this study, whose aim was to explore this step down growth process in detail, the edges of these islands were observed to be "finger-like", see Fig. 15, meaning that the growth front did not move coherently over a step [269]. Instead a mechanism was observed whereby part of the growth front, through some fluctuation, was able to attach to a lower terrace. This point on the island then presumably acts as a seed for the growth to continue onto the lower terrace.

In the same study a different growth pattern was observed at high temperatures and extremely low pressures that resulted in yet another growth process [269]. Ethene was deposited at 938 K at 2×10^{-8} mbar. The pressure was then reduced by shutting the ethene entry valve so that the only deposition was due to the molecules remaining in the dosing tube. Graphene islands under these conditions were observed not to overgrow the Ru step but instead to grow at the same rate as the Ru step as described in Fig. 16. The authors speculated that this growth process requires Ru atoms to be transported to sites underneath the graphene layer and they further suggested the source of Ru atoms are etched terraces, observed as the

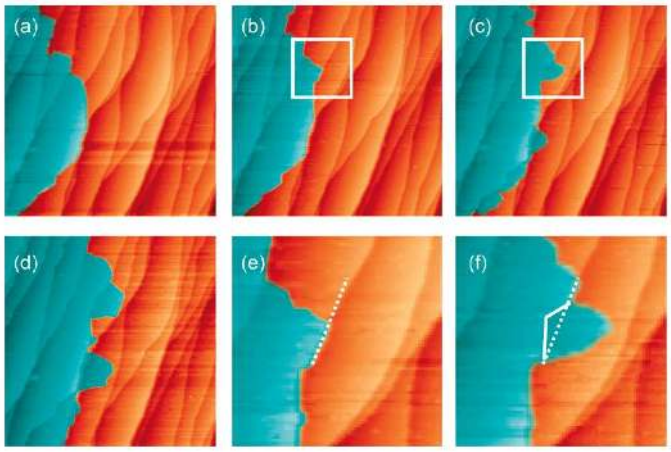

Figure 15: (a-d) A series of *in situ* STM images at 938 K showing the growth of graphene (blue) across the steps of the Ru(0001) surface (orange). (e,f) Details from panels (b) and (c); the dashed lines mark the changed step position between the consecutive panels (e) and (f). [Reprinted with permission from [269]. Copyright (2011) American Chemical Society.]

dark lines labelled "-Ru" in Fig. 16. Although graphene grown in this way was observed to be of extremely high quality, the low ethene pressures would inhibit the growth rate and, as the authors note, could limit the applicability of this procedure to the production of large graphene sheets.

Iridium. Unlike the growth of graphene on Ru, on iridium islands growing on lower terraces are not impeded by steps and so can grow both up and down iridium steps [57], although they still demonstrate a preference for growing down steps [92]. STM images taken at 300 K of islands grown at 1120 K and 5×10^{-10} mbar ethene pressure show a number of islands of uniform size after 20 s of growth [61], see Fig. 17. After 40 s of growth a drop in island density is seen indicating the coalescence of graphene islands. The growth rate of immobile islands on iridium has been shown to proceed by exactly the same cluster attachment mechanism as seen on Ru [54]. Whether only a limited number of rotational domain types exist on Ir(111) [106] or a scatter of orientations is present [99] remains an open question; this probably depends on the growth conditions. It has also been shown that graphene on Ir(111) exists in different rotational domains with respect to the Ir substrate [92]. This is discussed further in Section 6.1.4. Formation of different rotational domains has been shown to be temperature dependent and further that certain rotational domains seem to grow at a different rate to others [99, 92].

Copper. Graphene has been grown on both crystalline and polycrystalline surfaces of copper using CVD with different feed molecules and under different conditions. We consider here the growth on Cu(111), Cu(001) and on polycrystalline copper foils. Islands growing on these surfaces demonstrate a number of different morphologies which may indicate that growth proceeds by different processes depending on the experimental conditions. Copper and graphene interact only very weakly so that (i) graphene can easily ascend steps and (ii) graphene islands grow with many different rotational domains, like on Ir(111) (see the previous section) and on Pt(111) [48, 58].

It has been shown that it is possible to grow large single layer graphene sheets on Cu(111). In 2010 Gao *et al.* [253] deposited ethene at a partial pressure of 10^{-5} mbar onto Cu(111) while repeatedly cooling and flash heating the surface to 1273 K. For 0.35 % of the Cu(111) covered with graphene a number of hexagonal domains were observed with some of them bonded at substrate step edges. At larger coverages continuous graphene sheets were observed suggesting that smaller graphene domains coalesce. The sheets were shown to consist of different rotational domains although only two rotational domains were seen in high concentrations. Further, hexagonal domains were observed to form two different rotational domains with respect to the Cu lattice. Nie *et al.* [266] examined in detail the effect of Cu defects and growth temperatures on graphene morphology. Instead of exposing the surface to ethene and cooling, they deposited carbon obtained from heating a carbon rod onto a Cu(111) surface at different temperatures. The morphologies of graphene islands growing on Cu(111) during deposition of carbon from a graphitic rod have been shown to be strongly

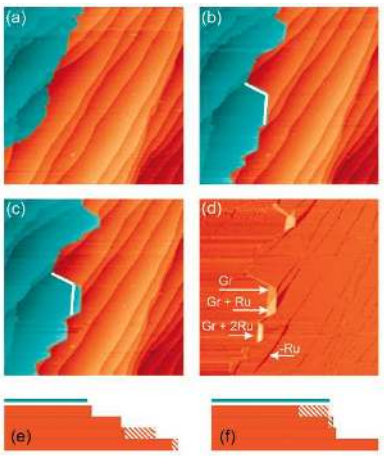

Figure 16: *In situ* STM images at 938 K, showing the single terrace mode. (a) After dosing 4.5 L of C_2H_4 at 2×10^{-8} mbar the ethene valve was closed. (b,c) Ru(0001) terraces grow and steps are no longer overgrown. (d) Differential image of (b) and (c), showing areas where Ru atoms are removed (dark) and areas where graphene has grown and one or two layers of Ru atoms deposited (bright). Colors as in Fig. 15. (e,f) Proposed growth mechanism with the shading indicating reshuffled Ru layers. [Reprinted with permission from [269]. Copyright (2011) American Chemical Society.]

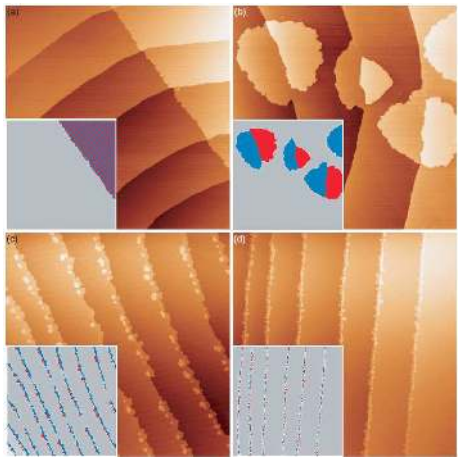

Figure 17: STM images of graphene on Ir(111) during CVD growth. Images taken at 300 K after growth has been allowed to continue for: (a) 80 s and (b)-(d) 40 s. Surface temperatures are: (a) 1320 K, (b) 1120 K, (c) 970 K, (d) 870 K, and in all cases the pressure of ethene during deposition was 5×10^{-10} mbar. Insets show graphene attached to ascending step edges (blue) and descending steps (red). [Reproduced from [61] by permission of IOP Publishing. All rights reserved.]

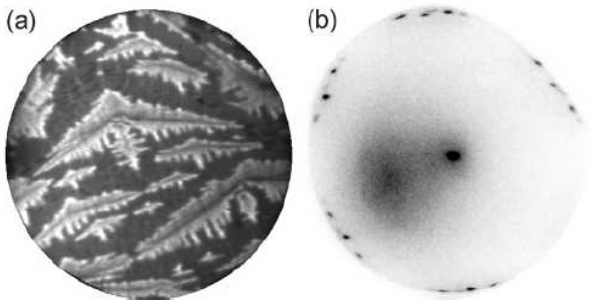

Figure 18: (a) Dendritic graphene growing on Cu(111) at 963 K. Field of view is 7μm. (b) LEED pattern (44 eV) from a 0.5-μm-diameter region of an island, showing that it is polycrystalline. [Reprinted with permission from [266]. Copyright (2011) by the American Physical Society.]

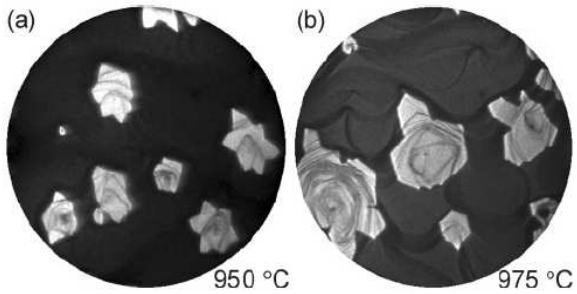

Figure 19: LEEM images of faceted islands grown at (a) 1223 K (950°C) (20-μm field of view) and (b) 1248 K (975°C) (14.5-μm field of view). [Reprinted with permission from [266]. Copyright (2011) by the American Physical Society.]

dependent on the temperature of the Cu surface as well as whether islands nucleate at step bunches or defect free regions. At lower growth temperatures ($\sim$ 963 K) islands are considerably more dendritic than those grown at higher temperatures, see Fig. 18, while at temperatures exceeding 1173 K graphene islands are more compact and are obviously faceted as demonstrated in Fig.19.

There is also considerable interest in the growth of graphene on polycrystalline copper, to some extent due to the low cost of Cu compared to other transition metal surfaces but also because of the low solubility of carbon in Cu. Early attempts to grow graphene on Cu by Li *et al.* [263] resulted in graphene grains up to tens of micrometres in size. Here the graphene produced can itself be considered "polycrystalline" in that it contains regions with different rotations with respect to the substrate. As discussed this can have detrimental effects on the transport properties of electrons in graphene. Recently efforts have been made in decreasing the nucleation density, especially by improving the surface of Cu with careful polishing and by lowering the proportion of carbon precursor with respect to that of the inert gas and etching gas (H_2) [270, 271]. This allows production of single-crystal graphene grains with sizes of up to a few millimetres [271].

One of the common surface terminations of Cu grains in polycrystalline foils and films is the (100) facet. On this surface graphene forms a distinct four lobed structure, Fig. 20, with each lobe having a different crystallographic orientation with respect to the copper lattice [262, 263]. Wofford *et al. [262]* used LEEM images to observe *in situ* the formation of graphene islands growing on the (100) surface, Fig. 20. The nucleation of graphene islands was only observed for growth temperatures greater than 1063 K and occurred heterogeneously at defect sites and imperfections. The 4-lobed structure was attributed to the simultaneous nucleation of graphene crystals with different orientations at a single nucleation site. Eventually these graphene islands coalesce to form a single polycrystalline film.

A detailed study of graphene formation kinetics has been attempted by Celebi *et al.* [267]. In these CVD experiments the copper surface was exposed to ethene and a small amount of hydrogen gas at the same time. It was found that the growth is sustained by continuous hydrocarbon input, but is hampered by copper sublimation. The latter has a complex effect: on the one hand, sublimation produces surface defects which may facilitate dehydrogenation reactions of the feedstock molecules and likely serve as nucleation centers,

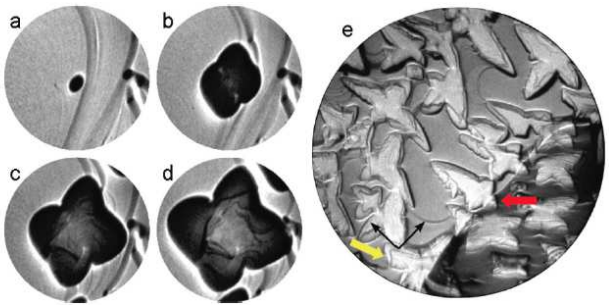

Figure 20: LEEM images of the evolution of a graphene island on Cu(100) at 1115 K after (a) 15 s of C deposition, (b) 90 s, (c) 240 s, and (d) 390 s (field of view is 10 μm). This process results in distinctly four-lobed islands (e). The axes of the graphene lobes tend to align along the Cu⟨001⟩ directions (black arrows). Graphene lobes are able to grow across Cu grain boundaries (red arrow) and can be distorted by large Cu step bunches (yellow arrow, field of view is 46 μm, grown at 1063 K). [Reprinted with permission from [262]. Copyright (2011) American Chemical Society.]

but on the other hand the evaporated Cu atoms facilitate desorption of hydrocarbon molecules thereby reducing the density of active species on the surface, see the schematics in Fig. 21(a). It was also found that maintaining a high temperature after the supply of ethene was switched off did not increase further the mean flake size. The authors also studied the effect of hydrogen gas on graphene CVD growth and found little difference with and without it. It was also observed that secondary graphene flakes grow underneath existing primary flakes, and their growth is stopped only when the primary graphene layer is complete. Interestingly, the shapes of secondary flakes are clearly hexagonal, while the primary flakes are observed to be mostly circular. It is suggested that the circular shape of the primary flakes is due to Cu sublimation; it is suppressed when secondary flakes are formed underneath the primary ones resulting in hexagonal shapes.

Using regimes for which individual graphene islands could be resolved, their mean area $A(t)$ as a function of time was measured from the SEM images as shown in Fig. 21(c) for two temperatures; typical SEM micrographs over a 4 minute time interval are shown in Fig. 21(b). The island's growth shows a typical sigmoidal ("S-shaped") time dependence [272] : initially when the density of active carbon species is low, the growth is limited by the small number of nucleated seeds (incubation); with time growth progresses faster due to attachment of active carbon species to existing nuclei and new nuclei are formed; finally, as the supply of active carbon species becomes scarce due to their fast previous consumption, growth slows down again. Assuming that the flakes' areal enlargement rate, dA/dt, is proportional to the their area, A, with a proportionality constant which decays exponentially with time (dispersive kinetics), i.e.

$$\frac{dA}{dt} \sim Ae^{-kt} \ , \tag{14}$$

the Gompertz type of the area time dependence is obtained:

$$A(t) = A_{max} \exp\left\{ - \exp\left[\frac{e\mu_m}{A_{max}} (t - \lambda) + 1 \right] \right\} \ , \tag{15}$$

where A_{max} is the maximum possible flake size ($t \to \infty$), and the other constants (λ and μ_m, the latter being the growth rate at the inflection point where dA/dt has a maximum) are fitting parameters (e is the base of the natural logarithm). This Gompertzian kinetics was found to fit extremely well the observed time dependence of the area of the flakes measured at different temperatures, see examples in Fig. 21(c), which shows that underlying assumptions made when writing Eq. (14) are probably reasonable. Finally, this type of kinetic analysis of flake size was performed at different temperatures, and effective activation energies (time dependent) were analyzed. It was argued that the rate limiting step in graphene growth on copper can be related to the dissociation of hydrocarbon species, which involves large energy barriers. Different processes essential for an understanding of graphene growth are depicted schematically in Fig. 21(a).

5.1.3. CVD with carbide as a transient state

The phase diagram of the metal-carbon system is complex in some cases. Not only graphene on a metal, carbon dissolved in the bulk, but also carbon-metal alloys may exist within different ranges of composition

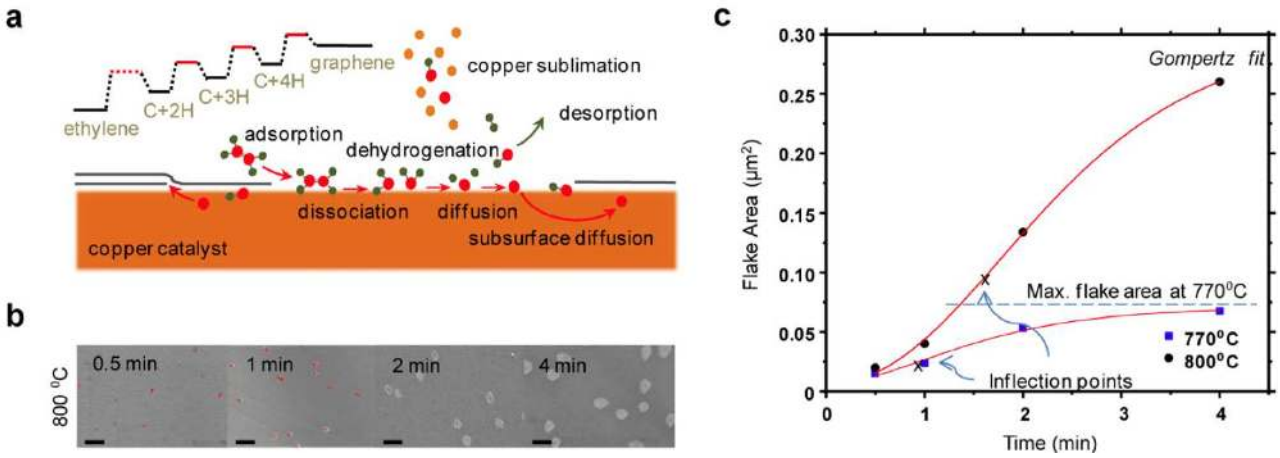

Figure 21: (a) General picture of processes taking place during CVD growth of graphene on copper; (b) typical SEM micrographs showing evolution of graphene islands with time (800°C (1073 K), scale bar is 1 μm); (c) evolution of the measured mean area of graphene flakes with time at two temperatures demonstrating Gompertzian kinetics. Inflection points in both cases are also indicated. [Reprinted with permission from [267]. Copyright (2013) American Chemical Society.]

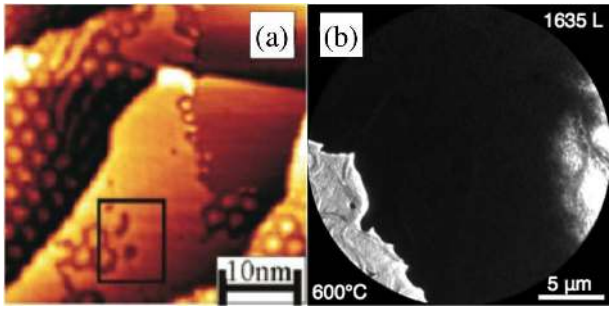

Figure 22: (a) Coexistence of a surface carbide and graphene on Ni(111), as shown by STM at room temperature of a sample prepared at 730 K. (b) LEEM image showing the carbon-free Ni surface between graphene and the carbide, in growth conditions at 870 K. [Reprinted with permission from [255]. Copyright (2010) American Chemical Society (a) and [273]. Copyright (2012), AIP Publishing LCC (b).]

and temperature. This is especially true on metals such as Fe, Ni, Rh, or Re. While in some cases the formation of a surface carbide state must be avoided because it is more thermodynamically stable than the graphene phase itself, as was found on Fe(110) [258], in other cases the carbide can be an intermediate state during CVD process during the growth of graphene. This is what was found on Ni(111), a surface on which a well-known surface carbide, Ni_2C, readily forms at a few 100 K above room temperature. Around 770 K, it was found that the carbide phase, which corresponds to a high density carbon phase, transforms into a graphene layer whose zigzag rows are 3°-rotated with respect to the Ni dense-packed rows [255], see Fig. 22(a). If the system is quenched to room temperature the transformation is stopped and the coexistence of neighboring (touching) carbide and graphene regions is observed. How this transformation occurs remains unknown. At slightly higher temperature (50 K higher), a different transformation is observed: graphene islands nucleate after the carbide fully covers the substrate surface, and progressively grow by depleting the Ni surface from the carbide, as observed by *in operando* LEEM [273], see Fig. 22(b). In the case of Re(10$\bar{1}$0) it was found that saturating the bulk at high temperature (1700 K) with carbon yields an α-carbide. After formation of this carbide, graphene forms on the surface of the crystal at high temperature [260].

5.2. Temperature Programmed Growth (TPG)

5.2.1. Method

Another method of growing graphene on transition metals is to first adsorb carbon-containing species at room temperature on the surface, and then to progressively heat the sample. In this method, the reaction

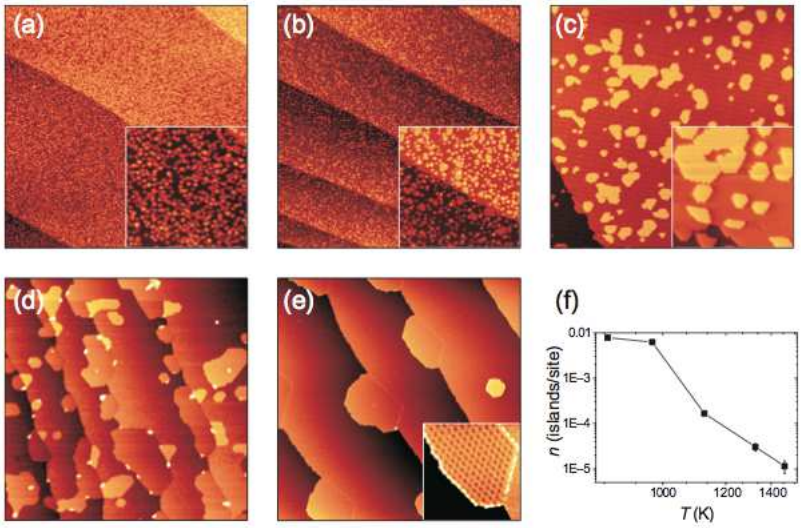

Figure 23: STM images of graphene grown on the Ir(111) surface with TPG after heating to (a) 870 K, (b) 970 K, (c) 1120 K, (d) 1320 K, and (e) 1470 K for 20 s. (f) Graphene island density n for the different annealing temperatures T. [Reproduced from [61] by permission of IOP Publishing. All rights reserved.]

between the adsorbed species, which drives the formation of graphene, is triggered by the temperature increase. Thus the method has been coined "temperature programmed growth" (TPG) [61]. The main difference with the CVD method is that in TPG the carbon containing species are added to the 'cold' surface with subsequent annealing to stimulate the growth, while in CVD the species are added to the surface which is already 'hot'.

TPG experiments are performed in an ultra high vacuum (UHV) to prevent contamination. As in CVD, the surface of the transition metal is initially cleaned. The metal is maintained at room temperature and exposed to the hydrocarbon source, and the molecules become adsorbed onto the surface. The system is then heated to a fixed temperature (TPG temperature). Upon heating, the adsorbed molecules experience progressive dehydrogenation. After full dehydrogenation, the resulting carbon species readily assemble to form carbidic species, whose structure gets better ordered as the temperature increases, eventually yielding graphene islands. Depending on the heating temperature the graphene growth will progress and the properties of the islands change. STM, performed both after cool-down [61] and during heating [63], have provided valuable insights into graphene growth by CVD.

5.2.2. Observations

The growth of graphene has been imaged on Ir(111) [61], Rh(111) [63, 251] and Ru(0001) surfaces for a range of TPG temperatures varying from around 770 K to 1470 K. On Ir(111) at temperatures below 870 K carbon species are found randomly distributed on the surfaces. Islands formed from these structures have non-uniform height and a diameter less than 2 nm. Also the moiré structure that is characteristic of graphene (see Section 6) is not observed. At these temperatures hydrocarbons have decomposed but graphene formation has not yet begun. At TPG temperatures between 870-970 K an increase in the graphene island density is noticed and small graphene islands with a moiré structure are identified. Therefore graphene starts to form on these surfaces in this temperature range. At temperatures larger than 970 K a decrease in graphene island density is observed because of an increase of the mean island size, Fig. 23(f). The formation temperature also varies depending on the surface. The lowest temperatures at which graphene formation is initiated during TPG experiments are summarized in Table 2. At higher TPG temperatures the graphene islands are found to be larger in size and are located primarily at step edges. It was also found that at higher temperatures the difference in orientation between the islands becomes smaller (the direction distribution is narrower) as some orientations are more energetically favorable. The orientations found are influenced by the underlying substrate [61, 63]. The dynamics of graphene growth on the Ir(111) surface for various annealing temperatures is shown in Fig. 23.

Surface	Carbon species	Graphene	Ref.
Rh(111)	770 K	870 - 973 K	[251]
Rh(111)	$<$ 870 K	808 - 969 K (dissolves at 1053 K)	[63]
Ir(111)	870 K	970 - 1470 K	[61]
Ru(0001)	No results	973 - 1173 K	[274]
Ru(0001)	900 K	1000 - 1100 K	[275]
Pt(111)	900 K	1000 - 1100 K	[275]
Re(0001)	No results	1100 K	[141]
Co(0001)	$<$410 K	600 K	[256]

Table 2: The temperature ranges where carbon species and graphene were observed on different surfaces.

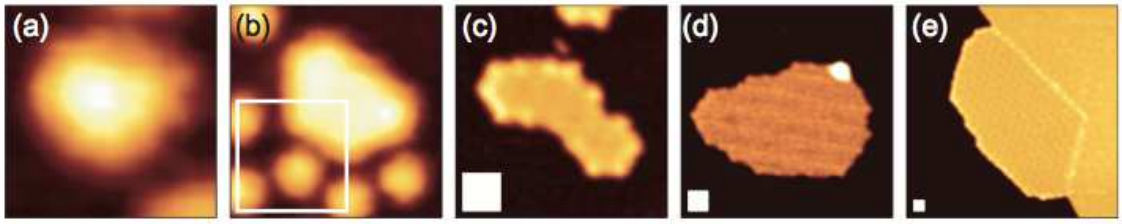

Figure 24: STM topographs of graphene islands grown with TPG on Ir(111) after heating to (a) 870 K, (b) 970 K, (c) 1120 K, (d) 1320 K, and (e) 1470 K for 20 s. At low temperatures, (a) and (b), the islands are compact, then at intermediate temperatures (c) they become non-compact. They return to being compact at higher temperatures (d), (e). [Reproduced from [61] by permission of IOP Publishing. All rights reserved.]

5.2.3. Ripening

By imaging the growth at a range of TPG temperatures different stages in the growth of graphene can be identified. From this useful conclusions about how the growth progresses have been drawn. Coraux *et al.* [61] observed how the size and shape of the graphene islands changes at various TPG temperatures. They annealed the sample to a particular temperature and then cooled it so that the surface can be imaged with STM. At higher annealing temperatures the graphene growth is noticed to be more advanced. At 970 K when graphene starts to form, the islands are small and have a compact shape, shown in Figure 24(a) and (b). As the temperature is increased to 1120 K the islands appear larger, with a non-compact irregular shape, see Figure 24(c). At even higher temperatures of 1320 K and 1470 K the islands continue to grow in size, however their shape is compact again as demonstrated by Figure 24(d) and (e).

These observations suggest that the islands grow by ripening processes. Two possible mechanisms for this are Ostwald ripening and Smoluchowski ripening. In Ostwald ripening large islands grow by incorporating carbon adatoms arising from the dissolution of smaller islands [276], whereas in Smoluchowski ripening entire mobile islands coalesce [277]. For Ostwald ripening adatoms need to be able to detach from the smaller islands, which is unlikely at temperatures below 1500 K [61]. Since the temperature range of the TPG experiment is below this, it is concluded [61] that the main mechanism for graphene growth must be Smoluchowski ripening. This causes the reduction in observed particle density as the growth progresses due to island migration and subsequent joining together. Their high mobility may be facilitated by increased distance of the graphene islands from the transition metal surface [205], see also Section 6, as this effectively reduces the interaction between a graphene flake and the metal and decreases the diffusion energy barrier. The Smoluchowski ripening process is also suggested by the changes in the compactness of the islands. As temperature increases the islands become more mobile. At 1120 K the islands have enough mobility to make contact with each other and coalesce. However, it is argued [61], that at intermediate temperatures there is not enough energy for the recently coalesced islands to reshape themselves in the time period during which the heat is applied. This causes non-compact islands to form. At 1320 K and above, large islands are located mainly at the step edges of the substrate where they have become attached. As the islands are less mobile at the step edges the chances of further coalescence are rarer and their shape stabilizes over time. Smoluchowski ripening has also been reported for Rh(111) and Ru(0001) surfaces [251, 274].

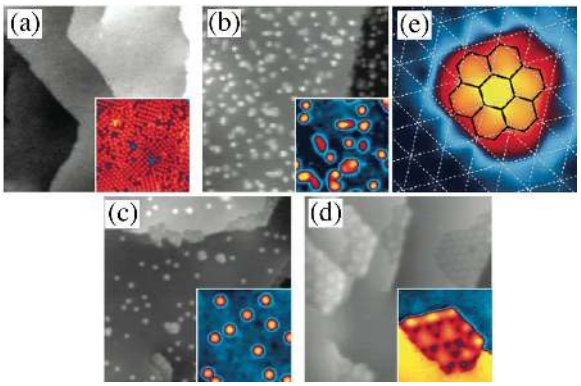

Figure 25: STM images of the Rh(111) surface annealed to (a) 470 K, (b) 770 K, (c) 870 K, and (d) 973 K after ethene deposition. (e) A STM topograph of clusters seen in (b) and (c). [Reprinted with permission from [251]. Copyright (2011) American Chemical Society.]

5.2.4. Cluster Formation

The initial shape of clusters growing on Ir(111) has been investigated using *in situ* high-resolution photoelectron spectroscopy [139]. It was discovered that in the early stages of growth a number of carbon clusters are formed. These clusters vary in size but all were observed to be dome-like, with the interaction between cluster and surface occurring only at edge sites.

In a TPG study of graphene growth on Rh(111) initiated by the ethene deposition, the presence of randomly distributed small clusters was found to coincide with the formation of graphene islands [251]. STM images show that just prior to graphene formation the size distribution of the clusters is dramatically reduced and the cluster particle density decreases. At this point carbon clusters were identified with a distinct size of 1 nm across. With high STM magnification these were identified as a carbon honeycomb of 7 hexagons joined together (known as $7C_6$), see Fig. 25(e). DFT calculations determined that the most stable structure for the clusters is a dome shape, with the outer atoms interacting more strongly with the surface. The relative concentration of these clusters with respect to all carbon species increases with TPG temperature and eventually they are the only species present other than graphene islands. This led the authors to conclude that these uniformly sized clusters are the only precursors for graphene growth.

Once the temperature is high enough for ethene to decompose, the clusters start to form. At 770 K and 870 K, as is demonstrated by Fig. 25(b) and (c), the clusters are observed exclusively on terraces. Since there are no clusters at step edges, then they cannot have formed by using step sites to facilitate their growth e.g. via creating dimers from C monomers as was previously proposed [278]. They are suggested to have formed instead from the decomposition of heavy hydrocarbon species created from the polymerization of ethylidyne (cf. Sections 5.3 and 7.2.1). At 870 K clusters were observed to start diffusing on terraces towards steps (Smoluchowski ripening) where they coalesce into graphene flakes.

At 973 K the diffusion is greatly enhanced, and graphene islands that have been formed from the small clusters are found predominately at step edge sites, Fig. 25(d). This suggests that most of the mobile 1 nm clusters eventually settle at step edges, where they grow to form graphene by Smoluchowski ripening. However a few graphene islands are found on large terraces, and therefore it was deduced that it is the formation of the clusters rather than their attachment to step edges that limits the graphene growth rate. This is unlike graphene formation by other methods. For instance (see also discussion in Section 5.1.2), in the cases of hot C deposition onto Ir(111) it was determined that the formation of 5 atom carbon clusters (which are precursors for graphene growth in this case) occurs only as they attach to the substrate step edges [54]. The activation energy for this process is dependent on the step edge structure.

Cluster precursors to graphene growth using TPG have also been reported on Ir(111) [139] and Ru(0001) [275] surfaces. For coronene and ethene deposition onto a Ru(0001) surface two cluster types were found at 900 K, see Fig. 26(e): one the dome-shaped $7C_6$ type seen also on the Rh(111) surface [251] and the other a 3 hexagon carbon structure $3C_6$, also dome-shaped [275]. These clusters were inferred to have the structures shown in Fig. 26(f) and (i), respectively. At 1000 K the $3C_6$ clusters became dominant and with further heating to 1100 K eventually only graphene islands were present.

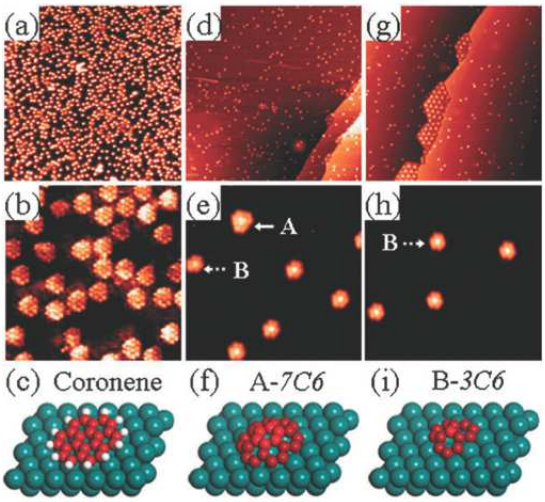

Figure 26: STM images of the Ru(0001) surface annealed to various temperatures: (a) 100 × 100 nm^2, 500 K; (b) 10 × 10 nm^2, 500 K; (d) 100 × 100 nm^2, 900 K; (e) 10 × 10 nm^2, 900 K; (g) 100 × 100 nm^2, 1000 K; (h) 10 × 10 nm^2, 1000 K. In (e) and (h) the labels A and B correspond to the $7C_6$ and the $3C_6$ clusters, respectively. The structures of (c) coronene, (f) the $7C_6$ cluster and (i) the $3C_6$ cluster on the Ru(0001) surface are also shown. The colored balls represent: cyan = Ru, red = C, white = H. [Reproduced from [275] with permission of The Royal Society of Chemistry (RSC) on behalf of the European Society for Photobiology, the European Photochemistry Association and the RSC.]

Studies on the Pt(111) surface found that clusters are not formed [275]. This is explained in terms of interactions between graphene and the different surfaces. For Ru(0001) and Rh(111) surfaces a strong interaction is assumed, whereas for Ir(111) and Pt(111) the interaction is thought to be weaker [138]. The interaction between graphene and the surface drives the formation of the clusters. The clusters are metastable on the surface and occur only at a particular temperature range. For larger clusters the stability increases [251].

5.2.5. Using TPG to Optimize Further Growth

In the work of Dong *et al.* [63] the growth of graphene was studied on Rh(111). To form the graphene the TPG method of adding ethene at room temperature before heating was compared with depositing ethene directly on the surface held at high temperatures (which is basically the CVD procedure). In both cases the growth of graphene was imaged simultaneously with the heating using a high temperature STM. In the case of the TPG method, graphene was found over a wide range of temperatures, from 808 to 1053 K, and therefore there is a large temperature window for graphene nucleation. The graphene formed had partial surface coverage and different regions had multiple orientations with respect to the substrate. This is undesirable as it leads to domain boundaries where graphene islands meet each other when growing further and coalescing.

For ethene deposition at high substrate temperature (as in Section 5.1), the temperature range which ensured graphene growth was much narrower: graphene was only found when the ethene was deposited between 1016 and 1053 K. At lower deposition temperatures a rhodium carbide structure forms instead. Moreover, this structure was observed not to transform into graphene upon increasing the temperature and at 1016 K it dissolves into the substrate. When ethene was deposited at 1028 K, graphene was produced with complete coverage and good alignment with the substrate. However upon cooling the graphene moiré pattern distorted. This is believed to be due to segregation of C adatoms that can dissolve into the bulk at high temperatures. The segregated C adatoms could cause the nucleation of new graphene and carbide islands on the surface, which may distort the previously formed graphene layer above.

To optimize graphene growth the nucleation and growth stages were proposed to be separated using the following method. First graphene islands are nucleated using TPG. Then the growth of these is maintained by depositing ethene onto the hot surface kept at 975 K. As graphene has already nucleated it continues to grow and if the ethene flux is sufficiently low the formation of carbides is prevented. With this method the entire surface was eventually covered with graphene as shown in Fig. 27(b). From direct observation of the

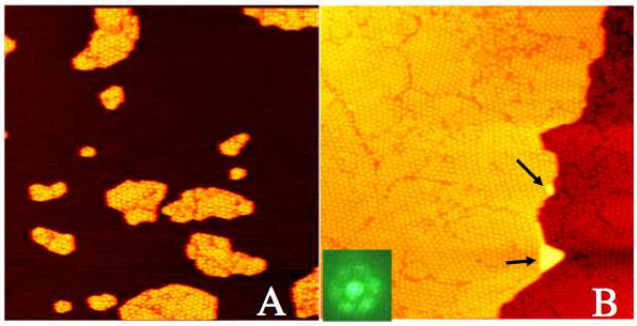

Figure 27: (A) The starting Rh(111) surface for graphene growth prepared using TPG. Ethene is deposited onto the surface at room temperature, which is then heated to 975 K. (B) The surface after ethene has been deposited onto the surface in (A) and then kept for 76 min at 975 K. Complete graphene coverage has been achieved with a nearly uniform orientation. [Reproduced from [63] by permission of IOP Publishing. All rights reserved.]

growth with *in situ* STM it was found that when two domains with different orientations meet the growth continues in the direction closest to the substrate orientation. As a result the density of domain boundaries in the final structure was lower than in graphene grown with regular TPG which is indeed highly desirable for practical applications. Upon cooling the moiré pattern remained unchanged.

5.3. Carbon Feedstock

The crucial step in graphene formation in CVD and TPG processes is the dehydrogenation of hydrocarbon molecules (the feedstock). Unraveling the involved mechanisms is essential for understanding the initial stages of graphene growth just before (or maybe during) the nucleation of carbon species into graphene islands. There is an essential difference though between the CVD and TPG procedures. In CVD experiments the impinging molecules possess non-zero kinetic energy (which can be controlled in experiments) and may even be vibrationally excited (if evaporated at sufficiently high temperatures), and these may facilitate their sticking to the surface and initial partial dehydrogenation [279]. In TPG experiments the molecules are adsorbed on the surface prior to temperature treatment and hence the surface temperature is the only factor that controls their decomposition.

Temperature programmed high-energy XPS (TP-XPS) is an especially powerful technique that can be used to determine temperature windows in which various carbon species appear and disappear on the surface of a metal as its temperature is gradually increased. This is done by monitoring the position of the $1s$ core level of the carbon atoms, which is very sensitive to the immediate chemical environment. At the same time, one can monitor the core levels of the transition metal atoms, and these can give invaluable information, for example on how the metal is affected at different temperatures by the adsorbed hydrocarbon species, and may even indicate specifically when graphene starts forming. Combined with the temperature programmed desorption (TPD) measurements which provide precise information on the species desorbing from the surface during the experiments, it is possible to build a detailed picture of the thermal evolution of carbon species on the given surface and hence determine the processes that occur during the initial stages of graphene growth.

The thermal evolution of feedstock on transition metal surfaces has been investigated by several authors with the aim of determining the carbon species that are actively involved in these early stages of growth, and whether the choice of carbon feedstock and growth conditions can affect how graphene is produced. Lizzit and Baraldi [140] studied thermal evolution of ethene on the Ir(111) surface. Throughout the experiment the temperature was raised from 170 to 1120 K. The TP-XPS spectra of the C 1s and the Ir $4f_{7/2}$ levels were studied in order to monitor changes in their core electron binding energies and thereby determine the different species present during the thermal treatment. Also the photoemission intensity thermal evolution, S factor and vibrational splitting were used to identify the species through comparison with previous XPS results.

The evolution of ethene C_2H_4 as the temperature is increased is shown in Fig. 28. Initially it is assumed that both ethene and ethylidene $CHCH_3$ are chemisorbed on the surface. At 170 K the ethene molecules are suggested to begin to transform to ethylidene, which is the only species found at temperatures between 235 and 250 K, i.e. complete conversion (isomerization) $C_2H_4 \rightarrow CHCH_3$ is believed to have taken place

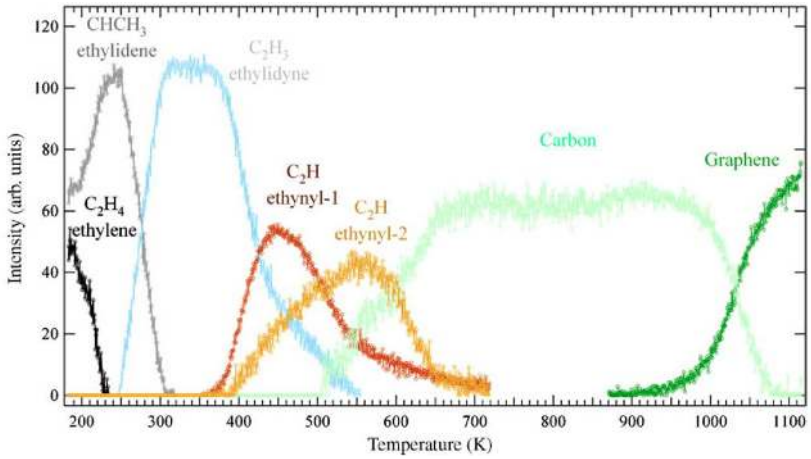

Figure 28: The thermal evolution of ethene into different surface species on the Ir(111) surface during the course of the TP-XPS experiments. [Reprinted from [140], with permission from Elsevier.]

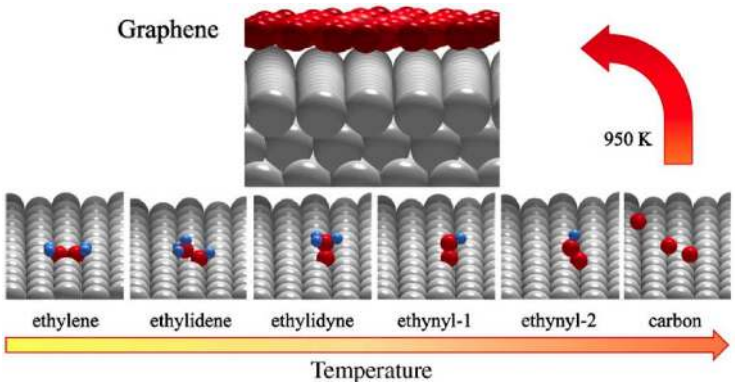

Figure 29: Schematic of the thermal evolution of ethene (ethylene) into graphene on the Ir(111) surface. [Reprinted from [140], with permission from Elsevier.]

by 235 K. Upon increasing the temperature, dehydrogenation of ethylidene occurs; the ethylidene feature disappears at around 310 K and subsequently C_2H_3 (ethylidyne) and later on C_2H (ethynyl) species are found on the surface. The dehydrogenation processes are accompanied by a clear H_2 TPD signal [102]. Two types of signals associated with the ethynyl are attributed to two possible configurations of the species on the surface. At 500 K complete dehydrogenation of the existing carbon species starts which correlates well with the second hydrogen TPD feature between 630 and 730 K reported in [102]; pure adsorbed carbon species start forming eventually leading to the appearance of graphene at around 900 K.

The onset of graphene formation is also supported by the evolution of the Ir $4f_{7/2}$ core level: the corresponding XPS feature approaches its position for the clean Ir surface indicating graphene formation, as it is known that graphene interacts weakly with the Ir surface. It is concluded in these experiments that on the Ir(111) surface ethene undergoes complete dehydrogenation. Moreover, it is clear that the evolution is quite complex and involves many stages as depicted in Fig. 29, characterized by dehydrogenation and isomerization processes leading to coexistence of various species on the surface at the same conditions. Interestingly, as follows from the schematics in the Figure, the authors assumed that only atomic carbon is present at the very last stages on the surface prior and during graphene formation. This may however not be the case as it is well known that much higher activation energies (over 2 eV [280]) are required for breaking the C-C bonds, and hence there must be a certain distribution of C_2 species alongside atomic carbon on the surface prior to the formation of larger carbon clusters and graphene nucleation.

Similar work has been conducted for the Pt(111) surface [279] albeit for a much limited temperature range corresponding to the very initial stages of ethene decomposition. It was found that ethene completes

its transformation into ethylidyne C_2H_3 on this surface at the higher temperature of 290 K (230 K on Ir(111)). Therefore the barrier for converting ethene into C_2H_3 must be higher on Pt(111) and it is a poorer catalyst for C-H breaking than Ir(111). As with the case of the Ir(111) surface, the authors also observed ethylidene $CHCH_3$ as an intermediate product for temperatures of up to 290 K. At the same time, during the conversion $C_2H_4 \rightarrow C_2H_3$ a hydrogenation reaction takes place as well whereby ethene C_2H_4 forms again and desorbs from the surface (40%). This effect was not observed on Ir(111) [140] though.

Decomposition of the simplest hydrocarbon, methane CH_4, on the Pt(111) surface was also considered in [279]. At 120 K methane immediately dehydrogenates into methyl CH_3 which from 260 K starts partially transforming into CH species. The dehydrogenation is confirmed by the corresponding TPD signal. At the same time, the backward hydrogenation competes with the dehydrogenation reaction resulting in formation of methane again which desorbs from the surface at these temperatures. At temperatures above and around 300 K, CH is established as a stable species.

The comparison of these two studies, on Ir(111) and Pt(111) surfaces, clearly shows that mechanisms governing decomposition of the carbon feedstock, although involving the same intermediates, may however differ in detail, i.e. each particular surface requires individual consideration.

In order to produce graphene, various hydrocarbon feedstocks have been successfully used. However, very little is known about the effect of feedstock on the growth mechanism and graphene quality. To our knowledge, comprehensive comparative study of various feedstocks has not yet been done; however, single studies indicate the fundamental effect of using various molecules as a feedstock in growing graphene. Methane (in the gaseous form) and benzene C_6H_6 (liquid) precursors were compared as the carbon source for growing graphene on Cu foils in [281]. It was found that when using methane the graphene structure could not be identified below 873 K. For benzene SEM images showed that even at temperatures as low as 573 K high quality graphene monolayer flakes can be formed. This was explained by two considerations illustrated by DFT calculations: (i) dehydrogenation of benzene requires lower barriers than for methane; moreover, in the latter case the required reactions may be quite complex and multistage, resulting in a mixture of various CH_x species on the surface prior to nucleation in the case of methane; (ii) benzene after dehydrogenation already has a carbon ring, the main building block of graphene, and hence the nucleation step may effectively require a smaller barrier than in the case of methane where coalescence of single carbon atoms needs to take place. Therefore nucleation and coalescence are expected to require more energy when methane is used as a precursor. The higher energy profile for methane compared with benzene throughout all stages of growth (adsorption, dehydrogenation, nucleation) explains the difference in growth temperatures required for producing graphene.

5.4. Segregation

A less frequently used method to produce graphene layers is to make use of carbon solubility in different substrates. Here we will consider carbon precipitation from both nickel [282] and ruthenium [283, 91], but the method also applies to most of the metals that are usually employed for CVD and TPG, provided that they are heated to sufficiently high temperature so that their carbon solubility becomes non-negligible [58, 284]; note that as a consequence of the presence of grain boundaries in the metal [285], the carbon solubility is also increased. The method begins with heating the material to high enough temperatures to allow carbon to dissolve into the bulk. This temperature is strongly dependent on the specific material. The carbon may be added in a usual way, e.g. using hydrocarbon molecules. The whole sample is then cooled slowly, leading to a reduced solubility of C in the material and hence causing C atoms to segregate from the bulk onto the surface and form graphene islands there.

5.4.1. Ru(0001)

Sutter *et al.* [91] used electron scattering and microscopy as well as micro-Raman spectroscopy to observe and characterise graphene grown on Ru(0001) using the segregation method. Here carbon was deposited at high temperatures (>1423 K) onto the Ru surface and subsequently absorbed into the bulk. The sample was then cooled to 1098 K driving carbon atoms to the surface. Graphene islands were observed to nucleate sparsely and grow by incorporation of carbon species at edges. Interestingly, it was also found that growth only occurs down Ru steps and not up, producing a number of "lens" shaped graphene islands, see Fig. 30.

To investigate how the segregation of carbon atoms from the bulk affects graphene growth on Ru(0001), McCarty *et al. [283]* performed experiments under two different conditions required to grow graphene by

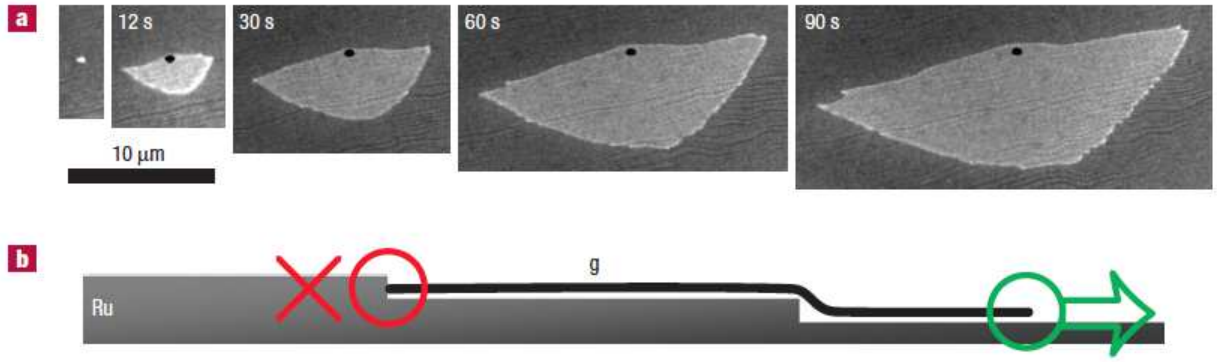

Figure 30: (a) LEEM images of a first-layer graphene island growing on Ru(0001) at 1123 K in real time. (b) Schematics illustrating the predominant growth down the steps. [Reprinted by permission from Macmillan Publishers Ltd: Nature Materials [91], copyright (2008).]

segregation and deposition, respectively, and used LEEM measurements to measure the adatom concentration during growth. The segregation of bulk carbon was examined by first heating the surface to a high enough temperature for absorption to occur. While the authors do not explicitly state what temperature they heated the surface to (only briefly mentioning 1404 K (1131°C) in Fig. 31), presumably it is similar to that of Sutter *et al.* [91]. The surface is then cooled to 973-1223 K (700-950°C) (a rate of cooling was not stated). To make quantified comparisons they deposit carbon onto a different Ru(0001) surface heated to a lower temperature and measured the concentration of adatoms in equilibrium with graphene islands [54]. This method of production is described in Section 5.2. Both experiments were performed in UHV.

By measuring the change in reflectivity of the surface at 1404 K and at lower temperatures the authors were able to measure the amount of carbon that has segregated from the bulk, see Fig. 31. As can be seen in the Figure the increase in adatom concentration at 1223 K is an indication of segregation from the bulk. At 1046 and 1074 K the adatom concentration begins to increase before decreasing sharply as is seen in Fig. 32, and the authors connect this decrease in concentration with the appearance of a graphene island at ∼450 s.

In exactly the same way as described in [54] the authors measured the velocity of the island growth front and found that the results obtained for segregation and deposition agreed. Therefore, the nucleation of islands and early growth is due to the segregated carbon atoms, not by direct attachment of bulk carbon, and thus the mechanisms involved in the nucleation and growth of graphene on Ru(0001) seem to be independent of how carbon atoms reach the surface. In other words, the way in which the carbon atoms are delivered to the surface (either from adsorbed molecules, as in CVD and TPG, or from the bulk as in segregation methods) is not the main rate-determining process for the growth, as the formation of graphene islands happens on a much longer timescale. A slow enough cooling procedure would limit the influx of C atoms from the bulk and would leave enough time for the C atoms on the surface to diffuse around and eventually nucleate with a low density, whereby a higher quality graphene, with a low density of defects such as grain boundaries, would result.

5.4.2. Nickel

The experimental procedure of growing graphene on Ni(111) and polycrystalline Ni surfaces usually begins with heating the surfaces to above 1170 K [286, 282]. In a number of experiments the formation of monolayer, bilayer and trilayer graphene has been observed with the number of monolayers grown being strongly dependent on temperature [282, 286]. However, for CVD temperatures between 733-923 K growth on Ni(111) is self-terminating after one monolayer (growth is limited to one layer) [273] and for growth below 673 K a surface carbide phase has been observed [287, 273].

Multilayer graphene has been observed on both Ni(111) and polycrystalline substrates. The difference between growth on these surfaces has been examined by Zhang *et al.* [282]. They grew graphene by initially depositing methane at atmospheric pressure onto the Ni surface at 1173 K. The sample was then cooled to 773 K and examined using Raman spectroscopy and AFM. They found that while on Ni(111) monolayer and bilayer graphene is formed, on polycrystalline surfaces the number of layers increases.

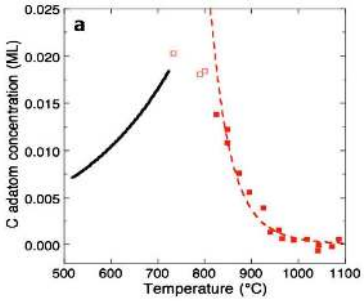

Figure 31: The concentration of adatoms in equilibrium with carbon dissolved in the Ru bulk. The initial temperature before cooling was 1404 K (1131°C). Open red squares show the concentration of metastable carbon just before nucleation of graphene and red-filled squares indicate the concentration of adatoms on the surface. The black curve shows the adatom concentration in equilibrium with graphene [54]. The red dotted line is a fit to the Langmuir-McLean model of segregation. [Reprinted from [283], with permission from Elsevier.]

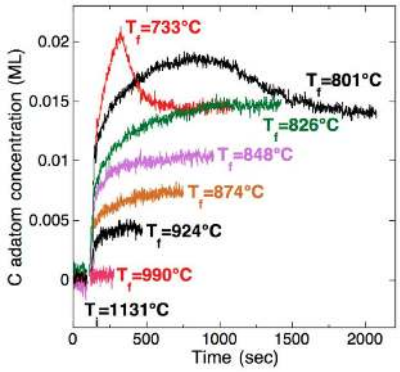

Figure 32: The adatom concentration on the surface of Ru(0001) as a function of time during a temperature decrease from 1401 K (1131°C). After an initial increase, the plots for both 733 and 801°C (1006 and 1074 K) show an eventual decrease in concentration which the authors connect to the nucleation of graphene. [Reprinted from [283], with permission from Elsevier.]

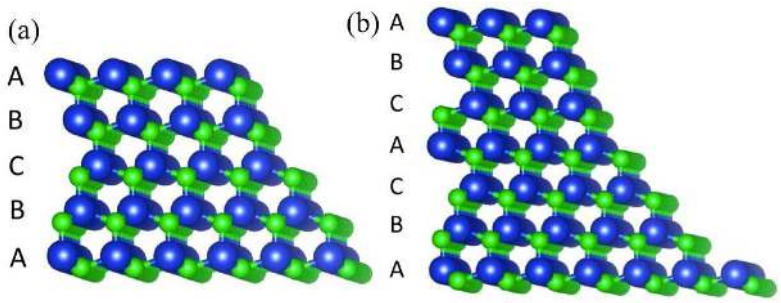

Figure 33: The lattice structure for (a) 4H-SiC and (b) 6H-SiC. The letters indicate the stacking sequences. C and Si atoms are shown with green and blue colors, respectively. [Reproduced with permission from [292].]

Similar behavior on Ni(111) has been observed using LEEM [286]. Here carbon is absorbed into the bulk after the surface is exposed to benzene at 1200 K for ten minutes. The surface is then cooled to 1125K whereby graphene begins to nucleate and the coverage eventually reached a full layer. Cooling the temperature further to 1050 K results in a second graphene layer and the initial nucleation of a third monolayer. The edge structure on the first and third layers is hexagonal while the second layer demonstrates dendrite structures. It should also be mentioned that growth of the first layer was observed to be almost ten times faster than that of the second or third layers.

There appear to be much fewer nucleation sites on Ni(111) compared to polycrystalline Ni [282, 286], where it has been suggested that nucleation occurs at grain boundaries between different crystalline surfaces [282]. This leads to a large graphene sheet with a single rotational domain.

5.5. SiC Sublimation

5.5.1. Graphene on SiC

An alternative approach to producing epitaxial graphene is to grow it on silicon carbide. Heating to high temperatures causes sublimation of silicon from the surface of SiC. The remaining carbon atoms form a carbonic surface, and by controlling growth conditions they can arrange themselves to form a graphene layer. It is believed (although not yet fully established) that as the growth progresses graphene layers are formed between current graphene layers and the SiC surface, i.e. secondary layers grow underneath the primary one. This is a bottom-up process, which is unlike other growth methods discussed above where new layers are formed on top of the previous layers (top-down processes).

While the initial studies involving growth under UHV required heating to about 1600 K for control of the thickness of the graphene film [101], now samples of better controlled quality are grown under rougher conditions, but require higher heating temperatures. Under a Si-rich atmosphere [288] or by using a buffer gas [289, 290, 291], high quality samples are indeed prepared at temperatures of about 1900 K.

Graphene formation is dependent on the structure of the SiC surface. The most commonly used SiC polytype structures for growing epitaxial graphene are 4H-SiC and 6H-SiC. The unit cells of these structures are both hexagonal and contain 4 and 6 SiC bilayers, respectively, with different stacking sequences. Each bilayer is composed of a plane of C atoms and a plane of Si atoms. The structure of these lattices is shown in Fig. 33. The occupation site positions are denoted with the letters A, B and C for each distinct SiC layer. For 4H-SiC and 6H-SiC the stacking sequences are ...(ABCB)... and ...(ABCACB)..., corresponding to 4 and 6 distinct layers, respectively, which are then periodically repeated.

Both of these lattices have either a Si- or C-terminated surface. These are the (0001) surface for Si termination and the $(000\bar{1})$ surface for C termination. The growth of the graphene and its final structure are dependent on which of these surfaces is initially exposed. On the Si-terminated surface the graphene layer produced has an orientation of 30° with respect to the SiC plane [293, 98]. For the C-surface the growth is faster [294] but the graphene has a variety of different orientations [293, 98]. Because of this most studies of graphene growth on SiC have focused on the Si-terminated surface.

Pre-patterned SiC surfaces, for instance, with arrays of trenches with abrupt walls created by lithography, were found to spontaneously transform into inclined facets with a well-defined surface normal other than (0001) or $(000\bar{1})$ under annealing. Graphene growth on such patterned surfaces was found to be preferential

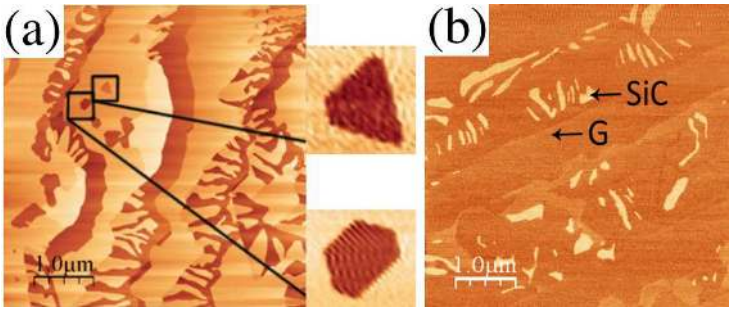

Figure 34: AFM topography of the SiC surface after heating to (a) 1748 K and (b) 1823 K. At 1673 K no graphene is present (shown using AFM phase measurements). At 1748 K fingers are formed with graphene in between them (a) (two terrace pits highlighted in the AFM image are shown separately at high resolution) and these eventually erode to become islands (b). At 1873 K the islands have completely eroded and graphene covers the whole surface. [Reprinted with permission from [73]. Copyright (2009) by the American Physical Society.]

on the inclined facets, so that extended graphene ribbons, with size determined by the depth of the initial trenches, can be obtained in a rather versatile manner [295].

5.5.2. The Growth Process

To produce graphene using Si sublimation, the SiC surface must first be treated. Scratches are removed by etching with hydrogen, and then the SiC is rapidly heated to the growth temperature, typically between 1473 and 1933 K, for a specific time. During the heating process a Si flux is applied to remove any produced SiO gas and maintain the concentration of Si on the surface [293, 296, 297]. Alternatively, growth can be performed under an Ar atmosphere. The SiC is then cooled at a slower rate until reaching room temperature. The etching process forms regular steps along the surface of the SiC, which are a unit cell in height.

To understand how graphene grows from this process, the 4H-SiC(0001) surface was monitored as the growth temperature and heating time were separately varied [73]. In each case AFM (tapping mode) and STM were used to observe the changes on the surface and the progression of graphene growth. Scans were performed in a nitrogen environment at atmospheric pressure. To determine the temperature dependence of the growth the SiC was heated to a range of different temperatures between 1673 and 1873 K for 10 minutes. At 1673 K no graphene was found on the surface, however pits in the SiC surface had started to develop on the terraces. Increasing the temperature increased the fraction of the surface covered by pits. At 1748 K, see Fig. 34(a), the bottom of a pit was analyzed with high STM magnification. Taking a 2D Fast Fourier transform of the STM data revealed the hexagonal structure of graphene. From this it was assumed that there are two phases present on the surface: reconstructed SiC on the surface terrace and graphene further down. From this the contrast in the phase data from AFM images was interpreted to determine the surface composition at each temperature.

The origin of a pit formation has been tracked to the processes governing the nucleation and growth of the buffer layer [74], an intermediate layer formed before graphene is grown (at lower temperature) and eventually sandwiched between graphene and the substrate (see 5.5.3). This buffer layer nucleates on SiC terraces upon consumption of the Si atoms expelled from the SiC(0001) step edges (actually $\left(\sqrt{3}\times\sqrt{3}\right)$-reconstructed ones) above 1300 K, leaving regions elongated along the SiC step edges, which are three SiC bilayers-deep, see Fig. 35(a,b). Continued growth of the buffer layer proceeds upon retraction of $\left(\sqrt{3}\times\sqrt{3}\right)$-reconstructed SiC steps until these encounter a region covered by a buffer layer uphill of the step (Fig. 35(c)). In practice this leads to stripes of the buffer layer parallel to the initial substrate step edge pattern, except at some locations where the buffer layer stripes are not continuous, where the retraction of the $\left(\sqrt{3}\times\sqrt{3}\right)$-reconstructed SiC steps can continue, which leads to the formation of pits (Fig. 35(d)).

At the same time, finger-like structures associated with pits can be found on the surface at 1748 K as illustrated in Fig. 34(a). These fingers are formed perpendicular to a step edge and correspond to reconstructed SiC with graphene between them. At higher temperatures as the step edges diminish, the fingers lengthen and eventually become islands after an entire step front has eroded. These islands are found at 1823 K, Fig. 34(b). Above this temperature the SiC islands shrink further and finally the surface is completely covered by graphene.

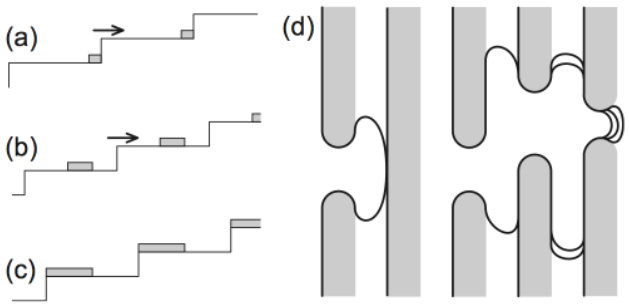

Figure 35: (a) The buffer layer (gray) nucleates at the lower sides of $\left(\sqrt{3}\times\sqrt{3}\right)$-reconstructed SiC steps. (b) $\left(\sqrt{3}\times\sqrt{3}\right)$-reconstructed SiC steps retract uphill as the buffer layer grows. (c) Eventually a state is reached in which all $\left(\sqrt{3}\times\sqrt{3}\right)$-reconstructed SiC steps have been consumed. (d) Pits form when the domains of the buffer layer on each terrace are not continuous and $\left(\sqrt{3}\times\sqrt{3}\right)$-reconstructed SiC steps (thick black lines) advance to the next terrace. [Reprinted with permission from [74]. Copyright (2008) by the American Physical Society.]

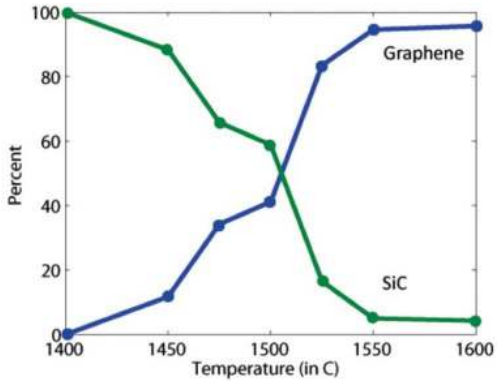

Figure 36: The surface coverage of both graphene (blue) and SiC (green) as a function of annealing temperature. [Reprinted with permission from [73]. Copyright (2009) by the American Physical Society.]

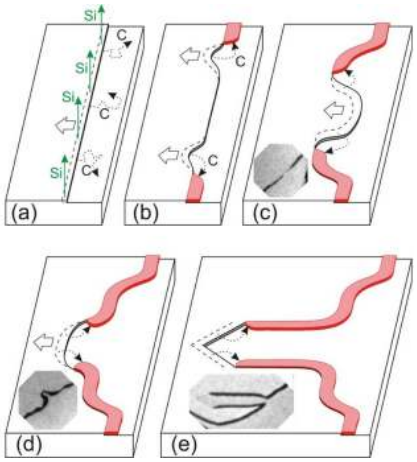

Figure 37: Schematic of the formation of an arrow feature. The insets show static LEEM images of SiC steps at similar stages of evolution. LEEM images are 2×2 μm^2 (c,d) and 4×2 μm^2 (e). [Reprinted with permission from [298]. Copyright (2010) by the American Physical Society]

The surface coverage of SiC and graphene at different temperatures is shown in Fig. 36. The increase in graphene coverage above 1773 K is accompanied by the reduction of surface features such as pits and fingers, as a graphene layer begins to cover them. At 1873 K graphene completely covers the surface.

The time dependence of the growth was studied by keeping the growth temperature fixed at 1748 K and varying the growth time between 0 and 60 minutes. AFM images taken at different time intervals show that the surface progresses in almost the same way as when the temperature dependence was studied. Fingers are formed after 2-14 minutes of growth, which become islands at 16 minutes. After 60 minutes the graphene layer is nearly entirely complete. This shows that the growth mechanism for graphene from SiC is the same whether the temperature or heating time is varied.

A better quality of graphene prepared on SiC far from UHV conditions motivated a few studies aiming at unraveling growth processes which could be specific to such conditions. For a SiC(0001) surface almost fully covered by the buffer layer after a 1820 K annealing procedure under Ar atmosphere, further UHV growth yields high quality graphene [298] as obtained by Emstev *et al.* [291] who used only non-UHV conditions throughout growth. These findings question a qualitative understanding that the reduction of Si evaporation rate due to the presence of the Ar atmosphere is crucial for slowing down graphene growth close to thermodynamic equilibrium. Instead, the formation of a high quality buffer layer, with the help, for instance, of a high temperature treatment in Ar atmosphere, seems to be the prerequisite for growing high quality graphene. Such a high quality buffer layer should consist of straight triple SiC step edges, separated by large reconstructed (buffer layer) terraces. Such terraces indeed contain about the right amount of carbon necessary for building a full graphene layer on top of the buffer layer in a step flow fashion [298]. The presence of single SiC steps should be avoided as they lead to the formation of graphene on their side, which, unlike in the case of triple SiC steps, inhibits Si evaporation due to strong C-Si bonds at the SiC-graphene interface. In practice, this leads to the formation of arrow-like growth fronts, as explained in Fig. 37, instead of smooth ones, thanks to which high quality graphene can be obtained.

In a UHV study, graphene of very high quality has been obtained using evaporation of Si (actually disilane, which readily transforms into Si upon reaching the substrate surface at high temperature, H atoms resulting from its decomposition being efficiently desorbed into vacuum) [290]. In this study, different surface transformations of SiC(0001) upon heating could be slowed down considerably, and even reversed by applying an appropriate Si partial pressure. This produced a series of surface transitions in conditions much closer to thermodynamic equilibrium, yielding graphene with a much more uniform number of layers (1-2) and larger-scaled features (few microns) as compared to the situation without Si evaporation (few 100 nm features and 1-4 layers) at the same growth temperature [290]. Further increase in the growth temperature and Si pressure (in ranges not suitable for the utilization of the LEEM instrument used in Ref. [290]) is expected to yield further improved morphology and structure.

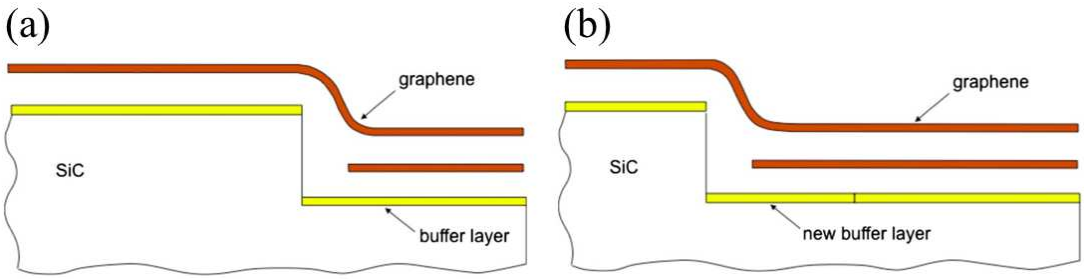

Figure 38: Growth of a second graphene layer at a step edge from the state in (a) to the state in (b). [Reprinted with permission from [301]. Copyright (2009) by the American Physical Society.]

5.5.3. Multilayer Growth

SiC sublimation often produces multiple graphene layers on top of one another. They can have different properties depending on their interaction with each other and the SiC substrate.

To determine the thickness of graphene layers STM observations of the surface have been used [299]. It was found that the surface roughness can be related to the layer thickness with an exponential relationship. By measuring the surface roughness, steps between upper and lower terraces were identified with a height of 0.4 nm. This height does not correspond to the usual gap between two graphene layers of 0.335 nm. The difference is attributed to the existence of a buffer layer in between the SiC(0001) surface and the graphene layers. This layer has a honeycomb lattice structure with a $(6\sqrt{3} \times 6\sqrt{3})$R30° reconstruction [52] involving the formation of strong C-Si bonds [53], thus not exhibiting the electronic properties typical of graphene [300].

As a second graphene layer grows it is calculated from the C density that 3 layers of SiC must be consumed [299]. Because the initial graphene layer continues to cover the surface, it is suggested that the additional layer grows underneath it. Above 1473 K the SiC underneath the buffer layer on the upper terrace decomposes, Si atoms desorb and the liberated C atoms create a graphene layer and a new buffer layer underneath [301]. This bottom-up growth process is depicted in Fig. 38.

Evolution of the growth of graphene multilayers has been observed using LEEM [90]. In order to achieve this, the contrast in the LEEM images was interpreted as the number of graphene layers on the SiC surface. As a check, angle-resolved photoemission spectroscopy (ARPES) was used to determine the populations of the layers from their different photoemission intensities. This was compared with the layer populations found from the LEEM image contrast. As these populations were the same it shows that the LEEM contrast indeed corresponds to the different layer thicknesses.

Using LEEM images of the SiC surface the population fraction of the different graphene layers was determined at 1553 K and 1583 K, see Fig. 39(e). The light, medium and dark gray regions of the image show graphene-free, single layer and bilayer graphene, respectively, Fig. 39(a) and (b). Heating from 1553 to 1583 K causes the graphene-free population to decrease and the single layer and bilayer populations to increase. This shows how multilayer graphene on SiC develops, with new layers growing underneath previous layers, causing the increase in thickness as the temperature is raised.

6. Structure of Graphene on Substrates

6.1. Metallic Substrates

When graphene is grown on transition metal surfaces, various properties arise due to the lattice mismatch between the metal and graphene. The C-C bond is extremely strong, much stronger for instance than C-metal bonds. As already pointed out, this translates into a superior stiffness of graphene. Biaxial strain in graphene, which may arise from epitaxial stress during graphene growth on a substrate, is consequently especially energetically costly. More than about 1% strain is actually prohibitively costly, and even such strain cannot be achieved in the graphene metal systems where C-metal bonds are weak. With the exception of Co(0001) and Ni(111), graphene cannot have its lattice sufficiently strained to form a commensurate structure on the substrate. The so-called moirés result, which may be described by the number of graphene hexagon

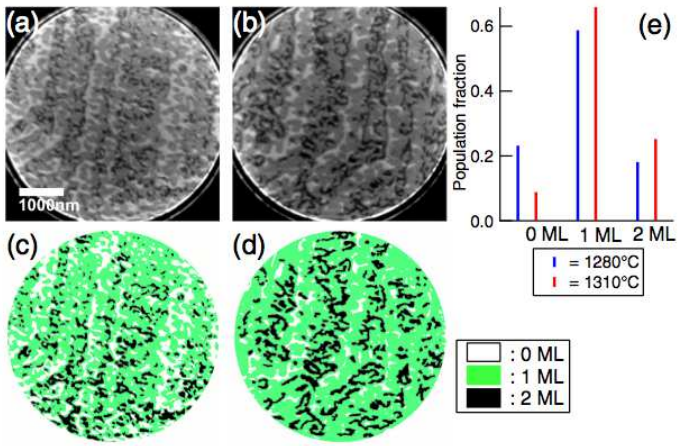

Figure 39: LEEM images of graphene on SiC after heating to (a) 1553 K and (b) 1583 K. (c) and (d) show the regions of different layer thicknesses for (a) and (b) after an object extraction process has been applied. (e) The population fraction of each of these layers at both of the temperatures. [Reproduced from [90] by permission of IOP Publishing. All rights reserved.]

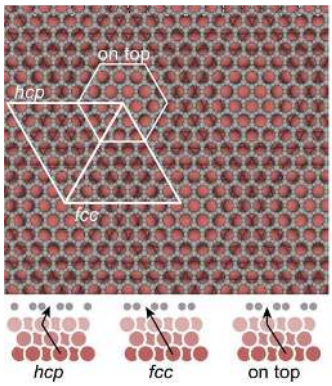

Figure 40: Ball-model of the distinctive moiré sites, top view (upper panel) and side view (bottom panels); the so-called hcp, fcc, and on top sites are also indicated.

units $(m \times m)$ matching $(n \times n)$ surface cells of the substrate, in the case of commensurate structures. In a moiré structure, carbon atoms are located at different positions with respect to the atoms of the substrate, and it is usually named after the position of the center of the carbon ring with respect to the underlying metal stacking (see Fig. 40 for the definition of "hcp", "fcc", and "on top" sites). Their position affects the strength of the interaction between the surface and the carbon atoms. Across the moiré superstructure there are bonding and nonbonding regions where the C atoms are mostly found on top of substrate atoms or in between them. Periodic corrugations as well as changes in the separation between graphene and the substrate are observed. For Ni, however, the lattice mismatch is small and there is no moiré structure.

Graphene can also orientate itself at different angles with respect to the substrate lattice. For one particular surface there may be many graphene rotational domains that can form. A graphene lattice whose zigzag rows align to the dense-packed rows of the metal is denoted as the R0 domain. Other domains are defined in terms of the angle between them and the R0 phase, such as R30 where the graphene lattice is rotated by 30° with respect to the substrate lattice. Each of the domains have an individual moiré structure, and are therefore corrugated differently too. Here we report experimental and theoretical results of the details of the graphene structure on the Ru(0001), Rh(111), Ir(111), Pt(111), Ni(111), Re(0001), Au(111), Co(0001) and Cu surfaces. The main results for the different domains found on each of these surfaces are listed in Table 3 along with details of their moiré structure and the corrugation. We note that the occurrence of the different moirés, as well as the lattice parameter of graphene (thus the type of commensurability or incommensurability with the metal underneath) is expected to depend on the growth temperature. Indeed, roughly speaking,

one would expect the graphene to lock in on the substrate at the given growth temperature, with a structure which is influenced by the lattice parameter of the substrate at that temperature. This might explain the observation of different structures in graphene/Ru(0001) [51, 302] and graphene/Ir(111) [132] systems.

Before we move on to discuss each particular metallic substrate, it is worthwhile to say a few words here on the role of the dispersion interaction (Section 4.1.2) in stabilising adsorption of a single layer of graphene on metals. As this is a layered geometry, one would expect that the role of dispersion interaction is fundamental in binding graphene. Various DFT based methods were recently compared for the graphene adsorption on Ni(111) [313, 314], Cu(111) and Co(0001) [314]. The calculations were performed using LDA, PBE, various flavours of vdW-DF and RPA methods. In the latter case exact exchange was also applied. Because of the fact that RPA is extremely expensive computationally, only primitive cells were considered in these calculations with the graphene lattice being appropriately scaled to that of the underlying metal. In all cases LDA calculations resulted in a strong binding of graphene with the distance of around $d = 2$ Å to the metal. PBE simulations yielded binding only in the case of Co(0001) which was found rather weak; no minimum was obtained in the cases of Cu(111) and Ni(111) substrates. Calculations using the vdW-DF methods resulted in all three cases in a minimum at rather large distance of $d = 3.7$ Å to the metal indicating physisorption with the adsorption energy (per C atom) of around 40 meV [314]. However, RPA simulations showed that the situation is much more complex as there is a subtle balance between the chemical (short range) and dispersion (long range) interactions in these systems. In particular, while for Cu(111) only a single minimum with $d = 3.25$ Å was found (which is between the values given by LDA and vdW-DF), for Ni(111) and Co(0001) two minima were found corresponding to chemisorption and physisorption. For instance, in the case of Ni(111) these were at the distances of 2.3 and 3.25 Å, respectively, with the physisorption state being by 4-8 meV per C atom (depending on the k-point sampling used) more favourable. Interestingly, two minima were also found in a similar study [313], however, the chemisorption state was found to be more energetically favourable by 7 meV per C atom. These energy differences are however too small to conclude decisively at which distance graphene is preferentially adsorbed on these metals. The most likely conclusion from these studies is that the potential energy surface for graphene adsorbed on a metal surface as a function of d between 2.3 and 3.3 Å is rather flat. It is clear however that there is subtle balance between the chemical and dispersive interactions in these systems which RPA method captures successfully, while other methods do not, so great care is indeed needed when applying DFT based technique to this type of system.

6.1.1. Ru(0001)

Graphene can be grown on the Ru(0001) surface using any of the methods described in Sections 5.1, 5.2 and 5.4. The strong interaction between Ru and carbon results in the graphene growth having only the R0 rotational domain. When graphene is grown on the Ru(0001) surface, a moiré superstructure is formed due to the lattice mismatch between Ru and graphene. This structure has a hexagonal lattice with a measured repeat distance of around 30 Å [305]. A variety of methods such as LEED, STM and surface X-ray diffraction (SXRD) studies have been used to identify the moiré superstructure. STM measurements have suggested periodicities of graphene/metal as (11×11)C/(10×10)Ru [302], and (12×12)C/(11×11)Ru [51, 315]. SXRD studies, which allowed unprecedented resolution, have shown that the moiré structure has a periodicity of (25×25)C/(23×23)Ru [303, 104]. Using LEEM coupled to micro-LEED experiments, it was found that the actual structure of the samples varies slightly about this second order R0 commensurability, with small deviations from R0 [316].

Due to the strong interaction between graphene and Ru(0001) the graphene becomes highly corrugated. Measurements of the peak to peak height of these corrugations have been made with LEED, from helium atom scattering (HAS) data and using X-ray diffraction. Each method observes different corrugation heights with LEED, HAS and XRD measuring the height as 1.5 Å [104], 0.15 Å [304] and 0.82±0.15 Å [303], respectively. DFT calculations determine a corrugation of 1.5 Å [131] and 1.59 Å [104]. As a result of the corrugation the separation between the graphene and the Ru surface also varies. LEED studies have found that the separation changes from 2.1 to 3.64 Å across the periodicity of the cell [104]. A similar result of 2 to 3 Å has been found with X-ray diffraction [303]. The model of graphene on the Ru(0001) surface is shown in Fig. 41.

The graphene-Ru interaction has also been found to cause corrugation in the Ru substrate. For the first Ru layer the corrugation was measured as 0.23 Å with LEED [104] and 0.1±0.02 Å with SXRD [303]. For the layers further below this the corrugation is reduced and it eventually decays into the bulk substrate [131]. This is unlike the graphene layers where additional layers on top of the first layer are unaffected by the Ru

Table 3: Structure of graphene on various surfaces. The surfaces are listed in order from the strongest interaction with graphene (Ru(0001)) to the weakest (Pt(111)) [185]. The corrugation is described in terms of the peak-to-peak height, with the data in parentheses obtained from DFT (where available).

Surface	Metal lattice constant (Å)	Angle between graphene zig-zag rows and metal densely-packed rows	Graphene Moiré superstructure	Corrugation (Å)
Ru(0001)	2.71	0°	(25×25) [303, 104] (13×13) [104] (12×12) [305]	0.82 [303], 1.53 [104], 0.15 [304], (1.5 [131]) (1.59 [104]) (1.5 [305])
Rh(111)	2.69	0°	(12×12) [261]	0.5–1.5 [261]
Ir(111)	2.72	0° [106, 306] $\sim 14°$ [106, 306] 19° [306] 23° [306] 26° [306] 30° [106, 306]	incommensurate [132] (10×10) [306] (4×4) [306] (3×3) [306] $(\sqrt{19} \times \sqrt{19})$ [306] $(\sqrt{37} \times \sqrt{37})$ [306] (2×2) [306]	~ 0.3 [50, 106] 0.423 [306] (0.101 [306]) (0.051[306]) (0.022[306]) (0.015[306]) 0.04 [106] (0.014 [306])
Pt(111)	2.77	30° 19° 14° 6° [307] 3° 2°	(2×2) (3×3) (4×4) [307], $(\sqrt{37} \times \sqrt{37})$ [308] $(\sqrt{61} \times \sqrt{61})$ $(\sqrt{67} \times \sqrt{67})$	< 0.3 ——— [307] 0.5–0.8
Ni(111)	2.49	0° $17° \pm 7°$ [311]	(1×1) [103, 309, 310]	
Cu(111)	2.56	0° 7° [253]		
Pd(111)	2.75	−2° −5° 17° [312] 22° 26°	$(3\sqrt{7} \times 3\sqrt{7})$–$R\,19°$ $(\sqrt{39} \times \sqrt{39})$–$R\,16°$ $(\sqrt{21} \times \sqrt{21})$–$R\,11°$ [312] $(\sqrt{13} \times \sqrt{13})$–$R\,14°$ $(\sqrt{7} \times \sqrt{7})$–$R\,19°$ (7×7)	
Au(111)	2.88	0° 11° 14° [259] 26°		
Re(0001)	2.76	0° [141, 247]	(8×8) [247]	1.7 [247]
Fe(110)	2.87/4.06	0° [258]	(6×18) [258]	0.9 [258]

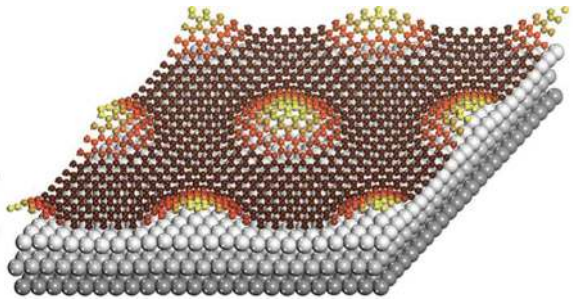

Figure 41: The 3D surface structure model of graphene on Ru(0001) showing the corrugation across the lattice, as determined from LEED. For better visibility, the vertical displacements of the C and Ru atoms are enhanced by factors of 3 and 7, respectively. [Reprinted with permission from [104]. Copyright (2010) by the American Physical Society.]

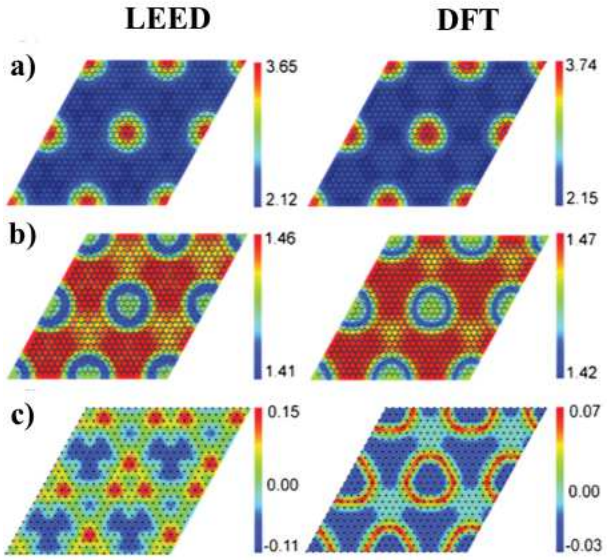

Figure 42: LEED and DFT results for (a) the corrugation of the graphene layer, (b) the C-C bond length in the graphene layer, (c) the corrugation of the upper Ru layer.[Reprinted with permission from [104]. Copyright (2010) by the American Chemical Society.]

substrate.

In the work of Moritz *et al.* [104] DFT was used to study the graphene corrugation, the bond length of the graphene layer and the corrugation of the Ru underlayer for a simulated (13×13)C/(12×12)Ru moiré lattice. The results are shown in Fig. 42 along with the results for the same properties as determined by LEED experiments. The variation in the C-C bond length throughout the moiré superstructure can be related to the strength of the binding in different regions across the lattice. Where the C-C binding is strong the C atoms have shorter bonds to each other and are close to the Ru substrate, whereas in the weakly bound regions they are found further from the substrate. This gives rise to the corrugations shown in Fig. 42(a). At the corrugation maxima the bond lengths match that of freestanding graphene, while in the minima the bonds are stretched due to the interaction with the Ru substrate. In comparison to the LEED data the DFT calculated results are similar, but the graphene corrugation height is overestimated with DFT and the corrugation of the Ru surface is underestimated. The difference in the Ru corrugation is suggested to be due to the fact that only two Ru layers were relaxed in the calculation, whereas experimental results have shown that the relaxation occurs for up to 7 Ru layers below the surface.

6.1.2. Rh(111)

Graphene on Rh(111) has similarities with that on Ru(0001) and in terms of the strength of interaction between the surface and graphene Rh lies in between Ir and Ru [261]. Further, graphene forms just a single

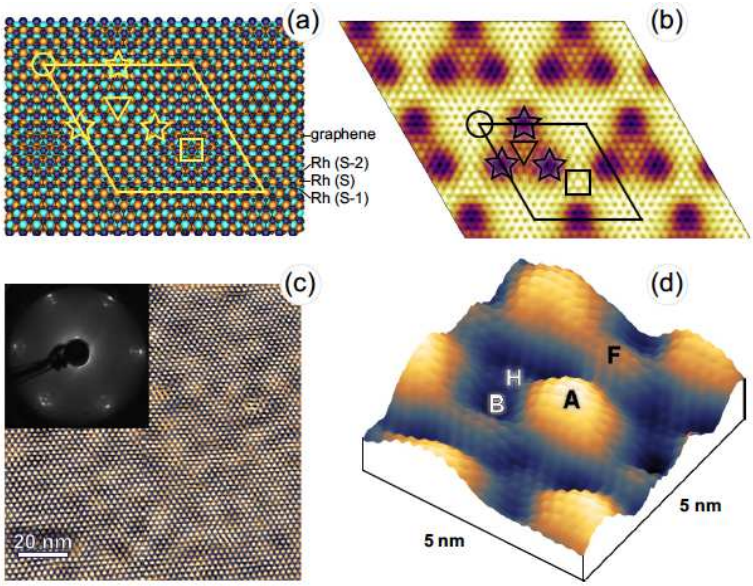

Figure 43: (a) Crystallographic structure showing the 12×12 supercell of graphene positioned on top of a 11×11 cell of Rh(111); (b) the corresponding calculated STM image of graphene/Rh(111). Here the symbols refer to positions of the centers of hexagonal units of graphene relative to the Rh lattice in high symmetry configurations [317] (labelled Rh(S), Rh(S-1) and Rh(S-2) in (a)). These are A sites whereby carbon atoms lie on top of Rh(S-2) and Rh(S-1) atoms, (circles); H sites where atoms lie on top of Rh(S) and Rh(S-2) atoms (down-triangle); F sites where atoms lie on top of Rh(S) and Rh(S-1) (square), and finally B sites which bridge (star). (c) Large scale STM image of the graphene layer on Rh(111). Tunneling conditions: U_T=+1 V, I_T=1 nA. (d) 3D view of the 5×5 nm^2 region from (c) showing the structure of the graphene layer on Rh(111). Tunneling conditions: U_T=0.55 V, I_T=10 nA. [Reprinted with permission from [261]. Copyright (2012), AIP Publishing LLC.].

rotational domain on Rh(111) with a mismatch corresponding to a 12×12 graphene cell occupying 11×11 Rh supercell [261, 317]. This has been observed experimentally using both AFM and STM, see Fig. 43. These images demonstrate a moiré structure with a measured corrugation of between 0.5 - 1.5 Å. In this study, Voloshina *et al* [261] used AFM to examine the differences in bonding between graphene and Rh at the different sites that carbon atoms in graphene occupy on the Rh surface. These regions correspond to the different arrangements of carbon atoms on top of Rh(111) as explained in the caption of Fig. 43(a). They found that the strongest bonded region corresponds to the bridge region and the most weakly bound region is the A region or the T region in the notation of Wang *et al.* [317]. Unsurprisingly, due to the changes in the interaction strength the different regions vary in height above the Rh(111) surface. In the A region the C atoms are 3.15 Å above the surface, whereas for the strongly bound bridge region the gap between graphene and the substrate is much lower, about 2.08 Å. Thus, just like Ru(0001), graphene on Rh(111) forms a strongly corrugated sheet with regions that interact much more strongly with the underlying substrate than others.

6.1.3. Re(0001)

The preparation of graphene on Re(0001) is achieved either by repeated TPG cycles [141] or by segregation from thin films [247]. Graphene on Re(0001) exhibits many similarities with that on Ru(0001) and Rh(111), given the relatively strong interaction between graphene and Re. The moiré of graphene on Re may consist of different coincidence lattices [141, 247], presumably depending on the preparation conditions. These coincidences correspond preferentially to carbon zig-zag rows aligning Re dense packed rows, for instance, with 8 carbon rings matching 7 ones. In this configuration, DFT calculations including van der Waals interaction predict a 1.7 Å corrugation along the moiré sites, with the lowest-lying sites being 2.2 Å and the highest-lying ones 4 Å above Re atoms [247].

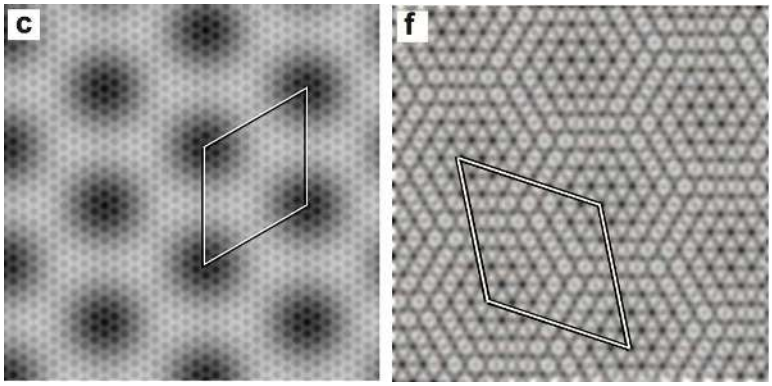

Figure 44: Schematic illustrations from STM images of the graphene on Ir(111) rotated by (a) 0° (R0 phase) and (b) 30° (the R30 phase) with respect to the Ir(111) lattice. [Reprinted with permission from [106]. Copyright (2009) by the American Physical Society.]

6.1.4. Ir(111)

Preparation of graphene on Ir(111) is usually achieved using hydrocarbon decomposition either with TPG (Section 5.2) or CVD (Section 5.1). In these methods the surface acts as a catalyst for the growth of graphene from hydrocarbons. Due to this and the fact that carbon has low solubility in Ir, graphene growing on Ir(111) is usually limited to just one layer. The graphene formed on the Ir(111) surface has a moiré structure, whose geometry is more complex than that of graphene/Ru(0001), as shown by a recent SXRD study revealing the incommensurate nature of the moiré between graphene and Ir(111) [132]. The repeat distance of the R0 domain moiré structure (where the graphene and Ir lattices are aligned) was found from LEED and STM measurements to be 25.8±2 Å and 25.2±0.4 Å, respectively [318], and depends on preparation temperature [132].

Unlike graphene on Ru(0001), the Ir(111) surface gives rise to the growth of graphene with various orientations, see Fig. 44. As well as the commonly found R0 phase [318, 61, 106], multiple domain phases which are rotated by various angles with respect to the R0 phase have been identified on the Ir(111) surface [106, 306], the most frequently found are listed in Table 3. These domains each have different structural properties such as moiré repeat distance, G-Ir separation and corrugation. The cause of these multiple domains is suggested to be due to the interaction strength between the graphene and the substrate surface. For Ru(0001) the interaction is strong, and hence there is large corrugation and strong orientational dependence on the surface that allows only one R0 orientation. For Ir(111) the interaction with graphene is weaker [138] and it is possible then that multiple orientations exist due to the limited influence of the surface. The various growth alignments found on Ir(111) have also been shown to be temperature dependent [99]. In a TPG study of the growth from ethene deposition and then annealing to temperatures between 1000 and 1530 K the preferred orientation was determined at different temperatures. Below 1200 K the orientation distribution of the domains is rather broad. At 1255, 1350 and 1460 K there is evidence of the R0 and R30 phases as well as randomly orientated domains. At 1530 K the graphene becomes well-ordered with only the R0 phase present.

The corrugation of graphene on Ir(111) has been estimated with STM for the 0° and 30° orientations. For the R0 phase the corrugation is measured as approximately 0.3 Å, whereas for R30 the corrugation is lower at 0.04 Å, see Fig. 44. This suggests that the R0 domains interact more strongly with the surface than the R30 domains [106]. The corrugation of the R0 phase was later confirmed in a reliable manner with XSW [150] and AFM [69, 76] experiments (STM, in principle, only provides information about apparent heights). It was found that the corrugation depends on the internal strain in graphene islands [150].

Additional graphene rotational domains were found on the Ir(111) surface with LEED and STM [306]. R14, R19, R23 and R26 domains have been reported, but also in some preparation conditions a continuous spread of orientations [99], like on Pt(111) [48], is observed. The moiré periodicity of these domains is listed in Table 3 along with the corrugation determined from DFT calculations which included van der Waals forces as well. The size of the corrugations is claimed to be due to the positions of the C atoms within the moiré structure. For the R0 domain C atoms are found in distinct regions which are either on top of Ir atoms in

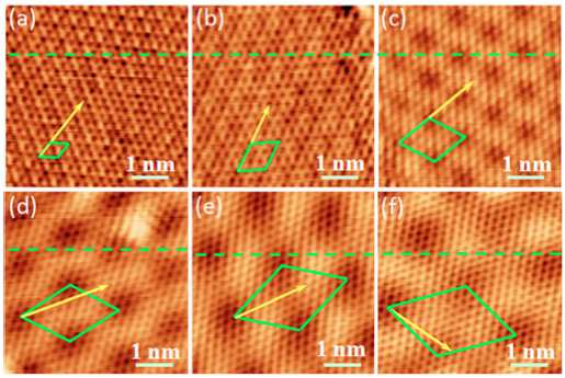

Figure 45: STM images of the graphene lattice on the Pt(111) surface rotated by (a) 30°, (b) 19°, (c) 14°, (d) 6°, (e) 3°, and (f) 2° with respect to the Pt lattice. The moiré supercells are highlighted in each case. [Reprinted with permission from [307]. Copyright (2011), AIP Publishing LLC.]

the first (top region), second (fcc region) and third (hcp region) layers [50]. Therefore the corrugation is large. For R23 and R26 no fcc or hcp regions can be noticed with STM and accordingly the graphene is less corrugated. In R30 graphene the fcc and hcp regions are similar due to its small size and the corrugation is also small. The separation between graphene and the Ir(111) surface was also calculated in the same manner. The size of the gap between the lowest carbon atom and the first layer of Ir substrate was shown to vary by about 0.1 Å across all of the orientations. The smallest gap found was for the R0 domain (3.159 Å), which was also the most corrugated structure of the different domains. Those with the smallest corrugations also had the largest graphene-Ir separations [306].

6.1.5. Au(111)

The structure of graphene on Au(111) was investigated by STM, which revealed that different orientations, like on Ir(111), coexist, corresponding to 0°, 11°, 14° and 26° rotations between carbon zig-zag rows and Au dense packed ones [259]. Interestingly, the interaction between graphene and Au(111) is sufficiently weak that the herringbone reconstruction is not lifted after graphene growth, and can readily be observed in STM. This interaction is the weakest in the case of non-0° rotational domains, which translates into a different (non determined) corrugation along the moiré sites. Based on this observation, an upper limit for the graphene-metal interaction energy was given by trying to reproduce, in the framework of a Frenkel-Kontorova model, the features of the Au reconstruction in the presence of graphene. This upper limit was determined to be 13 meV per C atom [259].

6.1.6. Pt(111)

Compared to the other surfaces the interaction between the Pt(111) surface and the graphene is considerably weaker [138]. As a result of this a main feature of graphene grown on Pt(111) is that there are many rotational domains [307, 308, 58]. Some which have been reported are listed in Table 3. Each of the domains has a moiré type structure with unit cells that are each sized differently [307] as shown in Fig. 45. The structure of the domains is also corrugated across the unit cell with the amount of corrugation dependent on the cell size [307]. For the R30 and R19 domains the moiré unit cells are small (5 and 7.38 Å in size, respectively) and in both cases corrugation observed with STM has an apparent height less than 0.3 Å. For the domains with a larger repeating unit the measured corrugation is slightly more significant and ranges within 0.5 - 0.8 Å for the 14°, 6° and 2° rotations. As discussed previously, more corrugated structures are the result of a stronger interaction between the graphene and the surface. For the 7×7 and 2×2 moiré structures the separation between graphene and Pt was calculated to be above 3.1 Å. The large size of this gap is due to the weak graphene-Pt interaction [307].

In the experimental study [58] graphene was grown from segregation of C atoms from the Pt bulk. From a LEEM study it was found that smaller rotational-angle domains grow more quickly than larger domains. The suggested reason for this is that it is due to kinetic factors and that for the smaller domains there is a lower attachment barrier for C [58] (assuming of course that the growth progresses via atomic, not cluster,

attachments). This could relate to the fact that the interaction with the surface may be weaker for smaller rotational-angle domains (as seen in the corrugation data). A similar phenomena has been noticed on the Ir(111) surface, where the R30 domains grow faster than the R0 domains [92]. Of the two it is probable that the R0 domain is more corrugated and is assumed to interact more strongly with the surface [106]. This may cause the attachment barrier for C monomers or clusters to be greater.

In the work by Merino *et al.* [308] the composition of the graphene grown on Pt(111) was analyzed in order to find the fractional coverage of the different rotational domains. The study was based on hundreds of STM images. From this it was noticed that only some particular domains are present, which make up a larger fraction of the total graphene coverage. To understand these results a model was proposed where the mismatch between the graphene and the surface for each of the domains was related to how frequently the structures form. The model suggests that rotational domains with smaller mismatch should be found more frequently on the surface, which agrees with the experimental observations. This explains why graphene grows along only some particular angles with respect to the Pt lattice.

6.1.7. Ni(111) and Co(0001)

The discussion in this subsection is mainly concerned with the Ni(111) surface. However, it is worth keeping in mind that the Co(0001) surface has a lattice very similar to that of Ni(111), and therefore its mismatch and hence interaction with graphene are expected to be similar.

The Ni(111) surface has a lattice constant that is very similar to the free-standing graphene lattice and so under most growth conditions graphene forms a commensurate structure on Ni(111) with a very small lattice mismatch. Thus, unlike graphene growth on many transition metal surfaces, usually no moiré pattern is observed during high temperature growth.

As a result usually (1×1) commensurate structures are formed, which are characterized by a short graphene-metal distance [309]. Among the many possible (1×1) structures [310], corresponding to hcp, fcc, ontop configurations of Fig. 40, other kinds of configurations, e.g. with the centre of carbon rings atop Ni bridge sites of the different Ni layers, have been identified in experiments. High resolution XPS recently showed that, besides the hcp configuration inferred from LEED measurements [103], a configuration with carbon ring centres atop the bridge sites of the topmost Ni layers was formed [310]. It has also been shown that under some specific growth conditions it is possible to form graphene which exists in two different rotational domains with respect to the Ni(111) lattice [311, 287], and that in the case when a surface carbide forms as an intermediate during graphene preparation, a graphene phase rotated by $17 \pm 7^\circ$ with respect to the Ni lattice forms [311]. DFT works [319, 320, 321, 322, 323, 313, 310] have focused on determining which of the (1×1) commensurate structures is most favorable. Most of these works rely on DFT calculations which do not include the dispersion interaction leading, as was already mentioned in Section 6.1, to artificial binding with LDA and no binding at all with PBE. Thus, as follows from the above mentioned studies, a conclusion concerning which structure is the most stable, should be taken with care. Whether DFT calculations which account for dispersion interaction [323, 310] can make reliable predictions about the stability of the graphene/Ni(111) system seems questionable at the moment [313] (see also discussion in Section 4.1.2). Correspondingly, the question of whether graphene is weakly adsorbed on Ni(111) or not is still under debate.

6.1.8. Cu(111) and Cu(100)

As described by Gao *et al.* [253] STM images of graphene grown on Cu(111) using CVD have been observed to form two different rotational domains which are rotated with respect to the Cu(111) lattice by 0° and 7°, see Fig. 46. These correspond to a periodicity of $\sim$6.6 nm and 2 nm, respectively. Note that other periodicities have been observed as well, albeit in a lower concentration. On Cu(100) graphene shows moiré patterns which are not triangular [324]; this is due to the different symmetries of graphene and Cu(100).

6.2. SiC

To investigate the importance of C clusters on the SiC surface at the nucleation stage of formation of the buffer layer, Inoue *et al.* [325] studied clusters of up to 20 atoms on the surface employing a DFT method and geometry relaxation. Their approach was based on starting from a hexagonal cluster C_6, see Fig. 47(a), and then adding one-by-one single C atoms to various available sites of the cluster at each step; the geometry of all clusters built in that way were optimized and formation energies calculated. This process was continued

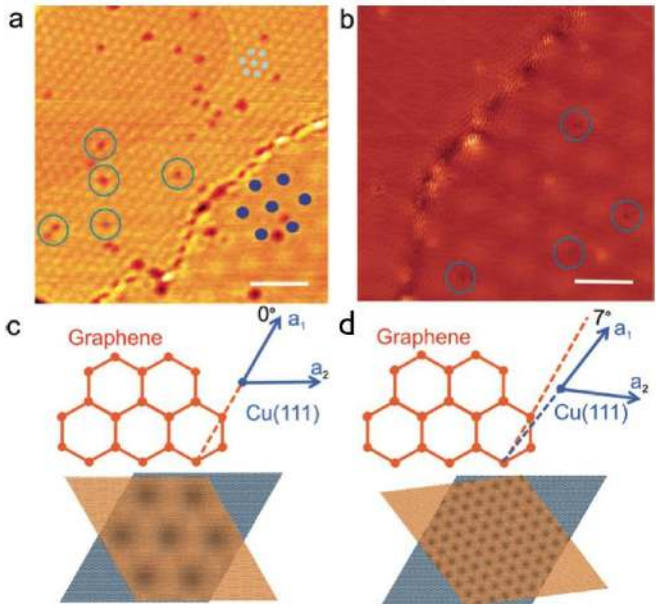

Figure 46: STM topography images at the domain boundaries of graphene on Cu(111). (a) STM image at a domain boundary showing two different moiré patterns in the two domains. The periodicity of the moiré pattern for the upper left domain is ∼2.0 nm, and that for the lower right domain is around 5.8 nm. Scale bar: 10 nm. (b) Atomic resolution STM image at a domain boundary, showing the honeycomb structure of graphene. The moiré pattern in the upper left domain cannot be observed under these scanning conditions. The periodicity of the moiré pattern in the lower right domain is ∼3.0 nm. Scale bar: 4 nm. Blue circles indicate some of the adsorbates on the graphene surface in (a) and (b). (c) The most observed (∼30%) moiré pattern of graphene on Cu(111) with around 6.6 nm periodicity. The lattice orientation of graphene is strictly aligned with that of Cu(111) surface. (d) Another typical moiré pattern of graphene on Cu(111) with a periodicity of ∼2.0 nm and the misorientation angle of ∼7°. [Reprinted with permission from [253]. Copyright (2010) American Chemical Society.]

until a C_{20} cluster was finally constructed. The formation energy was calculated using essentially Eq. (5), with the chemical potential μ_C taken to be that of C in graphene on the surface; however, the energy per C atom was actually presented. Analyzing the bond lengths formed by the initial seed C_6 with the SiC surface, it was concluded that C atoms of the hexagonal cluster form covalent bonds with the nearest Si atoms of the surface which explains why this particular cluster was found to be the most appropriate choice for the seed. Once C atoms are added, however, hexagonal structures were found to be less favorable in bigger clusters; instead, penta-heptagonal clusters were found to have lower formation energies. This was explained by a greater flexibility of their cages to distortion caused by the mismatch with the SiC surface, as compared to the hexagonal cages. These results suggest that non-hexagonal clusters must play important role in nucleating graphene on SiC. It was also explicitly shown in [325] that the chemical potential of individual C atoms on the surface becomes greater at larger coverages than the average chemical potential of C atoms in clusters which indicates that at some coverage the formation of clusters becomes indeed energetically favorable, and hence clusters provide a driving force for growth.

Varchon *et al.* [53] examined the structure of both the buffer layer and the graphene layer on top of the buffer layer for the Si and C terminations of the 6H-SiC surface using DFT. In the case of the Si-terminated SiC surface, the first (buffer) layer was found to be strongly corrugated, with a height variation of 1.20 Å. These corrugations are induced by strong covalent bonding between carbon and silicon at parts of their hexagonal lattices where they are commensurate with each other, Fig. 48, in a similar way to what was found in graphene on transition metal surfaces (Section 6). The corrugation of the buffer layer has a noticeable effect on the second (graphene) layer as well, where a rather small calculated corrugation of 0.4 Å (ripples) running with periodicity of over 19 Å was found, see Fig. 49. In the case of the C-terminated SiC surface, much stronger interaction between the buffer layer and the C atoms underneath was found, and the ripple effect characteristic for the Si-terminated SiC surface was not observed. The average height of the buffer layer from the SiC surface was also calculated using DFT in [300], but the value they found (2.58 Å) was considerably larger.

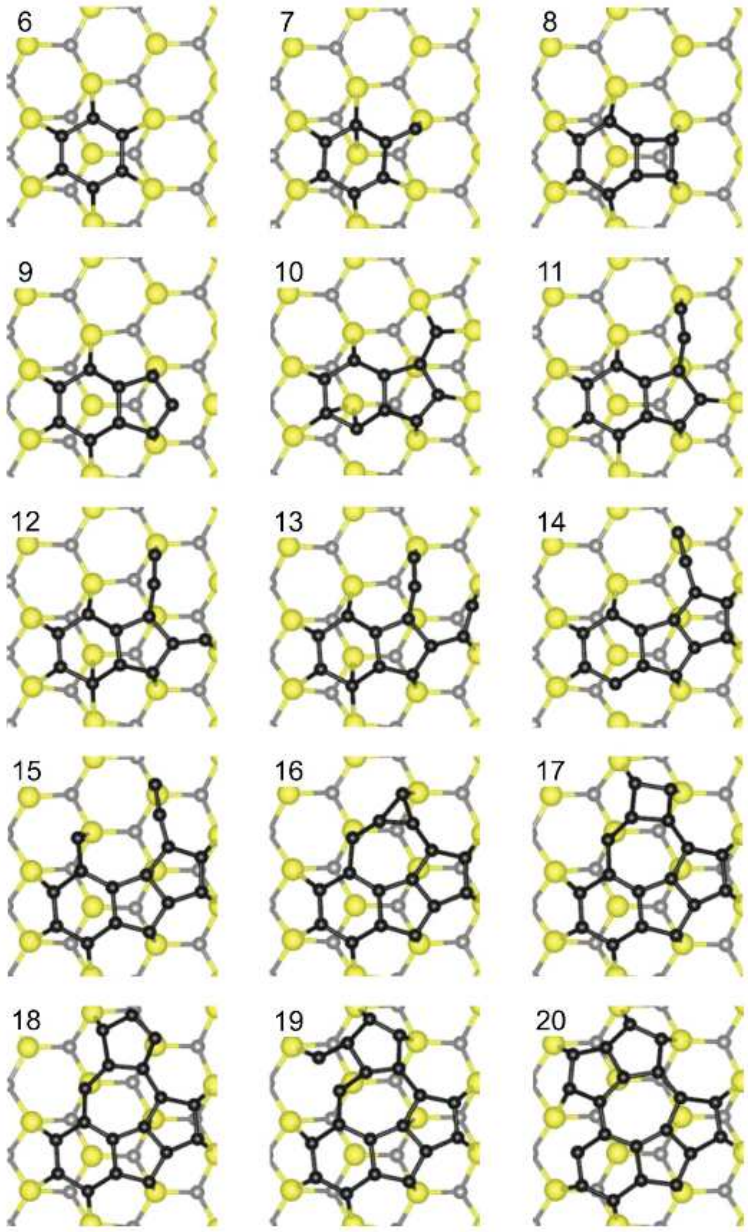

Figure 47: Structural models of clusters obtained by adding single C atoms one-by-one to the initial seed cluster C_6 shown in the upper left corner. Numbers correspond to the total number of C atoms (shown as dark small circles) in the clusters. Si and C atoms of the SiC surface are shown as large yellow and smaller grey circles, respectively. [Reprinted with permission from [325]. Copyright (2012) by the American Physical Society.]

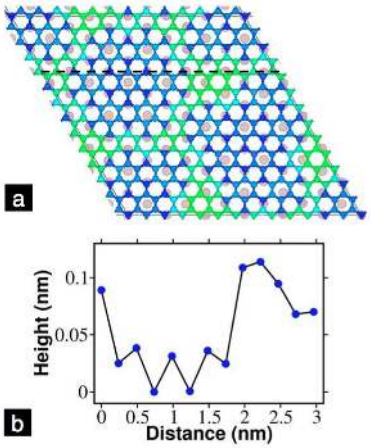

Figure 48: (a) Shown are atomic positions in the buffer layer on top of the Si-terminated SiC surface: gray circles represents the top layer Si atoms of the last SiC plane. C atoms of the buffer layer are shown with the color reflecting their height, ranging from blue close the substrate to green for those which are further away. (b) Heights of the buffer layer atoms along the black dashed line defined in (a). [Reprinted with permission from [53]. Copyright (2008) by the American Physical Society.]

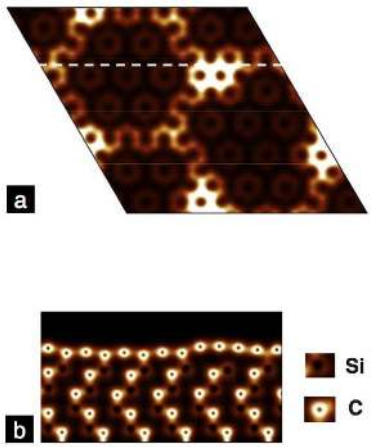

Figure 49: Calculated charge density of the graphene layer placed on top of a C buffer layer resting on the Si-terminated SiC surface. (a) Top and (b) side views. A cut through the system perpendicular to the surface and running along the dashed line indicated in (a) is shown in (b). [Reprinted with permission from [53]. Copyright (2008) by the American Physical Society.]

As discussed in Section 8 the growth of a carbon buffer layer precedes that of quasi-free standing graphene (QFSG) during annealing on SiC. DFT calculations of the buffer layer of graphene on SiC [326, 53] show that it does not display a number of graphene characteristics, most likely due to its strong covalent bonding to the SiC surface. An example of this would be the clear difference between the band structures of the buffer layer compared to free standing graphene demonstrated in [327, 300].

Other than first principle examinations, the first and second layers of graphene on SiC have also been examined using empirical potentials (EP) [328, 329, 330, 331]. These studies not only examined some aspects of the buffer layer on the Si face of SiC; they also have shown that EP in conjunction with molecular dynamics (MD) simulations can be used to obtain results that agree quite well with *ab initio* calculations where available [328]. This is of some interest because large scale and longer time simulations of growth mechanisms using EP could be performed that would not be possible for first principles based methods [328]. We shall now briefly review a selection of the results obtained using EP.

Lampin *et al.* [328] used the many-body empirical potentials EDIP [332] to perform simulations of a layer of carbon atoms on top of the Si face of SiC. EDIP potentials were fitted to be able to describe C and Si based crystals and their defects; they do not account for the dispersion interaction as is the case for

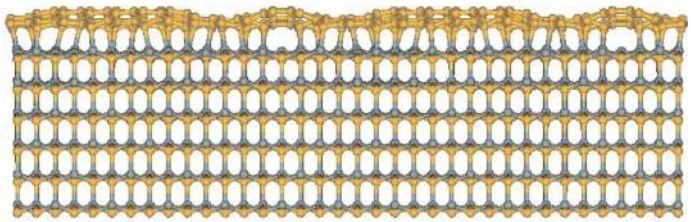

Figure 50: Side view of the EDIP relaxed C atoms buffer layer on top of the Si-terminated SiC surface. [Reprinted with permission from [328]. Copyright (2012), AIP Publishing LLC.]

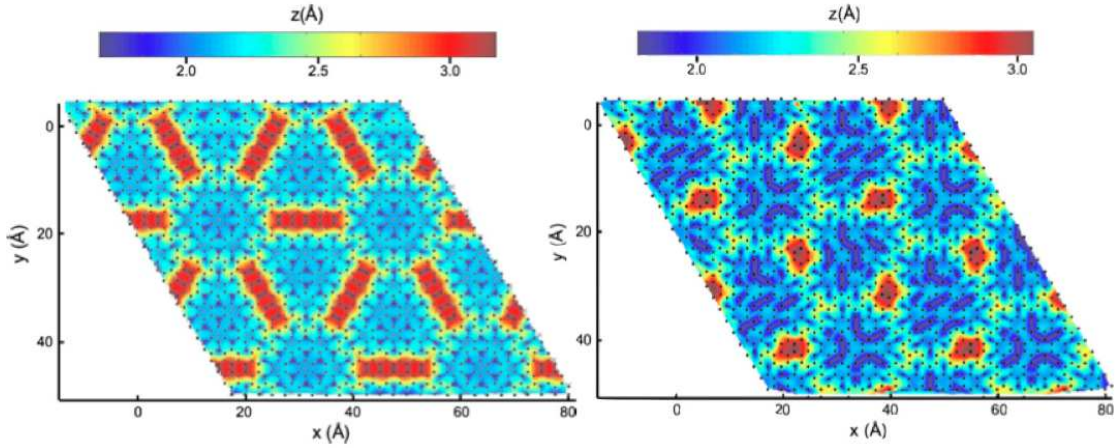

Figure 51: Representation of the heights of the carbon atoms in the buffer layer placed on top of the Si-terminated 6H-SiC surface calculated using EDIP (left) and DFT (right, from [53]) shown using different colors. Blue represents the closest atoms to the surface while red represents atoms further away from the surface. Black dots show C atoms in the buffer layer, while light crosses indicate the topmost Si atoms of SiC. The height z (in Å) corresponds to the vertical distance between the C atoms in the buffer layer and a reference plane associated with the topmost Si atoms of SiC prior to its relaxation. [Reprinted with permission from [328]. Copyright (2012), AIP Publishing LLC.]

the standard density functionals commonly used in DFT calculations. After relaxing a number of different starting configurations they obtained the lowest energy structure, shown in Fig. 50, which broadly agrees with corresponding DFT calculations discussed above. The separation between the Si surface and the lowest carbon atom in graphene was found to be 1.68 Å with the graphene sheet itself being strongly corrugated with an amplitude of 1.50 Å (1.20 Å with DFT [53, 300]). Similar rippled structures of the buffer layer were obtained by Tang *et al.* [329] who used modified Tersoff potentials [333] and simulated annealing to find the structure of graphene nanoribbons (GNR) of different widths on top of a Si-terminated SiC bulk. They reported corrugation of the buffer layer C atoms of the order of 1 Å and ripples with wavelength of around 18 Å. They also find that the ripples remain periodic up to some temperature (around 1500-2000 K depending on the GNR width), after which thermal fluctuations dominate the GNR structure.

The structure that both groups [329, 328] obtained have clear similarities with that found using DFT calculations [53], although in [328] there are some differences indicated in the heights from the surface of a number of carbon atoms of which the buffer layer comprises, see Fig. 51. Thus, the results obtained from EP calculations do agree globally with those obtained using *ab initio* methods, although there are discrepancies in some of the details in the obtained geometries. The results also seem to depend on the particular EP used in each case.

7. Simulation of graphene growth on metals

As should have become clear from the previous sections, the growth of graphene is a rather complicated process which happens across large length and time scales. Below we shall try to reflect on the recent progress in understanding the complexity of this phenomenon based on theoretical techniques.

We shall start by discussing phenomenological theories in section 7.1. The usefulness of these approaches stems from the fact that these may be directly compared to some of the experimental results, for instance, with time dependent measurements of the concentration of various carbon species on the surface; moreover, cumbersome experimental procedures (e.g. temperature ramp) can be easily incorporated as well. The main drawback of these methods is in their phenomenological character which lacks atomistic detail. In addition, spatial information (e.g. distribution of clusters and adatoms on the surface) is also not contained in these methods.

At the other end of the spectrum are atomistic approaches, mainly based on density functional theory (DFT) simulations; these will be covered in section 7.2. These methods enable one to uncover various elementary processes responsible for the growth phenomenon in great detail. These include the formation energies and mobilities of different carbon species on the given surface, including terraces and surface defects such as steps, the rate of attachment (detachment) of the species to (from) clusters and islands, and the favorable alignment of nuclei, and hence the growth of large clusters and islands, with respect to the substrate symmetry directions, etc. Moreover, rates of these elementary processes can be calculated and hence their importance for the graphene growth established. The ability to provide a detailed information on the nature of the binding of the carbon species to the substrate is also a particular strength of these techniques. However, only relatively small systems can be considered at this level of theory, and dynamical simulations may only be run over very short times, many orders of magnitude shorter than the growth process itself.

However, the atomistic information on the elementary processes and their rates can be incorporated into kinetic approaches, e.g. based on Kinetic Monte Carlo (KMC) simulations, which could provide a wealth of information on growth, such as e.g. the time dependent distribution of relevant carbon species on the surface, and this kind of information can be directly compared with experiment. Moreover, KMC rates can be fed back into the phenomenological rate equations and hence provide a platform for developing more refined phenomenological models. To our knowledge, just a few KMC simulations have been done to date on graphene growth, and we shall discuss them in detail in section 7.4.

But first we review the fundamental processes that are widely believed to occur during epitaxial growth of graphene.

7.1. Rate Equation Analysis of Growth

The detailed mechanism by which graphene growth occurs is not fully understood; moreover, the processes are also shown to be dependent on the type of surface and its orientation. From experimental observations of the graphene coverage using LEEM it was suggested that the rate of graphene growth on Ru(0001) [54] and Ir(111) [92] surfaces has a non-linear dependence on the C adatom concentration. In the experiment it was noticed that as C adatoms are deposited onto the surface, graphene islands start to nucleate at a critical concentration c^{nucl} at which point the growth of islands leads to a sudden drop in the concentration of carbon adatoms, see Fig. 52. When the C deposition is turned off the C adatom concentration, $c(t)$, decreases further until it reaches a concentration $c^{eq} = c(t = \infty)$, where an equilibrium is established between the two-dimensional "gas" of carbon adatoms on the surface and the formed graphene islands. It was assumed that c^{eq} has the Arrhenius form,

$$c^{eq} \propto e^{-E_{form}/k_B T} , \tag{16}$$

where the formation energy E_{form} can be found from its measured temperature dependence. Here k_B is Boltzmann's constant and T is the temperature. The change in the excess concentration (proportional to adatom supersaturation) $c(t) - c^{eq}$, over time was determined by observing the graphene coverage from LEEM images. The growth velocity v was also found; this is defined via

$$v = \frac{1}{P}\frac{dA}{dt} \tag{17}$$

where P is the island perimeter and dA/dt is the rate of change of the island area. Note that this growth velocity can only be considered as an order-of-magnitude estimate, as this expression is only valid for circular islands. By assuming that the velocity is proportional to the supersaturation, and that the barrier for a single C atom to attach to an island is much larger than for an attachment of a cluster containing n atoms, the authors obtained an equation for the dependence of the growth on the C adatom concentration:

$$v = m_n(c_n - c^{eq}) = m_n e^{-E_n/k_BT}\left[\left(\frac{c}{c^{eq}}\right)^n - 1\right] = B\left[\left(\frac{c}{c^{eq}}\right)^n - 1\right] , \tag{18}$$

where

$$c_n = e^{n\Delta\mu/k_BT - E_n/k_BT} = \left(\frac{c}{c^{eq}}\right)^n e^{-E_n/k_BT} \tag{19}$$

is the concentration of clusters containing n carbon atoms, and $\Delta\mu = k_BT\ln(c/c^{eq})$ is the excess chemical potential of the adsorbed C atoms. E_n in this expression is an excess free energy of cluster formation, denoted F_{ex} in Section 2.2. By fitting the experimental data to the form of equation (18), n was estimated as 4.8±0.5.

The value found is atypical of normal crystal growth where $n = 1$ (corresponding to growth via attachments of individual atoms). This suggests that intermediate states such as C clusters are indeed involved, which led to the conclusion that in this case the growth of graphene proceeds by the addition of 5 atom clusters, rather than C monomers, to graphene flakes.

Motivated by this result, Zangwill and Vvedensky formulated rate equations for the epitaxial growth of graphene on metal surfaces [334]. Based on the experiments by Loginova *et al.* [54, 92] the flux of the carbon atoms arriving at the surface, F, and the diffusion related constant for their motion across it, D, were used in rate equations for the homogeneous densities of carbon monomers $c(t)$, five atom clusters $c_5(t)$ and graphene islands G. It is assumed that $n = 5$ monomers collide to form a 5 atom cluster and then these clusters move across the surface in correspondence with a diffusion related constant D'. Then it is assumed that j of these clusters collide to form an island of nj carbon atoms. The value of j is decided from the temperature dependence of the carbon adatom concentration, which suggests that $j = 6$. Using these constants the authors determined the rate equations:

$$\frac{dc}{dt} = F - nDc^n + nKc_n - DcG + K'G , \tag{20}$$

$$\frac{dc_n}{dt} = Dc^n - Kc_n - D'c_nG - jD'c_n^j , \tag{21}$$

$$\frac{dG}{dt} = D'c_n^j . \tag{22}$$

Here K and K' are the cluster dissociation rate and the detachment rate of adatoms from the islands, respectively, while D and D' are the corresponding diffusion related constants; c_n is the concentration of $n-$atom C clusters. D, D', K and K' each have the Arrhenius from of $\nu e^{-E/k_BT}$, where E is the energy barrier of the process and $\nu = 2k_BT/h$ is a prefactor assumed to be the same for each of the rate parameters (h is Planck's constant). D, D', K and K' were determined by optimization of the energy barriers while taking into account some natural constraints on their values.

Using $n = 5$ and $j = 6$ the time dependence of c, c_n and G were calculated. The change in adatom concentration $c(t)$ over time determined from the rate equations, and shown in Fig. 52, compares well with the experimental results; however there are discrepancies. The rate equations underestimate the experimental value of the adatom density when graphene nucleation occurs and overestimate the steady adatom concentration after the onset of nucleation. This is thought to be due to the assumption that the densities are homogeneous and there is no spatial information about the locations of the clusters and islands on the surface built into the rate equations. In a recent study [335] a refined rate equation theory was presented which correctly accounts for the temperature dependence of the graphene island density. It was also shown that the values of j between 5 and 7 are almost equally likely.

In order to provide an inhomogeneous description of the attachment processes that accounts for the growth, multi-scale KMC approaches are necessary (section 7.4). These would be based on rates determined from first principles calculations (section 7.2.3 and 7.2.4). But before we enquire into these, let us first discuss available results on atomistic modeling of the early stages of growth which shed light on the relevant nucleation processes preceding the actual growth of graphene islands.

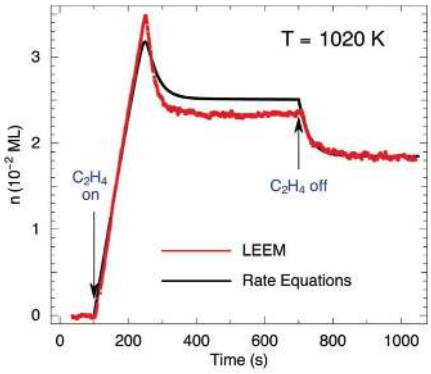

Figure 52: The change in the C adatom density over time as calculated from the rate equations (black line) and determined from LEEM data (red line). [Reprinted with permission from [334]. Copyright (2011) American Chemical Society.]

7.2. Atomistic approaches from first principles

7.2.1. Dehydrogenation

As was discussed in Section 5.3, initial stages of graphene growth rely on the dehydrogenation of hydrocarbon molecules. H atoms presumably detach from the molecules with the transition metal surface acting as catalyst to facilitate the reaction. The adsorbed atomic hydrogens would not desorb from the surface due to strong binding to it. Instead, it is most likely that they would diffuse across the surface until they collide with another adsorbed H atom to form the H_2 molecule which then is easily desorbed. However, it is also clear that the dehydrogenation must be associated not with one but with many competing processes, and that various intermediate species C_xH_y must be present on the surface until the dehydrogenation and desorption of hydrogen is complete and graphene nucleation starts. Although the existing literature related to dehydrogenation of hydrocarbons in the early stages of CVD (TPG) processes is rather scarce, DFT simulations which have been done are reviewed below in this Section, do illustrate the complexity of the processes leading to graphene nucleation.

We shall start with the simplest hydrocarbon which is methane. Its dehydrogenation on the Cu(111) surface was considered in [336] using plane wave spin-polarized DFT calculations in a supercell geometry. All possible adsorption sites on the surface for both the removed H atom and the CH_x species (x = 0 - 4) were considered to find the minimum energy pathway for dehydrogenation. The most favorable sites were used as the initial and final configurations in NEB calculations of the dehydrogenation process. The saddle points along the minimum energy path (MEP) were precisely located, which was confirmed by the existence of a single imaginary vibrational frequency. The energy profile of the chain of dehydrogenation reactions $CH_4 \rightarrow CH_3{+}H \rightarrow CH_2{+}2H \rightarrow CH{+}3H \rightarrow C{+}4H$ is shown in Fig. 53. Also in the Figure one can see the relative energies of the initial, final and all intermediate configurations and the corresponding energy barriers. The dehydrogenation reactions are all endothermic with the calculated energy barriers lying between 0.94 and 1.84 eV. The energy of the final state corresponding to the adsorbed C and four H atoms is 3.2 eV less favorable than the gas-phase CH_4 molecule and the Cu(111) surface, so at first glance the complete dehydrogenation of the methane molecule seems to be highly unfavorable on this surface. However, when the final state was compared with the energy of an adsorbed C_2 molecule, a reduction of 1.5 eV was found, see Fig. 53. This result led the authors to argue that forming carbon dimers on the surface after complete methane dehydrogenation must be an essential step in graphene nucleation; moreover, it was also speculated that formation of larger C_n ($n > 2$) carbon clusters on the surface would result in even larger energy gains and hence would be essential in understanding the kinetics of graphene growth.

The same system was independently considered also in [209]. The initial, final and transition states for each stage of the dehydrogenation reaction are shown in Fig. 54(a), and the complete energy profile in Fig. 55 (black curves). As can be seen by comparing this energy profile with the one shown in Fig. 53, the general picture is basically confirmed: the process of dehydrogenation alone leads to a highly energetically unfavorable state; each H dissociation step is endothermic and has an energy barrier between 1.0-2.0 eV, and hence complete dehydrogenation of methane is unfavorable on the Cu(111) surface. It was concluded from these calculations, and quite rightly, that various C_xH_y species must be present on the surface at the

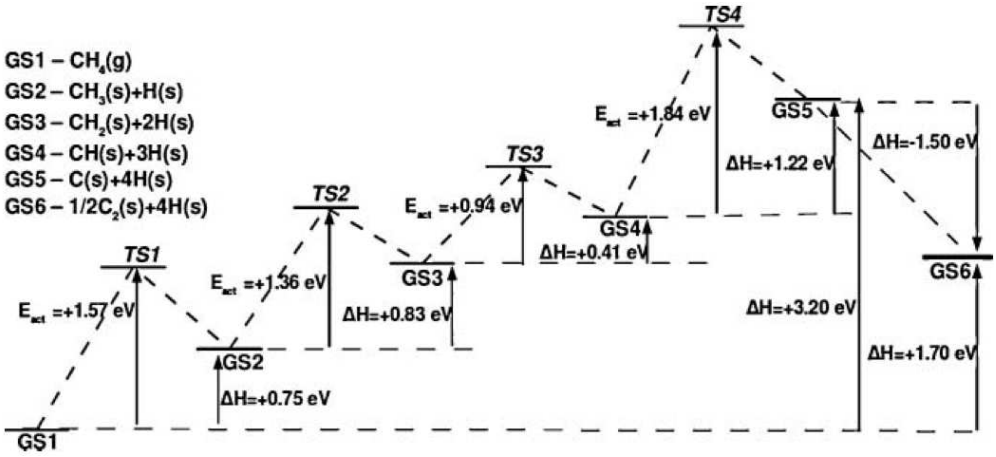

Figure 53: The energy profile of the complete dehydrogenation process of methane on the Cu(111) surface with subsequent formation of C_2 species (C dimers). [Reprinted with permission from [336]. Copyright (2011), AIP Publishing LLC.]

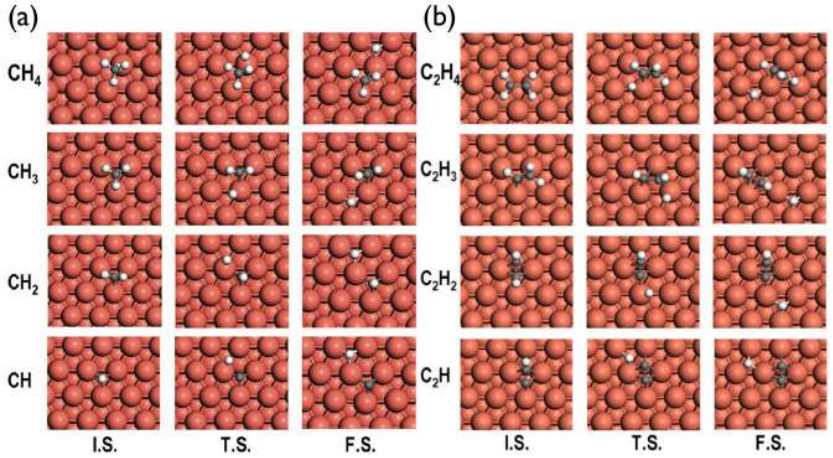

Figure 54: The structures of the initial (I.S.), transition (T.S.) and final (F.S.) states corresponding to the processes leading to complete dehydrogenation of (a) methane and (b) ethene on the Cu(111) surface. The red, white and grey spheres represent Cu, H and C atoms, respectively. [Reprinted with permission from [209]. Copyright (2011) American Chemical Society.]

same time: since dehydrogenation is not favored, coalescence reactions involving various species must be favored, leading to a rich variety of carbon-containing species on the surface. Indeed, it was found that the reaction CH+CH $\rightarrow$ C_2H_2 is exothermic by 1.94 eV with the energy barrier of only 0.3 eV. The attachment of additional CH in the reaction C_2H_2+CH $\rightarrow$ C_3H_3, although leading to 0.98 eV energy gain (i.e. is also exothermic), required a higher energy barrier of 1.1 eV. The authors also considered the Cu(100) surface, see again Fig. 55 (red curves), and arrived at the same conclusions. Complete dehydrogenation of ethene was studied as well in [209] leading to qualitatively similar conclusions: during the four dehydrogenation steps required to fully decompose the molecule into a C_2 (dimer) and four H atoms, the system energy increases by 0.48, 0.09, 0.67, and 0.62 eV, respectively.

We have seen above that direct dehydrogenation, at least on the Cu(111) surface, may be highly unfavorable, and that other reactions such as hydrogenation, may take place leading to a high likelihood of having a complicated mixture of various carbon-containing species on the surface during nucleation and growth. In fact, one can say with certainty that the actual kinetics of these reactions is quite complicated, and the models considered so far must be highly oversimplified. This conclusion can be made from the analysis of existing literature [337, 338, 166, 339] on the initial stages (Section 5.3) of ethene decomposition into ethylidyne CH_3C (or C_2H_3). The complete scheme of all reaction paths is shown in Fig. 56. The conversion of ethene into ethylidyne was suggested to occur by several different and competing mechanisms, composed of

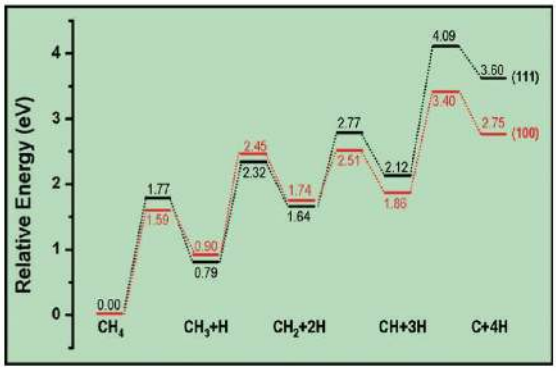

Figure 55: The energy profile of the complete dehydrogenation process of methane on the Cu(111) (black) and Cu(100) (red) surfaces. [Reprinted with permission from [209]. Copyright (2011) American Chemical Society.]

a sequence of hydrogenation, dehydrogenation and (possibly) isomerization steps in various orders. For all elementary reactions the corresponding energy barriers have been calculated using DFT [337, 338, 166, 339] which gave the complete set of all required transition rates.

However, as is stressed in [337], one cannot assess the preferred reaction path just on the basis of energy barriers (rates) as other factors such as availability of intermediate species (such as hydrogen) should be taken into account as well. This has been done in [337] using a KMC approach. It is based on considering ethene molecules on the surface with subsequent conversion reactions taking place according to the scheme of Fig. 56. In the case of hydrogenation reactions the reactant should be located in neighboring positions. Diffusion of molecules on the surface between reaction events was considered approximately by assuming a force field describing inter-molecular interactions and a local equilibrium which was accomplished by moving the molecules using a set of MC steps.

Simulations of the conversion of ethene to ethylidyne on Pt(111), Pd(111) [337, 166] and Rh(111) [338] surfaces demonstrated that the dominant mechanism is through vinyl and vinylidene, i.e. via a sequence of direct dehydrogenation reactions. For the Pt(111) surface the rate limiting step was the hydrogenation of the vinylidene to C_2H_3. Despite hydrogenation reactions having lower energy barriers than dehydrogenation reactions, the lack of atomic H adsorbed on the surface results in a low probability for this process to occur. On the Pt(111) surface it was found that the adsorbed H from dehydrogenation of ethene is mainly lost through H_2 production. In the case of Pd(111) the rate limiting process is the initial dehydrogenation of ethene. Due to these differences in the limiting process, the conversion of ethene into C_2H_3 was calculated to begin at a temperature of around 230 K on Pt(111), but is not complete until reaching 325 K.

It is clear that full consideration of the conversion of a given hydrocarbon feedstock into graphene, as suggested by TP-XPS experiments described in Section 5.3, would contain many more reaction paths and intermediates, and this would require a rather sophisticated and detailed modeling. This kind of modeling must not only rely on the calculations of energy barriers, but must also be based on the time evolution of all species involved which must take into account their diffusion across the surface. This kind of modeling can only be achieved using KMC type of approaches which are based on the spatial distribution of reactants and products over the surface, the stochastic nature of their diffusion and reactions between them requiring surmounting potential energy barriers. Such future modeling should also take into account a finite probability of C-C bond scission which would be possible at the high temperatures at which graphene is normally grown using TPG or CVD methods. As a result, one would be able to consider the actual distribution of carbon clusters C_n with $n \geq 1$ on the surface as a function of the given feedstock used in the given experiment.

7.2.2. Carbon monomers and dimers on metal surfaces

Before discussing stability and other properties of carbon clusters of different sizes adsorbed on metal surfaces, which is obviously related to the first stages of graphene growth, we shall first review theoretical studies in which monomers and dimers at different sites on the metal surfaces were investigated [278, 208, 340]. This may give us some essential information regarding the nucleation of graphene on a surface.

Recently Riikonen *et al.* [208] examined the adsorption energy of monomers and dimers at different

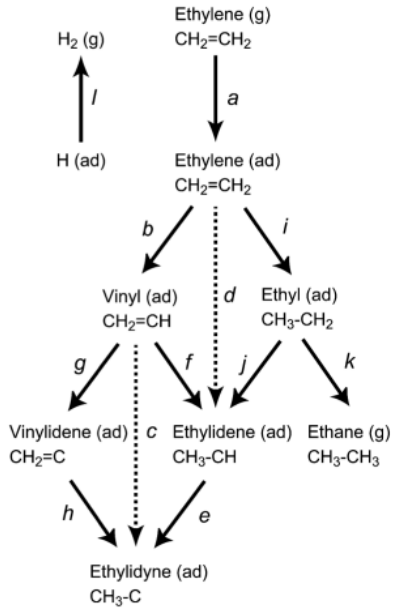

Figure 56: The different reaction mechanisms of ethene conversion to ethylidyne C_2H_3 on the Pt(111) and Pd(111) surfaces. Arrows pointing to the left and right indicate dehydrogenation and hydrogenation steps, respectively, while the dashed line arrows show possible isomerization routes. Down and up arrows represent adsorption and desorption, respectively. [Reprinted from [337], with permission from Elsevier.]

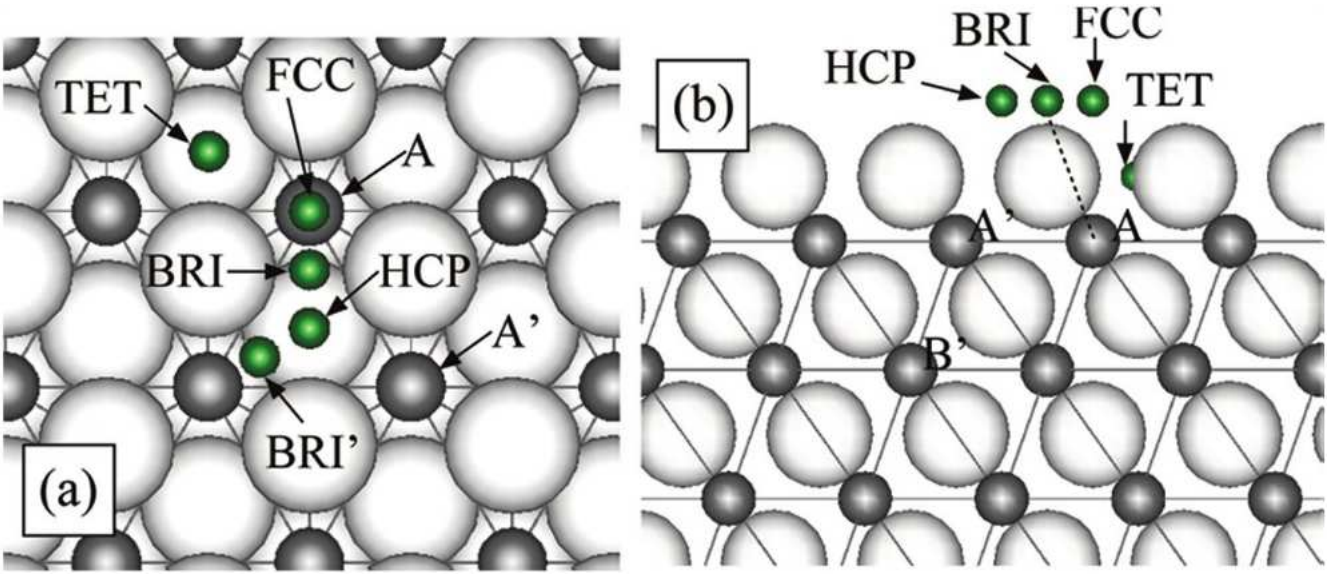

Figure 57: Various adsorption sites on the Cu(111) surface: (a) top and (b) side views. [Reprinted with permission from [208]. Copyright (2012) American Chemical Society.]

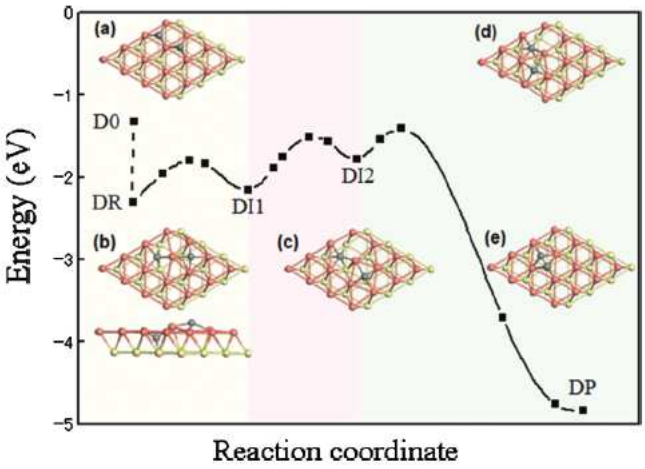

Figure 58: Calculated dimerization process path (a)-(e) showing formation of a dimer (e) on the Cu(111) surface from two monomers sharing the same Cu atom (a). Several intermediate states were found along the minimum energy path. [Reprinted with permission from [341]. Copyright (2010), AIP Publishing LLC.]

lattice sites, both on and below the surface of Cu(111), see Fig. 57. They also calculated the diffusion barriers of monomers between different equilibrium surface and bulk sites. Before discussing a number of interesting conclusions regarding the initial stages of nucleation on Cu(111) made in their study, it is interesting to mention an important technical point. The authors noted that energies may depend strongly on the simulation cell size: for instance, the C atom migration barrier obtained using a larger supercell was found to be almost 0.5 eV smaller than the previously reported value obtained using a smaller sized cell.

The most stable position found in [208] for a carbon monomer on Cu is the bulk interstitial site, referred to as A and A′ in Fig. 57. The surface sites labelled BRI, FCC and HCP are found to be metastable with respect to adsorption of a single C atom as it would quickly diffuse (with the barrier of the order of 0.1 eV) from these into either the A or A′ site. The diffusion deeper into the Cu bulk (A′ →B′) was found to require the crossing of an energy barrier of at least 1.5 eV in height. The formation of dimers from two carbon atoms lying on several nearby surface sites was found to require no activation energy, i.e. dimerisation is spontaneous. Further, the diffusion barrier they calculated for a dimer was found to be very small (0.27 eV). Thus, the energy required to dissociate a dimer is found to be actually larger than the diffusion barrier between different adsorption sites. This suggests that dimers are a persistent species and could possibly dominate the nucleation of larger carbon structures that eventually form graphene.

In a similar manner to the above study, Chen *et al.* [278] investigated the stability of monomers at different sites on the surfaces of Ru(0001), Ir(111) and Cu(111). The most stable sites on Ru and Ir were both found to be the HCP sites, with adsorption energies of -7.66 and -7.44 eV, respectively. In agreement with the results of Riikonen *et al.* [208], the most stable absorption site on Cu(111) was found to be the subsurface octahedral (A and A′ in the notation of Riikonen *et al.*. On both Ir and Ru similar values were obtained for the adsorption energy at step edges and it was also found that while the barrier for dimer formation is relatively high, 1.37 and 1.49 eV respectively, on Cu(111) the barrier for dimerization is much lower, 0.32 eV. The authors also found that the energy required to form a dimer is greatly reduced on Ru and Ir when dimerization occurs at a step edge. They further suggest that these results could possibly explain the observations of heterogeneous nucleation at step edges on Ir and Ru. Since the formation energy of dimers on the Cu(111) surface is so low, it was also suggested that nucleation on weakly interacting metals (like Cu) should occur homogeneously. On metals with a stronger C-metal bond the above results for dimer formation at step edges would mean that nucleation is more likely to occur at steps, i.e. heterogeneously. However, as noted by Wang *et al.* [251], while these results would predict that nucleation on Rh(111) would occur predominantly at steps, this was found not to be the case. Further, islands with different morphologies growing on Cu(111) have been found to exist predominantly at step edges and other defect sites [266].

A study by Wu *et al.* [341] used both DFT and MD to investigate steps in the reaction sequence describing dimer formation that had not previously been considered. Their work is based on the following observation:

while it is indeed true that spontaneous dimerization occurs when two atoms are placed on nearest neighbor sites, there are intermediate states that must occur before monomers occupy these sites. These states are derived by considering the beginning of the dimerization process with two monomers occupying next nearest neighbor sites, which share a common Cu atom. Relaxation of this state leads to the formation of novel structures shown in Fig. 58(b)-(d) which manifest themselves on the potential energy surface as metastable minima. The change in the activation barrier that occurs by considering these intermediate states in dimerization and other reaction sequences could be important in calculating the rates of processes occurring on the surface.

7.2.3. Early stages of growth: small C clusters

The phenomenological model described in Section 7.1 indicates that the nucleation of graphene islands could begin with the collision of a number of small clusters and indeed, several experimental papers reported relatively small carbon precursors present on the surfaces of Rh(111) [251] and Ir(111) [139]. Theoretical efforts have mostly relied on using DFT to examine the stability of various structures on different surfaces. In some studies thermodynamic models of nucleation are used to try and speculate on the minimum sizes of clusters that would be stable on a surface at a specific temperature and supersaturation. We now review a selection of papers that look at this aspect of growth theoretically.

The transformation of carbidic species to free-standing graphene has been explored by Lacovig *et al.* [139]. They compared the temperature dependence of surface core level shifts between 10^{-6} and 10^{-9} mbar at 300 K and subsequent annealing to 820, 970 and 1270 K, see Fig. 59. These spectra allowed the authors to deduce that three different carbon species, referred to as C_A, C_B and C_C, each interacting differently with the Ir surface, are present during growth. Further, the change in spectra with increasing temperature indicates that the number of these C species is temperature dependent. To explain these observations the authors performed a number of DFT calculations, relaxing carbon clusters of different sizes on an iridium surface after a simulated annealing procedure (this is a way to approach a global energy minimum in a system, i.e. the most energetically favorable structure: MD simulations are run starting at rather high T with subsequent slow cooling down to zero). The structures they obtained were distinctly "dome-like." The interactions between substrate and cluster were limited to carbon atoms found at the cluster edge, and a relatively large distance between central atoms of the clusters and the surface was found. This distance was seen to increase with the size of carbon clusters. Comparison of the surface core level shift (SCLS) obtained from simulations with those obtained experimentally allowed the authors to identify the three carbon species as belonging to cluster edges (C_A and C_C) and to the central carbon atom (C_B). The temperature dependence of the SCLS was then explained as follows: high temperature ripening processes occurring on Ir [61] cause the average size of carbon cluster to increase. Increasing cluster size causes the relative number of edge sites C_A and C_C to decrease while the amplitude of the peak in the C $1s$ spectrum associated with the central C_B species increases towards that found in graphene.

Similar carbon clusters have been identified on Rh(111) [251], Ru(0001) [275], and Ir(111) [61]. In a study by Yuan *et al.* [342] different sized carbon clusters C_N with $N = 16, \ldots, 26$ on the Rh(111), Ru(0001), Ni(111) and Cu(111) surfaces were explored using *ab initio* DFT calculations. The formation energies of these clusters were calculated as a function of N by determining the difference between the energy of the supported clusters and the energies of N carbon atoms in the free standing graphene (i.e. presumably using Eq. (5) with μ_C being the energy of a C atom in free-standing graphene). The results of these calculations are shown in Fig. 60(a).

There is a clear valley for all the surfaces around size $N = 21$. For the second derivative of the formation energy, $\Delta_2 E$, shown in Fig. 60(b), there is also a maximum for C_{21} and C_{24}. Therefore it is deduced, as previously shown in experiments [275, 61, 251], that both these cluster sizes are stable on the surfaces. This is in part attributed to their high symmetry and the tendency of the graphene edges to stand at some tilting angle to the metal surface; the latter explains the dome-like shape of most studied compact clusters. Fig. 60(c) and (d) show the DFT relaxed models of the C_{21} and C_{24} clusters, respectively, on the Rh(111) surface. Taking into account the substrate, the C_{21} cluster has $C_{3\nu}$ symmetry, whereas the C_{24} cluster is rotated by $\sim 15^\circ$ from the high symmetry position and therefore has a lower C_3 symmetry. A comparison of calculated STM images of the clusters (using the Tersoff-Hamann approximation [45]) with the experimental images, all shown in Fig. 60(e-h) and (i,j), respectively, clearly demonstrates that the C_{21} cluster must be the dominant species on the Rh(111) surface as only its image matches well the experimental one at both bias voltages. To

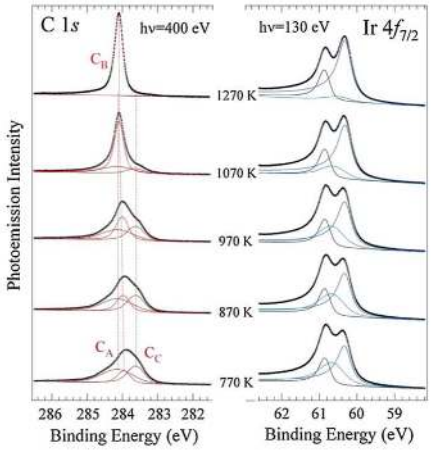

Figure 59: C 1s (left) and Ir $4f_{7/2}$ (right) spectra after annealing at different temperatures of the Ir(111) surface saturated with C_2H_4 at 300 K. The spectra were measured at 300 K. The different components represent inequivalent C and Ir atoms. [Reprinted with permission from [139]. Copyright (2009) by the American Physical Society.]

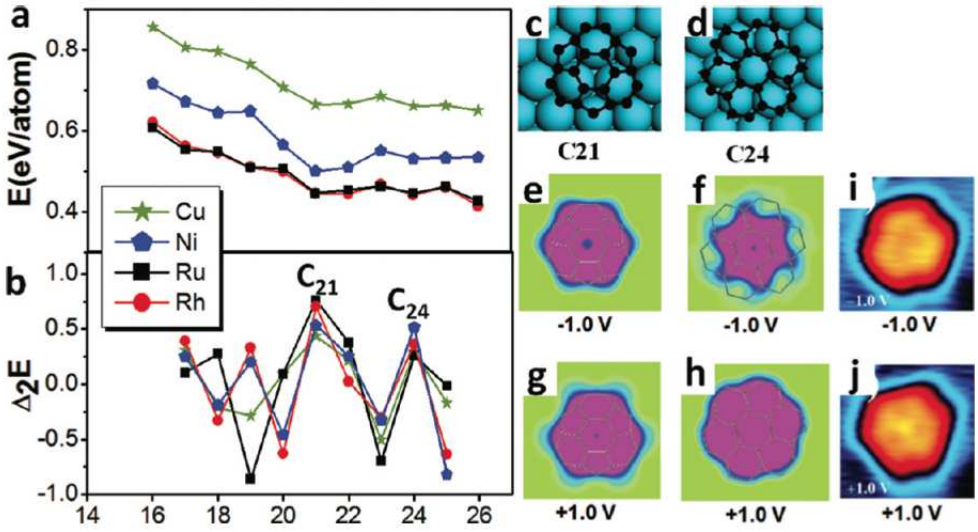

Figure 60: (a) The formation energies of carbon clusters C_N on Cu(111), Ni(111), Ru(0001) and Rh(111) with $N = 16, \ldots, 26$ and (b) the second derivative of the energy with respect to N. Top view images show (c) the C_{21} and (d) the C_{24} clusters on a Rh(111) surface. Calculated STM images of the (e,g) C_{21} and (f,h) C_{24} clusters for negative and positive bias voltages, and the corresponding experimental STM images of the most abundant carbon cluster (i,j). [Reprinted with permission from [342]. Copyright (2012) American Chemical Society]

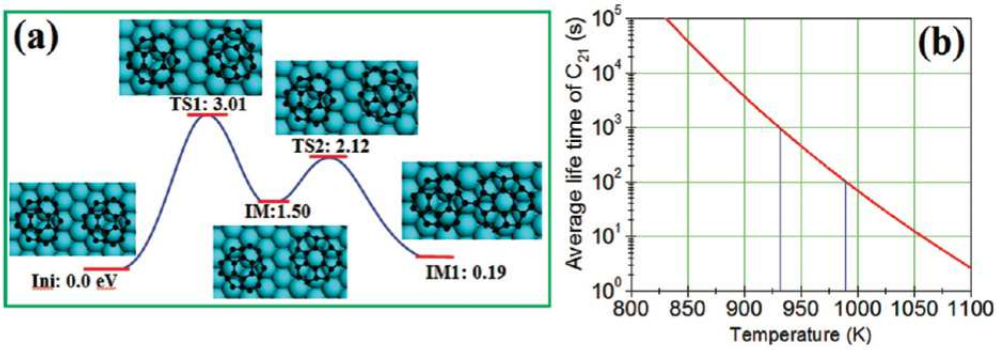

Figure 61: (a) The kinetic process of the dimerization of two C_{21} clusters on a Rh(111) surface and (b) the average lifetime of C_{21} on Rh(111) as calculated from the highest energy barrier in (a). [Reprinted with permission from [342]. Copyright (2012) American Chemical Society.]

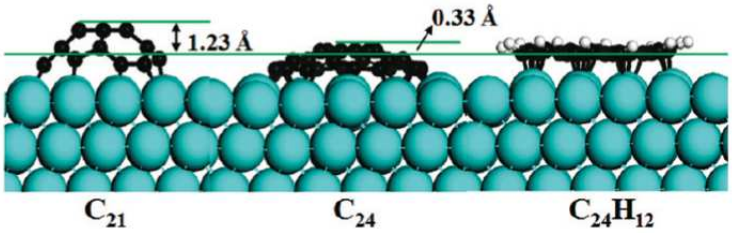

Figure 62: Side view images of the structure of the C_{21} and C_{24} clusters and coronene molecule $C_{24}H_{12}$ on the Rh(111) surface. The heights of the clusters with respect to the coronene molecule are also shown. [Reprinted with permission from [342]. Copyright (2012) American Chemical Society.]

explain the high stability of this particular "magic" cluster size, the authors note that its formation energy, as seen in Fig. 60(a), is the smallest amongst all smaller clusters ($N < 21$) and, at the same time, it is also smaller than that of the next $N = 22$ cluster. More or less the same is true for the C_{24} cluster, however, as it is larger, the C_{21} would be formed first and hence must be in relative abundance.

To understand formation of graphene islands from those clusters and estimate their lifetime, the authors studied their coalescence using a NEB like technique. The transition path involved several steps with the highest energy barrier ΔE during the dimerization process, shown in Fig. 61(a), calculated as 3.01 eV. From this the lifetime of the C_{21} cluster was estimated using a simplified transition-state theory [222] expression: $\tau = (h/k_B T)\exp(\Delta E/k_B T)$, where h is the Planck constant. In Fig. 61(b) it can be seen that in the temperature range of 930 - 985 K the lifetime is 100 - 1000 s. This agrees with the experimental observations that the coalescence of clusters into graphene islands occurs at ∼870 K on Rh(111) [251], at 1000-1100 K on Ru(0001) [275] and at 970 K on Ir(111) [57].

The high stability of these clusters is suggested to be due to the strong binding of their edge atoms to the surface [139, 251]. The side views of the clusters structures are shown in Fig. 62. The strong edge binding causes the islands to be dome-shaped which elevates their height above the surface when compared with the coronene molecule (which is basically a hexagonal C_{24} cluster in which all border C atoms are terminated by hydrogen atoms). The C_{21} cluster was calculated to be ∼1.2 Å higher off the surface than coronene and the C_{24} cluster is 0.3 Å higher. Overall it is concluded that formation of these clusters is not ideal for producing high quality graphene. This is because their lack of mobility is suggested to lead to the formation of a high concentration of small graphene islands. When these coalesce grain boundaries will form and the graphene quality will be reduced.

In the work of Wu *et al.* [343] the relative stability of small carbon species (clusters) on the Ir(111) surface was calculated with DFT. The stabilities of different clusters were compared by calculating their "potential energy"

$$E_p = \left(E_{C/Ir} - E_{Ir}\right)/N \,, \tag{23}$$

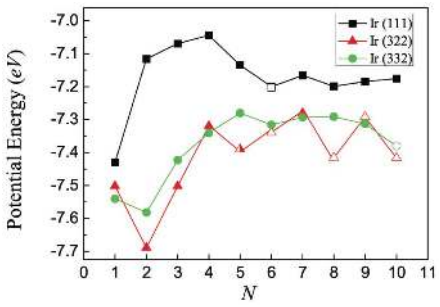

Figure 63: The calculated potential energy, Eq. (23), for different carbon species C_N on the Ir(111) surface and at the Ir(322) and Ir(332) steps. [Reprinted with permission from [343]. Copyright (2012) American Chemical Society.]

which is in fact the formation energy (per C atom) calculated relative to the energy of an isolated cluster C_N (i.e. in the gas phase). Here $E_{C/Ir}$ is the total energy of the cluster of N atoms on the Ir surface, and E_{Ir} is the energy of the surface. A stability comparison was performed in order to determine how different carbon species C_N with $N = 1, \ldots, 10$ are likely to evolve on the surface. The most stable site for carbon monomers to adsorb onto the surface was calculated to be the hollow hcp site, followed by the fcc site. For small carbon clusters the most stable formed structure is usually a chain structure, formed between two carbon atoms that both occupy an hcp site. Compact structures can also be formed, which are often dome-shaped. These are less stable than chains when the cluster size is small, but the compact structure stability increases with size. Results from the calculations, shown in Fig. 63, demonstrate that C monomers are more stable on the Ir(111) surface terraces than larger C clusters (the black line) and should therefore occur more frequently. Also, clusters of 5 atoms, C_5, were also identified as relatively stable on terraces meaning that their role in growth is expected to be significant. This is in accord with observations made in the LEEM study of Loginova *et al.* [54, 92]. The authors also considered C clusters placed near Ir(322) (red) and Ir(332) (green) steps and found them on average to be more stable than the same clusters on the terrace, Fig. 63. Interestingly, the dimer at step edges is more stable by about 0.2 eV than a monomer. These calculations suggest that C monomers and clusters migrating on the surface would eventually end up at step edges; in particular, migrating monomers may preferentially form dimers at steps. This conclusion is also supported by the calculated diffusion barriers for C_N species ($N = 1, 2, 3$) using the NEB method which were found to be in the range of 0.4-0.8 eV; these are thought to be perfectly accessible at the elevated temperatures used for graphene growth. Interestingly, some of the clusters diffuse atom-by-atom (e.g. C_2), but a concerted motion is the preferred mechanism for three-atom clusters; chains diffuse in a more complex manner by moving parts of their "bodies" at a time. Higher barriers were found for incorporation of a C atom into a cluster (1.42 eV) or a chain (0.86 eV), and a combination of two neighboring monomers required a 1.44 eV barrier to be overcome in order to coalesce. Generally then, diffusion of clusters and monomers is easier than their coalescence.

The formation energies of different optimized carbon clusters on Ni(111) were calculated using DFT in [206]. The formation energy was defined using Eq. (5) with μ_C being taken to be the energy of a C atom in a free standing graphene. The authors examined a number of different cluster structures that can be formed from a certain number of carbon atoms, $N = 1, \ldots, 24$. Various cluster types with the same N were systematically explored including chains, rings and sp^2-networks (the closest analog of the graphene-like structure) on the terrace of the Ni(111) surface with their formation energies shown in Fig. 64 as a function of N. It was shown that, as expected, the presence of a transition metal surface causes the energy of formation of linear chains to be greatly reduced, largely due to the saturation of the dangling bonds present at the free ends of the linear chains. Surprisingly, if graphene-like clusters (with the most hexagons) are the most favorable in the gas phase, on the surface these structures are less favorable then ones which have one to three pentagons. The authors explain this by the interaction with the metal which is sensitive to the number of edge atoms of the clusters. It follows from Fig. 64 that sp^2 networks for $N \preceq 12$ are less favorable than chains; however, this situation changes for larger N values and the sp^2 network structures become the most energetically favorable as one would expect.

Similar results were obtained on Cu(111) by Wesep *et al.* [207]. They also used DFT to compare the

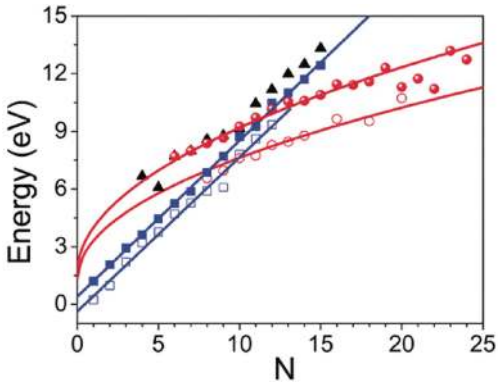

Figure 64: Calculated formation energies of N atom clusters on the terrace (solid symbols) and near the step (empty symbols) of the Ni(111) surface. Squares, triangles, and circles correspond to C chains, rings and sp^2 networks, respectively. Lines correspond to the fitting to analytical expressions. [Reprinted with permission from [206]. Copyright (2011) American Chemical Society].

formation energies (stabilities) of a number of different carbon clusters on the terraces and like [206] found that for $N < 13$ the most stable structures were chains of carbon atoms. The details of the structure of the clusters they studied on the surface are shown in Fig. 65. The chains of atoms can be seen to "arch" away from the surface, with the height of the middle atoms in the chain increasing with N. Wesep *et al.* [207] also examined the energy required to break a six member ring using the climbing image NEB (CI-NEB) method, and found a surprisingly low breakup energy of 0.66 eV. Thus, at the early stages of growth chains with $N < 13$ will be the dominant species on Cu(111). However, because removal of a C atom from islands larger than $N = 10$ would require at least two bonds to be broken, these clusters become more long-lived since it gets increasingly more difficult to break them up; correspondingly, the surface will likely end up being dominated by islands of $N = 10$ or 13 atoms.

The authors in [207] ignored steps in their consideration of the nucleation of graphene on Cu. Although this assumption was motivated by a theoretical study suggesting that nucleation on terraces should be dominant on Cu(111), recent experimental observations suggest that this might not be entirely correct [266]. Gao *et al.* [206] on the other hand repeated their calculations for structures on terraces, discussed above, but allowed carbon atoms to bond to a (110) Ni step edge. It was found that the formation energies E_N of N atom clusters close to the step edge decreased (by as much as 2 eV for $N > 12$), see Fig. 64, and it was also observed that for $N \succeq 12$ sp^2 network structures (those which are closest to that in graphene) become the most stable.

The calculated values for the formation energies of different clusters allowed the authors to apply the ideas of classical nucleation theory to estimate the nucleation barrier, $\Delta F^* = \Delta F(N^*)$, and critical nucleus size, N^*, for different values of $\Delta\mu$, the difference between the C atom chemical potentials in the carbon cluster and in the carbon feedstock. The ΔF^* and N^* were obtained by considering the maximum of the free energy function

$$\Delta F = E_N - N\Delta\mu \tag{24}$$

with respect to N. Comparing this with equation (1), notice that the entropic contributions to the right hand side are ignored: this is a common approximation employed when considering solid structures. The quantity E_N should correspond to the energetic part of the excess free energy of cluster formation. The calculated dependences, both for the case of the clusters on the terrace and near the step edge, are shown in Fig. 66. One can see that across almost the whole range of $\Delta\mu$ values studied, the nucleation barrier and the critical nucleus size are smaller at the step edge than on the terrace. Next, there is a region of $\Delta\mu$ where the nucleation barrier decreases linearly, but the critical cluster size is fixed at $N^* = 12$ and 10 for the terrace and step, respectively. For $\Delta\mu > 0.81$ eV the barrier drops to 0.2 eV, while $N^* \simeq 1$, implying that nucleation may occur from practically any cluster size, and hence the process of growth will be controlled by the rates of C deposition and diffusion on the surface. The authors believe, however, that this regime of rather high $\Delta\mu$ is less likely to arise during the CVD growth of graphene. In the other extreme of small $\Delta\mu$ values the

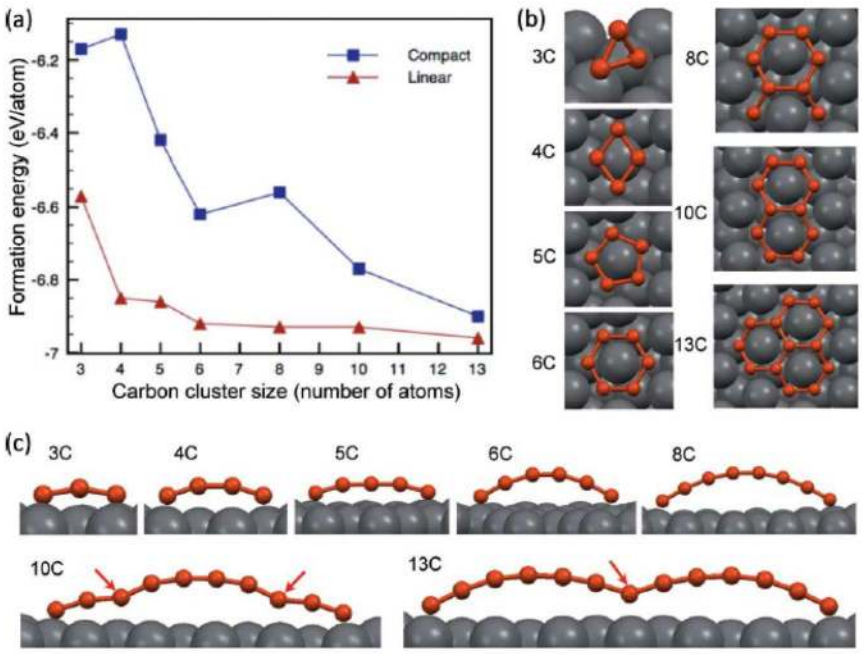

Figure 65: (a) The formation energies of the most stable ring and linear chain structures on Cu(111) with the corresponding structures shown in (b) and (c). [Reprinted with permission from [207]. Copyright (2011), AIP Publishing LLC.]

barriers and critical nucleation sizes are so large that it is concluded that nucleation is unlikely to occur in this supersaturation region. Consequently, the nucleation rate, calculated from the classical nucleation theory [37] (Section 2.2) as

$$R_{nucl} = R_0 \exp\left(-\Delta F^*/k_B T\right) \ , \tag{25}$$

rapidly increases with $\Delta\mu$, demonstrating extremely sensitive behavior to both T and $\Delta\mu$, with the nucleation rates at step edges being consistently larger than those on the terrace. At the same time, the authors warn that these results may not necessarily mean that nucleation starts at steps in all regions of the parameter space as the effective area at steps is much smaller than that at terraces. For instance, nucleation may be preferable at terraces for large values of $\Delta\mu$. Since in the parameter regions of large nucleation rates many nuclei would start forming at the same time, leading over time to coalescing graphene flakes with grain boundaries (which are not desirable for a high quality graphene), the regimes of relatively low R_{nucl} are preferable. The authors conclude that this regime is achieved at lower T and with $\Delta\mu$ in the region of 0.3-0.5 eV.

In a similar spirit, in order to understand better the driving force of graphene nucleation on the Cu(111) surface, thermodynamic considerations have been proposed in [209] based on the fact that both a carbon feedstock and the hydrogen gas are added simultaneously when growing graphene on Cu foils [281]. In the case of methane the chemical potential of C atoms in the methane gas above the surface (which is in equilibrium with H_2 gas as well) is given by (in eV)

$$\mu_C = -2\mu_H - 10.152 + 0.112 \ln \chi \ ,$$

where μ_H is the chemical potential of H atoms and $\chi = P_{CH_4}/P_{H_2}$ is the ratio of the partial pressures of the two gases. Both chemical potentials are functions of their partial pressures and temperature. On the other hand, one can calculate the chemical potentials μ_{C_N} of various carbon clusters C_N on the surface ($N \geq 1$) including carbon atoms ($N = 1$), and compare them with μ_C in the gas phase. If $\mu_{C_N} > \mu_C$ for the given ratio of pressures χ and temperature T, then the cluster C_N is deemed unstable and would decompose with subsequent reaction of C atoms with hydrogen to form methane, which desorbs from the surface into the gas phase. If however $\mu_{C_N} < \mu_C$, then the cluster C_N must be thermodynamically stable on the surface. One can see from the yellow area in Fig. 67(a) (shown for $\chi = 1$) that atomic carbon is indeed highly unfavorable at the typical pressures (the vertical line); however, the chemical potential of a carbon atom in a cluster C_6

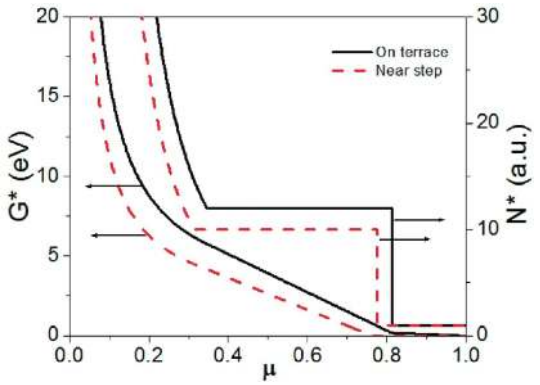

Figure 66: Calculated nucleus size, N^*, and nucleation barrier, here denoted G^*, as functions of the difference $\Delta\mu$ of the carbon chemical potential in clusters and in the C source. [Reprinted with permission from [206]. Copyright (2011) American Chemical Society.]

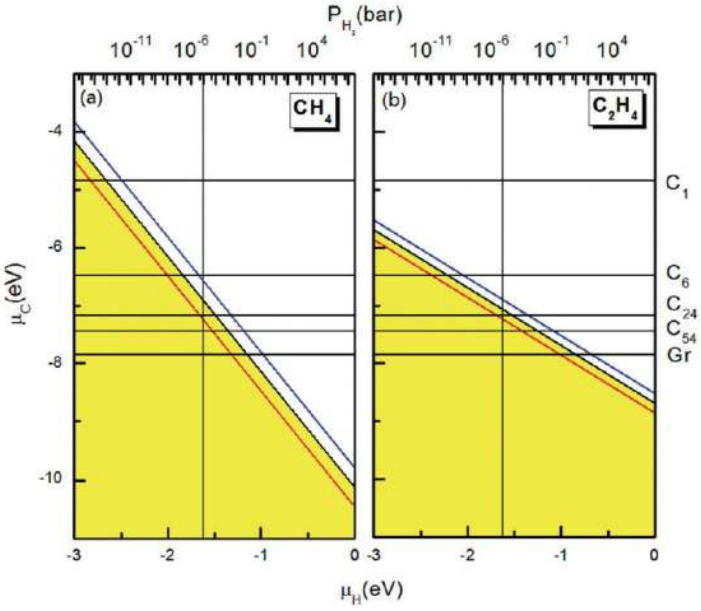

Figure 67: The relationship between the chemical potential of C and H for CVD growth on the Cu(111) surface at 1300 K with (a) methane and (b) ethene precursors. Different ratios of the partial pressures of CH_4 and H_2, $\chi = 1$, 20 and 1/20, are indicated by black, blue and red straight lines, respectively. A typical partial pressure of hydrogen gas in shown by a vertical line in each case. Horizontal lines indicate calculated chemical potentials of carbon atoms in clusters C_N with $N = 1, 6, 24, 54$; the carbon chemical potential of graphene on Cu(111) surface is also indicated as "Gr". [Reprinted with the permission of [209]. Copyright (2011) American Chemical Society.]

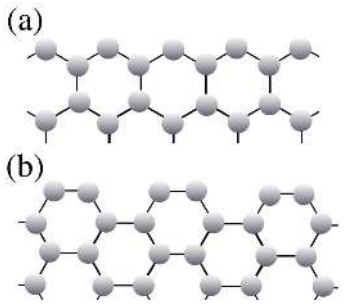

Figure 68: (a) Zigzag (ZZ) and (b) armchair (AC) edges of a graphene ribbon.

(calculated in a usual way and with respect to an isolated C atom in vacuum) becomes very close to μ_C. Increasing the number of carbon atoms in the adsorbed clusters results in the chemical potentials of their C atoms getting more negative, indicating their eventual stability on the surface starting from some critical size.

Similar consideration has been made for ethene as a feedstock as well, in which case

$$\mu_C = -\mu_H - 8.692 + 0.056 \ln \chi \ ,$$

with the corresponding stability diagram shown in Fig. 67(b). In this case it is noticed that the critical value μ_C of the carbon chemical potential is less sensitive to the ratio of partial pressures χ.

Controlling the nucleation size of carbon clusters is essential in growing graphene of sufficient quality and size. The considerations above demonstrate that reducing the partial pressure of the feedstock for a given hydrogen pressure (smaller χ) increases the rate of nucleation, but lowers the nucleation density. This creates higher quality graphene.

7.2.4. Atomistic Attachment Processes

Various carbon species that might serve as nuclei in the early stages of graphene growth have been discussed in the previous section. Once the graphene nucleus is formed, further growth will depend, in particular, on the structure of the graphene flake boundary (edge). Hence, determination of the most stable edge structures is a vital step in modeling graphene growth. A DFT investigation into the most stable edge structures on Ru(0001) [344] found that the zigzag (ZZ) edge is the most stable whereas on Cu(111) [345] the armchair (AC) structure passivated by Cu atoms from the bulk was shown to be preferred. Both edge terminations are illustrated in Fig. 68. It is essential to note the importance of the substrate in stabilizing particular edge configurations: the pentagon-heptagon termination being the most energetically favorable edge structure in vacuum is usually the least favorable on most metal surfaces used for graphene growth [346]. DFT studies were also conducted into the attachment of different species onto the edge of a graphene flake on Cu(111) [345], Ir(111) [343] and Ni(111) [346].

We shall start by mentioning recent calculations by Haghighatpanah *et al.* [204] in which the catalyst-free graphene ZZ and AC edges (i.e. free standing) and attachment of C atoms to them were considered. The authors used both DFT and tight binding (TB) models to describe the attachment energetics. A complete hexagon is formed after adding 3 atoms to the ZZ and 2 to the AC edges. After each C atom is added a geometry optimization follows. The formation energy for each of the structures is calculated from

$$E_f = E_{G/C} - E_G - N\mu_C \ , \tag{26}$$

where $E_{G/C}$ is the energy of the graphene ribbon with N carbon atoms attached to it, E_G is the energy of the isolated graphene ribbon and μ_C here denotes the energy of a single C atom.

For both the DFT and TB methods the energy decreases (becomes more negative) as C atoms are added, with the new atoms finally forming a stable low-energy hexagon structure in each case; obviously, the energy is gained every time a C atom is attached to the edge. These preliminary calculations were done to test the TB model parametrization intended for subsequent MC simulations of growth (unthinkable with DFT) which we shall discuss later on in Section 7.4. The comparison of the two methods shows that in the DFT calculations

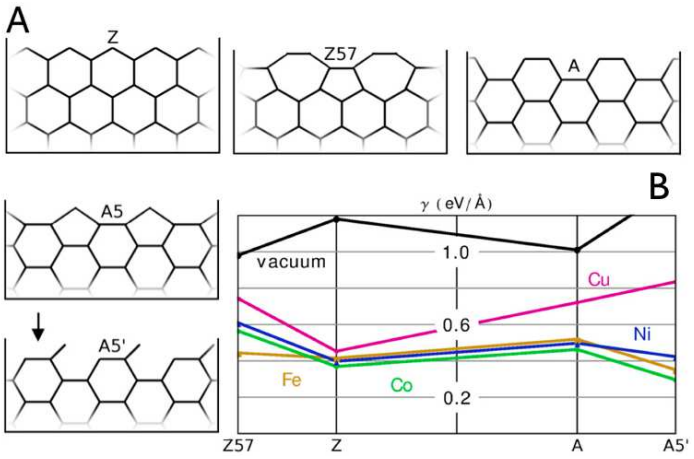

Figure 69: (A) Schematics of graphene edge structures: Z (zigzag), Z57 (pentagon-heptagon), A (armchair), A5 (armchair-pentagon) and A5' (open armchair). (B) Diagram showing DFT-calculated edge energies in the vacuum and on several metals (per unit length). [Reproduced with permission from [346].]

the energy is lower as the C-C bonds are determined to be stronger. In addition different structures are predicted following the addition of the first C atom with the two methods: the TB method yields a dangling bond, whereas for DFT ring structures are formed on both the ZZ and AC edges. However, the addition of further C atoms goes along the same path for both methods.

We shall now move on to discuss theoretical studies in which the effect of the metal substrate was taken into account. A number of experiments have observed the ZZ edge to be the predominant edge structure on polycrystalline Cu [347, 348, 349]. Several attempts have been made to explain these observations. Artyukhov *et al.* [346] considered the thermodynamics of different edge structures. They used DFT calculations in which graphene ribbon was considered with one side attached to a step edge of a metal and another free. This would be a very realistic configuration of a growing graphene flake nucleated at a step edge. Several basic terminations of the free edge were investigated as shown in Fig. 69. It is seen that the pentagon-heptagon termination Z57, being the most stable in vacuum, becomes the least stable on most metals. Similarly, interaction with the metals makes the AC edge (indicated as A edge in Fig. 69) less favorable than the ZZ one (Z in Fig. 69). Surprisingly, they also find that the open AC edge (denoted A5'), which is highly unfavorable in vacuum due to unsaturated dangling bonds, becomes more stable than the AC edge for most metals except Cu.

Further, to understand the thermodynamics of edge growth, up to 7 atoms were added one-by-one to the ZZ or AC edges, and in each case multiple possible geometries were investigated. Each structure is shown in Fig. 70 by a short horizontal line of either blue (attachment to ZZ edge) or red (to open AC) color. In the left part of the diagram states of a single C atom on the surface or in the bulk are shown, while on the right the chemical potential μ_C of C atoms in graphene is displayed. The horizontal green dashed line represents the position of the chemical potential of C atoms in the feedstock. The most favorable states in each case after adding a C atom are connected by dashed lines with the schematics at the bottom illustrating each structure. Although the corresponding barriers for the C atom additions were not calculated, these results still provide an interesting insight into the steps along the growth path. The growth of the ZZ edge involves an energy barrier for the addition of the first atom (leading to a noticeable nucleation barrier), and after that further additions become more favorable. As is seen from the blue structures at the bottom of Fig. 70, the newly formed hexagon serves as the nucleus for further growth which proceeds after that along the edge in both directions rather easily by two kinks propagating in both directions along the step edge. For the A5' edge (red) the first addition is favorable, but each subsequent addition requires energy intake. A slightly different propagating kink mechanism is at work here as well, as shown by a series of red structures at the bottom of Fig. 70. Using the calculated energies, directional growth velocities were then calculated which allowed the authors to work out the shapes of growing graphene islands. Since overall the nucleation barriers were estimated to be lower for the A5' edge than for the ZZ one, the A5' edges grow much faster with slow ZZ edges lagging behind, leading to predominantly ZZ edged hexagon shapes for the graphene islands

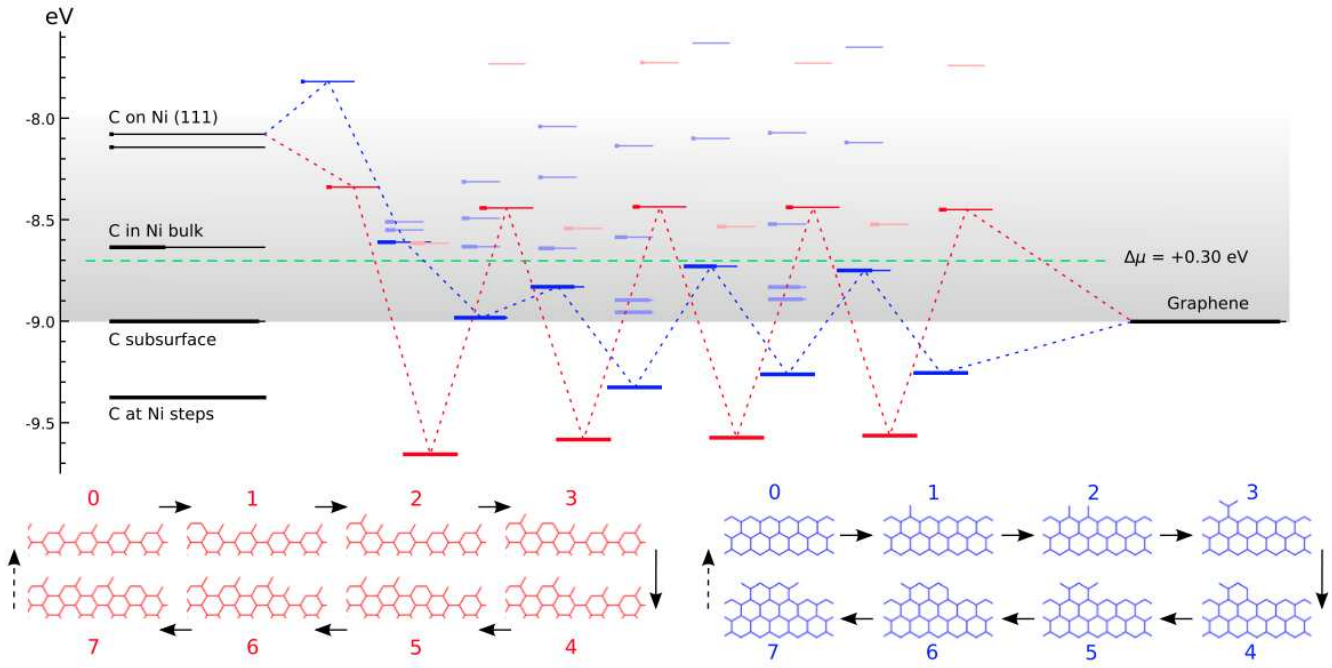

Figure 70: Energy diagram showing states of different structures formed on Ni(111) surface formed by adding (from left to right) up to 7 C atoms to either ZZ (blue) or A5' (red) graphene ribbon edge. The most favorable structures after each addition are shown at the bottom. [Reproduced with permission from [346].]

in agreement with experiments. The energy state diagram also suggests that adding C_2 clusters instead of monomers would be much more favorable and result in larger growth rates as this would avoid the calculated oscillations of the energy levels.

Another interesting observation made in [346] on the basis of their Fig. 70 concerns the dependence of the growth mechanism on the C atoms feedstock chemical potential μ_C ($\Delta\mu$ in the Figure). The derived sequence of states described above and based on μ_C =0.3 eV does not lead to defects during growth (the structures at the bottom of the Figure). However, higher μ_C values (a higher position of the dashed green line) would result in other structures being involved which would inevitably result in defective growth.

In a similar attempt to explain observations of the predominantly ZZ edges observed in growing isles, Shu *et al.* [345] carried out a comprehensive DFT study ranging from calculating stabilities of several edge terminations on the Cu(111) surface, their ability to incorporate additional C adatoms and the C_2 cluster, and finally estimating the growth rate of different edges and correspondingly the island shapes and their dominant termination during growth. In their calculations they attached either a ZZ or AC graphene nanoribbon (GNR) to a step on the metal surface, in a similar fashion to the study in [346]. In addition to considering the pristine termination of the GNR at the free end attached to the metal, however, either individual Cu atoms or their chain (Cu passivation) were added as well in some calculations, see Fig. 71. The stabilization (formation) energy was calculated using the formula:

$$E_f = \left(E_{tot} - E_{GNR} - E_M - N_{Cu}\mu_{Cu}\right)/L\,, \tag{27}$$

where E_{tot}, E_{GNR} and E_M are the DFT energies of the total system (metal and GNR), individual GNR and of the metal, respectively, while μ_{Cu} is the Cu atom chemical potential (at $T = 0$) taken from the DFT energy of the Cu bulk (the last term with μ_{Cu} is only needed when extra Cu atoms are added to passivate the GNR). The formation energy E_f is calculated per unit length L of the unit cell along the Cu step direction. The very important results they find were that the stability of the AC termination of GNR is greatly enhanced by passivating the edge with individual Cu atoms (in spite of the obvious energy penalty of μ_{Cu} required to bring additional Cu atoms from the bulk). At the same time, the pristine ZZ termination was found to be more favorable than the passivated ZZ edges. Next, incorporation of single C atoms and its smallest cluster C_2 to the GNR was considered with several edge structures using a set of NEB calculations. Note, as

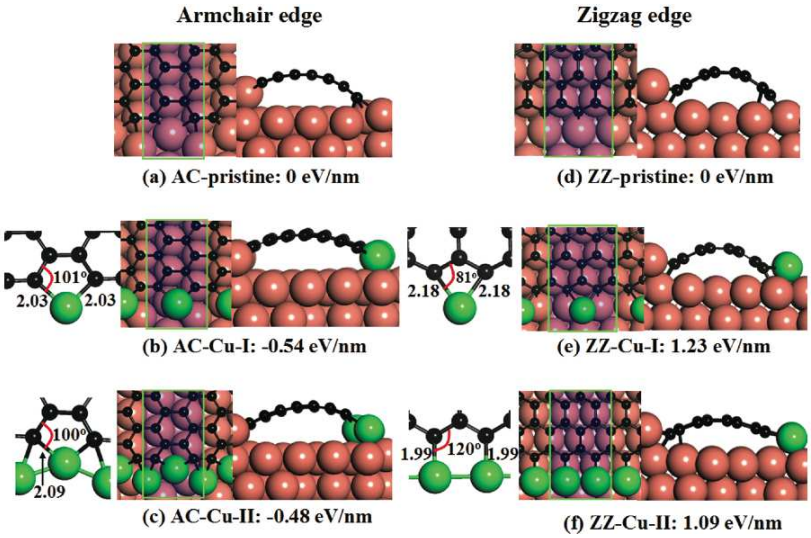

Figure 71: DFT calculated geometries of the AC (left panels) and ZZ (right panels) structures: pristine (upper row), with a single passivated Cu atom per cell (middle row) and attached Cu chain (bottom row). Both top and side views are shown together with the corresponding formation energies per unit length under the pictures. C atoms are shown in black, other colors are used for various Cu atoms. [Reprinted with permission from [345]. Copyright (2012) American Chemical Society.]

was mentioned above, that two C atoms need to be added to the AC structure to form a complete hexagon nucleus, while in the case of the ZZ edge three atoms are required. It was found that attachment of two single C atoms to the passivated AC edge involved a much lower barrier than attachment to the pristine AC edge; in either case the whole process is highly exothermic. On the other hand, attachment of three C atoms (one by one) to the ZZ edge requires considerably larger barriers. Qualitatively the same result is obtained when a dimer cluster C_2 was added instead. Hence, their results indicate that, in agreement with conclusions drawn in the study by Artyukhov *et al.* [346] (see above), the growth rate of AC edges must be much higher than that of ZZ edges, which agrees with the experimental observation of mostly ZZ terminated graphene islands during their growth. Therefore, the authors use the calculated energy barriers ΔE in expressions derived in [350] to obtain the rates of propagation of the two edges:

$$R \propto \exp\left(-\Delta E/k_B T\right) \ .$$

Since the whole attachment process was found to consist of several steps, ΔE from the threshold step (with the largest barrier) was considered in calculating the rate. On the basis of this model it was shown that the high-growth-rate AC edge quickly disappears, while the slowly growing ZZ edge dominates the graphene edges, in agreement with experiment and similar to the conclusion made in [346] as we have already mentioned. Also, the mechanism of growth of the ZZ edge was proposed to be the kink propagation mechanism, similar to that found in [346]. It was concluded that Cu passivation of the graphene AC edges plays an essential role in its growth on the Cu(111) surface.

In the work of Wu *et al.* [343] the attachment of carbon clusters to the ZZ edge of the R0 phase of graphene, fixed with one edge to the Ir(111) surface, was considered by adding different carbon species to the other (free) edge of the graphene ribbon and calculating their formation energies. This was then used to determine which C_N species are favorable for the attachment. The formation energy E_f per carbon atom for a particular attachment process of a carbon cluster of N atoms to the graphene ribbon placed on the surface was calculated (relative to the binding energy of a single C atom on the terrace) from

$$E_f = (E_{C+R/Ir} - E_{R/Ir} - E_{C/Ir} + E_{Ir})/N \ , \tag{28}$$

where $E_{C+R/Ir}$ is the total energy of the ribbon after the C cluster is attached, $E_{R/Ir}$ and $E_{C/Ir}$ are the energies of the ribbon and the cluster before the attachment, respectively (both on the surface); the energy of the surface, E_{Ir}, was added due to double counting of it in the preceding two energy terms. The formation energy is dependent on the metal sites that the additional carbon atoms occupy. For a carbon monomer to

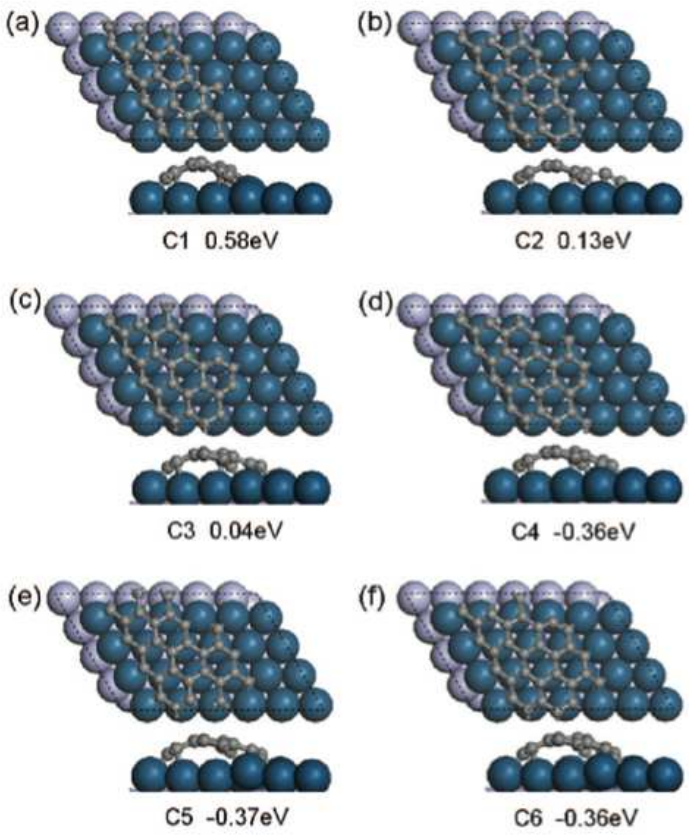

Figure 72: Selection of optimized structures of carbon clusters attached to the ZZ edge and their calculated formation energies E_f. [Reprinted with permission from [343]. Copyright (2012) American Chemical Society.]

attach and occupy a hollow hcp site E_f was calculated as -0.86 eV (with a barrier of 0.75 eV) and therefore a C atom attachment is energetically favorable. However carbon monomer attachment in a top site is unfavorable with E_f =0.58 eV, Fig. 72(a), i.e. the C monomers will detach faster from this site than they can attach. Instead the growth relies on the attachment of clusters. Dimer and trimer attachment, Fig. 72(b,c), is unfavorable, while the C_4, C_5, C_6 carbon clusters each have a formation energy of -0.36 eV, Fig. 72(d-f), and hence provide the driving mechanism for the edge attachment. This suggests a possible explanation for the 5 atom cluster growth mechanism that causes the non-linear growth observed in the Loginova *et al.* experiments [54, 106].

In addition to the growth of the Ir(111) R0 phase, the R30 phase was also investigated using DFT [343] which is important for understanding the effect that the orientation of the graphene island with respect to the substrate metal has on the growth. Since different edge atoms are not equivalent, the monomer attachment may be either energetically favorable or not. However, the growth can continue via attachment of clusters. In particular, C_2 and C_3 clusters can be attached to the ZZ edge. Since the number of C_2 clusters is the largest, their attachment would determine the growth of the ZZ edge. Compared to the R0 phase which relied on larger clusters, the R30 phase would then be growing faster since the concentration of C_2 clusters is very high. It is worth noting however that the edges of graphene on Ir(111) are not actually purely ZZ or AC, be they attached or not to a substrate edge: see [318] and a more recent work [351].

7.3. Role of defects

During graphene growth defects in the structure are formed. The impact on the properties of graphene is regarded either as negative, e.g. a strong reduction in its carrier mobility [347], or positive, e.g. a possible route to turning on magnetic moments in an otherwise diamagnetic material [352]. These defects mainly include grain boundaries which are formed where different domains meet during growth and also

point defects such as vacancies and other local imperfections of the pristine hexagonal network. The grain boundaries are created when the growth has begun at different nucleation sites. As these regions merge together during growth it leads to grain boundaries between the different crystalline domains. Point defects on the other hand could be due to a vacancy or impurity atoms becoming trapped in the structure during growth: their healing requires energy barriers to overcome and hence takes much longer then the time needed for new C atoms to attach. Consequently, graphene flakes grow with defects which heal on a much longer timescale. Point defects may also be the result of defects in the underlying metal surface (e.g. steps, kinks) which imprint on the graphene structure stimulating its growth away from the perfect C atom arrangement.

It is possible to reduce the amount of grain boundaries by carefully controlling CVD growth conditions so that graphene nucleation does not occur at many different sites. This was achieved e.g. by Yan *et al.* for graphene on a copper foil [271]. The graphene was grown using very low pressure CVD of methane with a low flow rate. Large domains of up to few mm were observed. For these large domains, transferred to SiO_2/Si, it was shown that the carrier mobility reaches values above $\sim$10000 $cm^2V^{-1}s^{-1}$. Such values approach those obtained with exfoliated graphene (in much smaller domains), which were also obtained with CVD graphene in single-crystal domains of few 100 microns in size, transferred to SiO_2/Si with the help of a dry process [353].

Point defects may also influence the electronic transport properties of graphene prepared on substrates, as do point defects induced in exfoliated graphene [354]. We note that, to our knowledge, the influence of defects on the conduction properties of a SiC graphene has not been much studied.

7.3.1. Defects in free standing graphene

Even though we are interested mostly in the growth of epitaxial graphene, consideration of defects in the free standing graphene is more than an academic exercise. This is not only because the free standing graphene seems to be the simplest system to consider; it is also that this rather simple model system may already suggest possible defective structures in the real situation of graphene on the metal substrate, even though one would expect that the metal might significantly affect the defective structures and introduce further complexity, not least due to the moiré pattern.

For free standing graphene many types of structural defect have been investigated. A detailed review of theoretical studies into these has been recently published [355], so that only a brief account of them will be given here. The types of point defects considered so far are single vacancies (SV), double vacancies (DV), interstitial carbon atoms, impurities or Stone-Wales defects. The structures of some of these defects are shown in Fig. 73. Stone Wales defects do not involve the removal of any carbon atoms, but are caused by rotation of a carbon bond that results in two pentagons and two heptagons being formed. Single vacancies result from the removal of one C atom. These can form a 5-9 structure (the notation used corresponds to the fact that instead of two hexagons, a pentagon (5 vertices) and an adjacent nonagon (9 vertices) are formed), where a C-C bond forms between two of the dangling bonds that remain. For double vacancies there are three different structures that are proposed. These include the 5-8-5 structure, where the dangling bonds form two pentagons and an octagon; the 555-777 structure, which consists of three pentagons and three heptagons; and its reconstruction, the 5555-6-7777 defect [356, 357].

In order to understand the stabilities of different point defects and hence assess the feasibility of their formation, knowledge of their formation energies is useful. The calculated formation energies of these defects are presented in Table 4. These calculations were performed using DFT, with the exception of [358] where tight binding molecular dynamics simulations were used. The formation energies of both SV and DV were found to be around 7 eV [359, 360, 361]. For SV this energy is high as there is a dangling bond left in the structure which is unfavorable. As DVs have two missing atoms, the energy per removed atom is lower than that for the SV and therefore thermodynamically the DVs will be more likely to form. Multiple vacancies may also be formed in graphene; however, it seems that it must be more favorable to have an even number of missing atoms rather than an odd number. This is because for the removal of an odd number of carbon atoms there will be a remaining dangling bond.

Once defects are present they can migrate across the graphene surface. The mobility of the various defects is determined by calculating their diffusion barriers. For mobile defects it is possible that they will migrate to the graphene edge where there is a greater chance for the defect to disappear and hence for the whole structure to heal. Moreover, two defects may merge together to create a larger defect and defects can reconstruct themselves by rotating particular bonds. Calculated diffusion barriers for the defects are given

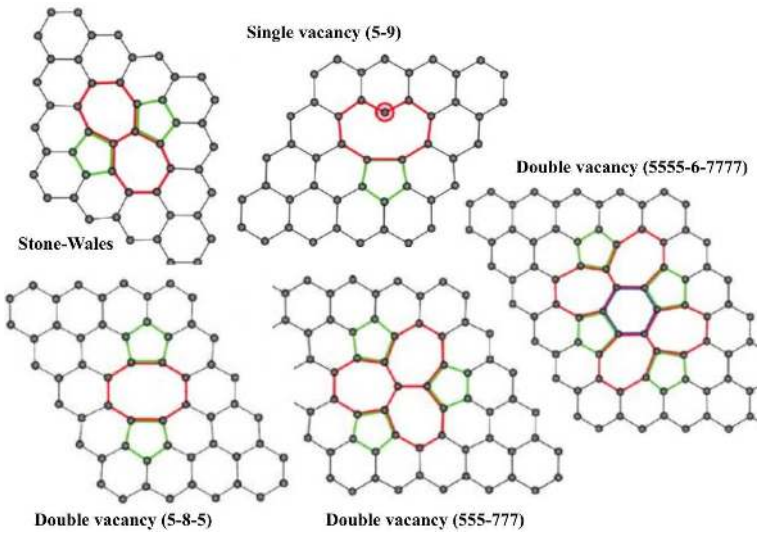

Figure 73: Relaxed structures of some of the point defects in free standing graphene. [Reprinted with permission from [355]. Copyright (2011) American Chemical Society.]

Defect	Formation Energy [eV]	Diffusion Barrier [eV]	Reference
Stone-Wales **55-77**	4.5-5.3	10	[360, 359]
Single Vacancy **5-9**	7.3-7.5	1.2-1.4	[361]
Double Vacancy **5-8-5**	7.2-7.9	7	[362, 361]
Double Vacancy **555-777**	6.4-7.5	6	[358, 363]
Double Vacancy **5555-6-7777**	7	6	[356, 357]

Table 4: Various defects found in free standing graphene and their formation energies and diffusion barriers calculated using DFT. [Adapted from [355].]

in Table 4.

It is seen from the table that SVs have a much lower diffusion barrier than DVs, and are therefore expected to be highly mobile, which can lead to the formation of DVs when two single ones coalesce. This was investigated by Lee *et al.* who found that at 3000 K two SVs can diffuse and coalesce to form 5-8-5 DV [358]. These vacancies can then reconstruct into a 555-777 vacancy by undergoing a Stone-Wales type transformation where a bond rotates by 90 degrees. The 555-777 vacancy was found to be more stable than the 5-8-5 vacancy. DVs have been judged to be less mobile but could possibly migrate via atom jumps [361] or switching between configurations [356].

7.3.2. Defects in graphene on transition metal surfaces

When graphene is grown with CVD or TPG, it is supported by a transition metal surface. In this case the structure, formation and mobility of any graphene point defects must be affected by the metal. Recently, theoretical work started to appear focused on determining defect properties on different growth surfaces in an attempt to find how to limit the formation of defects during graphene growth.

The formation of vacancy defects in graphene on the Cu(111), Ni(111) and Co(0001) surfaces has been studied using DFT calculations [364]. As mentioned above, for graphene grown on a surface different types

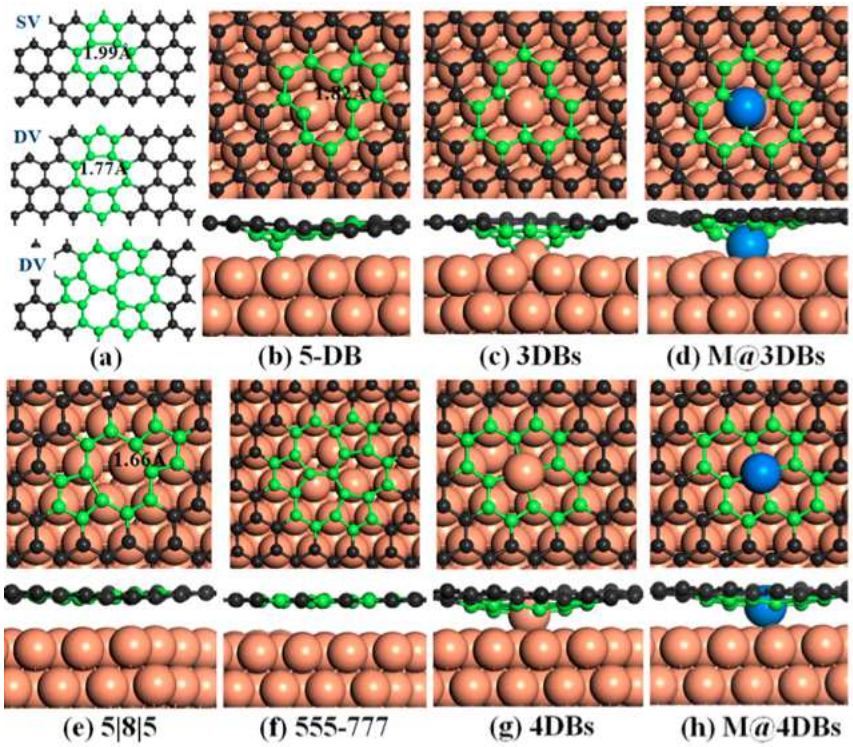

Figure 74: (a) Optimized structures of a SV (denoted 5-DB) and DVs (5-8-5 and 555-777) in free-standing graphene. The SV structures on the Cu(111) surface: (b) 5-DBs, (c) 3DBs (5-9) and (d) M@3DBs, as well as the DV structures (e) 5-8-5, (f) 555-777, (g) 4DBs and (h) M@4DBs. The carbon atoms around the defect and the extra metal adatom in the M@3DBs and M@4DBs structures are colored green and blue, respectively. [Reprinted with permission from [364]. Copyright (2013) American Chemical Society.]

of defects are possible due to the ability of the metal atoms to be incorporated into them. For instance, as is shown in Fig. 74, in the case of SVs the effect of the missing atom can be reduced by lifting a metal atom from the substrate (this defect is denoted 3DBs in the Figure and is also known as 5-9 defect in the free-standing graphene, see Fig. 73), or replacing it with an extra metal atom which would interact strongly with the defect (M@3DBs). Note that there are always free metal atoms on the surface diffusing across terraces between steps [365]; their concentration depends on the surface roughness and their mobility on temperature. The surface atom attaches to the three dangling carbon bonds left after C atom removal thereby forming a new type of the SV defect. For DVs there are the analogues of the 5-8-5 and 555-777 structures found in free-standing graphene (Fig. 73); however, structures where a metal atom passivates the four dangling bonds of the defect have also been proposed. As with SV, two possibilities have been considered [364]: either the metal atom comes from the substrate relaxing upwards (4DBs) or it is a free surface atom migrating around the surface and eventually being trapped by the defect (M@4DBs), see Fig. 74.

It is essential to know the formation energies of the point defects as these indicate how feasible is their formation and hence their likely concentrations. In [364] the formation energies were calculated using the C chemical potential from free-standing graphene, while the chemical potential of the metal atom (needed when an extra metal atom is involved as in the cases of M@3DBs and M@4DBs) was taken from the metal bulk energy. The DFT calculated formation energies of the vacancies are shown in Fig. 75. Of the SV structures the 3DB has the lowest formation energy for all surfaces. This is deduced to be due to the passivation of the double bonds by the metal atom. The M@3DBs structure has a higher energy possibly because of a steric effect as there is limited space for the extra metal atom. The vacancies formed on the Cu(111) surface have a higher formation energy compared to the other two surfaces, Ni(111) and Co(0001), and should therefore be a better catalyst for graphene growth with an expected lower defect concentration. Importantly, compared to the free-standing graphene the formation energies of SVs on a substrate are significantly lower. This is because the dangling bonds left behind around the vacancy after removal of the C atom bind to the metal

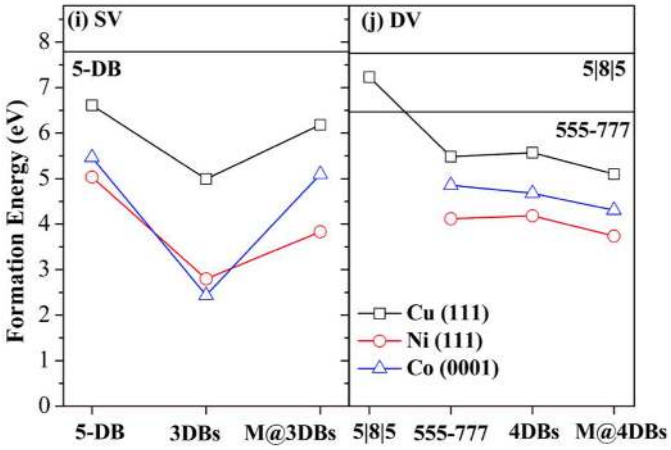

Figure 75: Formation energies of the various single and double vacancy structures in free standing graphene (black horizontal lines) and on the Cu(111), Ni(111) and Co(0001) surfaces. [Reprinted with permission from [364]. Copyright (2013) American Chemical Society.]

which reduces the system energy.

For DVs the calculated formation energies are also smaller than those for vacancies in free-standing graphene. The 5-8-5 structure was found to be stable only on the Cu(111) surface, since on the other two surfaces the strength of the graphene-metal interaction causes the C-C bonds to break, leading to the creation of the 4DBs structure instead. For the 555-777 structure on the Cu(111), Co(0001) and Ni(111) surfaces there is a drop in the formation energy of 0.92, 1.68 and 2.33 eV, respectively, compared to unsupported graphene. From this the authors concluded that the strength of the graphene-metal interaction increases in the order of Cu(111) $<$ Co(0001) $<$ Ni(111). The 4DBs and M@4DBs structures were found to be either similar to or even lower in formation energy than the 555-777 structure which shows the significance of the participation of the metal atoms in defect formation.

The diffusion of these vacancies on the surfaces was also calculated in [364] using the NEB method, the results of which are shown in Fig. 76(a-b) for the two most stable structures. Also included are the diffusion pathways for M@3DBs SV and M@4DBs DV on Cu(111). For SVs the diffusion barriers are higher than for free standing graphene. This is likely to be due to the interaction of the metal surface with the vacancy. The diffusion pathway depicted in Fig. 76(c) involves the detachment of the metal atom from the graphene, then switching of the carbon atoms and finally a different metal atom is lifted from the surface to fill the vacancy. For the diffusion pathway of the M@4DBs DV found by the authors the metal and carbon atoms switch places. The diffusion barriers on each of the substrates are higher than for SVs, and cannot be overcome at the growth temperature (1300 K). Therefore it is concluded that DVs must be immobile. Also note that the diffusion barriers for the SV across these three metals increase in the order G $<$ Cu $<$ Ni $<$ Co, while for the DV they increase in the opposite direction. Moreover, either order is different from that established from the stability of the 555-777 DV defect which was mentioned above. Therefore, care is needed in establishing relative strengths of the graphene-metal interaction on the basis of graphene defects.

Other than the work described above there has been very little theoretical work on defects in graphene on transition metal surfaces. The structure of a SV in graphene on the Pt(111) surface has been calculated in [366] using DFT with the van der Waals interaction included. It was found that the relaxed structure which most closely matches STM results is the 5-9 structure shown in Fig. 77. It is seen that two carbon atoms of the defect displace strongly towards the surface.

There has also been work on determining how graphene defects might heal once they have formed on transition metal surfaces. The healing pathway of a Stone-Wales defect on a Ni(111) surface was calculated by Jacobson *et al.* [367]. From this it was determined that compared to free-standing graphene the Stone-Wales defect is stabilized by the Ni(111) surface and has a formation energy 1.0 eV lower. Furthermore the barrier to healing the defect on Ni(111) is calculated as 2.88 eV, which is lower than the 4.10 eV required for healing in free-standing graphene. This is due to the presence of the surface breaking the symmetry of the transition state, which proceeds by the rotation of a C-C bond as in the free standing case. In the

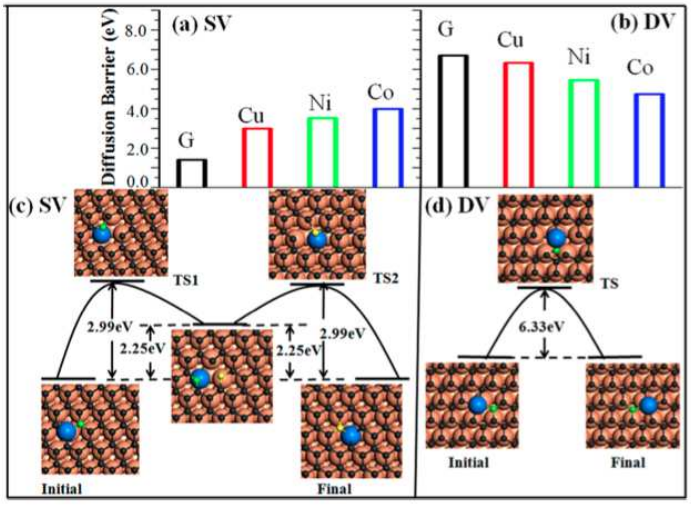

Figure 76: The diffusion barriers of (a) the M@3DBs single vacancy and (b) the M@4DBs double vacancy on the Cu(111), Co(0001) and Ni(111) surfaces. The corresponding values for the SV ad DV defects in the free standing graphene are also given for comparison (as G). The diffusion pathways for each of these vacancies on the Cu(111) surface are shown in (c) and (d), respectively. [Reprinted with permission from [364]. Copyright (2013) American Chemical Society.]

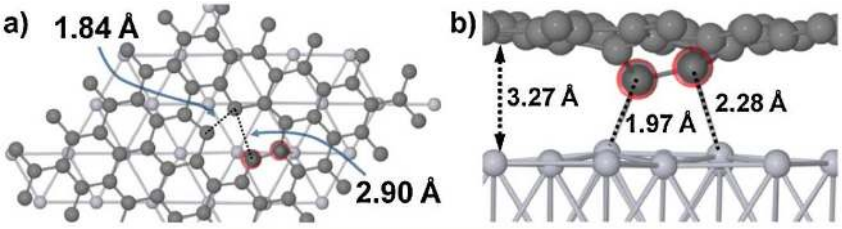

Figure 77: The top (a) and side (b) views of the relaxed SV in a 6 × 6 unit cell (4 cells of the 3 × 3 graphene Pt(111) moiré). The two carbon atoms that move towards the surface are highlighted. [Reprinted with permission from [366]. Copyright (2011) by the American Physical Society.]

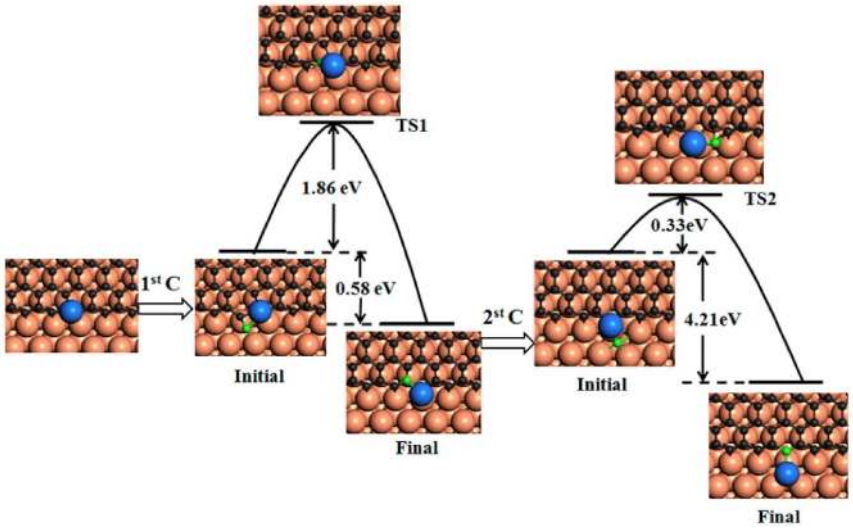

Figure 78: The healing process for an M@4DBs defect on a graphene edge on the Cu(111) surface. The barriers for each of the transition states are indicated. [Reprinted with permission from [364]. Copyright (2013) American Chemical Society.]

intermediate state the carbon atoms are stabilized by the surface and the barrier of the reconstruction is reduced.

The removal of metal atoms at the edge of a graphene front was investigated in [364]. If these remain in the graphene they would become embedded in the graphene as it grows, forming M@4DBs defects. To remove the metal atoms two carbon atoms are required to diffuse to the edge and then the suggested process occurs in two steps. First, one carbon atom must attach onto the metal atom to form a hexagon, and then the next carbon atom replaces the metal to complete the graphene edge. The whole process is depicted in Fig. 78 for graphene on the Cu(111) surface. The DFT calculated barriers in this case are 1.86 eV for the first transition state and 0.33 eV for the second transition state. By comparison of this process on the Ni(111) and Cu(111) surfaces it was deduced that healing in this manner has a higher rate on the latter surface for the commonly used growth conditions (with $T = 1300$ K and a growth rate of 10-100 nm/s).

7.4. Attempts to simulate the growth

Above we reviewed studies of monomers, dimers and various larger C clusters on several metal surfaces used for growing graphene. Not only stabilization energies of these C species were calculated (usually relative to the energies the C atoms would have in the graphene feedstock serving as their source), but also mechanisms of their migration across the surface were studied, as well as (in some limited specific cases) association and dissociation energies. It is widely agreed that C clusters tend to attach to metal steps where they are more stable, and hence nucleation of graphene may well start mostly at the steps, i.e. heterogeneously. Further growth would require attachment of monomers, dimers and other C species to the formed nucleus. If the C species are added extremely slowly, the growing film would have sufficient time to "heal" itself leading eventually to a reduction in free energy of the growing structure; however, depending on temperature and the supersaturation $\Delta\mu$, the influx of C atoms may be so fast that only partial healing is possible leading to a defective graphene structure (see also section 7.3.2). That is why it is paramount to model the growth kinetics in real time under different growth conditions in order to derive the best experimental procedure leading to large graphene sheets with a low concentration of defects.

In this Section several simulations of graphene growth found in the literature will be reviewed. This direction of research in application to graphene growth is in its infancy mostly due to the sheer complexity of the system; however, in the near future we should expect more simulations of this kind.

In the KMC simulations by Wu *et al.* [343] addition of carbon species to the edges of graphene islands on the Ir(111) surface was modeled based on first principles calculations performed for the adsorption of different carbon species on the surface, their diffusion and attachment to the graphene edges, as has already been described in Section 7.2.3. This allowed the authors to determine the dependence of the growth rate on

the C monomer concentration. For this study Wu *et al.* developed a multi-scale "growth-front-focused" KMC model. This allowed only the moving growth front to be considered in the actual simulation, and also the authors implemented a special procedure which takes into account the vastly different carbon species densities (and hence their fluxes) that vary over many orders of magnitude. In their model a honeycomb lattice was divided into a graphene region, a growth front, a diffusion layer and the far field, all shown in Fig.79(a). In the far field thermal equilibrium is assumed between differently sized C_N species, so that densities of the species with $N > 2$ (dimers, trimers, etc., up to hexamers) were directly related to the monomer density C_1 via the $NC_1 \rightleftharpoons C_N$ equilibrium condition. From the far field the various carbon species can diffuse across the diffusion layer with a flux that is calculated from the known species concentration in the far field region and the corresponding diffusion barriers calculated from first principles. Then at the growth front the attachment and detachment of the C_N species to and from the graphene edge are considered explicitly using the KMC method. The attachment and detachment rates for a particular species were determined from first principles calculations (section 7.2.4), which took into account the effect of the underlying Ir(111) surface. To overcome the problem of vastly different species fluxes, the authors proposed a scheme whereby at every single time only one species contributes to the growth until the growth gets stuck. At this point a different species with lower flux is "switched on" and this process is continued until the growth stops again. The simulation starts from monomers which are the only ones contributing to the flux in the diffusion layer region, then it is switched to dimers, then trimers, etc. Finally, after the last species (C_6) has been considered, attention is returned into the monomers again. Although this procedure is very artificial and is likely to be far from being realistic, this is undoubtedly an interesting attempt to tackle this vastly complicated problem of many species contributing in their own way to the growth under realistic conditions when their concentrations differ by many orders of magnitude. This clearly demonstrates the sheer complexity of modeling the growth of graphene at the atomic level which still needs to be properly addressed.

The nucleation stage of the growth process was not considered explicitly by Wu *et al.* [343]; it was assumed that the initial nucleus of the graphene ribbon was already formed, most likely at a step edge. This approach therefore can only be applied to the steady-state growth stage of the graphene islands. In particular, it can be used, and this is exactly what has been done by Wu *et al.* [343], to determine the steady-state rate, r, of graphene growth.

The results from these KMC simulations are shown in Fig. 79(b). It was found that the growth rate r can be fitted to an equation of the form

$$r = aC_1^n + d\,, \tag{29}$$

where C_1 is the monomer concentration and the constant $n = 5.25$. This agrees very closely with the experimental results from the LEEM studies of Loginova *et al.* [54] where it was found that the growth rate has a nearly quintic dependence on the monomer concentration. Unfortunately, no detailed analysis has been made in [343] concerning the origin of this highly non-linear dependence; in particular, it is not clear whether this result can be reproduced, at least qualitatively, by just accepting clusters C_N with N values of just 1 (monomers) and 5 (quintets), or whether the existence of other species is essential. Recall (section 7.1) that in the phenomenological rate equation-based study by Zangwill and Vvedensky [334] where the non-linear growth was also explained, only monomers and C_5 clusters were accounted for. In addition, only reactions between C_N and C_1 species were considered by Wu *et al.* [343] and since the decomposition of C_N clusters does not happen completely in one step, but rather gradually, producing smaller clusters along the way, it is not obvious how this assumption may have affected the calculated kinetics.

Haghighatpanah *et al.* used a Grand Canonical Monte Carlo (GCMC) method to determine how various factors, such as temperature T and chemical potential μ of the C feedstock, may affect the growth of graphene both in vacuum and on the Ni(111) surface [204]. As calculations of this type would be prohibitively expensive with DFT, a much computationally cheaper TB model was used instead whose parameters were fitted to the DFT results on a number of reference systems (as reported in section 7.2.4), and then used as a basis for their GCMC simulations. As C atoms are added to the structure, a certain equilibration consisting of a relatively large number of displacement moves was performed. Then, the average numbers of C atoms in hexagons N_H, non-hexagonal rings N_R, and strings N_S were determined and used to assess the quality of the growing graphene. From this the ideal temperature and chemical potential were determined for producing the highest quality graphene where N_H is large and N_R and N_S are small.

First, the most efficient parameters for the GCMC calculations were investigated using a free standing

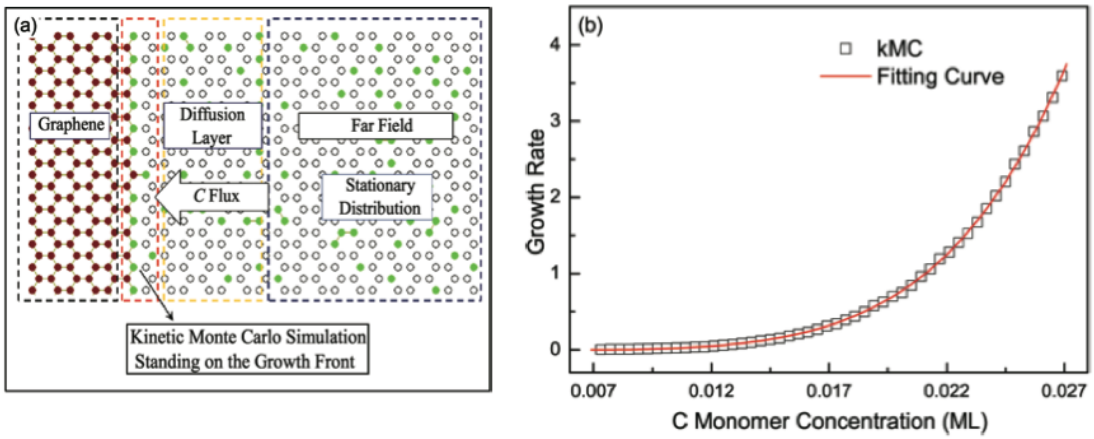

Figure 79: (a) The KMC model of graphene growth based on a division of the whole system into four regions (from left to right): already grown graphene ribbon, growth front where new species are able to attach/detach to/from the ribbon edge, diffusion layer providing influx of C_N species ($N = 1, \ldots, 6$), and the far field region where thermal equilibrium between C_N species is assumed; (b) the calculated dependence of the growth rate on the C monomer concentration showing the fifth power growth rate by the curve fitted to the KMC calculated growth rate (boxes). [Reprinted with permission from [343]. Copyright (2012) American Chemical Society.]

graphene sheet (no surface). It was noticed that at 1000 K defects were formed that were not easily healed and became embedded in the structure, whereas at 2000 K healing of defects was reduced due to the rapid motion of the C atoms. Therefore 1500 K was used as the growth temperature for production runs.

For all chemical potentials N_H, N_R and N_S increase with the number of added carbon atoms. For μ_C= -8.5 eV most carbon atoms attach at the end of chains as this is the most energetically favorable site. As a result the increase in N_H is lower than for the cases with higher chemical potentials where attachment is also likely at sites which are energetically less favorable (at hexagonal and non-hexagonal sites). Since fewer carbon atoms are added to the non-hexagonal rings in the early stages of growth for the chemical potential of -8.0 eV, this value of μ_C was used in further calculations. The changes in N_H, N_R and N_S were also investigated for different numbers of equilibration steps (denoted ND) computed between C atom additions, and the results show that larger ND values allow better healing of newly formed defective structures at the edges; however, once a defect is embedded inside the growing island, it stabilizes and its healing is found to be greatly suppressed.

Using $T = 1500$ K, μ_C = -8.0 eV and ND = 3×10^5 the growth of graphene was simulated first without any surface present, Fig. 80, and then on the Ni(111) surface, Fig. 81 (Note that the temperature used is to be rescaled downward when comparing theory and experiment since the melting temperature of Ni with this model is about 15% higher than measured [368].) The graphene produced with these conditions was optimized to grow without forming many strings and non-hexagonal rings, and this was successful for the free standing graphene. The situation is more complex, however, when calculations were performed on the Ni surface as exemplified in Fig. 81. It was found that C atoms may go to subsurface sites, form chains on the surface, and existing hexagons may rupture and then reconnect as more C atoms are added. It was also found that flakes become relatively more stable on the surface than in free space once they have grown in size: the defect-free area in flakes (with the same initial nucleus size and shape) on average is larger on the Ni surface. The two cases are not directly comparable as different nuclei were used in each case, shown in Figs. 80 and 81: the initial 5 hexagon graphene flake used in the simulation on Ni is much smaller than the graphene sheet used for the free standing graphene with no surface present. Still, a general conclusion was made, based on many such calculations, that the surface stabilizes the formation of graphene.

There are some indications that the calculations presented above may be incomplete. Indeed, after 25 atoms have been added N_S reaches around 6-8 atoms and then does not increase any further as more atoms are added. This is suggested to be because the surface stabilizes the formation of strings due to the strength of the Ni-C bond. It can also be noted that N_H and N_M increase with the addition of C atoms. Over time it is presumed that these values will saturate as the surface becomes covered in carbon, however, longer

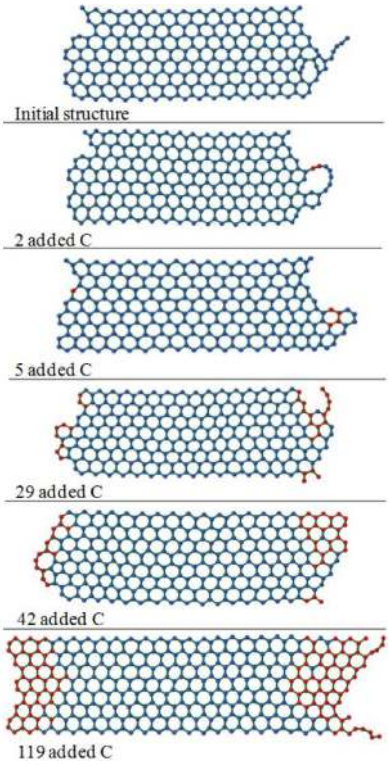

Figure 80: Snapshots of growth of free standing graphene during MC simulations starting from the initial structure (the top panel) as more C atoms are added. While the initial C atoms are shown in blue, newly added areas are colored in red. [Reprinted with permission from [204]. Copyright (2012) by the American Physical Society.]

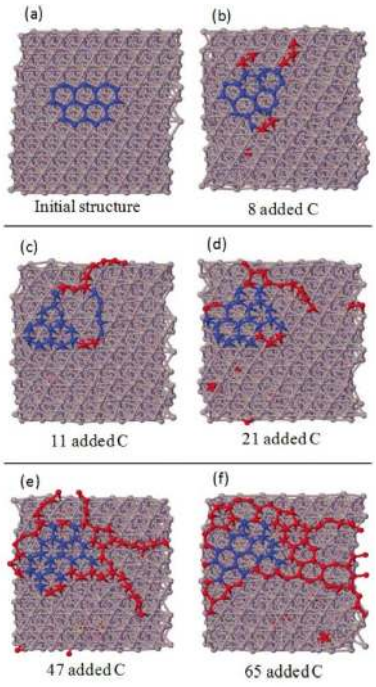

Figure 81: Selected snapshots of a graphene island grown on the Ni(111) surface. Blue and red colors correspond to initial and newly added C atoms. [Reprinted with permission from [204]. Copyright (2012) by the American Physical Society.]

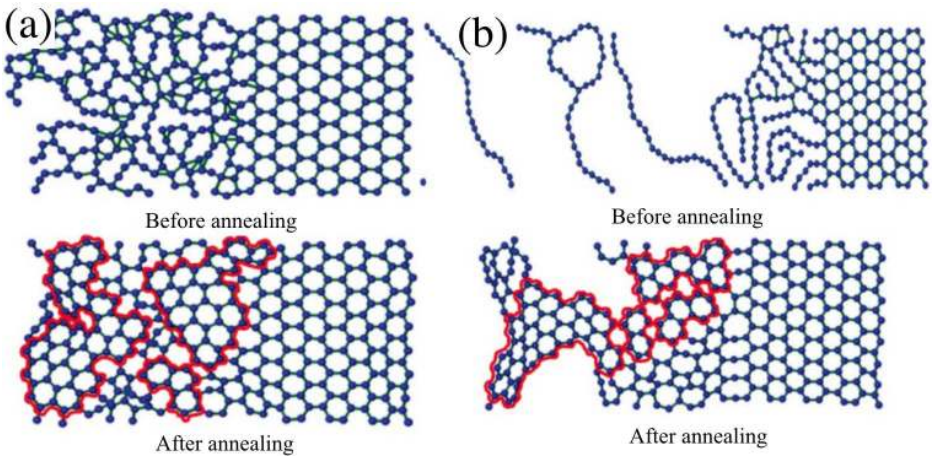

Figure 82: Defective graphene structures before and after thermal annealing at 1500 K for ND $\approx 2\times10^8$. The top panel structure in (a) is formed using a high chemical potential, whereas in (b) a low chemical potential was used. [Reprinted with permission from [204]. Copyright (2012) by the American Physical Society.]

simulations are needed to determine whether this is the case. Comparing the number of C atoms in hexagons for the growth on Ni(111) and without a surface suggests that graphene on the Ni surface is less stable.

Finally, Haghighatpanah *et al.* [204] tested the ability of a defected graphene sheet to heal under simulated annealing. For this the growth of two defected graphene sheets was simulated starting from one created with a very high chemical potential that gave 3D defects, Fig. 82(a), and another one grown using a very low chemical potential which resulted in long carbon strings, Fig. 82(b). To simulate the annealing process a temperature of 1500 K and ND $\approx 2 \times 10^8$ were used. The figure shows that the 3D and embedded defects do not heal easily when annealed. However chain and edge defects are more susceptible to healing and can normally form hexagons. Defect free hexagons formed during the annealing (shown in red) can become separated by defects that appear similar to domain boundaries. These are difficult to heal by annealing. Therefore it is suggested that in order to produce high quality graphene the initial growth conditions should be controlled rather than relying on annealing as a postprocessing procedure to remove defects, especially as the metal substrate stabilizes defects.

Although the results of the simulations like this one are undoubtedly useful, one has to be careful in interpreting them, as was noted in Section 4.2, as realistic simulations of growth. Indeed, everything depends on the nature of "moves" performed when equilibrating the system between C atom additions, where the C atoms were added, etc. In our view the GCMC simulations are to be used with care; however, KMC based simulations are capable of simulating the growth, though the latter are prone to yielding incorrect results if some of the essential elementary processes are missing or their barriers were under- or overestimated.

In GCMC simulations based on a TB model a wide range of temperature and C atom chemical potential μ_C was studied in order to understand the favorable conditions for formation of a graphene-like layer on the surface. In these simulations the MC moves corresponded only to C atoms being added and/or removed from the surface. Examples of the results of the simulations for 1000 K for five values of μ_C are shown in Fig. 83 (the less negative value corresponds to a higher "pressure" or "concentration" of C atoms in the feedstock with which C atoms on the surface are in equilibrium). At large negative values of μ_C carbon atoms penetrate inside the Ni. As the value of μ_C is increased (gets less negative), first the appearance of C chains creeping on the surface is observed ($\mu_C = -5.75$ eV), and then at $\mu_C = -5.0$ eV a graphene-like structure on the surface emerges. Note that the structure is defective which is most likely due to the fact that the simulation was not run for sufficiently long time, i.e. the system was not fully equilibrated. It is noted by the authors that the graphene-like structure appears only after chains start to "collide" and three-coordinated C atoms appear serving as nucleation sites for the carbon monolayer. This requires a sufficiently high value of the C chemical potential ($\mu_C \succeq -5.0$ eV) and a certain temperature window up to and around 1000 K. For instance, at 1500 K a carbidic phase was seen formed.

A recent study [369] based on the phase-field method has modelled the epitaxial growth of graphene islands on copper by CVD of methane (CH_4) in the presence of H_2. The calculations were based on a

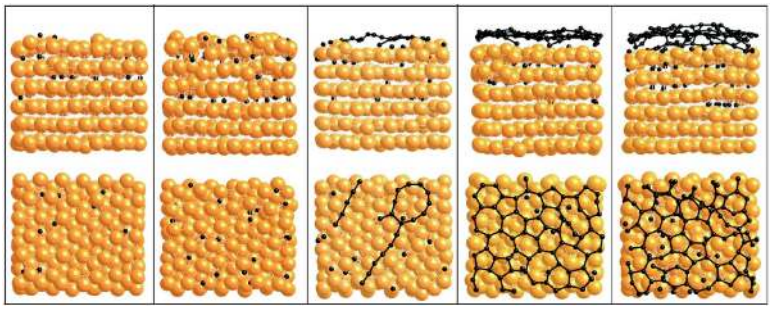

Figure 83: Snapshots of GCMC simulations of a Ni(111) surface in thermodynamic equilibrium at 1000 K with the C atom system at chemical potentials μ_C (from left to right) equal to -6.5, -6.0, -5.75, -5.0 and -4.5 eV. Lower panels: top view; upper panels: side view. [Reprinted with permission from [225]. Copyright (2006) by the American Physical Society.]

standard phase-field formulation of the motion of island boundaries, but with anisotropies in the kinetic coefficients, step energies, and diffusion, with the latter included to account for the crystallinity of the substrate. The calculations assumed an effective adatom deposition flux to avoid the complications of the reaction sequence of a polyatomic precursor. Experiments were carried out on several orientations of copper, such as (100), (310), (221) and (111), and the comparisons with phase-field calculations presented as an island morphological "phase diagram" shown in Fig. 84.

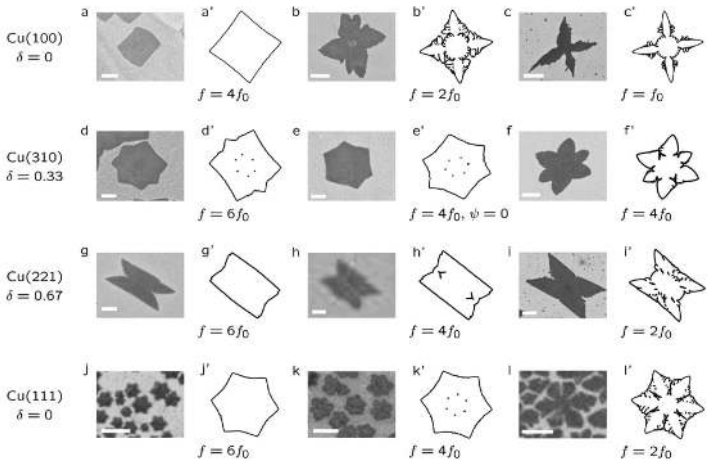

Figure 84: Shapes of graphene islands on copper facets with different exposure times and partial pressures of C_2H_4 and H_2 at $T = 1303$ K. (a), (b), (c): Cu(100) after 6, 4, and 2 min exposure with partial methane/hydrogen pressure ratios of $3{\times}10^{-4}$, 0.028, and 0.81, respectively. Scale bars are 10, 4, and 2 μm, respectively. (d), (e), (f): Cu(310) after 20, 10, and 2 min exposure with partial pressure ratios of $3{\times}10^{-4}$, $7.7{\times}10^{-3}$, and 0.028, respectively. Scale bars are 10, 10, and 4 μm, respectively. (g), (h), (i): Cu(221) after 7, 6, and 3 min exposure with partial pressure ratios of $1.6{\times}10^{-5}$, 0.028, and 0.035, respectively. Scale bars are 4, 4, and 2 μm, respectively. (j), (k), (l): Cu(111) after 7, 4, and 3 min exposure with partial pressure ratios of of $3{\times}10^{-6}$, $1.6{\times}10^{-5}$, and 0.026, respectively. Scale bars are 4, 2, and 2 μm, respectively. Shapes from simulations are presented next to the corresponding experimental images. [Reprinted with permission from [369]. Copyright (2013) American Chemical Society.]

The main features of this phase diagram are as follows. The graphene nuclei on Cu(100) begin as squares, but evolve into shapes with four approximately symmetric dendritic extensions. The phase-field calculations used six-fold symmetry for the kinetic and edge anisotropies and an isotropic diffusion tensor. The nuclei on Cu(111) show hexagonal symmetry with dendritic features which develop with time. The phase-field calculations used six-fold symmetry for the kinetic and edge anisotropies with isotropic diffusion. The nuclei on Cu(310) show a polygonal shape initially, which evolves into a distorted hexagon before developing cusps at the island boundary. A six-fold symmetry and an asymmetric diffusion constant was used for the phase-field calculations. Finally, the nuclei in Cu(221) exhibit approximately rectangular shapes with shallow depressions in the center of the shorter sides, which evolve into a "butterfly" shape. The phase-field calculations used a four-fold symmetry with an asymmetric diffusion constant.

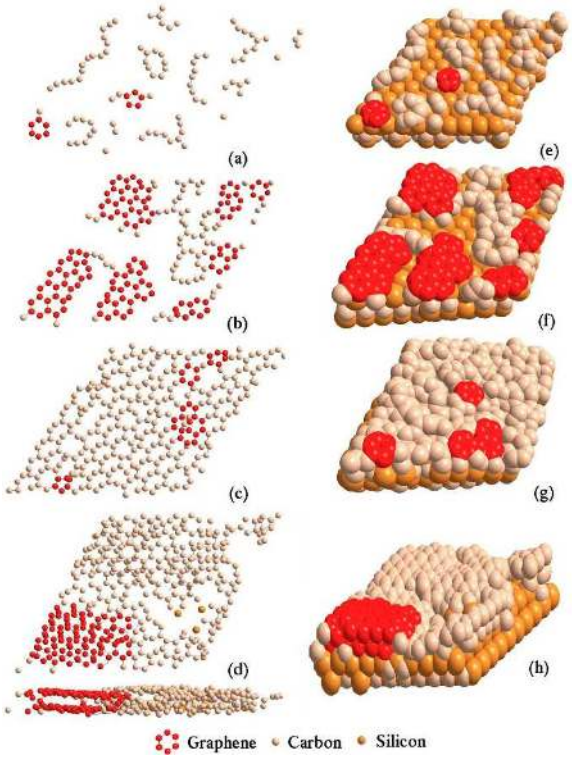

Figure 85: Typical calculated geometries of carbon atoms on top of the Si-terminated SiC surface for various C coverages achieved by removing Si atoms from a different number of SiC layers: (a,e) one; (b,f) two; (c,g) three; (d,h) four. The annealing temperature is 2000 K. Graphene-like clusters with hexagonal ordering are shown in red. The topmost layers of carbon atoms are shown in the left panels, while the SiC layer below is seen in the corresponding right panels. [Reprinted with permission from [330]. Copyright (2008), AIP Publishing LLC.]

These comprehensive phase-field calculations show that the main features of the complex morphologies of graphene islands on various copper surfaces result from the competing effects of the anisotropy of the kinetics of the growing graphene edge and the crystallographic orientation of the substrate through the anisotropy of surface diffusion. The value of performing experiments in tandem with theoretical calculations is evident, as the growth conditions (surface orientation, flux, temperature) can be varied systematically. This study provides a platform for simulations with atomistic spatial resolution, as was done some years ago for semiconductors [370, 371].

8. Simulations of graphene growth from silicon carbide

In spite of the fact that graphene growth from SiC is experimentally well established (Section 8), the corresponding theoretical effort is lagging behind. This is partially explained by the challenges this system presents, related, in the first instance, to the complexity of the SiC surface itself as was explained in Section 8 and the way graphene grows. Correspondingly, atomistic processes associated with graphene growth on the SiC surface are much less understood.

8.1. Explorations into growth of graphene on SiC

The previously described studies give useful information about the structure of the buffer and first graphene layers on SiC, but they do not really consider processes which might be relevant for the graphene growth. Several studies have been conducted to date in which some of the relevant processes were considered. In all these studies it was still assumed that the carbon for buffer and first layer graphene growth comes predominantly from the sublimation of SiC at step edges and also to a lesser degree from the sublimation of point defects on terraces.

Tang *et al.* [330] and Jakse *et al.* [331] have used different versions of Tersoff's EP [372, 333] based MD simulations to examine the transformation of carbon layers on top of SiC into graphene, and particularly the effect of annealing temperature and carbon coverage on the graphitization temperature which is the lowest temperature at which the graphene growth kicks in. This was accomplished by removing a number of Si layers from the top of 6H-SiC to provide a source of carbon atoms and then annealing to different temperatures and examining the structures that were subsequently formed after cooling down. In Ref. [330], using Tersoff potentials, it was found that a single layer of graphene clusters can only be produced after annealing a 6H-SiC surface with two Si layers removed and when the annealing temperature is greater than 1500 K, see Fig. 85(b,f); graphene did not form however if a single layer of Si atoms was removed from the 6H-SiC surface in which case only chains and ring-like structures were formed, Fig. 85(a,e). This result supports an assumption that an intermediate buffer layer between the graphene sheet and the SiC surface is formed during the graphene growth [68, 373] . When three layers were removed, small graphene clusters surrounded by amorphous C structures were seen, Fig. 85(c,g), while a graphene bilayer started to form when four layers of Si atoms were removed, Fig. 85(d,h).

Different results were obtained in [331]: using a modified Tersoff potential [374] it was found that graphene formed after annealing to between 1200 and 1260 K even when a single Si layer was removed. Furthermore, Jakse *et al.* [331] showed that using the original Tersoff potential parametrization gave a graphitization temperature that is about 100 K higher. The authors used a very similar methodology to that applied in [330], so the qualitative difference in the results must be attributed to subtle details of the simulations (e.g. the thermostat used, different annealing protocol, etc.). However, while both these simulations see graphene forming at temperatures similar to those observed in experiment, there is still no connection to observed growth processes. For example, there is no reference to nucleation at step edges or the observed step flow growth mode on SiC. Also, the way in which Si atoms are removed prior to MD simulations is artificial: in reality Si atoms are evaporated from SiC gradually at the same time as the buffer and graphene layers are formed. In spite of these drawbacks, these simulations have a potential for considering large cells in real time and hence provide a motivation for theorists to consider EP as a viable tool in further explorations of nucleation and growth on SiC.

A number of experimental observations have suggested that the nucleation and growth of graphene is influenced by SiC steps [68, 373, 375]. Kageshima *et al.* [376, 377] performed a series of DFT studies based on the geometry optimization of specific structures in order to uncover the main processes responsible for growth on SiC and the role of SiC steps. Two types of numerical experiments were performed inspired by the GCMC approach: (i) sublimation simulations in which, starting from some SiC surface structure, Si atoms were *removed* one-by-one and the structure thus obtained was relaxed, and (ii) aggregation simulations in which a C atom excess was created by *adding* C atoms to the surface one-by-one instead. In the case of each particular structure formed in this way the most energetically favorable geometry was sought, and its formation energy was calculated. For instance, in the case of a structure obtained by removing n Si atoms, the formation energy was calculated via

$$E_f(n) = E_{tot}(n) - E_{substr} + n\mu_{Si} \ ,$$

where $E_{tot}(n)$ is the total energy of the system with n removed Si atoms, E_{substr} is the initial energy of the system, and $\mu_{Si} = E_{SiC} - \mu_C$ is the chemical potential of Si atoms, related (assuming thermodynamic equilibrium) to the bulk energy of the SiC unit cell and the chemical potential of C atoms in the free-standing graphene. The authors also stressed that μ_{Si} can be controlled by Si gas pressure and temperature, assuming again a thermodynamic equilibrium between the Si atoms on the surface during growth and in the gas phase after their sublimation. Then, differences between formation energies, $\Delta E(n) = E_f(n) - E_f(n-1)$, were used to understand the energetics of adding (removing) C (Si) atoms to (from) the surface. The authors called these differences "growth barriers", however, this may be misleading as these are only differences in energies between two stable structures; the actual energy barriers must be larger.

In Fig. 86 the two types of calculations are compared. It is seen that in both cases a graphene layer is formed. In the cases (b) and (f) this is the buffer layer as it is still bound to the SiC; however, a proper graphene layer is seen to be formed in (c) after adding sufficient numbers of C atoms to the simulation cell, with the layer underneath serving as the buffer. In spite of some similarities in both cases, there are important differences. In particular, there is a considerable reconstruction of the surface layers in the sublimation case (for instance, Si vacancies may trap C atoms), and also the formation energies in the addition case are

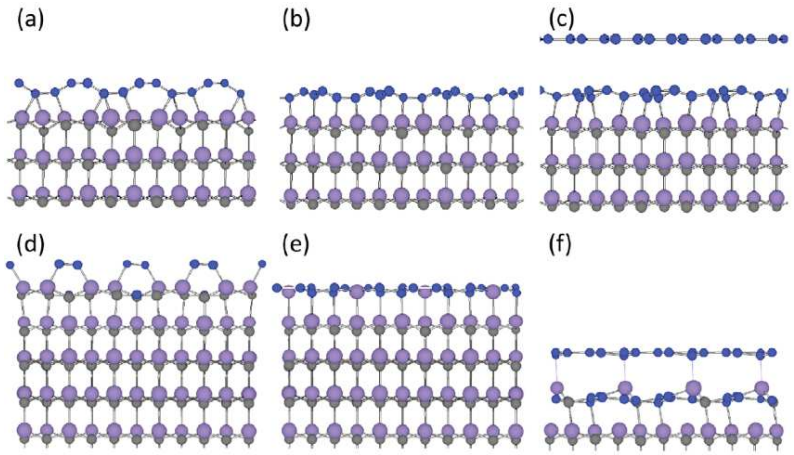

Figure 86: DFT relaxed geometries after adding C atoms (top panels) or removing Si atoms (bottom panels). The number of excess C atoms is: 4 (a,d), 5 (b,e) and 15 (c,f). Large and small circles correspond to Si and C atoms, respectively. [Reproduced from [377] by permission of IOP Publishing. All rights reserved.]

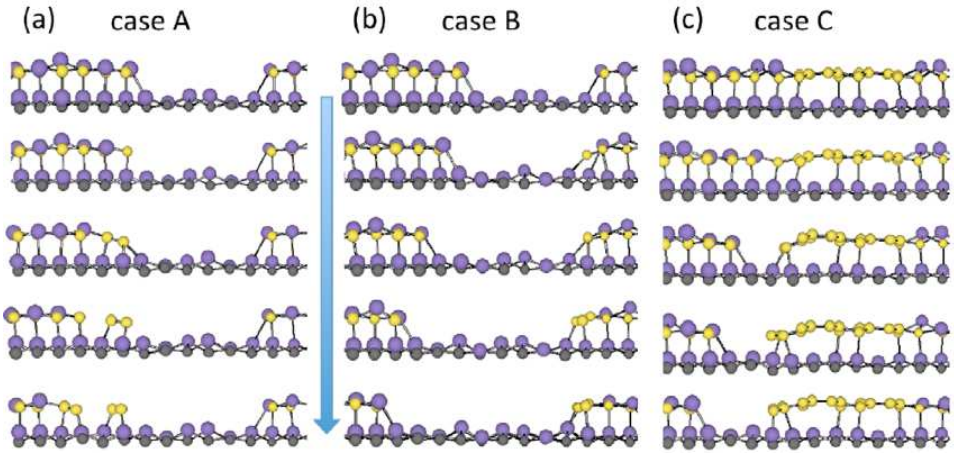

Figure 87: DFT relaxed geometries related to different possible routes of graphene growth near the steps. (a) Si atoms are removed from one of the steps; (b) while Si atoms are removed, the excess C atoms are moved across to the other step and form C aggregates; (c) a graphene ribbon is prepared, and excess C atoms are moved to its edge near the opposite step. [Reproduced from [377] by permission of IOP Publishing. All rights reserved.]

generally lower than in the sublimation case, i.e. it follows from these calculations that the sublimation route is generally harder.

In order to investigate the role of SiC steps in supplying excess C atoms to the surface, Kageshima *et al.* [377] also simulated several possible growth scenarios at the steps using again a series of simple relaxation calculations as shown in Fig. 87. Three cases were considered. In the first two, when Si atoms were removed, then either no additional steps were taken (case A), or excess C atoms were moved to the opposite step (case B). In the third case a graphene ribbon was prepared near one step and the excess C atoms were taken to its edge near the other step (case C). In case A only C dimers are formed; in case B a C aggregate forms serving as a nucleus for graphene growth. Finally, in case C the migrating C atoms help to increase the width of the ribbon. Formation energy calculations showed that the C atoms preferentially aggregate at step edges from where graphene starts to grow. This process is assisted by C atoms attaching to the edges of the graphene islands. Based on these observations a growth mechanisms was suggested [377] whereby carbon atoms released by one step aggregate at adjacent steps, and eventually grow to form the buffer layer. This mechanism obviously requires the diffusion of C atoms on SiC which has not been investigated. However, the authors raised a number of important issues which must also be addressed, for example, how Si atoms

that desorb under the buffer layer are able to escape and what effect this may have on the growth. Also, as pointed out in [378], the readsorption of Si to reform SiC could be another important process, as yet not considered, in the growth of graphene from SiC in a gaseous environment.

8.2. Simulations of growth dynamics

In order to understand the growth process of graphene on SiC Ming and Zangwill [379] studied the growth using both rate equations and one-dimensional KMC simulations. In the latter case it was suggested how the energy barriers for the various growth processes involved, such as nucleation at steps and growth of already nucleated graphene sheet, i.e. propagation of both the first and second layers, could be calculated from comparison with experiment. Unlike graphene growth on transition metals, first principles calculations of the barriers are not yet available as the structure of the buffer layer found on SiC is not yet fully understood; moreover, the steps on this layer have an unknown structure. Therefore, simulations of kinetics of growth based on fully first principles calculations of the barriers and processes have not yet been done to our knowledge.

In the KMC modeling [379] triple-bilayer (half unit cell) steps formed on a high-index (vicinal) SiC surface consisting of long terraces separated by steps, were considered. These steps act as nucleation sites for graphene growth, which propagates by the sublimation of Si atoms from a unit of the SiC step and its subsequent replacement by a unit area of graphene, because of mass conservation. In this model the buffer layer is assumed to be reconstructed from the SiC terrace immediately upon its exposure to the surface. The processes involved in this model for the growth are shown schematically in Fig. 90. In (a) an empty step is shown (green). With the nucleation rate of $r_{nuc} = v_0 \exp(-E_{nuc}/k_B T)$, where E_{nuc} is the corresponding barrier and $v_0 \approx 10^{12}$ s^{-1} the attempt frequency, the embryonic graphene sheet appears at the step as shown in (b). The effective nucleation barrier includes the combined effects of the Si atoms sublimating, the C atoms recrystallizing and the graphene growing at the step edge. The next step in the growth process is the propagation of the nucleated graphene sheet leading to an increase in the width of the graphene strip. This occurs via SiC step (red) sublimation, Fig. 90(c), when the step unit disappears and in its place a graphene strip is produced at a rate $r_{prop} = v_0 \exp(-E_{prop}/k_B T)$ with E_{prop} being the corresponding effective energy barrier. As the strip propagates, it may either run into an empty SiC step as shown in (d), or another graphene strip on the upper terrace, demonstrated in (f). In the first case the strip can "climb over" the upper terrace at the assumed rate r_{prop} and continue to propagate, as shown in (e); in the latter case the two strips coalesce, with the same assumed rate r_{prop}, see the transition from (f) to (g). Both of these processes cause a step edge to be covered by a graphene layer. After the SiC step is covered by the single layer of graphene, a second layer of graphene can nucleate underneath the graphene layer as schematically shown in (h), at the same rate r_{nuc} as used for the first layer nucleation. The second layer strip will then grow, see (i), at the rate of r_{prop} or at the slower rate of r'_{prop} related to a larger barrier E'_{prop}. The slower propagation rate of the second layer sandwiched between the first layer and the SiC surface is expected to be due to the fact that it must be more difficult to sublimate Si atoms from the SiC with the first graphene layer already present above. Because of the same reason, an assumption of the same nucleation rate for the second layer, used in this study, must also lead to a significant overestimation of the rate.

To model growth on the SiC surface, simulations consisting of 5000 steps were made, and up to 10^6 independent runs were averaged to accumulate enough statistics. Initially the graphene coverage of the surface was investigated as a function of the energy barrier difference $\Delta E = E_{nuc} - E_{prop}$. For this the dependence of the graphene coverage of the first layer Θ_1 on the total coverage Θ as well as the vicinal angle ϕ were considered. It was found that for increasing ΔE the coverage of layer one, Θ_1, decreases. This is suggested to be because when ΔE is large (and the nucleation barrier is much larger than the propagation barrier), the nucleation of new strips is less likely than the propagation of existing ones. In this case "climb over" steps are proposed to occur more frequently and second layer nucleation happens sooner. Since the second layer will have a longer time to grow, it will end up being larger, hence the first layer coverage decreases. As ΔE is further increased the probability of nucleation of the second layer is also reduced and the coverage of both layers becomes balanced. At $\Delta E = 0$ the step nucleation happens almost simultaneously, and then growing strips coalesce when sufficient overall coverage is achieved. The dynamics of growth was also found to depend on the difference $\Delta E' = E'_{prop} - E_{prop}$ of the propagation barriers between the second and first layers: as one would expect, the first layer coverage increases substantially with the increase of $\Delta E'$ as the propagation of the first layer is preferable. It is then suggested that the results of the simulations

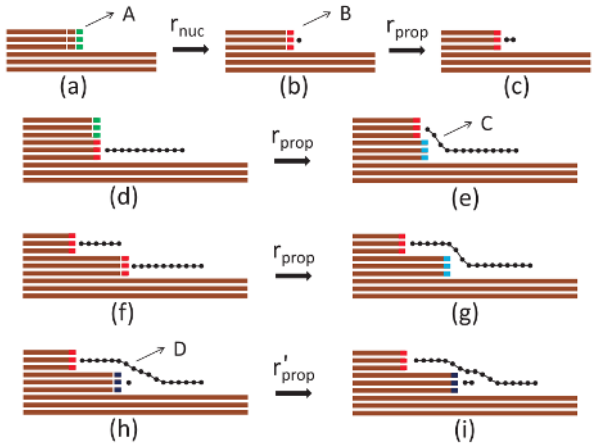

Figure 88: The kinetic processes for graphene growth on SiC used in the simulation in [379]. In the initial step structure (a) the Si atoms in the green cell are extracted, leaving a nucleus of the graphene cell formed (b), which then propagates to the left (c) by consuming the next SiC cell in the same manner. When the propagating graphene consumes the whole terrace (d), the graphene sheet propagates up carpeting the step (e). Alternatively, nucleation may happen at the step of the upper terrace (f), in which case the two graphene sheets may coalesce (g) upon further propagation. Once the step is fully covered with the graphene sheet as in (e) or (g), the step below is freed and the nucleation of the second layer underneath the first one may then start (h) and subsequently propagate further (i). [Reprinted with permission from [379]. Copyright (2011) by the American Physical Society.]

for both layers as a function of the total coverage can be used to extract the three parameters of the model (E_{nuc}, E_{prop} and E'_{prop}) from corresponding experimental dependencies.

It was also proposed that there is another way to extracting barriers, based on comparing directly observed on the surface, and simulated, distributions of strips with respect to their width. The comparison of experimental LEEM images of the graphene growth in Fig. 89 with simulated images using the KMC method shows that for increasing ΔE the number of strips decreases and the width of single strips becomes larger and the strips cover many steps. The best agreement with experiment is achieved for $\Delta E = 0$. The calculated strip width distributions demonstrate further details of the first and second layer growth. For instance, a uniform distribution upon the increase in the nucleation energy barrier E_{nuc} is observed, and this behavior is explained by the authors due to the fact that the "climb over" and coalescence processes occur at step edges during growth very rapidly.

This paper also presents a mean-field rate equation analysis for the growth mechanism described in Fig. 88 [379]. For this, four different types of steps are defined, identified in Fig. 88 as: (A) a bare SiC step (green); (B) a step which has a layer of graphene segment attached to it (red); (C) a step covered by a layer of graphene (blue), and (D) a step which has a second layer of graphene segment attached (purple). The proposed rate equations describe how the different steps are lost and gained. Steps (A) are lost by first layer nucleation events and climb-over processes. (B) steps are gained from nucleation events and lost from coalescence with other strips, whereas (C) steps are lost from second layer nucleation events and gained from both climb-over processes and the coalescence of steps. Finally, (D) steps are only created from the nucleation of the second graphene layer, i.e. they require type (C) steps to proceed. These rate equations provide good comparison with the KMC simulation results.

In further work by the same authors [380] graphene growth on a different type of SiC surface which contains nano-facets was studied using a similar method. In this paper nano-facets are described as several closely and evenly spaced triple bilayer steps on the SiC surface. These facets form when vicinal SiC with triple bilayer steps is heated to the graphitization temperature. The steps become bunched together on the surface, which is suggested to occur in order to minimize the surface free energy. Fig. 90(a) shows a nano-facet. The initial angle that the nano-facet makes with respect to the basal plane depends on the orientation of the substrate and the growth conditions. It is also dependent on the width and the spacing between subsequent steps.

For growth on the nano-facet it is assumed that the bottom layer nucleates first with the rate $r_{nuc} = v_0 \exp(-E_{nuc}/k_B T)$, as shown in Fig. 90(a,b). Then the growth continues up the steps of the facet with

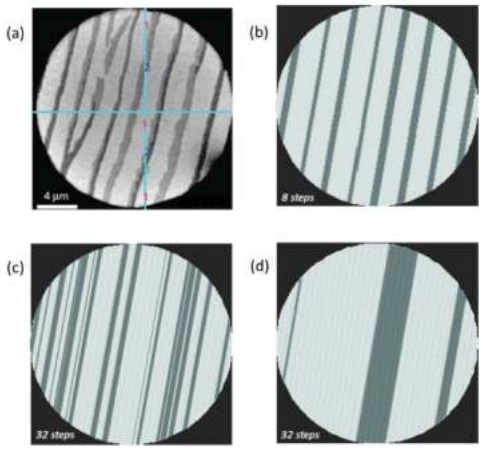

Figure 89: LEEM image (a) from [291] of graphene grown on SiC is compared with the simulated ones using KMC employing: $\Delta E/k_BT = 0$ (b), 5.8 (c) and 11.6 (d). The darker areas indicate that more than one graphene layer is present. The total coverage is 0.25, the vicinal angle is 0.9° and $\Delta E'$ was assumed to be zero. [Reprinted with permission from [379]. Copyright (2011) by the American Physical Society.]

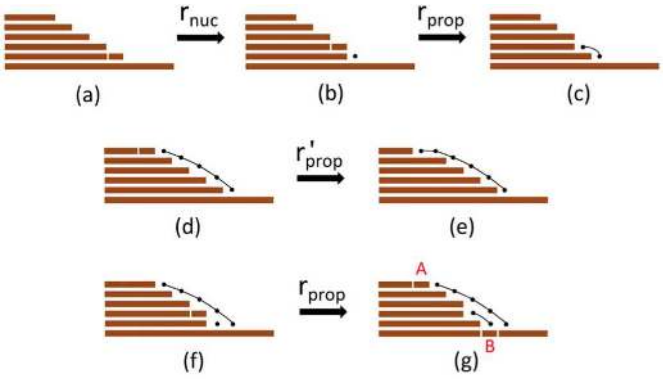

Figure 90: The kinetic processes accounted for in the KMC model for the growth of graphene on a nano-facetted surface [380]: (a) initial structure of the nano-facet; (b) a graphene layer nucleates at the bottom terrace with the rate r_{nuc} and then (c) propagates up the step with the rate r_{prop} until (d) it reaches the upper terrace where (e) the growth proceeds with a reduced rate $r'_{prop} < r_{prop}$; once the step is fully covered with the carpet of graphene first layer, the second layer underneath it nucleates (f) and start propagating up the step (g) with the rate r_{prop}. A and B are the step units at the edges of the top and the bottom terraces used for determining the fracture angle θ indicating the slope of the nano-facetted step. [Reproduced from [380] by permission of IOP Publishing. All rights reserved.]

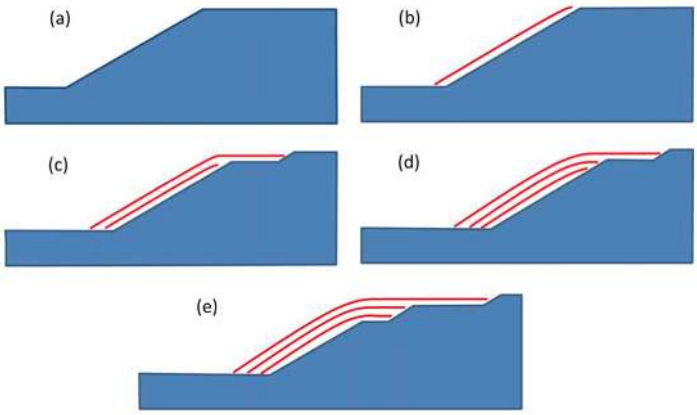

Figure 91: A possible formation process of graphene multilayers on a fractured nano-facet. [Reproduced from [380] by permission of IOP Publishing. All rights reserved.]

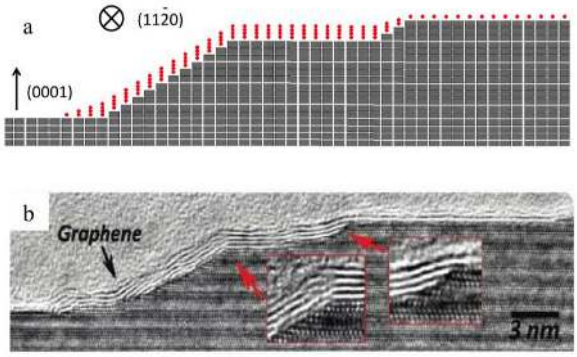

Figure 92: Images of graphene growth on a nano-facet from (a) a KMC simulation with total surface coverage $\Theta = 0.8$, $T = 1800$ K, $E_{nuc}/k_BT = 7.7$, and E'_{prop}/k_BT being either 3.9 or 7.1 for the top and the lower layers, respectively, and (b) a TEM image adapted from Robinson *et al.* [381]. [Reproduced from [380] by permission of IOP Publishing. All rights reserved.]

the propagation rate $r_{prop} = v_0 \exp(-E_{prop}/k_BT)$. As a complete coverage of the facet is almost always observed in experiments, the propagation barrier E_{prop} was set equal to zero, assuming that the propagation is the fastest kinetic process. Once the propagating strip reaches the top layer it will continue growing on the (0001) plane with the growth rate $r'_{prop} = \nu_0 \exp(-E'_{prop}/k_BT)$ which is assumed to be lower than the propagation rate up the step. This was concluded on the basis of analyzing experimental data on growth on multifaceted surfaces when it was noticed that many layers of graphene grow on the nano-facet before growth occurs on the (0001) plane; this seems to be a reasonable assumption since sublimation of Si atoms should be easier at the steps than on terraces. Once the first layer has grown over a step, as with the case of the vicinal surfaces [379] (see above), the second layer can nucleate underneath, Fig. 91 (f), and continue growing in the same way as the first layer, see (g).

Fig. 91 shows the formation process schematically where the fracturing of the nano-facet occurs after the first layer has started to propagate on the upper terrace shown in (b). Since its further propagation on the terrace would be slower than the propagation up the facets, the second layer quickly forms and propagates up as demonstrated in (c). This is followed by the formation and climbing (d) of the third layer and the corresponding fracturing of the original nano-facets at the top (e) by the second and third layers.

The results of the KMC simulations compare well with experimental TEM images of graphene growth as seen in Fig. 92. Both show graphene growth beginning sharply on the bottom terrace of the facet and being continuous along the nano-facet to the basal plane. The morphology of the surface imaged by TEM in Fig. 92(b) is the same as seen in Fig. 91(e), where two small nano-facets have been fractured from the original facet, one with a height of two triple bilayers and the other with a height of one triple bilayer.

Figure 93: AFM images of graphene growth on SiC at 1873 K and with a background pressure of Si of 1×10^{-5} torr. The field of view is 10 μm. [Reprinted with permission from [301]. Copyright (2009) by the American Physical Society.]

In order to quantify the fracturing of the nano-facet during the graphene growth in their KMC simulations, Ming and Zangwill [380] introduced the fracture angle θ characterizing the slope of the nano-facetted step with respect to the basal plane direction. Various distributions of the angle were obtained for different values of the difference between the nucleation and terrace propagation barriers $\Delta E_f = E_{nuc} - E'_{prop}$: for small ΔE_f the distribution is Gaussian, but at larger values it becomes a power-law. It was suggested that by comparing the calculated angle distributions with experimental observations of the fracture angle, ΔE_f can be determined.

8.3. Finger-like growth: phenomenological models

We shall finish this review of the literature by discussing the use of phenomenological models developed to explore the growth of graphene on SiC. The obvious advantage of such a treatment is that these works often suggest relevant atomistic processes which may then be modeled using *ab initio* methods. The interesting morphological characteristics of graphene grown on SiC by heating to 1873 K and then exposed to Si at a pressure of 1×10^{-5} torr take the form of finger-like structures as seen in Fig. 93. These observations motivated Borovikov and Zangwill [301] to use a continuum model to model the growth of graphene islands on SiC in order to understand the mechanism of growth of these peculiar features. Though the model was motivated by growth under specific conditions, because the same finger-like structures seen in Fig. 93 have also been observed under UHV conditions, this could suggest that similar growth processes occur for different conditions.

Graphene is assumed to form when the SiC layer which lies directly below the buffer layer decomposes. The released carbon then recrystallizes underneath the step to form a new buffer layer with the old buffer layer forming quasi-free-standing graphene. The authors assume that the decomposition of SiC step edges is dependent on the local curvature of the growth front. They then write down a continuum equation for the evolution of step height, $h(x,t)$,

$$\frac{\partial h(x,t)}{\partial t} = -V - aV\frac{\partial^2 h(x,t)}{\partial x^2} + \sigma\Gamma\frac{\partial^2 h(x,t)}{\partial x^2} - \sigma D\frac{\partial^4 h(x,t)}{\partial x^4} \ , \tag{30}$$

where the velocity of the growth front is V, a is the lattice constant of SiC, $\sigma = a^3\gamma/k_BT$ (γ is the SiC step stiffness), $\Gamma = \nu\exp(-E_1/K_BT)$ is the mean rate at which atomic species detach from a straight SiC step and $D = a^2\nu\exp(-E_2/K_BT)$ is the edge diffusion constant. The second term in Eq. (30) describes the change in the rate of step edge evaporation due to curvature. Thus, perturbations to a flat growth front which produce a concave (convex) region have a higher (lower) rate of decomposition. The authors also suggest a physical origin for this term whereby the release of heat by the recrystallization of carbon atoms into a new buffer layer increases the local temperature and drives further decomposition. The exact meaning of the last two terms in the above equations can be found in [301], but essentially the third term describes detachment of carbon atoms and eventual reattachment after diffusion along a terrace, and the fourth term models the diffusion of adatoms along a step edge.

The authors perform a linear stability analysis of Eq. (30) by assuming a solution of the form,

$$h(x,t) = -Vt + \varepsilon(t)\sin(2\pi x/\lambda) \ ,$$

where $\varepsilon(t)$ is the amplitude of a perturbation with wavelength λ. Growth or decay of this amplitude (and therefore the step edge) occurs exponentially when λ is greater or less than some critical wavelength. The wavelength for which growth occurs the fastest is given by

$$\lambda_m = \sqrt{\frac{8\pi^2\sigma D}{aV - \sigma\Gamma}}$$

and its temperature "phase diagram" is shown in Fig. 94. Using estimates for the various parameters occurring in Eq. (30) the authors plot this critical wavelength as a function of temperature for a range of pressures of SiC and thus obtain regions for which curvature effects drive instabilities at the growth front, producing the observed finger-like features during growth. Their analysis produces two temperatures of interest, T_G and T_S, both indicated in the Figure. Below T_G no graphene growth occurs and above T_S the growth front is stable so that for $T > T_S$ no finger-like structures are expected to grow. For the unstable growth, the values they obtain for λ_m agree well with the separation between fingers found in the experiments described in Fig. 93. Further, experimental observations of growth at higher pressures see only straight steps which agrees with the results shown in Fig. 94. Thus, the results obtained using continuum modeling of the growth process on SiC agree semi-quantitatively with experimental observations.

9. Discussion

Though much progress has been made since 2006 in understanding and controlling the growth of graphene on metals and SiC at experimental level, it is worth briefly pointing out that there are still unaddressed or unanswered questions that suggest future directions of research and new architectures based on graphene. First, only a limited region of the growth parameter space has been explored in a systematic manner. Systematic studies with varying growth temperature, carbon precursor pressure, or inert gas back-pressure, for instance, are needed in order to understand better the extent to which the structure (e.g. strain, defect density, number of layers) of graphene can be controlled. Such studies are usually time-consuming if performed with *ex situ* approaches, but may be considerably speeded up with the help of *in operando* analysis. This poses another problem, that of implementing *in operando* analysis in constrained growth environments, especially at high temperatures (above 1800 K) and pressures (above 10^{-6} mbar).

The case of graphene growth on SiC (e.g., how can a high quality buffer layer be prepared?) and on Cu foils (e.g., how do substrate defects impact graphene nucleation and structure?) under close-to-ambient-pressure reactors is a telling example. Probes exploiting light scattering seem here the best candidates. Overall, by extending the range of conditions accessible to *in operando* analysis and by more systematic exploration of the growth parameter space, one may expect, for example, new graphene growth modes (e.g. spiral, step-flow) to be unveiled. Most growth studies are motivated by the prospect of preparing high quality, defect-free graphene.

Obviously defect densities have been indeed much decreased in graphene samples on both metals and SiC, still it remains difficult to eliminate completely some kinds of defects, such as wrinkles, which actually do not form upon growth but during cooling down. Although strategies for preventing the formation of such defects remain to be imagined, one may expect that strain and substrate engineering may provide interesting angles of attack. In-plane rotations between successive layers in multilayers, which can also be viewed as defects, offer stimulating horizons for manipulating charge carrier transport in graphene. This example illustrates that defect engineering, rather than defect minimization, is also a stimulating avenue of research. Other examples include periodic modulations of strain and chemical doping (by impurities replacing C atoms for instance) or patterned growth of graphene. Only a few research studies to date report the bottom-up demonstration of such advanced graphene structures, mostly because few possibilities have been explored.

On the theoretical side, there is still much to be done to understand fully the growth mechanisms on different substrates and via different growth methods. Modeling the process of decomposition of hydrocarbons has only just started. In Fig. 2 we showed as an example all essential processes which happen in the CVD growth of graphene when ethene molecules E are deposited on the hot metal surface: upon impact with the surface the molecules decompose into intermediate species E_d (C_xH_y in this case) via a complex chain of interconnected dehydrogenation, isomerization and hydrogenation reactions. The original molecules E and the decomposed species E_d may diffuse on the surface, but their mobility is yet to be understood. Eventually, carbon monomers M and dimers D are produced which must be quite mobile. Because of the strong C-C

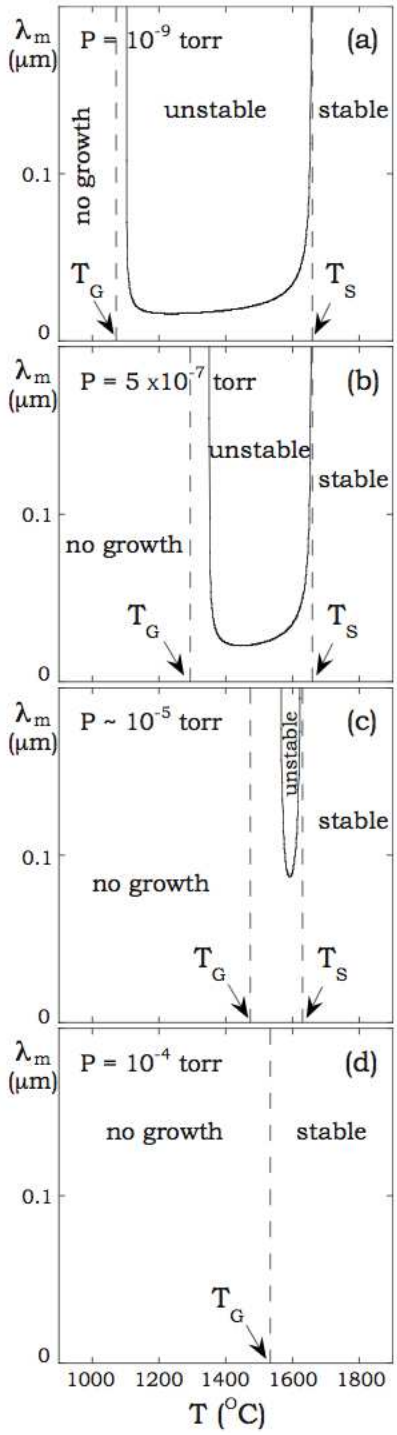

Figure 94: Temperature and pressure dependence of the fastest growing wavelength obtained from the analysis of the linear stability of Eq. (30). [Reprinted with permission from [301]. Copyright (2009) by the American Physical Society.]

bonds as compared to much weaker C-H bonds, one may expect the dimer concentration to be much larger than that of monomers. Colliding carbon species form larger clusters C which eventually nucleate islands G which grow if the flux of adsorbing species at their boundary exceeds the desorption flux. Island growth depends on whether they have reached their critical size. The H atoms, initially adsorbed on the surface after the dehydrogenation reactions, will freely diffuse across the surface and may either attach to the species E and E_d of the feedstock thereby transforming them, or may instead collide with other H atoms in which case H_2 molecules are formed. The latter can easily desorb, and this must be the main mechanism for the hydrogen to leave the surface as H atoms are relatively strongly bound to the surface as compared to the hydrogen molecules. Correct understanding of the multitude of these reactions for various hydrocarbon molecules and hence the distribution of their products (C clusters) on the surface during growth is necessary for correctly modeling growth kinetics (e.g. Avrami vs. Gompertzian type of kinetics [267]). It also seems plausible that the various reactions sketched above and their rates (and hence their significance in the global picture of growth kinetics) should depend on the particular hydrocarbon feedstock used. For instance, in the case of ethene one would expect abundance of carbon dimers as compared to monomers, whereas in the case of methane feedstock one might think that the opposite would be true.

Another important point affecting kinetics must be the spatial distribution of all species on the surface during the growth and their diffusion, as the reactions can only happen when the species collide. Clusters of various sizes and shapes may be formed and their mobility and ability to serve as nuclei for further growth would vary.

The corresponding theoretical simulations and experimental data that would help in understanding all these processes are either sketchy or simply missing.

The first steps in addressing the above issues from the theoretical side could be done by performing detailed *ab initio* based MD simulations in which various hydrocarbon molecules are made to impinge upon the surface and their decomposition is studied as a function of their kinetic energies. Note that care should be taken in considering correctly the dissipation of energy into the surface from the impinging molecules in these MD simulations: equilibrium thermostats which are widely applied in this kind of problems may not actually be appropriate (see e.g. discussion in [382]). The subsequent processes such as diffusion, further decomposition, cluster formation and nucleation and growth, can be investigated, e.g. with KMC based methods.

Modeling TPG growth is somewhat similar to that of the CVD as we described above, but there are important differences since one would expect that the impact of the hydrocarbon molecules with the surface is not significant in the decomposition of the molecules since deposition is performed when the surface is kept at room temperature. Instead, one starts with intact adsorbed molecules on top of the surface, then the surface is gradually heated up, the molecules become mobile, collide with each other and dehydrogenation reactions commence. Therefore, the distribution of various C_xH_y species on the surface during nucleation and growth may in this case be different to the CVD case, thereby modifying the kinetics. Consequently, MD simulations in the case of TPG may be unnecessary and what is required is detailed KMC-like modeling based on transition rates calculated from first principles simulations.

Further, kinetic modeling of nucleation events in real time, apart from a number of simulations made using the GCMC method within a TB Hamiltonian, are practically non-existent, and only a single KMC simulation of steady-state growth exists to date. An understanding of nucleation would enable one to rationalize the formation of rotational domains and discover how this can be prevented, if desired. Better understanding of the diffusion of clusters of various sizes and shapes, including large ones to explain the Smoluchowski ripening mechanism observed in many systems, will help in learning their detailed role in nucleation and growth. More also needs to be done on the formation of defects during growth, their mobility and the mechanism of their "healing" (e.g. by diffusion to the edges, coalescence or by decomposition of hydrocarbon molecules evaporated onto the surface). There are a number of simulations of particular aspects for the given system, but no systematic simulations even for a single growth method and a single transition metal has been done.

The situation with SiC is even worse because of the sheer complexity of this system: our understanding of the growth mechanism is at a rudimentary stage, and there are only a few simulations in which Si sublimation was modeled properly. However, without modeling sublimation in detail it is not possible to understand the formation of the buffer layer or assess, for instance, whether one needs a high graphitization temperature in order to promote both Si sublimation and C-clustering, or only the sublimation process.

Challenges posed by this very complicated system clearly show limitations of the current toolkit of computational methods, and hence the development of cheaper techniques retaining the precision of the most expensive methods is required so that larger systems can be studied. Problems in modeling realistic kinetics of growth of graphene call for applications of adaptive KMC based techniques [383]; however, at the moment for practical calculations these can only be combined with TB or EP methods; using standard DFT methods to explore the PES is still prohibitively expensive.

Note added in proof

Since this review went to press, we have become aware of several articles that bear directly on the nucleation and growth of graphene. Kim et al. [384] examined the growth of graphene on copper by using the chemical vapor deposition (CVD) of methane (CH_4).

Methane is deposited onto the Cu surface, decomposes, and the reaction products desorb, except for the carbon. This leads to an effective flux of carbon atoms and a supersaturation at the surface, that is, a concentration of carbon adatoms which exceeds that at equilibrium. The concentration continues to rise linearly until, at a critical supersaturation, graphene nuclei form and begin to grow. This supersaturation then drops until the nucleation ceases, and the carbon adatom concentration reaches a steady state, where the deposited atoms are incorporated into the growing domains. The resulting morphology of the graphene layer depends on the temperature and exposure time to the methane. The temperature ranges from 720 to 1000°C and the exposure time from a flash exposure to 30 min. Many small nucleation centres are discernible at the lower temperatures, but there are fewer and larger such centres at increasing temperatures. This is typical of growth dominated by diffusion. Even at the highest temperatures, however, the nuclei do not coalesce to form a continuous film (with grain boundaries). The light regions between the dark domains is the underlying copper substrate. We see from these samples that continuous films are obtained only for temperatures of about 1000°C and exposures of 30 min. To understand the mechanisms behind these results, the number of nuclei as a function of temperature taken from SEM images at the flash exposure were plotted as the natural logarithm of the density of nuclei as a function of $1/T$. There resulted two straight lines: one at low-temperatures (< 850°C) and the other at high-temperatures (> 850°C). This is suggestive of different mechanisms operating in the two temperature regimes and the authors identify these as the attachment-dominated regime at low temperatures, and the desorption-dominated regime at high temperatures. At low temperatures, desorption is negligible, so the formation and growth of clusters is dominated by the diffusion of carbon adatoms on the surface and their capture at the perimeters of the nuclei. At higher temperatures, desorption becomes activated (this has a much higher activation barrier than diffusion), so the nucleation rate is dominated by desorption.

Nemec et al. [385] used van der Waals corrected Perdew-Burke-Ernzerhof density functional theory to calculate surface phase diagrams of the precursor phase, monolayer, and bilayer graphene on the Si face of 3C-SiC(111). These calculations enable several observations related to the growth of graphene on these surfaces to be rationalized. The background pressures of Si and C are low in UHV and not well-defined, which leads to widely-varying experimental conditions and inferior morphologies. Maintaining a controlled Si partial pressure at a constant high temperature appears to be the most important factor in producing homogeneous graphene layers. The main conclusion from this study is that near-equilibrum conditions may provide the best opportunities for the expitaxial growth of graphene on SiC.

Acknowledgement

J.P. de B. was supported through a studentship in the Centre for Doctoral Training on the Theory and Simulation of Materials at Imperial College London funded by EPSRC under grant number EP/G036888/1, while H.T. was supported by EPSRC under grant number EP/K502868/1.

References

[1] J. C. Slonczewski, P. R. Weiss, Band structure of graphite, Phys. Rev. 109 (1958) 272–279.

[2] A. H. Castro Neto, F. Guinea, N. M. R. Peres, Drawing conclusions from graphene, Physics World 19 (2006) 33.

[3] K. S. Novoselov, A. K. Geim, S. V. Morozov, D. Jiang, Y. Zhang, S. V. Dubonos, I. V. Grigorieva, A. A. Firsov, Electric field effect in atomically thin carbon films, Science 306 (2004) 666–669.

[4] K. S. Novoselov, D. Jiang, F. Schedin, T. J. Booth, V. V. Khotkevich, S. V. Morozov, A. K. Geim, Two-dimensional atomic crystals, Proceedings of the National Academy of Sciences of the United States of America 102 (2005) 10451–10453.

[5] K. S. Novoselov, A. K. Geim, S. V. Morozov, D. Jiang, M. I. Katsnelson, I. V. Grigorieva, S. V. Dubonos, A. A. Firsov, Two-dimensional gas of massless Dirac fermions in graphene, Nature 438 (2005) 197–200.

[6] C. Berger, Z. Song, T. Li, X. Li, A. Y. Ogbazghi, R. Feng, Z. Dai, A. N. Marchenkov, E. H. Conrad, P. N. First, W. A. de Heer, Ultrathin epitaxial graphite: 2d electron gas properties and a route toward graphene-based nanoelectronics, J. Phys. Chem. B 108 (2004) 19912–19916.

[7] Y. Zhang, Y. Tan, H. L. Stormer, P. Kim, Experimental observation of the quantum Hall effect and Berry's phase in graphene, Nature 438 (2005) 201–204.

[8] A. H. C. Neto, F. Guinea, N. M. R. Peres, K. S. Novoselov, A. K. Geim, The electronic properties of graphene, Rev. Mod. Phys. 81 (2009) 109–162.

[9] C. Soldano, A. Mahmood, E. Dujardin, Production, properties and potential of graphene, Carbon 48 (2010) 2127–2150.

[10] P. Avouris, Graphene: Electronic and photonic properties and devices, Nano Lett. 10 (2010) 4285–4294.

[11] F. Bonaccorso, Z. Sun, T. Hasan, A. C. Ferrari, Graphene photonics and optoelectronics, Nature Photon. 4 (2010) 611–622.

[12] S. D. Sarma, S. Adam, E. H. Hwang, E. Rossi, Electronic transport in two-dimensional graphene, Rev. Mod. Phys. 83 (2011) 407–470.

[13] Y. Sun, Q. Wu, G. Shi, Graphene based new energy materials, Energy and Environmental Science 4 (2011) 1113–1132.

[14] K. S. Novoselov, V. I. Fal'ko, L. Colombo, P. R. Gellert, M. G. Chwab, K. Kim, A roadmap for graphene, Nature 490 (2012) 192.

[15] A. Hudson, Is graphene a miracle material?, 2011. URL: `http://news.bbc.co.uk/1/hi/programmes/click_online/9491789.stm`.

[16] P. R. Wallace, The band theory of graphite, Phys. Rev. 71 (1947) 622–634.

[17] S. V. Kusminskiy, D. K. Campbell, A. H. C. Neto, Lenosky's energy and the phonon dispersion of graphene, Phys. Rev. B 80 (2009) 035401.

[18] C. Lee, X. Wei, J. W. Kysar, J. Hone, Measurement of the elastic properties and intrinsic strength of monolayer graphene, Science 321 (2008) 385–388.

[19] S. Park, R. S. Ruoff, Chemical methods for the production of graphenes, Nature Nanotech. 4 (2009) 217–224.

[20] Y. Shao, J. Wang, H. Wu, J. Liu, I. A. Aksay, Y. Lin, Graphene based electrochemical sensors and biosensors: A review, Electroanalysis 22 (2009) 1027–1036.

[21] W. Choi, I. Lahiri, R. Seelaboyina, Y. S. Kang, Synthesis of graphene and its applications: a review, Critical Reviews in Solid State and Materials Sciences 35 (2010) 52–71.

[22] D. R. Dreyer, R. S. Ruoff, C. W. Bielawski, From conception to realization: An historial account of graphene and some perspectives for its future, Angew. Chemie Intern. Ed. 49 (2010) 9336–9344.

[23] P. N. First, W. A. de Heer, T. Seyller, C. Berger, J. A. Stroscio, J.-S. Moon, Epitaxial graphenes on silicon carbide, MRS Bulletin 35 (2010) 296–305.

[24] C. Riedl, C. Coletti, U. Starke, Structural and electronic properties of epitaxial graphene on sic(0001): a review of growth, characterization, transfer doping and hydrogen intercalation, J. of Physics D: Appl. Phys. 43 (2010) 374009.

[25] F. Schwierz, Graphene transistors, Nature Nanotech. 5 (2010) 487–496.

[26] A. A. Balandin, Thermal properties of graphene and nanostructured carbon materials, Nature Mater. 10 (2011) 569–581.

[27] A. H. C. Neto, K. Novoselov, New directions in science and technology: two-dimensional crystals, Rep. Prog. Phys. 74 (2011) 082501.

[28] M. Pumera, Graphene in biosensing, Mater. Today 14 (2011) 308–315.

[29] V. Singh, D. Joung, L. Zhai, S. Das Saiful, I. Khondaker, S. Seal, Graphene based materials: Past, present and future, Progr. Mater. Sci. 56 (2011) 1178–1271.

[30] A. F. Young, P. Kim, Electronic transport in graphene heterostructures, Ann. Rev. Cond. Matter Phys. 2 (2011) 101–120.

[31] M. Batzill, The surface science of graphene: Metal interfaces, CVD synthesis, nanoribbons, chemical modifications, and defects, Surf. Sci. Rep. 67 (2012) 83–115.

[32] F. Bonaccorso, A. Lombardo, T. Hasan, Z. Sun, L. Colombo, A. C. Ferrari, Production and processing of graphene and 2d crystals, Mater. Today 15 (2012) 564–589.

[33] H. Shen, L. Zhang, M. Liu, Z. Zhang, Biomedical applications of graphene, Theranostics 2 (2012) 283–294.

[34] R. J. Young, I. A. Kinlocha, L. Gonga, K. S. Novoselov, The mechanics of graphene nanocomposites: A review, Compos. Sci. Techn. 72 (2012) 1459–1476.

[35] Y. Zhang, L. Zhang, C. Zhou, Review of chemical vapor deposition of graphene and related applications, Acc. Chem. Res. 46 (2013) 2329–2339.

[36] I. J. Ford, Statistical mechanics of nucleation: a review, Proc. Instn Mech. Engnrs Part C: J. Mech. Eng. Sci. 218 (2004) 883–899.

[37] V. I. Kalikmanov, Nucleation Theory, Springer, 2012.

[38] I. J. Ford, Statistical Physics: an entropic approach, Wiley, 2013.

[39] I. J. Ford, Nucleation theorems, the statistical mechanics of molecular clusters, and a revision of classical nucleation theory, Phys. Rev. E 56 (1997) 5615–5629.

[40] S. A. Harris, I. J. Ford, A dynamical definition of quasibound molecular clusters, J. Chem. Phys. 118 (2003) 9216.

[41] M. Smoluchowski, Ann. Physik. (Leipzig) 21 (1906) 756.

[42] H. Vehkamäki, Classical Nucleation Theory in Multicomponent Systems, Springer, 2006.

[43] G. Binnig, H. Rohrer, C. Gerber, E. Weibel, Surface studies by scanning tunneling microscopy, Phys. Rev. Lett. 49 (1982) 57–61.

[44] P. K. Hansma, J. Tersoff, Scanning tunneling microscopy, J. Appl. Phys. 61 (1987) R1–R24.

[45] J. Tersoff, D. R. Hamann, Theory of the scanning tunneling microscope, Phys. Rev. B 31 (1985) 805.

[46] M. J. Rost, L. Crama, P. Schakel, E. Van Tol, G. B. E. M. van Velzen-Williams, C. F. Overgauw, H. Ter Horst, H. Dekker, B. Okhuijsen, M. Seynen, A. Vijftigschild, P. Han, A. J. Katan, K. Schoots, R. Schumm, W. van Loo, T. H. Oosterkamp, J. W. M. Frenken, Scanning probe microscopes go video rate and beyond, Rev. Sci. Instr. 76 (2005) 053710–053710.

[47] M. S. Hoogeman, D. G. van Loon, R. W. M. Loos, H. G. Ficke, E. de Haas, J. J. van der Linden, H. Zeijlemaker, L. Kuipers, M. F. Chang, M. A. J. Klik, J. W. M. Frenken, Design and performance of a programmable-temperature scanning tunneling microscope, Rev. Sci. Instr. 69 (1998) 2072–2080.

[48] T. A. Land, T. Michely, R. J. Behm, J. C. Hemminger, G. Comsa, STM investigation of single layer graphite structures produced on Pt(111) by hydrocarbon decomposition, Surf. Sci. 264 (1992) 261–270.

[49] P. Mallet, F. Varchon, C. Naud, L. Magaud, C. Berger, J.-Y. Veuillen, Electron states of mono- and bilayer graphene on SiC probed by scanning-tunneling microscopy, Phys. Rev. B 76 (2007) 041403(R).

[50] A. T. N'Diaye, S. Bleikamp, P. J. Feibelman, T. Michely, Two-Dimensional Ir Cluster Lattice on a Graphene moiré on Ir(111), Phys. Rev. Lett. 97 (2006) 215501.

[51] S. Marchini, S. Günther, J. Wintterlin, Scanning tunneling microscopy of graphene on Ru(0001), Phys. Rev. B 76 (2007) 075429.

[52] C. Riedl, U. Starke, J. Bernhardt, M. Franke, K. Heinz, Structural properties of the graphene-SiC(0001) interface as a key for the preparation of homogeneous large-terrace graphene surfaces, Phys. Rev. B 76 (2007) 245406.

[53] F. Varchon, P. Mallet, J.-Y. Veuillen, L. Magaud, Ripples in epitaxial graphene on the Si-terminated SiC(0001) surface, Phys. Rev. B 77 (2008) 235412.

[54] E. Loginova, N. C. Bartelt, P. J. Feibelman, K. F. McCarty, Evidence for growth by C cluster attachment, New J. Phys. 10 (2008) 093026.

[55] F. Hiebel, P. Mallet, F. Varchon, L. Magaud, J. Y. Veuillen, Graphene-substrate interaction on 6H-SiC $(000\bar{1})$: A scanning tunneling microscopy study, Phys. Rev. B 78 (2008) 153412.

[56] G. Otero, C. Gonzalez, A. L. Pinardi, P. Merino, S. Gardonio, S. Lizzit, M. Blanco-Rey, K. Van de Ruit, C. F. J. Flipse, J. Méndez, et al., Ordered vacancy network induced by the growth of epitaxial graphene on Pt(111), Phys. Rev. Lett. 105 (2010) 216102.

[57] J. Coraux, A. T. N'Diaye, C. Busse, T. Michely, Structural Coherency of Graphene on Ir(111), Nano Lett. 8 (2008) 565–570.

[58] P. Sutter, J. T. Sadowski, E. Sutter, Graphene on Pt(111): Growth and substrate interaction, Phys. Rev. B 80 (2009) 245411.

[59] L. B. Biedermann, M. L. Bolen, M. A. Capano, D. Zemlyanov, R. G. Reifenberger, Insights into few-layer epitaxial graphene growth on 4h-SiC$(000\bar{1})$ substrates from STM studies, Phys. Rev. B 79 (2009) 125411.

[60] N. Levy, S. A. Burke, K. L. Meaker, M. Panlasigui, A. Zettl, F. Guinea, A. H. C. Neto, M. F. Crommie, Strain-induced pseudo–magnetic fields greater than 300 tesla in graphene nanobubbles, Science 329 (2010) 544–547.

[61] J. Coraux, A. T. N'Diaye, M. Engler, C. Busse, D. Wall, N. Buckanie, F. J. M. zu Heringdorf, R. van Gastel, B. Poelsema, T. Michely, Growth of graphene on Ir(111), New J. Phys. 11 (2009) 023006.

[62] S.-Y. Kwon, C. V. Ciobanu, V. Petrova, V. B. Shenoy, J. Bareo, V. Gambin, I. Petrov, S. Kodambaka, Growth of semiconducting graphene on palladium, Nano Lett. 9 (2009) 3985.

[63] G. C. Dong, D. W. van Baarle, M. J. Rost, J. W. M. Frenken, Graphene formation on metal surfaces investigated by in-situ scanning tunneling microscopy, New J. Phys. 14 (2012) 053033.

[64] G. Binnig, C. F. Quate, C. Gerber, Atomic force microscope, Phys. Rev. Lett. 56 (1986) 930–933.

[65] F. J. Giessibl, G. Binnig, True atomic resolution on KBr with a low-temperature atomic force microscope in ultrahigh vacuum, Ultramicroscopy 42 (1992) 281–286.

[66] E. Meyer, Atomic force microscopy, Progr. Surf. Sci. 41 (1992) 3–49.

[67] F. J. Giessibl, Advances in atomic force microscopy, Rev. Mod. Phys. 75 (2003) 949.

[68] H. Hibino, H. Kageshima, M. Nagase, Epitaxial few-layer graphene: towards single crystal growth, J. Phys. D: Appl. Phys. 43 (2010) 374005.

[69] M. P. Boneschanscher, J. van der Lit, Z. Sun, I. Swart, P. Liljeroth, D. Vanmaekelbergh, Quantitative atomic resolution force imaging on epitaxial graphene with reactive and nonreactive AFM probes, ACS Nano 6 (2012) 10216–10221.

[70] K. S. Novoselov, A. K. Geim, S. V. Morozov, D. Jiang, Y. Zhang, S. V. Dubonos, I. V. Grigorieva, A. A. Firsov, Electric field effect in atomically thin carbon films, Science 306 (2004) 666–669.

[71] C. Berger, Z. Song, X. Li, X. Wu, N. Brown, C. Naud, D. Mayou, T. Li, J. Hass, A. N. Marchenkov, E. H. Conrad, P. N. First, W. A. de Heer, Electronic confinement and coherence in patterned epitaxial graphene, Science 312 (2006) 1191–1196.

[72] A. Reina, X. Jia, J. Ho, D. Nezich, H. Son, V. Bulovic, M. S. Dresselhaus, J. Kong, Large area, few-layer graphene films on arbitrary substrates by chemical vapor deposition, Nano Lett. 9 (2008) 30–35.

[73] M. L. Bolen, S. E. Harrison, L. B. Biedermann, M. A. Capano, Graphene formation mechanisms on 4H-SiC(0001), Phys. Rev. B 80 (2009) 115433.

[74] J. B. Hannon, R. M. Tromp, Pit formation during graphene synthesis on SiC(0001): In situ electron microscopy, Phys. Rev. B 77 (2008) 241204.

[75] Z. Sun, S. K. Hämäläinen, J. Sainio, J. Lahtinen, D. Vanmaekelbergh, P. Liljeroth, Topographic and electronic contrast of the graphene moiré on Ir(111) probed by scanning tunneling microscopy and noncontact atomic force microscopy, Phys. Rev. B 83 (2011) 081415.

[76] E. N. Voloshina, E. Fertitta, A. Garhofer, F. Mittendorfer, M. Fonin, A. Thissen, Y. S. Dedkov, Electronic structure and imaging contrast of graphene moiré on metals, Nature Sci. Rep. 3 (2013) 1072.

[77] E. Ruska, The early development of electron lenses and electron microscopy, Hirzel, 1980.

[78] M. Haider, S. Uhlemann, E. Schwan, H. Rose, B. Kabius, K. Urban, Electron microscopy image enhanced, Nature 392 (1998) 768–769.

[79] P. E. Batson, N. Dellby, O. L. Krivanek, Sub-ångstrom resolution using aberration corrected electron optics, Nature 418 (2002) 617–620.

[80] P. L. Hansen, J. B. Wagner, S. Helveg, J. R. Rostrup-Nielsen, B. S. Clausen, H. Topsøe, Atom-resolved imaging of dynamic shape changes in supported copper nanocrystals, Science 295 (2002) 2053–2055.

[81] J. A. Rodriguez-Manzo, C. Pham-Huu, F. Banhart, Graphene growth by a metal-catalyzed solid-state transformation of amorphous carbon, ACS Nano 5 (2011) 1529–1534.

[82] B. W. Smith, D. E. Luzzi, Electron irradiation effects in single wall carbon nanotubes, J. Appl. Phys. 90 (2001) 3509–3515.

[83] S. M. Irving, P. L. Walker, Interaction of evaporated carbon with heated metal substrates, Carbon 5 (1967) 399–402.

[84] G. Turner, E. Bauer, An ultrahigh vacuum electron microscope and its application to work function studies, Electron Microscopy 1 (1966) 163.

[85] W. Telieps, E. Bauer, An analytical reflection and emission UHV surface electron microscope, Ultramicroscopy 17 (1985) 57.

[86] W. Telieps, E. Bauer, The $(7 \times 7) \leftrightarrow (1 \times 1)$ phase transition on Si(111), Surf. Sci. 162 (1985) 163.

[87] E. Bauer, LEEM and UHV-PEEM: A retrospective, Ultramicroscopy 119 (2012) 18.

[88] R. M. Tromp, J. B. Hannon, A. W. Ellis, W. Wan, A. Berghaus, O. Schaff, A new aberration-corrected, energy-filtered LEEM/PEEM instrument. I. Principles and design, Ultramicroscopy 110 (2010) 852–861.

[89] T. Schmidt, S. Heun, J. Slezak, J. Diaz, K. C. Prince, G. Lilienkamp, E. Bauer, SPELEEM: Combining LEEM and spectroscopic imaging, Surf. Rev. Lett. 5 (1998) 1287.

[90] T. Ohta, F. E. Gabaly, A. Bostwick, J. L. McChesney, K. V. Emtsev, A. K. Schmid, T. Seyller, K. Horn, E. Rotenberg, Morphology of graphene thin film growth on SiC(0001), New J. Phys. 10 (2008) 023034.

[91] P. W. Sutter, J. Flege, E. A. Sutter, Epitaxial graphene on ruthenium, Nature Mater. 7 (2008) 406–411.

[92] E. Loginova, N. C. Bartelt, P. J. Feibelman, K. F. McCarty, Factors influencing graphene growth on metal surfaces, New J. Phys 11 (2009) 063046.

[93] R. van Gastel, A. T. N'Diaye, D. Wall, J. Coraux, C. Busse, N. M. Buckanie, F.-J. M. zu Heringdorf, M. H. von Hoegen, T. Michely, B. Poelsema, Selecting a single orientation for millimeter sized graphene sheets, Appl. Phys. Lett. 95 (2009) 121901.

[94] M. G. Lagally, Methods in Experimental Physics, volume 22, Elsevier, 1985, pp. 237–298.

[95] M. A. Van Hove, W. H. Weinberg, C. Chan, Low-energy electron diffraction, Springer-Verlag Berlin, 1986.

[96] U. Scheithauer, G. Meyer, M. Henzler, A new LEED instrument for quantitative spot profile analysis, Surf. Sci. 178 (1986) 441.

[97] N. Blanc, F. Jean, A. V. Krasheninnikov, G. Renaud, J. Coraux, Strains induced by point defects in graphene on a metal, Phys. Rev. Lett. 111 (2013) 085501.

[98] A. J. van Bommel, J. E. Crombeen, A. van Tooren, LEED and Auger electron observations of the SiC(0001) surface, Surf. Sci. 48 (1975) 463.

[99] H. Hattab, A. T. N'Diaye, D. Wall, G. Jnawali, J. Coraux, C. Busse, R. van Gastel, B. Poelsema, T. Michely, F.-J. M. zu Heringdorf, M. H. von Hoegen, Growth temperature dependent graphene alignment on Ir(111), Appl. Phys. Lett. 98 (2011) 141903.

[100] C. Vo-Van, A. Kimouche, A. Reserbat-Plantey, O. Fruchart, P. Bayle-Guillemaud, N. Bendiab, J. Coraux, Epitaxial graphene prepared by chemical vapor deposition on single crystal thin iridium films on sapphire, Appl. Phys. Lett. 98 (2011) 181903.

[101] I. Forbeaux, J.-M. Themlin, J.-M. Debever, Heteroepitaxial graphite on 6H-SiC(0001): Interface formation through conduction-band electronic structure, Phys. Rev. B 58 (2008) 16396.

[102] B. E. Nieuwenhuys, D. I. Hagen, G. Rovida, G. A. Somorjai, LEED, AES and thermal desorption studies of chemisorbed hydrogen and hydrocarbons (C_2H_2, C_2H_4, C_6H_6, C_6H_{12}) on the (111) and stepped [6(111) $\times$ (100)] iridium crystal surfaces; comparison with platinum, Surf. Sci. 155 (1976) 59.

[103] Y. Gamo, A. Nagashima, M. Wakabayashi, M. Terai, C. Oshima, Atomic structure of monolayer graphite formed on Ni(111), Surf. Sci. 374 (1997) 61.

[104] W. Moritz, B. Wang, M. Bocquet, T. Brugger, T. Greber, J. Wintterlin, S. Günther, Structure Determination of the Coincidence Phase of Graphene on Ru(0001), Phys. Rev. Lett. 104 (2010) 136102.

[105] S. K. Hämäläinen, M. P. Boneschanscher, P. H. Jacobse, I. Swart, K. Pussi, W. Moritz, J. Lahtinen, P. Liljeroth, J. Sainio, The structure and local variations of the graphene moiré on Ir(111)., submitted (2014).

[106] E. Loginova, S. Nie, K. Thürmer, N. C. Bartelt, K. F. McCarty, Defects of graphene on Ir(111): Rotational domains and ridges, Phys. Rev. B 80 (2009) 085430.

[107] E. Moreau, S. Godey, F. J. Ferrer, D. Vignaud, X. Wallart, J. Avila, M. C. Asensio, F. Bournel, J.-J. Gallet, Graphene growth by molecular beam epitaxy on the carbon-face of SiC, Appl. Phys. Lett. 97 (2010) 241907.

[108] C. Vo-Van, Z. Kassir-Bodon, Yang, J. Coraux, J. Vogel, S. Pizzini, P. Bayle-Guillemaud, M. Chshiev, L. Ranno, V. Guisset, P. David, V. Salvador, O. Fruchart, Ultrathin epitaxial cobalt films on graphene for spintronic investigations and applications, New J. Phys. 12 (2010) 103040.

[109] M. Von Ardenne, Das elektronen-rastermikroskop, Zeitschrift für Physik 109 (1938) 553–572.

[110] D. R. Biswas, D. K. Nath, Direct observation of sintering of VAD soot particles by hot stage scanning electron microscopy, J. Mater. Sci. Lett. 2 (1983) 245–248.

[111] H. Erhart, R. Wang, R. A. Rapp, In situ SEM study of the high-temperature oxidation of an Fe-Mn-Al-Si alloy, Oxidation of metals 21 (1984) 81–88.

[112] I. Vlassiouk, M. Regmi, P. Fulvio, S. Dai, P. Datskos, G. Eres, S. Smirnov, Role of hydrogen in chemical vapor deposition growth of large single-crystal graphene, ACS Nano 5 (2011) 6069.

[113] K. S. Kim, Y. Zhao, H. Jang, S. Y. Lee, J. M. Kim, K. S. Kim, J.-H. Ahn, P. Kim, J.-Y. Choi, B. H. Hong, Large-scale pattern growth of graphene films for stretchable transparent electrodes, Nature 457 (2009) 706.

[114] X. Li, W. Cai, J. An, S. Kim, J. Nah, D. Yang, R. Piner, A. Velamakanni, I. Jung, E. Tutuc, S. K. Banerjee, L. Colombo, R. S. Ruoff, Large-area synthesis of high-quality and uniform graphene films on copper foils, Science 324 (2009) 1312–1314.

[115] S. J. Chae, F. Günes, K. K. Kim, E. S. Kim, G. H. Han, S. M. Kim, H.-J. Shin, S.-M. Yoon, J.-Y. Choi, M. H. Park, C. W. Yang, D. Pribat, Y. H. Lee, Synthesis of large-area graphene layers on poly-nickel substrate by chemical vapor deposition: Wrinkle formation, Adv. Mater. 21 (2009) 2328.

[116] J. D. Wood, S. W. Schmucker, A. S. Lyons, E. Pop, J. W. Lyding, Effects of polycrystalline Cu substrate on graphene growth by chemical vapor deposition, Nano Lett. 11 (2011) 4547–4554.

[117] S. Subramanian, In situ high temperature environmental scanning electron microscopic investigation of sintering behavior in barium titanate, Ph.D. thesis, University of Cincinnati, 2006.

[118] X. Li, W. Cai, L. Colombo, R. S. Ruoff, Evolution of graphene growth on Ni and Cu by carbon isotope labeling, Nano Lett. 9 (2009) 4268.

[119] A. C. Ferrari, J. C. Meyer, V. Scardaci, C. Casiraghi, M. Lazzeri, F. Mauri, S. Piscanec, D. Jiang, K. S. Novoselov, S. Roth, A. K. Geim, Raman spectrum of graphene and graphene layers, Phys. Rev. Lett. 97 (2006) 187401.

[120] A. C. Ferrari, Raman spectroscopy of graphene and graphite: Disorder, electron-phonon coupling, doping and nonadiabatic effects, Solid State Comm. 143 (2007) 47.

[121] L. M. Malard, M. A. Pimenta, G. Dresselhaus, M. Dresselhaus, Raman spectroscopy of graphene, Phys. Reports 473 (2009) 51.

[122] P. H. Tan, W. P. Han, W. J. Zhao, Z. H. Wu, K. Chang, H. Wang, Y. F. Wang, N. Bonini, N. Marzari, G. Savini, A. Lombardo, A. C. Ferrari, The shear mode of multilayer graphene, Nature Mater. 11 (2012) 294.

[123] C. Casiraghi, Doping dependence of the Raman peaks intensity of graphene close to the Dirac point, Phys. Rev. B 80 (2009) 233407.

[124] A. Righi, S. D. Costa, H. Chacham, C. Fantini, P. Venezuela, C. Magnuson, L. Colombo, W. S. Bacsa, R. S. Ruoff, M. A. Pimenta, Graphene moiré patterns observed by umklapp double-resonance raman scattering, Phys. Rev. B 84 (2011) 241409.

[125] T. M. G. Mohiuddin, A. Lombardo, R. R. Nair, A. Bonetti, G. Savini, R. Jalil, N. Bonini, D. M. Basko, C. Galiotis, N. Marzari, K. S. Novoselov, A. K. Geim, A. C. Ferrari, Uniaxial strain in graphene by raman spectroscopy: G peak splitting, Grüneisen parameters, and sample orientation, Phys. Rev. B 79 (2009) 205433.

[126] A. Das, S. Pisana, B. Chakraborty, S. Piscanec, S. K. Saha, U. V. Waghmare, K. S. Novoselov, H. R. Krishnamurthy, A. K. Geim, A. C. Ferrari, A. K. Sood, Monitoring dopants by raman scattering on an electrochemically top-gated graphene transistor, Nature Nanotech. 3 (2008) 210–215.

[127] W. Marra, P. Eisenberger, A. Cho, X-ray total-external-reflection–Bragg diffraction: A structural study of the GaAs-Al interface, J. Appl. Phys. 50 (1979) 6927–6933.

[128] I. K. Robinson, Crystal truncation rods and surface roughness, Phys. Rev. B 33 (1986) 3830.

[129] R. Feidenhans'l, Surface structure determination by X-ray diffraction, Surf. Sci. Rep. 10 (1989) 105.

[130] J. Hass, R. Feng, J. E. Millán-Otoya, X. Li, M. Sprinkle, P. N. First, W. A. de Heer, E. H. Conrad, C. Berger, Structural properties of the multilayer graphene/4H-SiC(000$\bar{1}$) system as determined by surface x-ray diffraction, Phys. Rev. B 75 (2007) 214109.

[131] D. Martoccia, P. R. Willmott, T. Brugger, M. Björck, S. Günther, C. M. Schlepütz, A. Cervellino, S. A. Pauli, B. D. Patterson, S. Marchini, J. Wintterlin, W. Moritz, T. Greber, Graphene on Ru(0001): A 25 x 25 Supercell, Phys. Rev. Lett. 101 (2008) 126102.

[132] N. Blanc, J. Coraux, C. Vo-Van, A. T. N'Diaye, O. Geaymond, G. Renaud, Local deformations and incommensurability of high-quality epitaxial graphene on a weakly interacting transition metal, Phys. Rev. B 86 (2012) 235439.

[133] F. Jean, T. Zhou, N. Blanc, R. Felici, J. Coraux, G. Renaud, Effect of preparation on the commensurabilities and thermal expansion of graphene on Ir(111) between 10 and 1300 K, Phys. Rev. B 88 (2013) 165406.

[134] K. Siegbahn, K. I. Edvarson, β-ray spectroscopy in the precision range of $1 : 10^5$, Nucl. Phys. 1 (1956) 137–159.

[135] D. W. Turner, M. I. Jobory, Determination of ionization potentials by photoelectron energy measurement, J. Chem. Phys. 37 (1962) 3007.

[136] A. Nagashima, N. Tejima, C. Oshima, Electronic states of the pristine and alkali-metal-intercalated monolayer graphite/Ni(111) systems, Phys. Rev. B 50 (1994) 17487–17495.

[137] E. Rollings, G.-H. Gweon, S. Y. Zhou, B. S. Mun, J. L. McChesney, B. S. Hussain, A. V. Fedorov, P. N. First, W. A. de Heer, A. Lanzara, Synthesis and characterization of atomically thin graphite films on a silicon carbide substrate, J. Phys. Chem. Sol. 67 (2006) 2172–2177.

[138] A. B. Preobrajenski, M. L. Ng, A. S. Vinogradov, N. Mårtensson, Controlling graphene corrugation on lattice-mismatched substrates, Phys. Rev. B 78 (2008) 073401.

[139] P. Lacovig, M. Pozzo, D. Alfe, P. Vilmercati, A. Baraldi, S. Lizzit, Growth of dome-shaped carbon nanoislands on Ir (111): the intermediate between carbidic clusters and quasi-free-standing graphene, Phys. Rev. Lett. 103 (2009) 166101.

[140] S. Lizzit, A. Baraldi, High-resolution fast X-ray photoelectron spectroscopy study of ethylene interaction with Ir(111): From chemisorption to dissociation and graphene formation, Catalysis Today 154 (2010) 68 – 74.

[141] E. Miniussi, M. Pozzo, A. Baraldi, E. Vesselli, R. R. Zhan, G. Comelli, T. O. Menteş, M. A. Niño, A. Locatelli, S. Lizzit, et al., Thermal stability of corrugated epitaxial graphene grown on Re (0001), Phys. Rev. Lett. 106 (2011) 216101.

[142] D. Koningsberger, R. Prins, X-ray absorption: principles, applications, techniques of EXAFS, SEXAFS, and XANES, John Wiley and Sons, New York, NY, 1988.

[143] V. Y. Aristov, G. Urbanik, K. Kummer, D. V. Vyalikh, O. V. Molodtsova, A. B. Preobrajenski, A. A. Zakharov, C. Hess, T. Hänke, B. Büchner, I. Vobornik, J. Fujii, G. Panaccione, Y. A. Ossipyan, M. Knupfer, Graphene synthesis on cubic SiC/Si wafers. perspectives for mass production of graphene-based electronic devices, Nano Lett. 10 (2010) 992–995.

[144] P. A. Brühwiler, A. J. Maxwell, C. Puglia, A. Nilsson, S. Andersson, N. Mårtensson, π^* and σ^* excitons in c 1 s absorption of graphite, Phys. Rev. Lett. 74 (1995) 614.

[145] D. A. Fischer, R. M. Wentzcovitch, R. G. Carr, A. Continenza, A. J. Freeman, Graphitic interlayer states: A carbon K near-edge X-ray-absorption fine-structure study, Phys. Rev. B 44 (1991) 1427.

[146] V. Lee, C. Park, C. Jaye, D. A. Fischer, Q. Yu, W. Wu, Z. Liu, J. Bao, S.-S. Pei, C. Smith, P. Lysaght, S. Banerjee, Substrate hybridization and rippling of graphene evidenced by near-edge X-ray absorption fine structure spectroscopy, L. Phys. Chem. Lett. 1 (2010) 1247–1253.

[147] B. W. Batterman, Effect of dynamical diffraction in X-ray fluorescence scattering, Phys. Rev. B 133 (1964) A759.

[148] J. Zegenhagen, Surface structure determination with X-ray standing waves, Surf. Sci. Rep. 18 (1993) 202.

[149] D. P. Woodruff, Surface structure determination using X-ray standing waves, Rep. Progr. Phys. 68 (2005) 743.

[150] C. Busse, P. Lazić, R. Djemour, J. Coraux, T. Gerber, N. Atodiresei, V. Caciuc, R. Brako, A. T. N'Diaye, S. Blügel, J. Zegenhagen, T. Michely, Graphene on Ir(111): Physisorption with chemical modulation, Phys. Rev. Lett. 107 (2011) 036101.

[151] S. Runte, P. Lazić, C. vo-Van, J. Coraux, J. Zegenhagen, C. Busse, Graphene buckles under stress: an X-ray standing wave and scanning tunneling microscopy study, Phys. Rev. B 89 (2014) 155427.

[152] M. C. Payne, M. P. Teter, D. C. Allan, T. A. Arias, J. D. Joannopoulos, Iterative minimization techniques for abinitio total-energy calculations - molecular-dynamics and conjugate gradients, Rev. Mod. Phys. 64 (1992) 1045–1097.

[153] I. Stich, Computer simuations for the nano-scale, Acta Physica Slovaca 57 (2007) 1.

[154] L. Kantorovich, Quantum Theory of the Solid State: An Introduction, Kluwer, 2004.

[155] M. P. Allen, D. J. Tildesley, Computer Simulations of Liquids, Oxford University Press, 1987.

[156] R. G. Parr, W. Yang, Density-Functional Theory of Atoms and Molecules, Oxford Univ. Press, 1989.

[157] R. Martin, Electronic structure. Basic Theory and Practical Methods, Cambridge, 2008.

[158] D. Frenkel, B. Smit, Understanding Molecular Simulation. From Algorithms to Applications, Aced. Press, 2002.

[159] P. Hohenberg, W. Kohn, Inhomogeneous electron gas, Phys. Rev. 136 (1964) B864–871.

[160] W. Kohn, L. J. Sham, Self-consistent equations including exchange and correlation effects, Phys. Rev. 140 (1965) A1133–A1138.

[161] S. Baroni, S. de Gironcoli, A. Dal Corso, P. Giannozzi, Phonons and related crystal properties from density-functional perturbation theory, Rev. Mod. Phys. 73 (2001) 515–562.

[162] S. F. Boys, F. Bernardi, The calculation of small molecular interactions by the differences of separate total energies. Some procedures with reduced errors, Molecular Physics 19 (1970) 553.

[163] D. Wales, Energy Landscapes: Applications to Clusters, Biomolecules and Glasses, Cambridge Molecular Science, 2003.

[164] D. J. Wales, T. V. Bogdan, Potential energy and free energy landscapes, J. Phys. Chem. B 110 (2006) 20765–20776.

[165] S. Goedecker, W. Hellmann, T. Lenosky, Global minimum determination of the Born-Oppenheimer surface within density functional theory, Phys. Rev. Lett. 95 (2005) 55501.

[166] Z.-J. Zhao, L. V. Moskaleva, H. A. Aleksandrov, D. Basaran, N. Rösch, Ethylidyne Formation from Ethylene over Pt(111): A Mechanistic Study from First-Principle Calculations, J. Phys. Chem. C 114 (2010) 12190–12201.

[167] G. Henkelman, H. Jónsson, Theoretical Calculations of Dissociative Adsorption of CH_4 on an Ir(111) Surface, Phys. Rev. Lett. 86 (2001) 664–667.

[168] S. Goedecker, Linear scaling electronic structure methods, Rev. Mod. Phys. 71 (1999) 1085–1123.

[169] D. R. Bowler, T. Miyazaki, M. J. Gillan, Recent progress in linear scaling *ab initio* electronic structure techniques, J. Phys. Condens. Matter 14 (2002) 2781–2798.

[170] D. R. Bowler, J.-L. Fattebert, M. J. Gillan, P. D. Haynes, C.-K. Skylaris, Introductory remarks: Linear scaling methods, J. Phys. Cond. Matter 20 (2008) 290301.

[171] C. Skylaris, P. D. Haynes, A. A. Mostofi, M. C. Payne, Introducing ONETEP: Linear-scaling density functional simulations on parallel computers, J. Chem. Phys. 122 (2005) 084119.

[172] J. M. Soler, E. Artacho, J. D. Gale, A. García, J. Junquera, P. Ordejón, D. Sánchez-Portal, The SIESTA method for *ab initio* order-N materials simulation, J. Phys.: Condens. Matter 14 (2002) 2745–2779.

[173] D. M. Ceperley, B. J. Alder, ground state of the electronic gas by a stochastic method, Phys. Rev. Lett. 45 (1980) 566–569.

[174] J. Perdew, K. Burke, M. Ernzerhof, Generalized gradient approximation made simple, Phys. Rev. Lett. 77 (1996) 3865.

[175] J. Perdew, K. Burke, M. Ernzerhof, Perdew, burke, and ernzerhof reply, Phys. Rev. Lett. 80 (1998) 891.

[176] T. Bjórkman, A. Gulans, A. V. Krasheninnikov, R. M. Nieminen, Are we van der waals ready?, J. Phys.: Cond. Matter 24 (2012) 424218.

[177] T. Bjórkman, A. Gulans, A. V. Krasheninnikov, R. M. Nieminen, van der waals bonding in layered compounds from advanced density-functional first-principles calculations, Phys. Rev. Lett. 108 (2012) 235502.

[178] S. Grimme, Accurate description of van der waals complexes by density functional theory including empirical corrections, J. Comp. Chem. 25 (2004) 1463–1473.

[179] S. Grimme, Semiempirical gga-type density functional constructed with a long-range dispersion correction, J. Comp. Chem. 27 (2006) 1787–1799.

[180] S. Grimme, Density functional theory with London dispersion corrections, Comput. Mol. Sci. 1 (2011) 211–228.

[181] M. Dion, H. Rydberg, E. Schröder, D. C. Langreth, B. I. Lundqvist, Van der waals density functional for general geometries, Phys. Rev. Lett. 92 (2004) 246401.

[182] K. Lee, E. D. Murray, L. Kong, B. I. Lundqvist, D. C. Langreth, Higher-accuracy van der waals density functional, Phys. Rev. B 82 (2010) 081101(R).

[183] D. C. Langreth, B. I. Lundqvist, S. D. Chakarova-Käck, V. R. Cooper, M. Dion, P. Hyldgaard, A. Kelkkanen, J. Kleis, L. Kong, S. Li, P. G. Moses, E. Murray, A. Puzder, H. Rydberg, E. Schröder, T. Thonhauser, A density functional for sparse matter, J. Phys. Condens. Matter. 21 (2009) 084203.

[184] T. Bjórkman, van der waals density functional for solids, Phys. Rev. B 86 (2012) 165109.

[185] O. A. Vydrov, T. V. Voorhis, Nonlocal van der waals density functional: The simpler the better, J. Chem. Phys. 133 (2010) 244103.

[186] J. Klimeŝ, D. R. Bowler, A. Michaelides, Chemical accuracy for the van der waals density functional, J. Phys.: Cond. Matter 22 (2010) 022201.

[187] A. Tkatchenko, R. A. DiStasio Jr, R. Car, M. Scheffler, Accurate and efficient method for many-body van der Waals interactions, Phys. Rev. Lett. 108 (2012) 236402.

[188] A. Tkatchenko, A. Ambrosetti, R. A. DiStasio, Interatomic methods for the dispersion energy derived from the adiabatic connection fluctuation-dissipation theorem, J. Chem. Phys. 138 (2013) 074106.

[189] T. Buĉko, S. Lebégue, J. Hafner, J. G. Ángyán, Tkatchenko-scheffler van der waals correction method with and without self-consistent screening applied to solids, Phys. Rev. B 87 (2013) 064110.

[190] D. C. Langreth, J. Perdew, Exchange correlation energy of a metallic surface: wave-vector analysis, Phys. Rev. B 15 (1977) 2884–2901.

[191] J. Harl, G. Kresse, Accurate bulk properties from approximate many-body techniques, Phys. Rev. Lett. 103 (2009) 056401.

[192] J. Bamidele, J. Brndiar, A. Gulans, L. Kantorovich, I. Ŝtich, Importance of van der waals stabilization in strongly chemically bonded surfaces: Cu(110):o, J. Chem. Theory Comp. 9 (2013) 5578–5584.

[193] J. E. Jones, On the determination of molecular fields. II from the equation of state of a gas, Proc. Roy. Soc. A 106 (1924) 463–477.

[194] P. M. Morse, Diatomic molecules according to the wave mechanics. II. Vibrational levels, Phys. Rev. 34 (1929) 57–64.

[195] A. E. Carlsson, Solid State Physics: Advances in Research and Applications, volume 43, Academic Press, 1990.

[196] F. H. Stillinger, T. A. Weber, Computer simulation of local order in condensed phases of silicon, Phys. Rev. B 31 (1985) 5262–5271.

[197] J. Tersoff, New empirical model for the structural properties of silicon, Phys. Rev. Lett. 56 (1986) 632–635.

[198] J. Tersoff, New empirical approach for the structure and energy of covalent systems, Phys. Rev. B 37 (1988) 6991–7000.

[199] D. W. Brenner, Empirical potential for hydrocarbons for use in simulating the chemical vapor deposition of diamond films, Phys. Rev. B 42 (1990) 9458–9471.

[200] M. S. Daw, M. I. Baskes, Semiempirical, quantum mechanical calculation of hydrogen embrittlement in metals, Phys. Rev. Lett. 50 (1983) 1285–1288.

[201] M. S. Daw, M. I. Baskes, Embedded-atom method: Derivation and application to impurities, surfaces, and other defects in metals, Phys. Rev. B 29 (1984) 6443–6453.

[202] K. W. Jacobsen, J. K. Norskov, M. J. Puska, Interatomic interactions in the effective-medium theory, Phys. Rev. B 35 (1987) 7423–7442.

[203] M. W. Finnis, J. E. Sinclair, A simple empirical n-body potential for transition metals, Phil. Mag. A 50 (1984) 45–55.

[204] S. Haghighatpanah, A. Borjesson, Computational studies of graphene growth mechanisms, Phys. Rev. B. 85 (2012) 205448.

[205] H. Amara, J. M. Roussel, C. Bichara, J. P. Gaspard, F. Ducastelle, Tight-binding potential for atomistic simulations of carbon interacting with transition metals: Application to the Ni-C system, Phys. Rev. B 79 (2009) 014109.

[206] J. Gao, J. Yip, J. Zhao, B. I. Yakobson, F. Ding, Graphene nucleation on transition metal surface: Structure transformation and role of the metal step edge, J. Am. Chem. Soc. 133 (2011) 5009–5015.

[207] R. G. V. Wesep, H. Chen, W. Zhu, Z. Zhang, Communication: Stable carbon nanoarches in the initial stages of epitaxial growth of graphene on Cu(111), J. Chem. Phys. 134 (2011) 171105.

[208] S. Riikonen, A. V. Krasheninnikov, L. Halonen, R. M. Nieminen, The role of stable and mobile carbon adspecies in copper-promoted graphene growth, J. Phys. Chem. C 116 (2012) 5802–5809.

[209] W. Zhang, P. Wu, Z. Li, J. Yang, First-principles thermodynamics of graphene growth on Cu surfaces, J. Phys. Chem. C 115 (2011) 17782–17787.

[210] H. Jonsson, G. Mills, K. W. Jacobsen, Nudged elastic band method for finding minimum energy paths of transitions, Classical and Quantum Dynamics in Condensed Phase Simulations (1999) 385.

[211] G. Henkelman, H. Jónsson, Improved tangent estimate in the nudged elastic band method for finding minimum energy paths and saddle points, J. Chem. Phys. 113 (2000) 9978.

[212] G. Henkelman, B. P. Uberuaga, H. Jónsson, A climbing image nudged elastic band method for finding saddle points and minimum energy paths, J. Chem. Phys. 113 (2000) 9901.

[213] A. F. Voter, F. Montalenti, T. C. Germann, Extending the time scale in atomistic simulation of materials, Annu. Rev. Mater. Res. 32 (2002) 321–346.

[214] D. P. Landau, K. Binder, A Guide to Monte Carlo Simulations in Statistical Physics, Cambridge University Press, Cambridge, 2000.

[215] H. C. Kang, W. H. Weinberg, Dynamic Monte Carlo with a proper energy barrier: Surface diffusion and two-dimensional domain ordering, J. Chem. Phys. 90 (1989) 2824–2830.

[216] K. A. Fichthorn, W. H. Weinberg, Theoretical foundations of dynamical Monte Carlo simulations, J. Chem. Phys. 95 (1991) 1090–1096.

[217] D. T. Gillespie, A general method for numerically simulating the stochastic time evolution of coupled chemical reactions, J. Comp. Physics 22 (1976) 403–434.

[218] K. Reuter, C. Stampfl, M. Scheffler, Ab initio atomistic thermodynamic and stastical mechanics of surface properties and functions, volume A of *Handbook of Material Modeling*, Springer, 2005, p. 149.

[219] D. T. Gillespie, Stochastic simulation of chemical kinetics, Annu. Rev. Phys. Chem. 58 (2007) 35.

[220] A. F. Voter, Radiation effects in solids, Handbook of Material Modeling, Part A. Methods, Springer, NATO Publishing Unit, Dordrecht, The Netherlands, 2005.

[221] N. G. V. Kampen, Stochastic Processes in Physics and Chemistry, North-Holland, Amsterdam, 1981.

[222] A. Nitzan, Chemical Dynamics in Condensed Phases: Relaxation, Transfer, and Reactions in Condensed Molecular Systems, Oxford Univ. Press, 2006.

[223] A. Zangwill, Physics at Surfaces, Cambridge University Press, Cambridge, 1988.

[224] Z. Wang, E. G. Seebauer, Estimating pre-exponential factors for desorption from semiconductors: Consequences for *a priori* process modelling, Appl. Surf. Sci. 181 (2001) 111–120.

[225] H. Amara, C. Bichara, F. Ducastelle, Formation of carbon nanostructures on nickel surfaces: A tight-binding grand canonical Monte Carlo study, Phys. Rev. B 73 (2006) 113404.

[226] W. K. Burton, N. Cabrera, F. C. Frank, The growth of crystals and the equilibrium structure of their surfaces, Phil. Trans. R. Soc. Lond. A 243 (1951) 299–358.

[227] J. S. Langer, Directions in Condensed Matter Physics, World Scientific, 1986, pp. 164–186.

[228] R. F. Sekerka, Morphology: From sharp interface to phase field models, Journal of Crystal Growth 264 (2004) 530–540.

[229] K. Kassner, C. Misbah, J. Müller, J. Kappey, P. Kohlert, Phase-field modeling of stress-induced instabilities, Phys. Rev. E 63 (2001) 036117.

[230] F. Liu, H. Metiu, Stability and kinetics of step motion on crystal surfaces, Phy. Rev. E 49 (1994) 2601–2616.

[231] A. Karma, M. Plapp, Spiral surface growth without desorption, Phys. Rev. Lett. 81 (1998) 4444–4447.

[232] A. Rätz, A. Voigt, Various phase-field approximations for epitaxial growth, Journal of Crystal Growth 266 (2004) 278–282.

[233] M. Castro, Phase-field approach to heterogeneous nucleation, Phy. Rev. B 67 (2003) 035412.

[234] Y. Yu, B. Liu, Phase-field model of island growth in epitaxy, Phys. Rev. E 69 (2004) 021601.

[235] F. Ming, A. Zangwill, Phase field modeling of submonolayer epitaxial growth, Phys. Rev. B 81 (2010) 235431.

[236] D. Kim, W. Lu, Self-organized nanostructures in multi-phase epilayers, Nanotechnology 15 (2004) 667–674.

[237] J. A. Venables, G. D. T. Spiller, M. Hanbücken, Nucleation and growth of thin films, Rep. Prog. Phys. 47 (1984) 399–458.

[238] G. S. Bales, D. C. Chrzan, Dynamics of irreversible island growth during submonolayer epitaxy, Phys. Rev. B 50 (1994) 6057–6067.

[239] M. C. Bartelt, J. W. Evans, Exact island-size distributions for submonolayer deposition: Influence of correlations between island size and separation, Phys. Rev. B 54 (1996) R17359–R17362.

[240] J. G. Amar, M. N. Popescu, F. Family, Rate-equation approach to island capture zones and size distributions in epitaxial growth, Phys. Rev. Lett 86 (2001) 3092–3095.

[241] M. C. Bartelt, C. R. Stoldt, C. J. Jenks, P. A. Thiel, J. W. Evans, Adatom capture by arrays of two-dimensional Ag islands on Ag(100), Phys. Rev. B 59 (1999) 3125–3134.

[242] J. Wintterlin, M. L. Bocquet, Graphene on metal surfaces, Surf. Sci. 603 (2009) 1841–1852.

[243] H. Ago, Y. Ito, N. Mizuta, K. Yoshida, B. Hu, C. M. Orofeo, M. Tsuji, K. Ikeda, S. Mizuno, Epitaxial chemical vapor deposition growth of single-layer graphene over cobalt film crystallized on sapphire, ACS Nano 4 (2010) 7407–7414.

[244] T. Iwasaki, H. J. Park, M. Konuma, D. S. Lee, J. H. Smet, U. Starke, Long-range ordered single-crystal graphene on high-quality heteroepitaxial Ni thin films grown on MgO(111), Nano Lett. 11 (2011) 79–84.

[245] K. M. Reddy, A. D. Gledhill, C. Chen, J. M. Drexler, N. P. Padture, High quality, transferrable graphene grown on single crystal Cu(111) thin films on basal-plane sapphire, Appl. Phys. Lett. 98 (2011) 113117.

[246] P. W. Sutter, P. M. Albrecht, E. A. Sutter, Graphene growth on epitaxial Ru thin films on sapphire, Appl. Phys. Lett. 97 (2010) 213101.

[247] C. Tonnoir, A. Kimouche, J. Coraux, L. Magaud, B. Delsol, B. Gilles, C. Chapelier, Induced superconductivity in graphene grown on rhenium, Phys. Rev. Lett. 111 (2013) 246805.

[248] A. Al-Temimy, C. Riedl, U. Starke, Low temperature growth of epitaxial graphene on SiC induced by carbon evaporation, Appl. Phys. Lett. 95 (2009) 231907.

[249] A. Michon, S. Vézian, A. Ouerghi, M. Zielinski, T. Chassagne, M. Portail, Direct growth of few-layer graphene on 6H-SiC and 3C-SiC/Si via propane chemical vapor deposition, Appl. Phys. Lett. 97 (2010) 171909.

[250] J. Hwang, V. B. Shields, C. I. Thomas, S. Shivaraman, D. Hao, M. Kim, A. R. Woll, G. S. Tompa, M. G. Spencer, Epitaxial growth of graphitic carbon on C-face SiC and sapphire by chemical vapor deposition (CVD), J. Cryst. Growth 312 (2010) 3219–3224.

[251] B. Wang, X. Ma, M. Caffio, R. Schaub, W.-X. Li, Size-selective carbon nanoclusters as precursors to the growth of epitaxial graphene, Nano Lett. 11 (2011) 424–430.

[252] C. Hwang, K. Yoo, S. J. Kim, E. K. Seo, H. Yu, L. P. Biro, Initial stage of graphene growth on a Cu substrate, J. Phys. Chem. C 115 (2011) 22369–22374.

[253] L. Gao, J. R. Guest, N. P. Guisinger, Epitaxial graphene on Cu(111), Nano Lett. 10 (2010) 3512–3516.

[254] K. Yamamoto, M. Fukushima, T. Osaka, C. Oshima, Charge-transfer mechanism for the (monolayer graphite)/Ni(111) system, Phys. Rev. B 45 (1992) 11358.

[255] J. Lahiri, T. Miller, L. Adamska, I. I. Oleynik, M. Batzill, Graphene growth on Ni(111) by transformation of a surface carbide, Nano Lett. 11 (2010) 518–522.

[256] D. Eom, D. Prezzi, K. T. Rim, H. Zhou, M. Lefenfeld, S. Xiao, C. Nuckolls, M. S. Hybertsen, T. F. Heinz, G. W. Flynn, Structure and electronic properties of graphene nanoislands on Co(0001), Nano Lett. 9 (2009) 2844–2848.

[257] O. Rader, A. Varykhalov, J. Sánchez-Barriga, O. Marchenko, A. Rybkin, A. M. Shikin, Is there a Rashba effect in graphene on 3d ferromagnets?, Phys. Rev. Lett. 102 (2009) 057602.

[258] N. A. Vinogradov, A. A. Zakharov, V. Kocevski, J. Rusz, K. A. Simonov, O. Eriksson, A. Mikkelsen, E. Lundgren, A. S. Vinogradov, N. Mårtensson, A. B. Preobrajenski, Formation and structure of graphene waves on Fe (110), Phys. Rev. Lett. 109 (2012) 026101.

[259] S. Nie, N. C. Bartelt, J. M. Wofford, O. D. Dubon, K. F. McCarty, K. Thürmer, Scanning tunneling microscopy study of graphen on Au(111): growth mechanisms and substrate interactions, Phys. Rev. B 85 (2012) 205406.

[260] N. R. Gall, S. R. Mikhailov, E. V. Rutkov, A. Y. Tontegode, Carbon interaction with the rhenium surface, Surf. Sci. 191 (1987) 187–202.

[261] E. N. Voloshina, Y. S. Dedkov, S. Torbrügge, A. Thissen, M. Fonin, Graphene on Rh(111): Scanning tunneling and atomic force microscopies studies, Appl. Phys. Lett. 100 (2012) 241606.

[262] J. M. Wofford, S. Nie, K. F. McCarty, N. C. Bartelt, O. D. Dubon, Graphene islands on Cu foils: The interplay between shape, orientation, and defects, Nano Lett. 10 (2010) 4890–4896.

[263] X. Li, C. W. Magnuson, A. Venugopal, J. An, J. W. Suk, B. Han, M. Borysiak, W. Cai, A. Velamakanni, Y. Zhu, L. Fu, E. M. Vogel, E. Voelkl, L. Colombo, R. S. Ruoff, Graphene films with large domain size by a two-step chemical vapor deposition process, Nano Lett. 10 (2010) 4328–4334.

[264] C. Vo-Van, A. Kimouche, A. Reserbat-Plantey, O. Fruchart, P. Bayle-Guillemaud, N. Bendiab, J. Coraux, Epitaxial graphene prepared by chemical vapor deposition on single crystal thin iridium films on sapphire, Appl. Phys. Lett. 98 (2011) 181903.

[265] K. M. Reddy, A. D. Gledhill, C.-H. Chen, J. M. Drexler, N. P. Padture, High quality, transferrable graphene grown on single crystal Cu(111) thin films on basal-plane sapphire, Appl. Phys. Lett. 98 (2011) 113117.

[266] S. Nie, J. M. Wofford, N. C. Bartelt, O. D. Dubon, K. F. McCarty, Origin of the mosaicity in graphene grown on Cu(111), Phys. Rev. B 84 (2011) 155425.

[267] K. Celebi, M. T. Cole, J. W. Choi, F. Wyczisk, P. Legagneux, N. Rupesinghe, J. Robertson, K. B. K. Teo, H. G. Park, Evolutionary Kinetics of Graphene Formation on Copper, Nano Lett. 13 (2013) 967–974.

[268] B. Wang, S. Günther, J. Wintterlin, M.-L. Bocquet, Periodicity, work function and reactivity of graphene on Ru(0001) from first principles, New J. Phys. 12 (2010) 043041.

[269] S. Günther, S. Dänhardt, B. Wang, M. L. Bocquet, S. Schmitt, J. Wintterlin, Single Terrace Growth of Graphene on a Metal Surface, Nano Lett. 11 (2011) 1895–1900.

[270] X. Li, C. W. Magnuson, A. Venugopal, R. M. Tromp, J. B. Hannon, E. M. Vogel, L. Colombo, R. S. Ruoff, Large-area graphene single crystals grown by low-pressure chemical vapor deposition of methane on copper, J. Am. Chem. Soc. 133 (2011) 2816–2819.

[271] Z. Yan, J. Lin, Z. Peng, Z. Sun, Y. Zhu, L. Li, C. Xiang, E. L. Samuel, C. Kittrell, J. M. Tour, Toward the synthesis of wafer-scale single-crystal graphene on copper foils, ACS Nano 6 (2012) 9110.

[272] P. J. Skrdla, Roles of Nucleation, Denucleation, Coarsening, and Aggregation Kinetics in Nanoparticle Preparations and Neurological Disease, Langmuir 28 (2012) 4842–4857.

[273] R. Addou, A. Dahal, P. Sutter, M. Batzill, Monolayer graphene growth on Ni(111) by low temperature chemical vapour deposition, Appl. Phys. Lett. 100 (2012) 021601.

[274] L. Huang, W.-Y. Xu, Y.-D. Que, Y. Pan, M. Gao, L.-D. Pan, H.-M. Guo, Y.-L. Wang, S.-X. Du, H.-J. Gao, The influence of annealing temperature on the morphology of graphene islands, Chin. Phys. B 21 (2012) 088102.

[275] Y. Cui, Q. Fu, H. Zhang, X. Bao, Formation of identical-size graphene nanoclusters on Ru(0001), Chem. Commun. 47 (2011) 1470–1472.

[276] P. W. Voorhees, The theory of Ostwald ripening, J. Stat. Phys. 38 (1985) 231–252.

[277] C. R. Stoldt, C. J. Jenks, P. A. Thiel, A. M. Cadilhe, J. W. Evans, Smoluchowski ripening of Ag islands on Ag(100), J. Chem. Phys. 111 (1999) 5157–5166.

[278] H. Chen, W. Zhu, Z. Zhanh, Contrasting behaviour of carbon nucleation in the initial stages of graphene epitaxial growth on stepped metal surfaces, Phys. Rev. Lett. 104 (2010) 186101.

[279] T. Fuhrmann, M. Kinne, B. Tränkenschuh, C. Papp, J. F. Zhu, R. Denecke, H.-P. Steinrück, Activated adsorption of methane on Pt(111) - an *in situ* XPS study, New J. Phys. 7 (2005) 107.

[280] J. Andersin, N. Lopez, K. Honkala, DFT Study on the Complex Reaction Networks in the Conversion of Ethylene to Ethylidyne on Flat and Stepped Pd, J. Phys. Chem. C 113 (2009) 8278–8286.

[281] Z. Li, P. Wu, C. Wang, X. Fan, W. Zhang, X. Zhai, C. Zeng, Z. Li, J. Yang, J. Hou, Low-temperature growth of graphene by chemical vapor deposition using solid and liquid carbon sources, ACS Nano 5 (2011) 3385–3390.

[282] Y. Zhang, L. Gomez, F. N. Ishikawa, A. Madaria, K. Ryu, C. Wang, A. Badmaev, C. Zhou, Comparison of graphene growth on single-crystalline and polycrystalline Ni by chemical vapor deposition, J.Phys. Chem. Lett. 1 (2010) 3101–3107.

[283] K. F. McCarty, F. J. Feibelman, E. Loginova, N. C. Bartelt, Kinetics and thermodynamics of carbon segregation and graphene growth on Ru(0001), Carbon 47 (2009) 1806–1813.

[284] S. Nie, A. L. Walter, N. C. Bartelt, E. Starodub, A. Bostwick, E. Rotenberg, K. F. McCarty, Growth from below: Graphene bilayers on Ir(111), ACS Nano 5 (2011) 2298–2306.

[285] C. Su, A. Lu, C. Wu, Y. Li, K. Liu, W. Zhang, S. Lin, Z. Juang, Y. Zhong, F. Chen, L. Li, Direct formation of wafer scale graphene thin layers on insulating substrates by chemical vapor deposition, Nano Lett. 11 (2011) 3612–3616.

[286] G. Odahara, S. Otani, C. Oshima, M. Suzuki, T. Yasue, T. Koshikawa, In-situ observation of graphene growth on Ni(111), Surf. Sci. 605 (2011) 1095 – 1098.

[287] J. Lahiri, T. S. Miller, A. J. Ross, L. Adamska, I. I. Oleynik, M. Batzill, Graphene growth and stability at nickel surfaces, New J. Phys. 13 (2011) 025001.

[288] W. A. de Heer, C. Berger, X. Wu, P. N. First, E. H. Conrad, X. Li, T. Li, M. Sprinkle, J. Hass, M. L. Sadowski, M. Potemski, G. Martinez, Epitaxial graphene, Solid State Commun. 143 (2007) 92.

[289] C. Virojanadara, M. Syväjarvi, R. Yakimova, L. I. Johansson, A. A. Zakharov, T. Balasubramanian, Homogeneous large-area graphene layer growth on 6H-SiC(0001), Phys. Rev. B 78 (2008) 245403.

[290] R. M. Tromp, J. B. Hannon, Thermodynamics and Kinetics of Graphene Growth on SiC(0001), Phys. Rev. Lett. 102 (2009) 106104.

[291] K. V. Emtsev, A. Bostwick, K. Horn, J. Jobst, G. L. Kellogg, L. Ley, J. L. McChesney, T. Ohta, S. A. Reshanov, J. Röhrl, Towards wafer-size graphene layers by atmospheric pressure graphitization of silicon carbide, Nat. Mater. 8 (2009) 203–207.

[292] F. Ming, Theoretical studies of the epitaxial growth of graphene, Ph.D. thesis, Georgia Institute of Technology, 2011.

[293] I. Forbeaux, J.-M. Themlin, A. Charrier, F. Thibaudau, J.-M. Debever, Solid-state graphitization mechanisms of silicon carbide 6H-SiC polar faces, Appl. Surf. Sci. 162-163 (2000) 406–412.

[294] L. Muehlhoff, W. J. Choyke, M. J. Bozack, J. John T. Yates, Comparative electron spectroscopic studies of surface segregation on SiC(0001) and SiC(000$\bar{1}$), J. Appl. Phys. 60 (1986) 2842–2853.

[295] M. Sprinkle, M. Ruan, Y. Hu, J. Hankinson, M. Rubio-Roy, X. W. B. Zhang1, C. Berger, W. A. de Heer, Scalable templated growth of graphene nanoribbons on SiC, Nature Nanotech. 5 (2010) 727.

[296] L. Li, I. Tsong, Atomic structures of 6H-SiC(0001) and (000$\bar{1}$) surfaces, Surf. Sci. 351 (1996) 141–148.

[297] R. Kaplan, Surface structure and composition of β- and 6H-SiC, Surf. Sci. 215 (1989) 111–134.

[298] T. Ohta, N. C. Bartelt, S. Nie, K. Thürmer, G. L. Kellogg, Role of carbon surface diffusion on the growth of epitaxial graphene on SiC, Phys. Rev. B 81 (2010) 121411(R).

[299] P. Lauffer, K. V. Emtsev, R. Graupner, T. Seyller, L. Ley, S. A. Reshanov, H. B. Weber, Atomic and electronic structure of few-layer graphene on SiC(0001) studied with scanning tunneling microscopy and spectroscopy, Phys. Rev. B 77 (2008) 155426.

[300] A. Mattausch, O. Pankratov, *Ab Initio* study of graphene on SiC, Phys. Rev. Lett. 99 (2007) 076802.

[301] V. Borovikov, A. Zangwill, Step-edge instability during epitaxial growth of graphene from SiC(0001), Phys. Rev. B 80 (2009) 121406.

[302] A. L. Vázquez de Parga, F. Calleja, B. Borca, M. C. G. Passeggi, J. J. Hinarejos, F. Guinea, R. Miranda, Periodically rippled graphene: Growth and spatially resolved electronic structure, Phys. Rev. Lett. 100 (2008) 056807.

[303] D. Martoccia, M. Björck, C. M. Schlepütz, T. Brugger, S. A. P. nad B. D. Patterson, T. Greber, P. R. Willmott, Graphene on Ru(0001): a corrugated and chiral structure, New J. Phys. 12 (2010) 043028.

[304] B. Borca, S. Barja, M. Garnica, M. Minniti, A. Politano, J. M. Rodriguez-Garcia, J. J. Hinarejos, D. Farias, A. L. V. de Parga, R. Miranda, Electronic and geometric corrugation of periodically rippled, Self-nanostructured graphene epitaxially grown on Ru(0001), New J. Phys. 12 (2010) 093018.

[305] B. Wang, M.-L. Bocquet, S. Marchini, S. Günther, J. Wintterlin, Chemical origin of a graphene moiré overlayer on Ru(0001), Phys. Chem. Chem. Phys. 10 (2008) 3530–3534.

[306] L. Meng, R. Wu, L. Zhang, L. Li, S. Du, Y. Wang, H.-J. Gao, Multi-oriented moiré superstructures of graphene on Ir(111): experimental observations and theoretical models, J. Phys.: Condens. Matter 24 (2012) 314214.

[307] M. Gao, Y. Pan, L. Huang, H. Hu, L. Z. Zhang, H. M. Guo, S. X. Du, H.-J. Gao, Epitaxial growth and structural property of graphene on Pt(111), Appl. Phys. Lett. 98 (2011) 033101.

[308] P. Merino, M. Svec, A. L. Pinardi, G. Otero, J. A. Martin-Gago, Strain-driven moiré superstructures of epitaxial graphene on transition metal surfaces, ACS Nano 5 (2011) 5627–5634.

[309] R. Rosei, M. De Crescenzi, F. Sette, C. Quaresima, A. Savoia, P. Perfetti, Structure of graphitic carbon on ni (111): A surface extended-energy-loss fine-structure study, Phys. Rev. B 28 (1983) 1161.

[310] W. Zhao, S. M. Kozlov, O. Höfert, K. Gotterbarm, M. P. A. Lorenz, F. Viñes, C. Papp, A. Görling, H.-P. Steinrück, Graphene on Ni(111): Coexistence of different surface structures, J. Phys. Chem. Lett. 2 (2011) 759 – 764.

[311] A. Dahal, R. Addou, P. Sutter, M. Batzill, Graphene monolayer rotation on Ni(111) facilitates bilayer graphene growth, Appl. Phys. Lett. 100 (2012) 241602.

[312] Y. Murata, E. Starodub, B. Kappes, C. Ciobanu, N. Bartelt, K. McCarty, S. Kodambaka, Orientation-dependent work function of graphene on pd (111), Applied Physics Letters 97 (2010) 143114.

[313] F. Mittendorfer, A. Garhofer, J. Redinger, J. Klime, J. Harl, G. Kresse, Graphene on Ni(111): Strong interaction and weak adsorption, Phys. Rev. B 84 (2011) 201401(R).

[314] T. Olsen, J. Yan, J. J. Mortensen, K. S. Thygesen, Dispersive and covalent interactions between graphene and metal surfaces from the random phase approximation, Phys. Rev. Lett. 107 (2011) 156401.

[315] H. Zhang, Q. Fu, Y. Cui, D. Tan, X. Bao, Growth Mechanism of Graphene on Ru(0001) and O_2 Adsorption on the Graphene/Ru(0001) Surface, J. Phys. Chem. C 113 (2009) 8296–8301.

[316] K. L. Man, M. S. Altman, Small-angle lattice rotations in graphene on Ru (0001), Phys. Rev. B 84 (2011) 235415.

[317] B. Wang, M. Caffio, C. Bromley, H. Fruüchtl, R. Schaub, Coupling epitaxy, chemical bonding, and work function at the local scale in transition metal-supported graphene, ACS Nano 4 (2010) 5773.

[318] A. T. N'Diaye, J. Coraux, T. N. Plasa, C. Busse, T. Michely, Structure of epitaxial graphene on Ir(111), New J. Phys. 10 (2008) 043033.

[319] G. Bertoni, L. Calmels, A. Altibelli, V. Serin, First-principles calculation of the electronic structure and EELS spectra at the graphene/Ni(111) interface, Phys. Rev. B 71 (2005) 075402.

[320] G. Kalibaeva, R. Vuilleumier, S. Meloni, A. Alavi, G. Ciccotti, R. Rosei, Ab initio simulation of carbon clustering on an Ni (111) surface: a model of the poisoning of nickel-based catalysts, J. Phys. Chem. B 110 (2006) 3638–3646.

[321] G. Giovannetti, P. A. Khomyakov, G. Brocks, V. M. Karpan, J. Van den Brink, P. J. Kelly, Doping graphene with metal contacts, Phys. Rev. Lett. 101 (2008) 026803.

[322] M. Fuentes-Cabrera, M. I. Baskes, A. V. Melechko, M. L. Simpson, Bridge structure for the graphene/Ni(111) system: a first principles study, Phys. Rev. B 77 (2008) 035405.

[323] M. Vanin, J. J. Mortensen, A. K. Kelkkanen, J. M. Garcia-Lastra, K. S. Thygesen, K. W. Jacobsen, Graphene on metals: A van der waals density functional study, Phys. Rev. B 81 (2010) 081408.

[324] H. I. Rasool, E. B. Song, M. J. Allen, J. K. Wassei, R. B. Kaner, K. L. Wang, B. H. Weiller, J. K. Gimzewski, Continuity of graphene on polycrystalline copper, Nano Lett. 11 (2010) 251–256.

[325] M. Inoue, H. Kageshima, Y. Kangawa, K. Kakimoto, First-principles calculation of 0^{th}-layer graphene-like growth of C on SiC(0001), Phys. Rev. B 86 (2012) 085417.

[326] S. Kim, J. Ihm, H. J. Choi, Y.-W. Son, Origin of anomalous electronic structures of epitaxial graphene on silicon carbide, Phys. Rev. Lett. 100 (2008) 176802.

[327] F. Varchon, R. Feng, J. Hass, X. Li, B. N. Nguyen, C. Naud, P. Mallet, J.-Y. Veuillen, C. Berger, E. H. Conrad, L. Magaud, Electronic structure of epitaxial graphene layers on SiC: Effect of the substrate, Phys. Rev. Lett. 99 (2007) 126805.

[328] E. Lampin, C. Priester, C. Krzeminski, L. Magaud, Graphene buffer layer on Si-terminated SiC studied with an empirical interatomic potential, J. Appl. Phys. 107 (2010) 103514.

[329] C. Tang, L. Meng, L. Sun, K. Zhang, J. Zhong, Molecular dynamics study of ripples in graphene nanoribbons on 6H-SiC(0001): Temperature and size effects, J. Appl. Phys. 104 (2008) 113536.

[330] C. Tang, L. Meng, H. Xiao, J. Zhong, Growth of graphene structure on 6H-SiC(0001): Molecular dynamics simulation, J. Appl. Phys. 103 (2008) 063505.

[331] N. Jakse, R. Arifin, S. K. Lai, Growth of graphene on 6H-SiC by molecular dynamics simulation, Condens. Matt. Phys. 14 (2011) 43802.

[332] G. Lucas, M. Bertolus, L. Pizzagalli, An environment-dependent interatomic potential for silicon carbide: calculation of bulk properties, high-pressure phases, point and extended defects, and amorphous structures, J. Phys.: Condens. Matter 22 (2010) 035802.

[333] J. Tersoff, Structural properties of a carbon-nanotube crystal, Phys. Rev. Lett. 73 (1994) 676.

[334] A. Zangwill, D. Vvedensky, Novel growth mechanism of epitaxial graphene on metals, Nano Lett. 11 (2011) 2092–2095.

[335] J. Posthuma de Boer, I. Ford, L. Kantorovich, D. Vvedensky, Optimization algorithm for rate equations with an application to epitaxial graphene, J. Phys. Cond. Matter 26 (2014) 185008.

[336] G. Gajewski, C. W. Pao, Ab initio calculations of the reaction pathways for methane decomposition over the Cu(111) surface, J. Chem. Phys. 135 (2011) 064707.

[337] H. A. Aleksandrov, L. V. Moskaleva, Z.-J. Zhao, D. Basaran, Z.-X. Chen, D. Mei, N. Rösch, Ethylene conversion to ethylidyne on Pd(111) and Pt(111): A first-principles-based kinetic Monte Carlo study, J. Catal. 285 (2012) 187 – 195.

[338] M. Li, W. Guo, R. Jiang, L. Zhao, X. Lu, H. Zhu, D. Fu, H. Shan, Mechanism of the Ethylene Conversion to Ethylidyne on Rh(111): A Density Functional Investigation, J. Phys. Chem. C 114 (2010) 8440–8448.

[339] Y. Chen, D. G. Vlachos, Hydrogenation of Ethylene and Dehydrogenation and Hydrogenolysis of Ethane on Pt(111) and Pt(211): A Density Functional Theory Study, J. Phys. Chem. C 114 (2010) 4973–4982.

[340] S. Saadi, F. Abild-Pedersen, S. Helveg, J. Sehested, B. Hinnemann, C. C. Appel, J. K. Norskov, On the role of metal step-edges in graphene growth, J. Phys. Chem. 114 (2010) 11221.

[341] P. Wu, W. Zhang, Z. Li, J. Yang, J. G. Hou, Communication: Coalescence of carbon atoms on Cu(111) surface: Emergence of a stable bridging-metal structure motif, J. Chem. Phys. 133 (2010) 071101.

[342] Q. Yuan, J. Gao, H. Shu, J. Zhao, X. Chen, F. Ding, Magic carbon clusters in the chemical vapor deposition growth of graphene, J. Am. Chem. Soc. 134 (2012) 2970.

[343] P. Wu, H. Jiang, W. Zhang, Z. Li, Z. Hou, J. Yang, Lattice mismatch induced nonlinear growth of graphene, J. Am. Chem. Soc. 134 (2012) 6045–6051.

[344] D. Wei, F. Wang, Relative stability of armchair, zigzag and reczag graphene edges on the Ru(0001) surface, Surf. Sci. 606 (2012) 485 – 489.

[345] H. Shu, X. Chen, X. Tao, F. Ding, Edge structural stability and kinetics of graphene chemical vapor deposition growth, ACS Nano 6 (2012) 3243–3250.

[346] V. I. Artyukhov, Y. Liu, B. I. Yakobson, Equilibrium at the edge and atomistic mechanisms of graphene growth, Proc. Nat. Acad. Sci. 109 (2012) 235502.

[347] Q. Yu, L. A. Jauregui, W. Wu, R. Colby, J. Tian, Z. Su, H. Cao, Z. Liu, D. Pandey, D. Wei, T. F. Chung, P. Peng, N. P. Guisinger, E. A. Stach, J. Bao, S. S. Pei, Y. P. Chen, Control and characterization of individual grains and grain boundaries in graphene grown by chemical vapour deposition, Nature Mater. 10 (2011) 443–449.

[348] L. A. Jauregui, H. Cao, W. Wu, Q. Yu, Y. P. Chen, Electronic properties of grains and grain boundaries in graphene grown by chemical vapor deposition, Solid State Commun 151 (2011) 1100 – 1104.

[349] J. Tian, H. Cao, W. Wu, Q. Yu, Y. P. Chen, Direct imaging of graphene edges: Atomic structure and electronic scattering, Nano Lett. 11 (2011) 3663–3668.

[350] Y. Liu, A. Dobrinsky, B. I. Yakobson, Graphene edge from armchair to zigzag: The origins of nanotube chirality?, Phys. Rev. Lett. 105 (2010) 235502.

[351] S. Phark, J. Borme, A. L. Vanegas, M. Corbetta, D. Sander, J. Kirschner, Atomic structure and spectroscopy of graphene edges on Ir(111), Phys. Rev. B 86 (2012) 045442.

[352] O. V. Yazyev, Emergence of magnetism in graphene materials and nanostructures, Rep. Progr. Phys. 73 (2010) 056501.

[353] N. Petrone, C. R. Dean, I. Meric, A. M. van der Zande, P. Y. Huang, L. Wang, D. Muller, K. L. Shepard, J. Hone, Chemical vapor deposition-derived graphene with electrical performance of exfoliated graphene, Nano Lett. 12 (2012) 2751–2756.

[354] J. Chen, W. G. Cullen, C. Jang, M. S. Fuhrer, E. D. Williams, Defect scattering in graphene, Phys. Rev. Lett. 102 (2009) 236805.

[355] F. Banhart, J. Kotakoski, A. V. Krasheninnikov, Structural defects in graphene, ACS Nano 5 (2011) 26–41.

[356] J. Kotakoski, A. V. Krasheninnikov, U. Kaiser, J. C. Meyer, From point defects in graphene to two-dimensional amorphous carbon, Phys. Rev. Lett. 106 (2011) 105505.

[357] J. Kotakoski, J. C. Meyer, S. Kurasch, D. Santos-Cottin, U. Kaiser, A. V. Krasheninnikov, Stone-wales-type transformations in carbon nanostructures driven by electron irradiation, Phys. Rev. B 83 (2011) 245420.

[358] G.-D. Lee, C. Z. Wang, E. Yoon, N.-M. Hwang, D.-Y. Kim, K. M. Ho, Diffusion, coalescence, and reconstruction of vacancy defects in graphene layers, Phys. Rev. Lett. 95 (2005) 205501.

[359] J. Ma, D. Alfè, A. Michaelides, E. Wang, Stone-wales defects in graphene and other planar sp^2-bonded materials, Phys. Rev. B 80 (2009) 033407.

[360] L. Li, S. Reich, J. Robertson, Defect energies of graphite: Density-functional calculations, Phys. Rev. B 72 (2005) 184109.

[361] A. A. El-Barbary, R. H. Telling, C. P. Ewels, M. I. Heggie, P. R. Briddon, Structure and energetics of the vacancy in graphite, Phys. Rev. B 68 (2003) 144107.

[362] A. V. Krasheninnikov, P. O. Lehtinen, A. S. Foster, R. M. Nieminen, Bending the rules: Contrasting vacancy energetics and migration in graphite and carbon nanotubes, Chem. Phys. Lett. 418 (2006) 132 – 136.

[363] O. Cretu, A. V. Krasheninnikov, J. A. Rodriguez-Manzo, L. Sun, R. M. Nieminen, F. Banhart, Migration and localization of metal atoms on strained graphene, Phys. Rev. Lett. 105 (2010) 196102.

[364] L. Wang, X. Zhang, H. L. Chan, F. Yan, F. Ding, Formation and healing of vacancies in graphene chemical vapor deposition (CVD) growth, J. Am. Chem. Soc. 135 (2013) 4476–4482.

[365] W. W. Pai, N. C. Bartelt, J. E. Reutt-Robey, Fluctuation kinetics of an isolated Ag (110) step, Phys. Rev. B 53 (1996) 15991.

[366] M. M. Ugeda, D. Fernández-Torre, I. Brihuega, P. Pou, A. J. Martínez-Galera, R. Pérez, J. M. Gómez-Rodríguez, Point defects on graphene on metals, Phys. Rev. Lett. 107 (2011) 116803.

[367] P. Jacobson, B. Stöger, A. Garhofer, G. S. Parkinson, M. Schmid, R. Caudillo, F. Mittendorfer, J. Redinger, U. Diebold, Disorder and defect healing in graphene on Ni(111), J. Phys. Chem. Lett. 3 (2012) 136–139.

[368] J. H. Los, R. J. M. Pellenq, Determination of the bulk melting temperature of nickel using Monte Carlo simulations: Inaccuracy of extrapolation from cluster melting temperatures, Phys. Rev. B 81 (2010) 064112.

[369] E. Meca, J. Lowengrub, H. Kim, C. Mattevi, V. B. Shenoy, Epitaxial graphene growth and shape dynamics on copper: Phase-field modeling and experiments, Nano Lett. 13 (2013) 5692–5697.

[370] M. Itoh, G. R. Bell, A. R. Avery, T. S. Jones, B. A. Joyce, D. D. Vvedensky, Island nucleation and growth on reconstructed GaAs(001) surfaces, Phys. Rev. Lett. 81 (1998) 633–636.

[371] P. Kratzer, M. Scheffler, Reaction-limited island nucleation in molecular-beam epitaxy of compound semiconductors, Phys. Rev. Lett. 88 (2002) 036102.

[372] J. Tersoff, Modeling solid-state chemistry: Interatomic potentials for multicomponent systems, Phys. Rev. B 39 (1989) 5566.

[373] C. Virojanadara, R. Yakimova, A. A. Zakharov, L. I. Johansson, Large homogeneous mono- bi-layer graphene on 6H-SiC(0001) and buffer layer elimination, J. Phys. D: Appl. Phys. 43 (2010) 374010.

[374] P. Erhart, K. Albe, Analytical potential for atomistic simulations of silicon, carbon, and silicon carbide, Phys. Rev. B 71 (2005) 035211.

[375] J. B. Hannon, R. M. Tromp, Pit formation during graphene synthesis on SiC(0001):*In situ* electron microscopy, Phys. Rev. B 77 (2008) 241404.

[376] H. Kageshima, H. Hibino, H. Yamaguchi, M. Nagase, Theoretical study on epitaxial graphene growth by Si sublimation from SiC(0001) surface, Jpn. J. Appl. Phys. 50 (2011) 095601.

[377] H. Kageshima, H. Hibino, S. Tanabe, The physics of epitaxial graphene on SiC(0001), J. Phys.: Condens. Matter 24 (2012) 314215.

[378] X. Wu, Two-Dimensional Carbon - Fundamental Properties, Synthesis, Characterization, and Applications, Pan Stanford Publishing, 2013.

[379] F. Ming, A. Zangwill, Model for the epitaxial growth of graphene on 6H-SiC(0001), Phys. Rev. B 84 (2011) 115459.

[380] F. Ming, A. Zangwill, Model and simulations of the epitaxial growth of graphene on non-planar 6H-SiC surfaces, J. Phys. D: Appl. Phys. 45 (2012) 154007.

[381] J. Robinson, X. Weng, K. Trumbull, R. Cavalero, M. Wetherington, E. Frantz, M. LaBella, Z. Hughes, M. Fanton, D. Snyder, Nucleation of Epitaxial Graphene on SiC(0001), ACS Nano 4 (2010) 153.

[382] D. Totton, C. D. Lorenz, N. Rompotis, N. Martsinovich, L. Kantorovich, Temperature control in molecular dynamic simulations of non-equilibrium processes, J. Phys.: Condens. Matter 22 (2010) 074205.

[383] L. Xu, G. Henkelman, Adaptive kinetic Monte Carlo for first-principles accelerated dynamics, J. Chem. Phys. 129 (2008) 114104.

[384] H. Kim, C. Mattevi, M. Reyes Calvo, J.C. Oberg, L. Artiglia, S. Agnoli, C.F. Hirjibehedin, M. Chhowalla, E. Saiz, Activation energy paths for graphene nucleation and growth on Cu, ACS Nano 6 (2012) 3614-3623.

[385] L. Nemec, V. Bluym, P. Rinjke, M. Scheffler, Thermodynamic equilibrium conditions of graphene films on SiC, Phys. Rev. Lett. 111 (2013) 065502.